Blast Retrofit of Reinforced Concrete Walls and Slabs

by

Eric Jacques

Thesis submitted to the
Faculty of Graduate and Postdoctoral Studies
in partial fulfillment of the requirements for the degree of

Master of Applied Science

in Civil Engineering

Under the auspices of the Ottawa-Carleton Institute for Civil Engineering

uOttawa

University of Ottawa

February 2011

Abstract

Mitigation of the blast risk associated with terrorist attacks and accidental explosions threatening critical infrastructure has become a topic of great interest in the civil engineering community, both in Canada and abroad. One method of mitigating blast risk is to retrofit vulnerable structures to resist the impulsive effects of blast loading. A comprehensive research program has been undertaken to develop fibre reinforced polymer (FRP) retrofit methodologies for structural and non-structural elements, specifically reinforced concrete slabs and walls, subjected to blast loading. The results of this investigation are equally valid for flexure dominant reinforced concrete beams subject to blast effects. The objective of the research program was to generate a large volume of research data for the development of blast-resistant design guidelines for externally bonded FRP retrofit systems. A combined experimental and analytical investigation was performed to achieve the objectives of the program.

The experimental program involved the construction and simulated blast testing of a total of thirteen reinforced concrete wall and slab specimens divided into five companion sets. These specimens were subjected to a total of sixty simulated explosions generated at the University of Ottawa Shock Tube Testing Facility. Companion sets were designed to study one- and two-way bending, as well as the performance of specimens with simply-supported and fully-fixed boundary conditions. The majority of the specimens were retrofitted with externally bonded carbon fibre reinforced polymer (CFRP) sheets to improve overall load-deformation characteristics. Specimens within each companion set were subjected to progressively increasing pressure-impulse combinations to study component behaviour from elastic response up to inelastic component failure. The blast performance of companion as-built and retrofitted specimens was quantified in terms of measured load-deformation characteristics, and observed member behaviour throughout all stages of response. The results show that externally bonded FRP retrofits are an effective retrofit technique to improve the blast resistance of reinforced concrete structures, provided that debonding of the composite from the concrete

substrate is prevented. The test results also indicate that FRP retrofitted reinforced concrete structures may survive initial inbound displacements, only to failure by moment reversals during the negative displacement phase.

The experimental test data was used to verify analytical techniques to model the behaviour of reinforced concrete walls and slabs subjected to blast loading. The force-deformation characteristics of one-way wall strips were established using inelastic sectional and member analyses. The force-deformation characteristics of two-way slab plates were established using commonly accepted design approximations. The response of all specimens was computed by explicit solution of the single degree of freedom dynamic equation of motion. An equivalent static force procedure was used to analyze the response of CFRP retrofitted specimens which remained elastic after testing. The predicted maximum displacements and time-to-maximum displacements were compared against experimental results. The analysis indicates that the modelling procedures accurately describe the response characteristics of both retrofitted and unretrofitted specimens observed during the experiment.

Acknowledgments

I would like to thank my thesis supervisor, Dr. Murat Saatcioglu, for his continued guidance, encouragement and financial support throughout this research project. I would also like to thank my fellow graduate student, Mr. Alan Lloyd, for his assistance in the laboratory and the many educational discussions we had on response of structures to blast loading.

Thanks go out to my parents and sister for giving me the foundation necessary to reach this milestone. Also, I am indebted to Ms. Jennifer Ried for her support and encouragement throughout this academic adventure.

I would also like to thank Rick Guilbeault and Lorne McCauley from the Canadian Explosive Research Laboratory for assistance with instrumentation and high-speed photography during the preliminary phase of experimental testing. The contributions of NSERC, for providing financial assistance during the research, and of Fyfe Co. LLC, for assisting with the financing of some of the CFRP retrofit materials, are also acknowledged and greatly appreciated. The financial support received from CBRNE Research and Technology Initiative (CRTI) of the Government of Canada under Project No: CRTI-06-0150TD is gratefully acknowledged.

Table of Contents

List of Figures

List of Tables

Notations

Acronym		Definition
ANFO	=	Ammonium nitrate fuel oil
CFRP	=	Carbon fibre reinforced polymer
DBD	=	Displacement based design
DLF	=	Dynamic load factor
DMF	=	Dynamic magnification factor
EB	=	Externally bonded
ESF	=	Equivalent static force
EVD	=	Equivalent viscous damping
FRP	=	Fibre reinforced polymer
GFRP	=	Glass fibre reinforced polymer
HSC	=	High strength concrete
HSS	=	High strength steel
NSC	=	Normal strength concrete
NSS	=	Normal strength steel
PI	=	Pressure-impulse
RC	=	Reinforced concrete
SDOF	=	Single degree of freedom
SRP	=	Steel fibre reinforced polymer

Symbol		Definition
A	=	Area, loaded area
A_{LTD}	=	Area, load transfer device
d	=	Effective depth
E_f	=	Modulus of elasticity of FRP
E_s	=	Modulus of elasticity of steel
f_c'	=	Peak concrete stress
f_{cd}	=	Dynamic concrete stress
f_{cs}, f_c	=	Static concrete stress
f_d	=	Atmospheric transmission factor
f_{dy}	=	Dynamic steel yield stress
f_{FRP}	=	FRP stress
f_u	=	Ultimate steel stress
f_y	=	Static steel yield stress
F_{cc}	=	Internal concrete compressive force
F_{FRP}	=	Internal FRP tensile force
F_s	=	Internal steel tensile or compressive force
I	=	Impulse
I^-	=	Impulse during the negative pressure phase

I_r	=	Reflected Impulse
k_L	=	Load transformation factor
k_{LM}	=	Load-mass transformation factor
$k_{LM}(u)$	=	Nonlinear load-mass transformation factor function
k_M	=	Mass transformation factor
K	=	Elastic spring constant
L	=	Length
L_d	=	Driver length
L_{pl}	=	Plastic hinge length
m	=	Mass
$\overline{m}$	=	Distributed mass
m_s	=	System mass
M	=	Moment
M_i	=	Incremental moment
M_{max}	=	Maximum moment
n	=	Number of samples
P	=	Pressure
P_a	=	Ambient pressure
P_d	=	Driver pressure
P_o	=	Standard atmospheric pressure
$P_r, P_r(t)$	=	Reflected pressure
P_{so}	=	Peak incident overpressure of the shock front
P_{so}^-	=	Peak incident underpressure of the shock front
Q_{exp}	=	Mass specific energy of an explosive
Q_{TNT}	=	Mass specific energy of TNT
R	=	Distance from the point of detonation to a target; Resistance
R_i	=	Incremental resistance
$R(u)$	=	Nonlinear resistance function
R^2	=	Coefficient of determination
t	=	Time
t_d	=	Positive phase duration
t_d^-	=	Negative phase duration
t_E	=	Time to yield reinforcing steel
t_f	=	Thickness of FRP composite
t_d/T_N	=	Non-dimensional time parameter
t_{max}	=	Time to maximum displacement
T	=	Temperature
T_N	=	Natural period
T_o	=	Standard atmospheric temperature
$u(t), u$	=	Single degree of freedom displacement
$\dot{u}(t), \dot{u}$	=	Single degree of freedom velocity
$\ddot{u}(t), \ddot{u}$	=	Single degree of freedom acceleration
u_{max}	=	Maximum dynamic single degree of freedom displacement
u_o	=	Initial displacement
u_{st}	=	Maximum static displacement

u_{td}	=	Displacement at time t_d
U_s	=	Wave front velocity of the shock wave
v_o	=	Initial velocity
v_{td}	=	Velocity at time t_d
w	=	Distributed load
w_i	=	Incremental distributed load
W	=	Equivalent explosive mass of TNT
z	=	Shear span
Z	=	Scaled distance
α	=	Dimensionless waveform parameter
γ_c	=	Unit weight of concrete
δ	=	Displacement
δ_{max}	=	Maximum displacement
δ_{res}	=	Residual displacement
ε	=	Strain
ε_c	=	Concrete strain
ε_{cu}	=	Peak concrete strain
ε_o	=	Strain at peak concrete stress
ε_{fd}	=	FRP debonding strain
ε_{FRP}	=	FRP strain
ε_{fu}	=	FRP design rupture strain
ε_{max}	=	Maximum strain
ε_s	=	Steel strain
$\dot{\varepsilon}$	=	Strain-rate
$\dot{\varepsilon}_c$	=	Concrete strain-rate
$\dot{\varepsilon}_{FRP}$	=	FRP strain-rate
$\dot{\varepsilon}_s$	=	Steel strain-rate
θ	=	Support rotation
θ_{max}	=	Maximum support rotation
μ	=	Ductility ratio or displacement ratio
ρ	=	Atmospheric density; Reinforcing steel ratio
ρ_o	=	Standard atmospheric density
ϕ, ϕ_i	=	Curvature; Incremental curvature
$\Phi, \Phi(x)$	=	Displaced shape function
ω	=	Natural frequency

Chapter 1. Introduction

1.1. General

Mitigation of the blast risk associated with terrorist attacks and accidental explosions threatening critical infrastructure has become a topic of great interest in the civil engineering community, both in Canada and abroad. Due to the geopolitical scope and uncertainty of these threats, a multi-facetted socio-economic approach must be adopted to eliminate the risk of an explosive event injuring Canadian citizens and affecting the economic and social well-being of our communities. As a part of this multi-facetted approach, the performance of civil engineering structures subjected to blast loading is currently an active area of research for government, private and military organizations around the globe. These groups share a common goal: the development of documents governing the design and construction of new structures, and the retrofit of existing structures, to resist impulsive blast loading. Owing to the danger, prohibitive cost and uncertainty of experimental blast research, a limited number of publications currently address the issue of blast resistant construction and retrofitting.

In the majority of cases, replacing existing blast-deficient structures with new, blast resistant construction is not feasible for economic, aesthetic and heritage reasons. In these situations, some type of blast resistant retrofit may be required to improve structural performance. Potential retrofit techniques which may mitigate blast hazards on structures and structural systems can be listed as outlined below (ASCE, 1999):

- *Increasing the stand-off distance* reduces the intensity of the blast wave impacting a target. Achieving the same appreciable level of damage at the increased stand-off distance may require an explosive mass which may be too large to be practical.

- *Increasing strength* results in members with a greater ultimate resistance but sustain low levels of deformation. Examples of blast retrofits which increase strength are: externally bonded FRP laminates; increasing section depth; adding additional rein-

forcement; and column jacketing. Generally, these types of retrofits trade reduced ductility for increased strength.

- *Increasing ductility* results in structures which have a higher displacement capacity at the expense of lower ultimate resistance. Blast effects are attenuated by allowing the formation of plastic hinges at regions of maximum moment. Crushing of concrete and yielding of reinforcing steel dissipates blast energy.

- *Increasing mass* may also be an effective retrofit technique for structures which respond in the impulsive loading regime.

Modifying geometry, end conditions and ensuring proper continuity of structural members may also contribute to improved blast resistance.

Externally bonded fibre reinforced polymer (FRP) retrofits for reinforced concrete elements provide an efficient, economical and accepted method of improving structural performance. Externally bonded FRP retrofits have been successfully used to retrofit seismically deficient structures and structures suffering from corrosion related problems. FRPs have several advantages – adaptability, high strength-to-weight ratio and chemical inertness – and are economical as the cost associated with retrofit installation and facility down-time are usually less than similar retrofit systems. A large volume of research has been conducted on FRP retrofitted structures under static and quasi-static loads. Previous research has resulted in the publication of numerous retrofit design methodologies, including those outlined in ACI 440 (2008) and CSA S806-02 (2007) documents. However, only a limited number of publications address the issue of designing FRP retrofit systems to resist blast induced impulsive loads.

In seismic design, ductility – the ability to sustain large inelastic deformations prior to exhibiting excessive strength loss – is a desirable structural characteristic. Proper detailing is required to ensure seismically-induced kinetic energy can be absorbed and dissipated by crushing of concrete and yielding of reinforcing steel in plastic hinge regions. These traits are as desirable in seismic design as they are in blast resistant design. However, excessive inelastic deformations are typically avoided in FRP retrofitted structures; large crack widths generated by plastic hinging lead to highly localized interfacial shear stresses at the location of the FRP

laminate and the edge of the crack. Debonding of the FRP sheets from the concrete substrate will occur if the interfacial stresses exceed either the bond capacity of the matrix or the tensile capacity of concrete. Ultimately, loss of bond between externally bonded FRP and the concrete will lead to a loss of composite action and failure of the structural system. Furthermore, FRP has brittle characteristics, with linearly elastic material behaviour, posing challenges in enhancing member ductility.

The improvement in strength and stiffness behaviour resulting from externally bonded FRP retrofits comes at the expense of reduced ductility and energy dissipation characteristics. Consequently, the dynamic properties of the system will be drastically altered, affecting the response of said system to short duration-high pressure blast loading. For instance, eliminating plastic behaviour and increasing elasticity increases the likelihood of moment reversal during free-vibration response. Secondly, increasing member stiffness increases the likelihood of brittle shear response caused by the activation of higher vibration modes. In addition, the effect of high strain-rates on FRP material properties is poorly understood. Finally, the bond strength between FRP and concrete under blast induced loading is vague at best. The safe, economical and efficient design of blast-resistant externally bonded FRP retrofits depends on the ability to address these challenges.

Improved blast resistance can be expected from properly designed externally bonded FRP retrofit systems. However, several critical issues pertaining to the design of these retrofit systems remain unanswered: (i) how should externally bonded FRP retrofit systems be proportioned to best resist blast loads? (ii) what strain level should the FRP be designed to sustain to reduce the likelihood of debonding failures? (iii) should special detailing be provided to enhance anchorage and bond characteristics? (iv) what analysis procedure is appropriate for design of externally bonded FRP retrofitted structures? This thesis will describe the results of a comprehensive research program underway at the University of Ottawa to develop FRP retrofit methodologies for structural and non-structural reinforced concrete elements subjected to simulated blast loading.

1.2. Previous Blast Research of RC Flexure Members

P.A. Buchan, and J.F. Chen, 2007

Buchan and Chen compiled published literature on the use FRP composites to increase the blast resistance of reinforced concrete beams, columns, slabs, walls and masonry walls. The use of advanced composite retrofits overwhelmingly resulted in structures which exhibited improved blast resistance. FRP debonding from concrete/masonry substrate was commonly reported as the primary mode of failure for retrofitted structures subjected to blast loading.

Commenting on the nature of published results, the authors note that the precise behaviour of FRP retrofitted structures under blast loading is poorly understood and that current research is generally qualitative in nature. This is attributed to the difficulty and prohibitively costly nature of live explosive testing. This necessitates the use of alternative means of simulating the effects of blast. Buchan and Chen also state that design guidelines and best practices need to be established prior to the widespread adoption of blast resistant FRP retrofits.

K.M. Mosalam and A.S. Mosallam, 2001

The objective of this study was to investigate the performance of carbon fibre reinforced polymer (CFRP) retrofits as applied to reinforced concrete slabs subjected to blast loads. Two simply supported square slabs, *2640 mm x 2640 mm x 76.2 mm*, were constructed and reinforced on the tension side only with *9.52 mm* diameter Grade *413 MPa* steel grid reinforcement with bar spacing of *305 mm*. One slab served as a control specimen, while the other was retrofitted with externally bonded CFRP/epoxy laminate in both principle directions on the tension face only; CFRP sheets were *460 mm* wide and *0.584 mm* thick.

Both specimens were tested under static conditions using a high pressure water bag to validate a nonlinear static finite element model of the slabs. A nonlinear transient dynamic analysis was then performed using finite element methods to analyze retrofit performance under blast conditions. Three slabs were considered in the dynamic analysis; both the control slab and the slab with CFRP retrofit on the tension face were analyzed, in addition to a retrofitted slab with CFRP laminate applied to both compression and tensions faces. The following conclusions were drawn as a result of the hybrid experimental/analytical testing regime:

1. Externally bonded CFRP retrofit increased the capacity of the retrofitted slab by *200%*, under static conditions.

2. Slab failure, in both the experimental and analytical results, was controlled by material failure of concrete and steel; material and bond failure of CFRP laminates was not observed.

3. Using the fundamental frequency as a damage index, the CFRP retrofitted slab had a *50%* reduction in fundamental frequency, compared with an *85%* reduction for the control specimen.

4. Externally bonded CFRP retrofits controlled the propagation of steel yielding, both as a function of time and space.

5. Due to reversal of internal forces during rebound of slabs during numerical blast loading, externally bonded CFRP retrofits applied to both faces of slabs was found to be most effective retrofit technique

S.D. Robert, and C.F. Johnson, 2009

An experimental investigation into the benefits of using high strength concrete and high strength vanadium steel reinforcement on the blast performance of reinforced concrete panels was performed. Each panel had dimensions *1625 mm x 857 mm x 101 mm* and reinforced with *#3* (10M equivalent) rebar spaced at *100 mm* in the major bending plane and at *304 mm* in the minor bending plane. Various materials were parameterized and studied: *468 MPa* normal strength steel (NSS); *571 MPa* high strength vanadium steel (HSS); *27 MPa* normal strength concrete (NSC); and *104 MPa* high strength concrete (HSC). Three panels were constructed from high strength concrete and high strength steel, two panels using high strength concrete and normal strength steel, three panels using normal strength concrete and high strength steel and two panels of regular strength concrete and steel. Panels were subjected to simulated blast pressure using a shock tube. Applied pressure was on the order of *380 kPa* and impulse of *7700 kPa-ms*. Panels were configured to behave in one-way bending and were simply supported.

The authors qualitatively concluded that:

1. Using high strength construction materials resulted in reduced deflections and support rotations.

2. High strength concrete/high strength steel showed the best performance, while any combination of HSC/NSS or NSC/HSS showed moderate increases compared with NSC/NSS panels.

3. The possibility of design optimization is afforded by making use of high performance materials.

P.F. Silva, and B. Lu, 2007

The primary objective of this research was to investigate the blast performance of one-way reinforced concrete slabs using both CFRP and steel reinforced polymer (SRP) retrofits. The secondary objective was to study the use of a modified displacement based design (DBD) methodology to predict the charge weight and stand-off distance required to produce a given level of damage. The authors propose a DBD methodology to relate the equivalent viscous damping ratio (EVD) of a linear system to the dynamic magnification factor (DMF).

Five one-way simply supported reinforced concrete slabs were constructed and subjected to live explosive testing. Slab dimensions were *1200 mm x 1200 mm x 90 mm* with a clear span of *1048 mm* in both horizontal directions. One specimen served as an unretrofitted control, two specimens were retrofitted with externally bonded (EB) CFRP retrofits and two specimens with EB SRP retrofit. One of each of the two CFRP and SRP retrofit specimens had retrofit applied to one face, and a corresponding specimen had retrofit applied to both faces. Slabs had a reinforcing ratio of *0.18%,* resulting in the use of three *9.5 mm* steel bars as internal steel reinforcement on the tension face only.

In support of the objectives of the research, the following conclusions were drawn:

1. Externally bonded FRP retrofits are more effective when applied to both faces of a slab due to the development of moment reversal during dynamic response.

2. Debonding of composite materials was not observed. However, increasing the flexural capacity of the slabs resulted in shear failure under blast loading.

3. SRP composite retrofits achieved nearly the same performance of CFRP retrofitted slabs, with the advantage of being more cost effective.

4. The DBD methodology proposed in the paper accurately predicts slab damage levels for given charge weight and stand-off distances provided that slabs are retrofitted on both faces and the damage level is less than ultimate.

Lawver et al., 2003

The authors identified the loading/unloading areas of buildings to be at a high level of vulnerability. Accordingly, they investigated various retrofit techniques to mitigate the blast hazard associated with these areas. Seven full scale test structures were constructed and tested using live explosives. Test slabs had dimensions of *30 ft x 30 ft x 8 in* (*9144 mm x 9144 mm x 203 mm*) thick with a *20 ft x 20 ft* (*6096 mm x 6096 mm*) square bay supported on four reinforced concrete columns. One slab was constructed following conventional RC construction; another constructed using "blast resistant" design consisting of additional upper tension bars. The remaining slabs were constructed using conventional RC design but were retrofitted with various externally bonded FRP composite systems. These systems consisted of four plies of *[0°/90°]* cross-ply unidirectional lamina using unidirectional carbon or unidirectional E-glass fibres. A non-linear finite element simulation accompanied the live explosive testing.

It was concluded that:

1. Externally bonded FRP composites performed well as blast resistant retrofits.

2. Unretrofitted slabs suffered severe damage while retrofitted slabs reduced blast damage to a moderate level.

3. Delamination of FRP and concrete was observed in both numerical and experimental testing.

4. Midspan slab deflection was reduced as the number of plies increased. However this reduction decreases with increasing number of plies, indicating a practical upper limit on the number of additional plies to increase blast capacity.

5. Slab response was controlled by ply tensile capacity and not ply stiffness. Furthermore, a practical upper limit of ply tensile capacity appears to exist, beyond which blast performance ceases to increase.

Razaqpur et al., 2007

Live explosive testing of GFRP retrofitted reinforced concrete panels was performed to investigate the effect of GFRP composite retrofit on blast-induced performance. Eight reinforced concrete panels were constructed and tested with live explosives. Panels were *1000 mm x 1000 mm x 70 mm* and doubly reinforced with diameter *5.74 mm* steel welded wire mesh with bar spacing of *152 mm*. Four panels were retrofitted on each face with *500 mm* wide GFRP strips in a *[0°/90°]* cross-ply configuration, while the remaining four panels served as control specimens. Panels were subjected to explosions created from combinations of *22.4 kg* and *33.4 kg* of ANFO at a stand-off distance of *3.1 m*. Panel performance was quantified by damage levels (light, moderate, heavy, severe) which was measured in terms of crack width, loss of FRP/concrete bond, severity of permanent deformations and FRP rupture. The post-blast static residual capacity of specimens was also used as a performance indicator.

The results of this research indicate that:

1. Under explosive loading of *22.4 kg* of ANFO at *3.1 m*, GFRP retrofitted panels showed significantly better performance than unretrofitted panels. GFRP retrofit resulted in a *75%* increase in residual static capacity over control specimens.

2. Under explosive loading of *33.4 kg* of ANFO at *3.1 m*, retrofit performance was contradictory; some retrofitted panels performed better than their unretrofitted companions, while some retrofitted panels were completely destroyed and companion panels suffered only moderate damage. This may indicate that this charge weight/stand-off combination is at the upper limit of the particular composite retrofit system studied in this research.

3. Generally, the authors qualitatively note that externally bonded GFRP retrofit systems increase the performance and survivability of RC panels, however, more research is required.

D.A Dunkman, A.E.A. Yousef, P.M. Karve, and E.B. Williamson, 2009

Post- and pre-tensioned reinforced concrete panels were tested under simulated blast loading using a shock tube. Panels were *1028 mm* wide, *90 mm* thick and simply supported with a clear span of *2440 mm*. The specimens were subjected to simulated explosions of increasing destructiveness, with the largest shot, resulting in complete collapse of the test specimens, generated a reflected pressure of *753.7 kPa*, duration of *35.5 ms* and reflected impulse of *1309 kPa-ms*. In general, the post-tensioned specimen displayed consistently high damage levels than the pre-tensioned specimen. Both specimens had displacement ratios which exceeded the commonly accepted design limits for post- and pre-tensioned members.

J. Magnusson, 2007

The author performed static and simulated blast testing of 89 reinforced concrete beams of various compressive strengths, ranging from *30 MPa* to *200 MPa*. 49 specimens were constructed with various conventional reinforcement configurations, while the remaining specimens were constructed with steel fibre reinforced concrete with a fibre content of *1%* by volume. Blast loading was simulated using an explosive driven shock tube. Little information is reported on applied pressure-impulse combinations generated by the shock tube.

All reinforced beams failed in flexure during static testing. However, a combined shear-flexure failure mode was observed during dynamic testing. Magnusson reported that stiffer members exhibited a greater tendency to fail in shear, whereas less stiff beams were more likely to fail in flexure. The change from a flexure to shear failure for stiff members was attributed to the activation of higher modes of vibration during impulsive loading resulting in higher shear forces than similar soft elements.

Dynamic analysis of the specimens subjected to blast loading was performed using a single degree of freedom model. The experimental and theoretical displacement time-histories were found to be in general agreement. PI diagrams were generated for flexural failure modes based on the SDOF method using idealized load-time functions, and the results were found to be conservative, particularly for large displacement tests.

C.A. Ross, M.R. Purcell, E.L. Jerome, 1997

The authors investigated the blast response of simply supported CFRP retrofitted beams and slabs subjected to detonation of *110.7 kg* of ANFO explosive at a stand-off distance ranging

from *4.38 m* to *5.34 m*. Six *200 mm x 200 mm x 2740 mm* beams were constructed, each reinforced with two *#5* (15M equivalent) reinforcing bars on the tension face. Three beams were retrofitted with a three ply *[0°/90°/0°]* CFRP retrofit applied to the bottom and sides. Two *200 mm x 3050 mm x 3050 mm* slabs were also constructed, with *#5* reinforcing steel bars spaced at *305 mm* on the tensile face. One slab was retrofitted with a *[0°/±45°/90°]* CFRP angle ply on the tensile face. Lightweight high strength concrete, with a compressive strength of *84.3 MPa* containing nylon fibres, was used. The following conclusions were reached:

1. Beams retrofitted with CFRP survived the initial inbound displacement, however suffered more damage as a result of rebound displacements and reversal of internal moments.

2. Both slabs did not have any residual displacements. However, the formation of *45°* yield line crack pattern on both faces of the slabs indicated moment reversal.

3. All CFRP retrofitted beams and slabs experienced some level of composite debonding, typically occurring on the laminate applied to the sides of the beams and along the edge of the slabs.

4. Application of CFRP retrofit materials to concrete structures will result in stiffer members with increased blast resistance. Difficulties with instrumentation resulted in limit experimental data to further substantiate the test observations.

1.3. Research Needs

The literature review summarized in the preceding section clearly indicates lack of sufficient experimental data on structures subject to blast loading. This may be explained by the difficulty involved in live explosive testing. Furthermore, the little information that is available provides limited data due to the classified nature of this type of research, coupled with concerns over damaging expensive instrumentation which have prevented the collection of critical data, such as shock wave parameters or displacement time-histories.

The consideration of externally bonded fibre reinforced polymers to improve blast performance of reinforced concrete structures is becoming increasingly popular. FRP's offer tremen-

dous potential for strengthening structural and non-structural members in buildings while also improving out-of-plane performance of walls and slabs, and enhancing membrane action to contain blast-induced fragmentation. Though FRP retrofits potentially offer economically viable and structurally sound solutions to blast load resistance, the use of FRP's in buildings is not well understood, particularly under high strain-rates.

The knowledge gap indicated above demonstrates urgent needs for research involving the application of FRP's on building components for protection against blast loads to improve safety and security of Canadians. Therefore a systematic research program was designed to undertake experimental and analytical investigations on FRP retrofitted building components at the University of Ottawa. The current research project forms part of the overall scope, addressing specifically reinforced concrete slabs, walls and beams.

1.4. Objective

The main objective of this research program is to evaluate the use of externally bonded carbon fibre reinforced polymer sheets as a retrofit to improve the resistance of one- and two-way reinforced concrete members subjected to blast loading. Blast loading was simulated using a shock tube. The objective also includes the generation of experimental data on shock wave response of as-built and retrofitted reinforced concrete members, development of analytical modelling techniques to predict member response to blast loading, and development of design recommendations for FRP retrofits of reinforced concrete walls, beams and slabs.

1.5. Scope

The scope of this research program is as follows:

1. Review of previous research into the use of fibre reinforced polymers to retrofit reinforced concrete structures to resist blast loading.

2. Brief review of dynamic analysis and structural response as related to blast loading of reinforced concrete structures. This includes single-degree-of-freedom modelling, material properties under high strain-rates and discussion on FRP failure modes.

3. Design, construction and instrumentation of 9 one-way reinforced concrete panels and 4 two-way reinforced concrete specimens.

4. Retrofit approximately one-third of the specimens with externally bonded carbon fibre reinforced polymer sheets.

5. Testing of 13 specimens using the University of Ottawa's Shock Tube Testing Facility under simulated shock wave loading.

6. Evaluation and interpretation of the experimental data with respect to the performance of retrofitted and as-built specimens.

7. Generate analytical force-deformation characteristics of as-built and retrofitted one- and two-way specimens

8. Perform single-degree-of-freedom dynamic analysis to model the blast induced behaviour of as-built and retrofitted specimens.

9. Compare analytical and experimental results.

10. Formulation of design recommendations for FRP retrofit of structures to resist blast loads.

11. Preparation of a thesis and presentation of experimental data, research findings, and the design methodology.

Chapter 2. Blast Loading and Structural Response

2.1. General

Retrofitting structures to resist blast requires an understanding of three equally important topics: explosive shock propagation to define the loading-time function of an explosion; dynamic analysis to determine blast induced structural response; and structural behaviour to understand the expected behaviour and potential failure modes of blast loaded structures. The following chapter is intended to be a general overview of these fundamental concepts.

2.2. Blast Loading

2.2.1 Blast Characteristics

All explosions are characterized by a rapid release of energy in the form of a gaseous volume change. Depending on the nature of the explosion – physical, chemical or nuclear – this release of energy may also be accompanied by the release of radiation, projectiles, high temperatures and other chemical by-products.

The supersonic combustion of a high explosive is known as detonation. This results in a self-propagating exothermic chemical reaction which transforms the original energetic material into vast quantities of gas. The initial detonation of a high explosive produces pressures of *10 – 30 GPa* and temperatures of *3000-4000 °C* (Smith & Hetherington, 1994). The combustion of a low explosive, known as deflagration, is also a self-propagating exothermic reaction. However, the rate of combustion is much lower and the corresponding shock front is much less powerful than similar high explosives. Regardless of the speed and violence of combustion, both result in the formation of a blast wave as the ambient atmosphere is forcibly compressed by the expanding high pressure gas. This spherical blast wave produces an instantaneous increase, followed by exponentially decreasing blast pressures as the wave travels away from the point of detonation. Eventually, as blast energy is dissipated by the continual expansion of gas and heat, blast pressures decrease to ambient atmospheric conditions.

Meanwhile, a negative suction phase follows the decrease to ambient conditions as the inertia imparted to the surrounding air mass results in a region of negative pressure directly behind the shock front (Smith and Hetherington, 1994). The duration of the negative phase is the time required for the underpressure to return to ambient conditions. As the blast wave continues to propagate, energy loss associated with the continual expansion of the shock front results in decreased peak overpressures at the expense of increased shock wave duration.

2.2.2 Blast Scaling Laws

All parameters required to fully describe the shock wave may be conveniently expressed in terms of a constant of proportionality. Known as blast scaling, two self-similar blast waves will be generated at different distances provided the explosive masses are proportional to the cube root of the energy release. However, it is important to recognize that even minor variations in the surrounding atmospheric medium will have a large impact on the blast waveform parameters. Factors such as temperature, relative humidity, altitude, time of day, season and weather all effect the propagation of explosive shock waves in air (Kinney and Graham, 1985).

Therefore, it is convenient to define a composite term, known as the scaled distance, Z, to describe the similarity between explosions under various atmospheric conditions as

$$Z = f_d \frac{R}{W^{1/3}} \qquad [2.1]$$

where R is the distance from the point of detonation to the target, W is the equivalent mass of trinitrotoluene (TNT) and f_d is a dimensionless atmospheric transmission factor and is defined as

$$f_d = \left(\frac{\rho}{\rho_o}\right)^{1/3} = \left(\frac{P}{P_o}\right)^{1/3} \times \left(\frac{T}{T_o}\right)^{1/3} \qquad [2.2]$$

where ρ, P, and T are the atmospheric density, pressure and temperature respectively. The subscript o denotes values of atmospheric conditions at a reference value. Standard atmospheric conditions are typically defined in terms of the U.S. Standard Atmosphere with a ref-

erence pressure of *101.325 kPa* at *15 °C* at mean sea level (Kinney and Graham, 1985). The effects of relative humidity are not generally considered.

The cube-root scaling law, described in equation [2.1], is defined in terms of a reference mass of TNT, W. TNT equivalency is a standard used to compare the potential explosive energy of a given substance to the explosive potential of TNT. One method of TNT equivalency is to compare the mass specific energy, Q, (measured in *kJ/kg*), of a given explosive material to that of TNT (Esparza, 1986). Therefore, the equivalent weight of TNT, given by UFC-03-340-02 (2008), is

$$W = \frac{Q_{EXP}}{Q_{TNT}} W_{EXP} \qquad [2.3]$$

where Q_{EXP} is the mass specific energy of a given explosive, Q_{TNT} is the mass specific energy of TNT and W_{EXP} is the mass of a given explosive. It is important to note that the shape of the explosive mass exerts great influence on the resulting shock wave and associated blast wave parameters and care must be taken when scaling explosions with different mass shapes.

2.2.3 Blast Waveform and Blast Waveform Parameters

Consider the typical blast waveform in Figure 2.1 caused by free-air detonation of a high explosive at a stand-off distance, R. The blast wave propagates outward radially with decreasing velocity, U_s. The time required for the shock front to propagate a distance R from the point of detonation is known as the time of arrival, t_a. An observer located a distance R from the point of detonation will experience an instantaneous increase in pressure from ambient pressure, P_a, to the peak overpressure of the shock front, P_{so}. As the blast wave continues to propagate, the observer will experience an exponential decay in pressure until atmospheric conditions are reached. This duration of positive blast pressures, t_d, is known as the positive phase duration. The instantaneous increase in pressure is followed by a rapid decrease and formation of a region of negative pressure after the positive phase has passed. The duration of the negative phase is denoted by t_d^-. This negative phase is created by the rapid return of atmospheric conditions rushing to fill the void left by the blast front. Peak underpressure is denoted by P_o^-. The area under the positive pressure portion of the blast curve is known as the positive impulse, I. Similarly, I^- denotes the negative specific impulse. The type of

waveform depicted in Figure 2.1 is known as an incident waveform as it has not interacted with any obstructions.

An exponential decay function may be used to describe the pressure-time history of a high-explosive blast. The incident overpressure, $P(t)$, is written as

$$P(t) = P_o\left(1 - \frac{t}{t_d}\right)e^{-\alpha t/t_d} \qquad [2.4]$$

where α is a dimensionless waveform parameter. This waveform parameter is characteristic to specific explosions and is a function of shock front intensity (Kinney and Graham, 1985). The wave form parameter may be determined by interpolating scaled distances, Z, of tabulated reference explosions from references such as Kinney and Graham (1985).

The impulse, I, imparted by a blast wave on an object is the area under the pressure-time history during the positive phase duration and is calculated by

$$I = \int_0^{t_d} P(t)dt \qquad [2.5]$$

Many references, such as Kinney and Graham (1985) and UFC-03-340-02 (2008), have published figures and tables containing all relevant blast wave parameters as a function of scaled distance, Z, for a reference explosion of TNT in U.S. Standard Atmosphere. These tabulated results are useful in blast resistant design as they allow for efficient determination of blast wave parameters caused by a given charge-weight/stand-off distance under non-standard atmospheric conditions.

2.2.4 Reflection of Blast Waves

Blast waves propagate outward from the point of detonation. When these waves interact with surfaces which are not parallel to direction of the blast, a magnification of incident pressures is experienced. These magnified pressures are known as reflected pressures, P_r.The degree of magnification depends primarily on the size and geometry of the reflecting surface and the magnitude of the incident pressures (Mays and Smith,1995). Reflected pressures are generally more critical than incident pressures for design purposes as the magnification varies from approximately *2* to an order of magnitude larger than incident pressures.

2.3. Dynamic Analysis

2.3.1 Single-Degree-of-Freedom (SDOF) Analysis

By identifying one ordinate that accurately describes the dynamic motion of a complex system, the dynamic response of a structure to blast may be reduced to a single-degree-of-freedom (SDOF) system. Although more detailed and complex methods of dynamic analysis are available, the approximate SDOF method is considered to give acceptable results in lieu of the large uncertainties associated with blast design (Biggs, 1964).

Consider the SDOF mass-spring representation of a structural system, shown in Figure 2.2, subjected to an external forcing function. Based on static equilibrium of dynamic forces, the response of the system may be written as

$$m\ddot{u}(t) + ku(t) = AP(t) \qquad [2.6]$$

where m is the mass of the system, k is the stiffness, A is the area exposed to blast loading, $P(t)$ is the time-variant forcing function and u and $\ddot{u}$ are the displacement and acceleration of the mass, respectively. Due to the short duration of structural response to blast, damping is typically neglected (Biggs, 1964).

A closed-form solution to the equation of motion is most convenient when the forcing function is simple and member resistance is proportional to the displacement of the system. Numerical integration of the equation of motion is preferred when member response is expected to be non-linear or the forcing function is a set of discrete pressure-time points. Replacing the spring force, $ku(t)$, in equation [2.6] with a non-linear resistance term, $R(u)$, the following non-linear SDOF equation of motion is obtained:

$$m\ddot{u}(t) + R(u(t)) = AP(t) \qquad [2.7]$$

A number of numerical techniques are described in literature to solve this type of equation of motion; however, the average acceleration method is particularly useful due to its ease of use and unconditional stability (UFC-03-340-02, 2008).

Several closed-form approximations of blast pressure-time history exist, the most common being a linearly decreasing function and an exponentially decreasing function (e.g. equation

[2.4]). Due to simplicity, an idealized linearly decreasing forcing function may used to describe the first positive phase of blast loading (UFC-03-340-02, 2008). This forcing function, shown in Figure 2.2 c), is given as

$$P_r(t) = P_r\left(1 - \frac{t}{t_d}\right) \qquad [2.8]$$

where P_r is the peak reflected pressure and t_d is the duration of the first positive phase. The impulse, I, is the area under the pressure-time history and is defined as

$$I = \int_0^{t_d} P_r(t)dt = \frac{P_r t_d}{2} \qquad [2.9]$$

Equating equations [2.6] and [2.8] yields the following second order differential equation:

$$m\ddot{u}(t) + ku(t) = AP_r\left(1 - \frac{t}{t_d}\right). \qquad [2.10]$$

The solution to equation [2.10] during the forced-vibration phase when $0 \leq t \leq t_d$ is

$$u(t) = \left(u_o - \frac{AP_o}{k}\right)\cos \omega t + \frac{\left(v_o + {AP_o}/{kt_d}\right)}{\omega}\sin \omega t + \frac{AP_o}{k}\left(1 - \frac{t}{t_d}\right) \qquad [2.11]$$

where $\omega = \sqrt{k/m}$ is the natural frequency of the structure and u_o and v_o are the initial displacement and velocity, at time $t = 0$, respectively.

The free-vibration response of the system in equation [2.10] during the free-vibration phase when $t \geq t_d$ is given by

$$u(t) = u_{t_d} cos\omega(t - t_d) + \frac{v_{t_d}}{\omega}\sin\ \omega(t - t_d) \qquad [2.12]$$

where u_{t_d} and v_{t_d} are the displacement and velocity of the mass at time $t = t_d$, respectively, obtained from equation [2.11].

2.3.2 Modelling Structures as Equivalent SDOF Systems

It is possible to describe the motion of a multi-degree of freedom structure by the motion of a single ordinate through the use of transformation factors. The use of transformation factors to approximate the response of a distributed system has been described in detail by Biggs (1964) and UFC-03-340-02 (2008) but is summarized here for completeness.

An equivalent system is selected such that the displacement-time history of the equivalent ordinate is the same as that of an ordinate of the real structure. This equivalent ordinate is typically taken at the location of maximum displacement. In this way, the mass of the distributed system is lumped at the position of the equivalent ordinate and the distributed force and stiffness are lumped as a series of point loads acting on the lumped mass. Transformation factors for an equivalent SDOF system are generated by assuming deflected shapes caused by the static application of the dynamic loads (Biggs, 1964).

The selection of an appropriate shape function is critical in generating transformation factors. Shape functions must be selected that capture anticipated member behaviour. The formation of plastic hinges indicates a transition from elastic bending to rigid body motion and this behaviour must be described by the shape function to yield adequate results (Biggs, 1964).

In reality, the on-set of plastic behaviour will result in a gradual change in dynamic properties of the system; employing discontinuous shape functions to describe this behaviour will introduce some uncertainty to the calculations, although this is generally regarded as acceptable in context of the approximate SDOF method (Biggs, 1964).

The mass factor, k_M, is required to transform a system with distributed mass into an equivalent SDOF system with lumped mass. The mass factor is defined as

$$k_M = \frac{\int_0^L \bar{m}\Phi(x)^2 dx}{\bar{m}L} \qquad [2.13]$$

where $\bar{m}$ is the mass per unit length of the member and $\Phi(x)$ is the shape function of the member.

The load factor, k_L, is used to transform distributed force and stiffness to a single point load and is computed by the following equation

$$k_L = \frac{\int_0^L P\Phi(x)dx}{PL} \quad [2.14]$$

It is convenient to define a single load mass factor, k_{LM}, as the ratio of the mass factor to the load factor

$$k_{LM} = \frac{k_M}{k_L} \quad [2.15]$$

The equation of motion of an equivalent single degree of freedom system with non-linear resistance incorporating k_{LM} thus becomes

$$k_{LM}m\ddot{u}(t) + R(u(t)) = AP(t) \quad [2.16]$$

The above procedure may be utilized to transform almost any structural element into an equivalent single-degree-of-freedom model, provided appropriate shape functions are selected which adequately describe structural behaviour as the member progresses from elastic to plastic response regimes. Furthermore, non-rigid supports, such as the flexible beam-column joint in a frame structure, may also be modelled using this technique.

Common transformation factors have been published as design aids in several references, notably in Biggs (1964) and UFC-03-340-02 (2008). These design aids are applicable for both one-way and two-way flexure members, under a variety of common support conditions subjected to both distributed and concentrated point loads.

2.3.3 Equivalent Static Force Procedure

The dynamic load factor (DLF) is typically defined as the ratio between the maximum dynamic displacement, u_{max}, to maximum static displacement, u_{st}. The DLF may also be defined in terms of resistance and internal forces for an *elastic* structure, as these values are proportional to displacement (Biggs, 1964). The DLF defined in terms of displacement is given as

$$DLF = \frac{u_{max}}{u_{st}}. \quad [2.17]$$

A non-dimensional time parameter, t_d/T_N, is typically defined in conjuction with the use of the DLF (Biggs, 1964), where the natural period of the system is given as $T_N = 2\pi/\omega$. Consider Figure 2.3, a typical response plot for an elastic structure excited by a linearly decreasing load. The response plot shows the variation in both the DLF and the ratio between time-to-maximum displacement and natural period, t_{max}/T, versus the non-dimensional time parameter t_d/T. If the duration of the loading is much less than the natural period ($t_d/T \ll 1$), the dynamic displacement will be much less than the static displacement. Furthermore, this displacement will be achieved at a time much greater than the duration of the load. This behaviour is known as an *impulsive response* as the structure has not had sufficient time to develop a sufficient level of resistance of overcome the initial impulse imparted to the structure by the load (Magnusson, 2007). Similarly, when blast duration is much greater than the natural period, ($t_d/T \gg 1$), the maximum dynamic displacement will be equal to twice the static displacement. Furthermore, the time-to-maximum displacement of such a system will be far less than the duration of the load itself. This is known as a *quasi-static response*. The asymptotic nature of the DLF in the impulsive and quasi-static regimes is convenient for design purposes when the ratio of blast duration to natural period is either quite large or quite small. However, when $t_d/T \approx 1$, the DLF is no longer asymptotic and a dynamic analysis must be used to determine member response. This is known as *dynamic response*.

The use of a dynamic load factor greatly simplifies the analysis procedure as the equation of motion does not need to be solved explicitly to determine maximum member response. Maximum member response is computed by applying an equivalent static force (ESF) to the structure. This equivalent static force is the dynamic peak pressure acting on the system multiplied by the DLF. Equivalent static force analysis generally yields good results for linear elastic structures (Biggs, 1964).

2.3.4 Pressure-Impulse (PI) Diagrams

Mays and Smith (1995) proposed a set of limits on the product ωt_d defining the impulsive, dynamic and quasi-static response regimes:

$$\begin{aligned} 0.4 > \omega t_d &\text{ Impulsive response} \\ 0.4 < \omega t_d < 40 &\text{ Dynamic response} \\ \omega t_d > 40 &\text{ Quasi-static response} \end{aligned} \qquad [2.18]$$

Depending on the characteristics of the blast load (i.e. pressure-impulse combination), it is possible for a structure to achieve the same response level following either an impulsive, dynamic or quasi-static regime. From a protective design standpoint, a logical extension of this is the development of a pressure-impulse (PI) diagram (Mays and Smith, 1995). A PI diagram is simply an iso-damage or iso-response contour plot consisting of a series of pressure-impulse combinations which generate the same level of structural response. Structural response may be observed qualitatively (i.e. high, medium, low blast damage) or measured quantitatively (displacement, ductility ratio, support rotation, etc). This phenomenon is illustrated in the PI diagram shown in Figure 2.4. The contour plot on the PI diagram represents a specific level of structural response, in this case maximum displacement, u_{max}. Pressure-impulse combinations which lie to the left and below the contour indicate response levels less than maximum displacement, while those which lie above and to the right will result in response levels greater than the defined limit. In this regard, a PI diagram is conceptually similar to a P-M interaction diagram used in column design. By generating a PI diagram for a given structural element, and plotting pressure-impulse combinations corresponding to various anticipated explosive threats, the performance of the structure may be evaluated graphically.

2.4. Force-deformation Characteristics

The force-deformation characteristics required to perform dynamic analysis are the resistance, R, of a member and the corresponding load-mass transformation factors, k_{LM}. The resistance curve is the total statically applied load resisted by a structure and the resulting

member displacement at the location of the equivalent ordinate used in the SDOF analysis. The force-deformation characteristics used in the dynamic analysis should include the effect of dynamic strength of materials under high strain-rate loading and should describe the transition from elastic to plastic behaviour. Member resistance and displacement (and hence transformation factors) are inherently related. Therefore, detailed member resistance curves and variable transformation factors may be determined through non-linear analysis techniques. However, these may also be approximated using simplified force-deformation relationships published in literature. Simplified force-deformation properties, such as those found in by Biggs (1964) and UFC 03-340-02 (2008), generally yield approximate results relative to more detailed analysis methods.

Consider the idealized force-deformation curve of an as-built (unretrofitted) reinforced concrete member in flexure shown in Figure 2.5, shown as the solid black line with white dots. Initially, the member remains elastic until reinforcing steel begins to yield. As deflections continue to increase, member resistance begins to plateau as reinforcing continues to yield. A collapse mechanism has formed once concrete begins to crush and member resistance decreases with the progression of plastic hinging. Retrofitting the as-built reinforced concrete flexure member with externally bonded fibre reinforced polymers will result in increased member strength and stiffness, as illustrated by the red dashed line in Figure 2.5. Due to the large amount of elastic strain energy stored within the FRP, the retrofitted structure is expected to remain elastic until failure of the retrofit. Failure of the retrofit may be precipitated by rupture or delamination of the composite material. Alternatively, failure may be caused by debonding of FRP from the concrete substrate. The post-FRP failure force-deformation characteristics of retrofitted reinforced concrete flexure members is assumed to follow the force-deformation characteristics of the unretrofitted structure. However, as the energy required to fail the retrofit is so large, it is likely that the post-retrofit failure capacity is insignificant.

2.4.1 Composite Debonding Failure

Under static conditions, failure of FRP retrofitted reinforced concrete flexure members is generally controlled by debonding of the composite from the concrete substrate (Teng and Chen, 2009). A summary of various FRP retrofitted beam failure modes is shown in Figure 2.6. Debonding failures, d) through g) in Figure 2.6, may be broadly lumped into two catego-

ries: intermediate crack debonding and plate end debonding. Intermediate crack debonding failures occur when large flexure and/or shear cracks form, resulting in high local interfacial stresses between the concrete substrate and the FRP sheet. Once the interfacial stress demand exceeds the bond capacity of the retrofit, debonding failure of the laminate will propagate in the direction of the nearest sheet end. Plate end debonding failures occur at the location of the ends of the FRP sheet caused by high normal and shear interfacial stresses exceeding the tensile capacity of concrete (Teng and Chen, 2009). Both types of failure are characterized by a "zipper" effect as the FRP debonds along the plane of highest interfacial stress. In an effort to prevent interfacial crack debonding under static conditions, ACI 440.2R-08 (2008) recommends limiting the strain in FRP reinforcement at which debonding may occur, ε_{fd}, as given by the following equation:

$$\varepsilon_{fd} = 0.41\sqrt{\frac{f_c'}{nE_f t_f}} \leq 0.9\varepsilon_{fu} \qquad [2.19]$$

Similarly, in Canada, CSA S806-02 (2007) limits maximum strain in flexural FRP, ε_{FRP}, to *0.007* for design purposes. However, both the upper limit on strain in the Canadian code and equation [2.19] were developed based on static test data. Accordingly, its application to blast loaded structures may or may not be applicable. No FRP debonding models currently exist for dynamic loading debonding failures (Buchan and Chen, 2007).

ACI 440.2R-08 (2008) permits the use of supplemental mechanical end-anchorages, such as FRP anchors, to mitigate the likelihood of debonding failures, provided the effectiveness of these systems has been substantiated through testing. FRP anchors are a rolled-up tube of resin-saturated fibre reinforced polymer material which has been inserted into a hole in the concrete substrate and then bonded to the existing FRP sheet. FRP anchors "nail" FRP sheets in place, effectively supplementing the primary mechanism of chemical bond between concrete and the resin by resisting tensile normal stresses in the FRP sheet. Relative movement between the FRP sheet and concrete substrate is required to activate the FRP anchors. Consequently, the performance of any retrofit system incorporating FRP anchors is not affected until debonding of the sheet has begun to occur and the anchors have been activated (Quattlebaum, 2005). Saatcioglu, Serrato and Foo (2005) reported that FRP anchors effectively

prevented delamination of CFRP covered masonry infill walls during seismic response. Orton, Jirsa and Bayrak (2008) performed static testing of FRP retrofitted reinforced concrete beams with FRP anchors to prevent progressive collapse. They found that the full tensile capacity of externally bonded CFRP can be developed without debonding failure when using FRP anchors. Ozbakkalogu and Saatcioglu (2009) performed static pullout testing of FRP anchors of various diameters, embedment depths and inclination angles. Results indicate that FRP anchors can be designed to resist large pull-out forces and can be used to prevent or delay premature debonding of externally bonded FRP sheets. Lam and Teng (2001) studied the performance of GFRP retrofitted cantilever slabs with GFRP fibre anchors subject to monotonic loading. They reported that debonding was less likely to occur when GFRP fibre anchors were used, and that if debonding did occur, the anchors were able to stop debonding progression. Results of static testing of FRP anchors indicate that these anchorages may be effective at mitigating debonding failures. However, more research is required to determine their behaviour under impulse blast loading.

2.4.2 Material Properties at High Strain-Rates

Materials experience an increase in strength caused by high strain-rates. Bischoff and Perry (1991) proposed criteria for defining the type of loading, as a function of strain-rate, $\dot{\varepsilon}$, shown in Figure 2.7. Static loads are associated with strain-rates on the order of $10^{-5}\ sec^{-1}$, while dynamic loads, such as hard impacts and blast, are associated with strain-rates on the order of 10^{1}-$10^{3}\ sec^{-1}$. Accounting for the effects of high strain-rates is critical in the analysis and design of members subjected to blast as the increase in material strength caused by high strain-rates affects structural response by increasing member strength and stiffness.

The dynamic increase factor, DIF, is defined as the ratio of dynamic material strength to static material strength. It is defined as a function of material yield strength and the time required to yield reinforcement, t_E (UFC 03-340-02, 2008). Typical high strain-rate stress-strain curves for concrete and steel are shown in Figure 2.8 a) and b), respectively. The strain-rate of concrete, $\dot{\varepsilon}_c$, is defined as

$$\dot{\varepsilon}_c = \frac{\varepsilon_o}{t_E} \qquad [2.20]$$

where ε_o is the peak strain of concrete and t_E is the time required to yield reinforcement.

Similarly, the strain-rate of reinforcing steel, $\dot{\varepsilon}_s$ is defined as

$$\dot{\varepsilon}_s = \frac{f_{dy}}{E_s t_E} \quad [2.21]$$

where f_{dy} is the dynamic yield strength of steel.

Concrete

For both the tensile and compressive behaviour of concrete under high strain-rates, two distinct regions of behaviour may be identified; at moderately high strain-rates, the relative strengths of concrete remain relatively low, while a sharp transition associated with rapidly increasing dynamic increase factors occurs at higher strain-rates. The discontinuous change observed in DIF is indicative of a change in physical response of the material to dynamic loading (Biscoff and Perry, 1991). At strain-rates below $1\ s^{-1}$, porosity and free water within concrete pores exert considerable influence on dynamic strength (Toutlemonde, et al., 1995). However, at strain-rates above $1\ s^{-1}$, a time lag in radial acceleration associated with Poisson's effect, known as lateral inertial confinement, results in a sharp increase in DIF (Biscoff and Perry, 1995).

To account for the strength enhancement caused by high strain-rate loading of concrete in compression, a DIF for concrete in compression has been adopted by the CEB Model Code (CEB, 1990). This formulation defines the DIF for concrete in compression as

$$DIF = f_{cd}/f_{cs} = \left(\frac{\dot{\varepsilon}}{\dot{\varepsilon}_s}\right)^{1.026\alpha} \text{ For } \dot{\varepsilon} \leq 30\ s^{-1} \quad [2.22]$$

$$DIF = f_{cd}/f_{cs} = \gamma_s \left(\frac{\dot{\varepsilon}}{\dot{\varepsilon}_s}\right)^{1/3} \text{ For } 30\ s^{-1} < \dot{\varepsilon} \leq 300\ s^{-1} \quad [2.23]$$

with

$$\log \gamma_s = 6.156\alpha_s - 2 \quad [2.24]$$

$$\alpha_s = \frac{1}{5 + 9\, f_{cm}/f_{cmo}} \quad [2.25]$$

where f_{cd} is the dynamic strength of concrete in compression (in MPa), f_{cs} is the static strength of concrete in compression (in MPa), f_{cmo} is equal to 10 MPa, $\dot{\varepsilon}$ is the strain-rate (in s^{-1}) and $\dot{\varepsilon}_s$ is the quasi-static strain-rate ($-30 \times 10^{-6}\ s^{-1}$).

Similar relationships describing the effect of strain-rate on the tensile strength of concrete have been discussed in literature (Malvar, 1998a) however they have not been discussed here as the tensile strength of concrete may be conservatively ignored in flexural response.

Steel

Similar to concrete, reinforcing steel experiences an increase in material properties due to dynamic loading. However, unlike concrete, the DIF for steel is understood with a greater level of confidence. This is partly due to material isotropy and the high degree of standardization and precision associated with steel manufacturing (Fu, Erki and Seckin, 1991). Malvar (1998b) performed a review of existing research on dynamic material behaviour of reinforcing steel and found that the DIF of both yield and ultimate stress are inversely proportional to yield stress; high grade reinforcing steel experiences a smaller DIF than lower grade steel. Furthermore, the ultimate strength of steel experiences a much smaller increase than the yield strength. Modulus of elasticity is independent of strain-rate.

Based on the relationship proposed by Malvar (1998b), the DIF for both the yield and ultimate stress is given by:

$$DIF = \left(\frac{\dot{\varepsilon}_s}{10^{-4}}\right)^{\alpha} \qquad [2.26]$$

where the DIF for the yield strength of steel may be determined by substituting $\alpha = \alpha_{f_y}$ in equation [2.26] by the following

$$\alpha_{f_y} = 0.074 - \frac{0.040 f_y}{414} \qquad [2.27]$$

where f_y is the static yield strength of steel (in MPa). Similarly, the DIF for the ultimate strength of steel may be determined by substituting $\alpha = \alpha_{f_u}$ in equation [2.26] by the following

$$\alpha_{f_u} = 0.019 - \frac{0.009 f_y}{414} \quad [2.28]$$

The above formulations are valid for strain-rates in the range of 10^{-4} and $225\ s^{-1}$ and for yield strengths between *290* and *710 MPa* (Malvar, 1998b).

Unidirectional CFRP

Harding and Welsh (1983) performed high strain-rate testing of unidirectional carbon/epoxy composites using a modified split Hopkinson's pressure bar. Strain rates between $10^{-4}\ s^{-1}$ to $1000\ s^{-1}$ were achieved. At these levels of strain, the authors observed that the mechanical properties of unidirectional CFRP were found to be independent of strain-rate and no significant change in static properties was observed. Sample high strain-rate stress-strain curves for the CFRP samples tested are shown in Figure 2.11.

Incorporating Material DIF into Analysis

Determining the correct values for the DIF of reinforced concrete is an iterative procedure. This procedure, recommended by UFC 03-340-02 (2008), is as follows:

1. Assume initial DIF factors for analysis based on those listed in Table 2.1 for close-in or distant explosions.
2. Generate static force-deformation characteristics of the structure, incorporating appropriate material dynamic increase factors to account for high strain-rate effects.
3. Perform dynamic analysis and determine time to yield, t_E, of reinforcing steel.
4. Calculate strain-rate of concrete and steel by equations [2.20] and [2.21], respectively.
5. Determine new DIF based on the strain-rates computed in step 3:
    - If the new DIF are significantly different than those of the previous step, return to step 1 incorporating the new DIF.
    - If the new DIF are the same as the old DIF, the procedure has significantly converged and appropriate DIF have been selected.

In lieu of performing an iterative analysis to find the correct strain-rate and material increase factor, UFC 03-340-02 (2008) permits the use of assumed high strain-rates depending on the nature of the blast. For reinforced concrete members in flexure subject to a distant explosion, an assumed strain-rate of $0.1\ s^{-1}$ is recommended. Similarly, a strain-rate of $0.3\ s^{-1}$ is recommended for a close-in explosion. Common material dynamic increase factors utilized for design purposes are shown in Table 2.1.

2.4.3 Blast Performance Criteria

Blast performance of reinforced concrete structures is typically measured as a function of maximum displacement, δ_{max} . Three such criteria exist:

- Support rotation, θ, is calculated based on the maximum rotation of the supports of a flexure member corresponding to a maximum member deflection and is typically reported in degrees
- Ductility ratio, $\mu = \frac{\delta_{max}}{\delta_y}$, is the ratio of maximum member displacement to member yield displacement, δ_y
- Deflection ratio, $\frac{\delta_{max}}{L}$ is the ratio of maximum member displacement to span length, L and is typically reported as a percentage

UFC 03-340-02 (2008) suggests that blast resistant structures be designed according to support rotations, while ASCE (1999) suggests performance be measured in terms of deflection ratio. These performance criteria are summarized in Table 2.2. Those criteria defined in UFC 03-340-2 may be considered conservative for design purposes, while those described by ASCE are empirical and are less suited for design (ASCE, 1999).

Table 2.1: Dynamic increase factors for reinforced concrete members (UFC 03-340-02, 2008).

TYPE OF STRESS	FAR DESIGN RANGE			CLOSE-IN DESIGN RANGE		
	Reinforcing Bars		Concrete	Reinforcing Bars		Concrete
	f_{dy}/f_y	f_{du}/f_u	f'_{dc}/f'_c	f_{dy}/f_y	f_{du}/f_u	f'_{dc}/f'_c
Bending	1.17	1.05	1.19	1.23	1.05	1.25
Diagonal Tension	1.00	------	1.00	1.10	1.00	1.00
Direct Shear	1.10	1.00	1.10	1.10	1.00	1.10
Bond	1.17	1.05	1.00	1.23	1.05	1.00
Compression	1.10	------	1.12	1.13	------	1.16

Table 2.2: Blast Performance criteria for reinforced concrete flexure members.

	Performance Criteria Definition	
	ASCE (1999)[1]	**UFC 03-340-02 (2008)**
Damage Level	**Displacement ratio, $\frac{\delta}{L}$**	**Support Rotation, θ**
Light/Low	4%	2°
Moderate/Medium	8%	6°
Severe\High	15%	12°

1 – Reinforcing ratio, $\rho > 0.5\%/face$

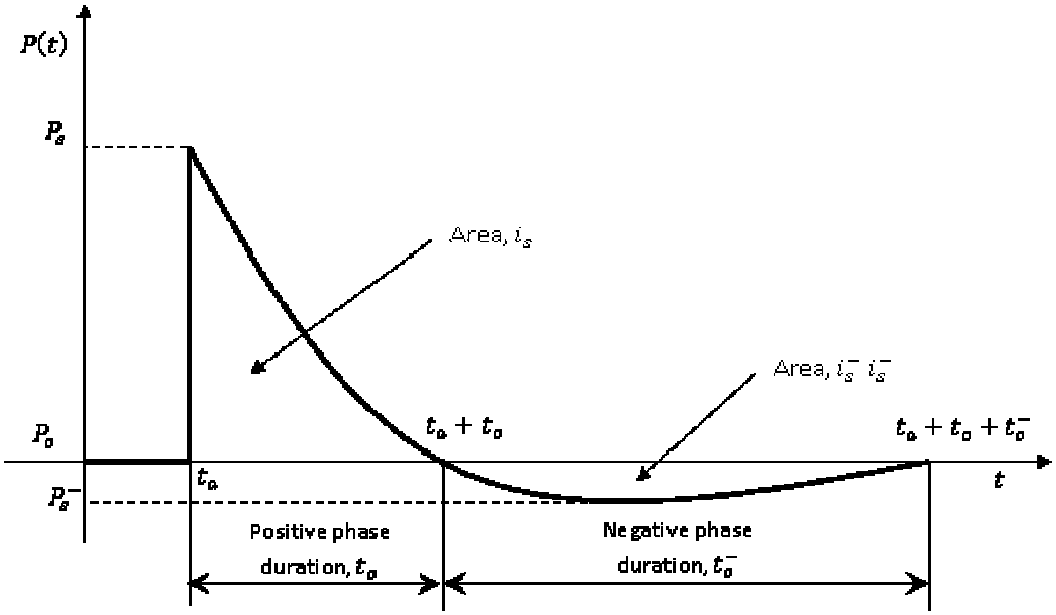

Figure 2.1: Typical Blast Pressure Waveform Generated by Detonation of High Explosive.

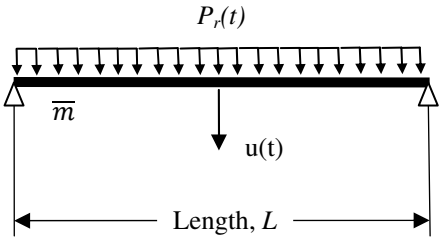

a) Real structure

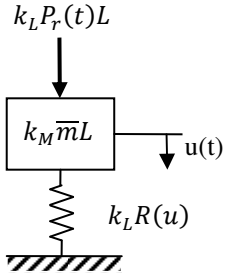

b) Equivalent SDOF system

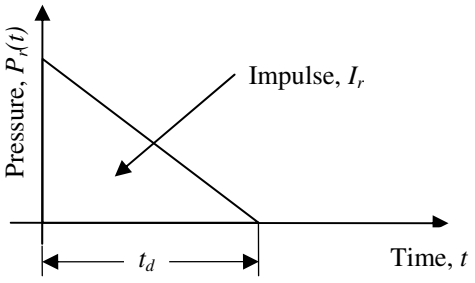

c) Idealized pressure-time history

Figure 2.2: Single-degree-of-freedom system.

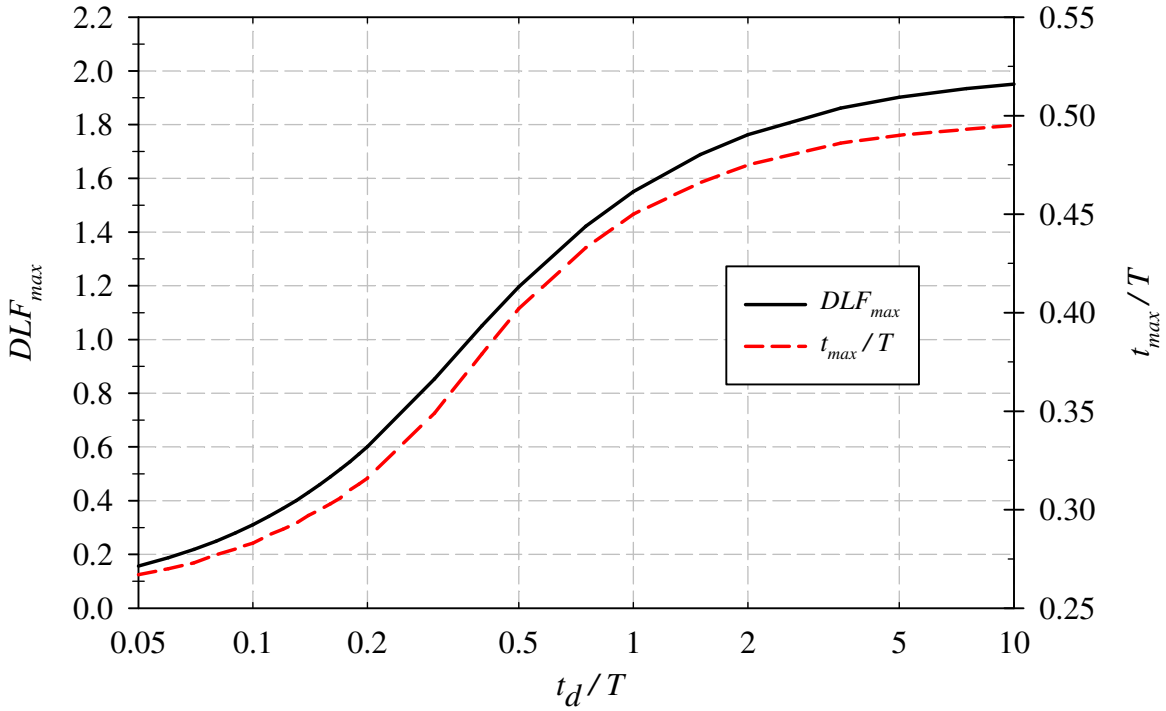

Figure 2.3: Response Plot for an Elastic Structure Subject to a Linearly Decreasing Pressure Function.

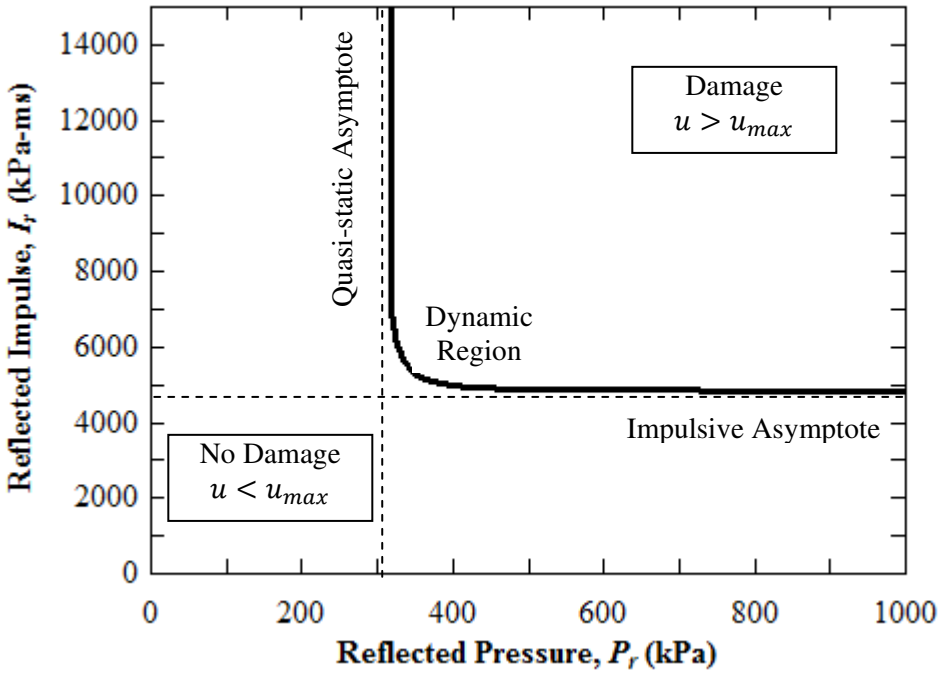

Figure 2.4: Typical Iso-damage Contour Plot/Pressure-Impulse (PI) Diagram.

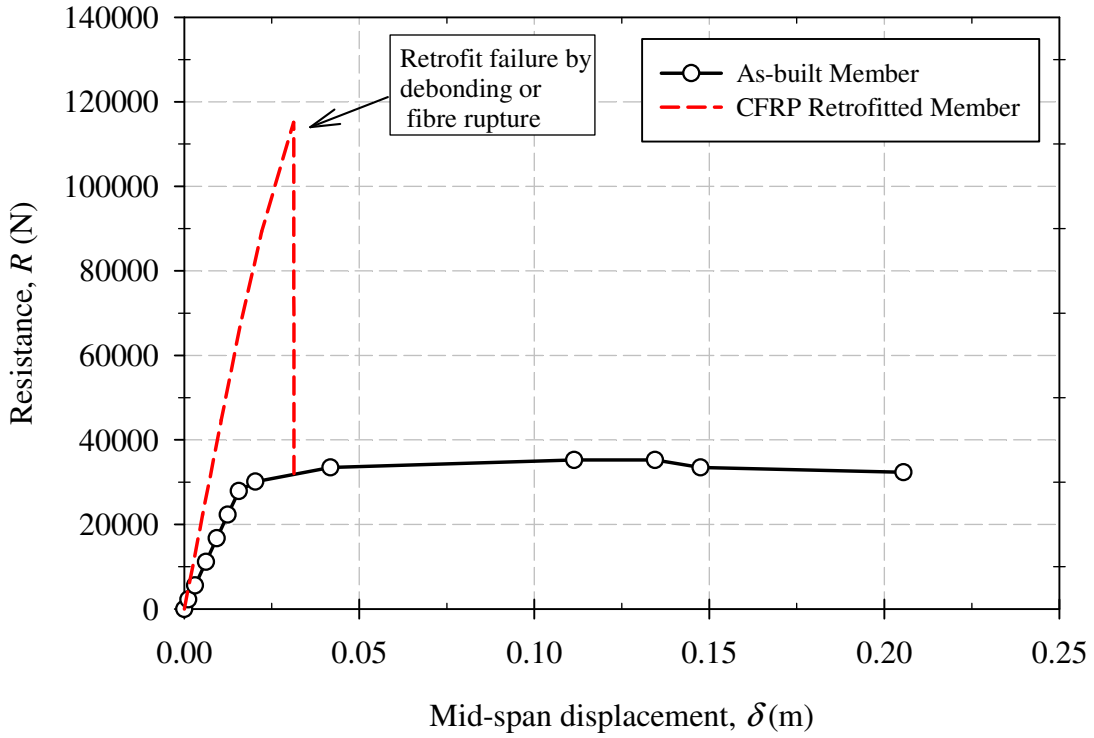

Figure 2.5: Typical Resistance Curves for As-built and CFRP Retrofitted RC Flexure Members.

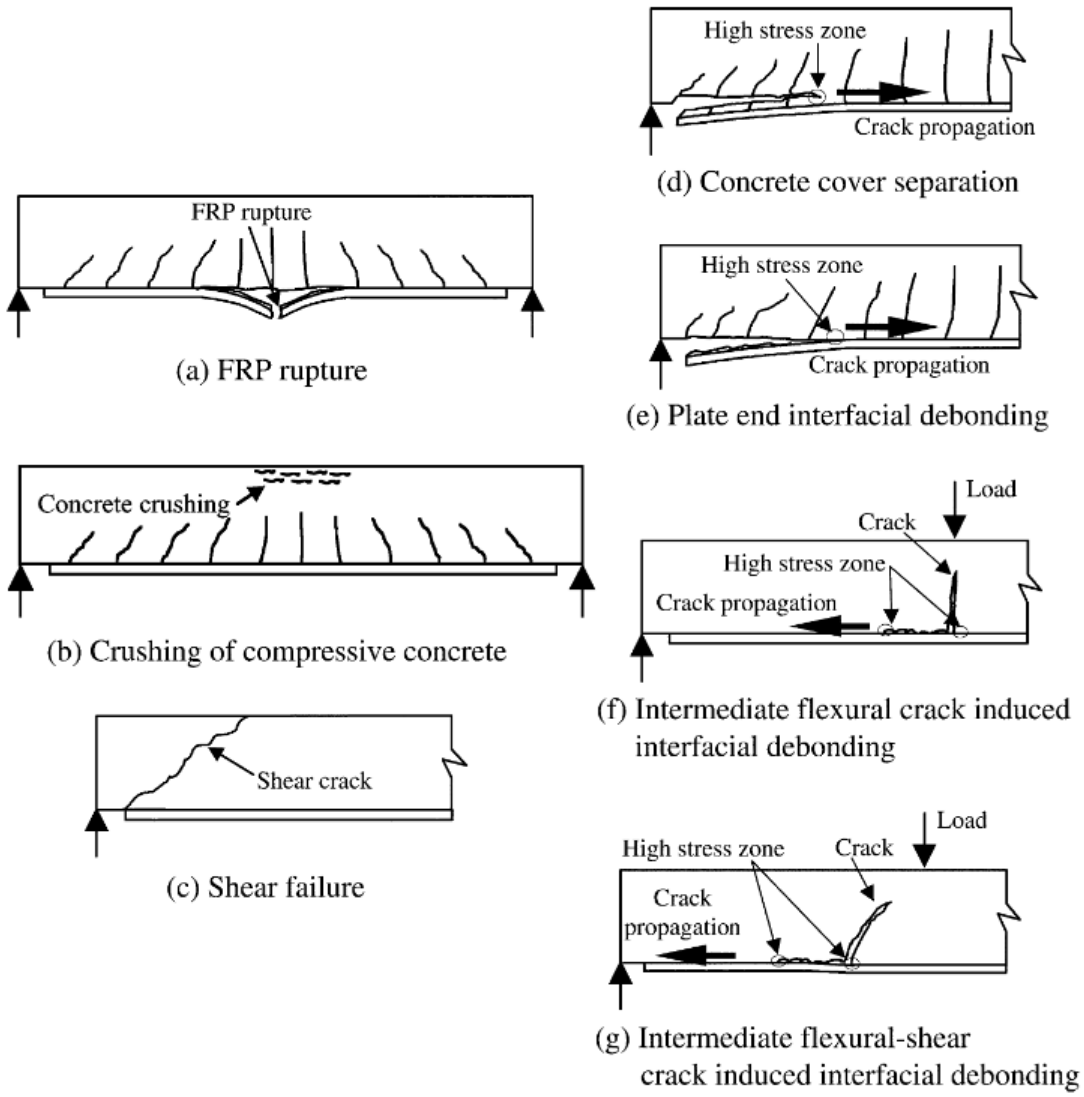

Figure 2.6: Potential FRP Retrofitted Beam Failure Modes (Teng et al, 2003).

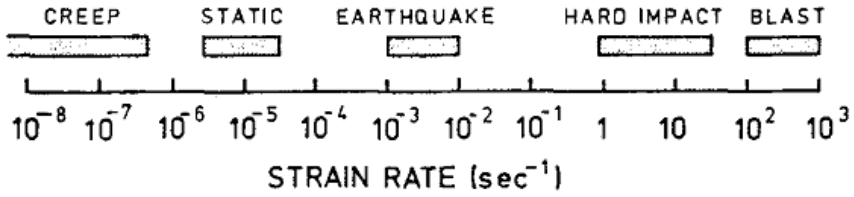

Figure 2.7: Magnitude of Strain-rates Expected for Different Loading Cases (Bischoff and Perry, 1991).

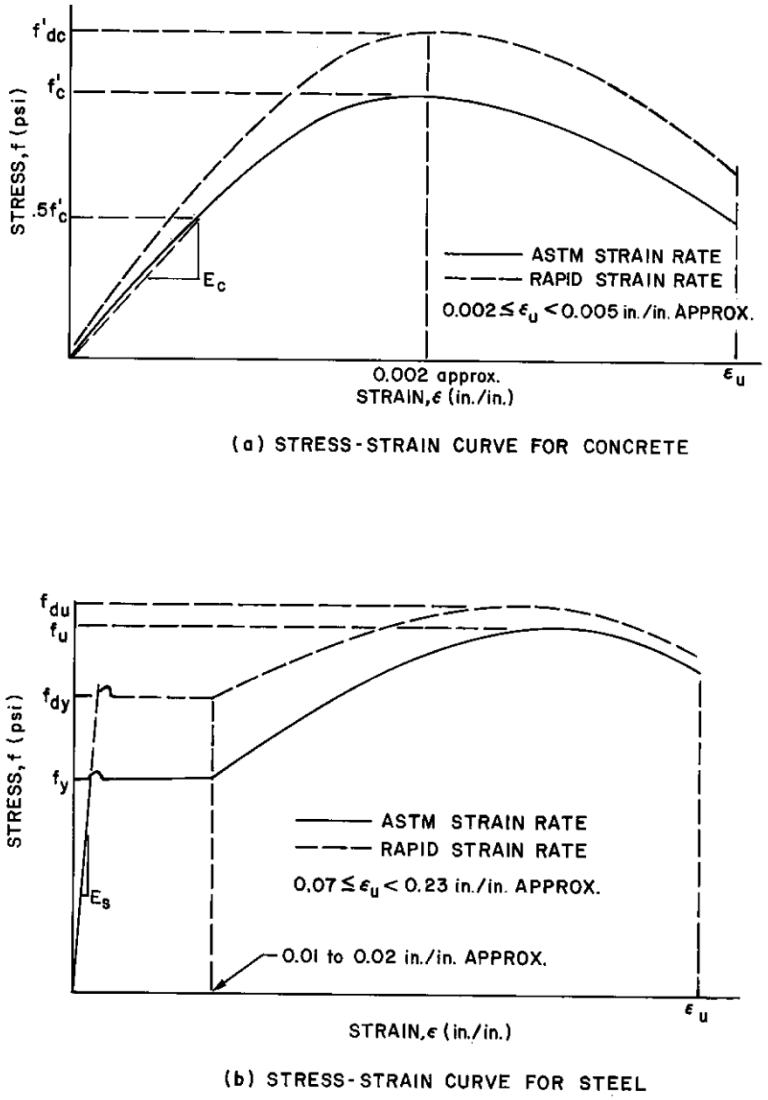

Figure 2.8: Typical Stress-strain Curves for Concrete and Reinforcing Steel (UFC 03-340-02, 2008)

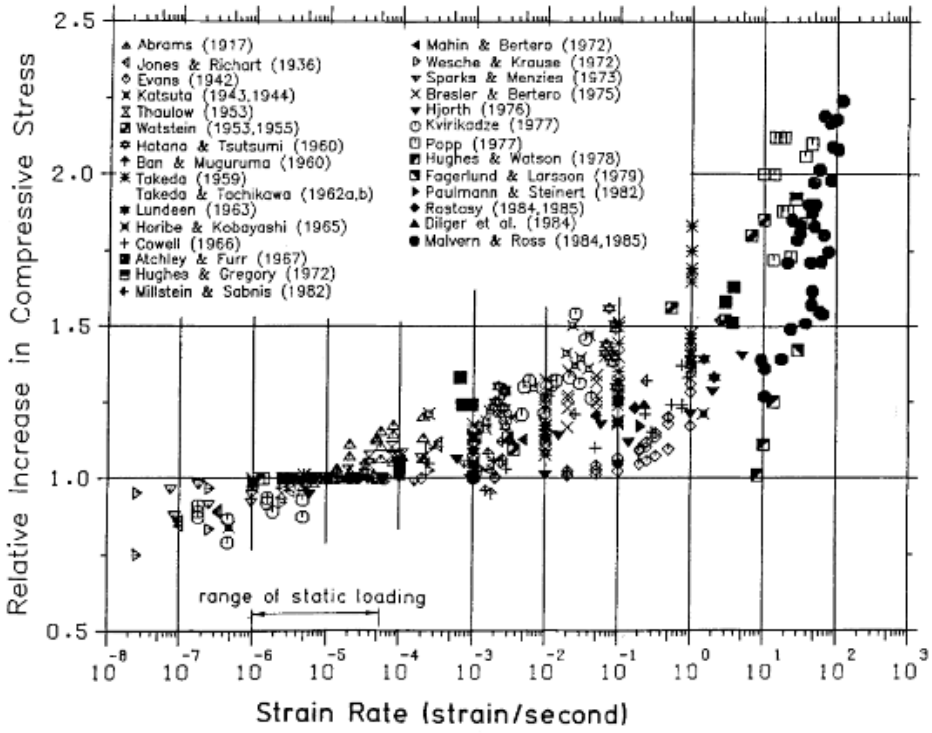

Figure 2.9: Strain-rate Influence on Compressive Strength of Concrete (Bishcoff and Perry, 1991).

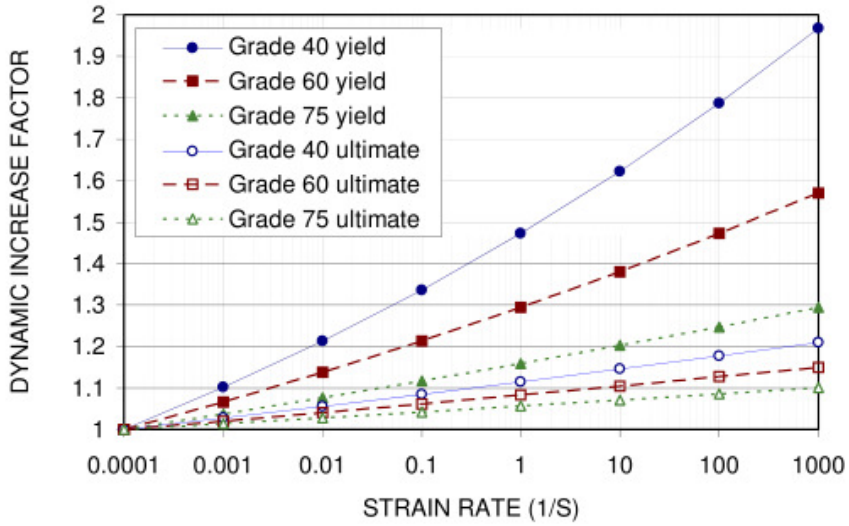

Figure 2.10: Strain-rate Influence on Yield and Ultimate Strengths of Various Steels (Malvar, 1998b).

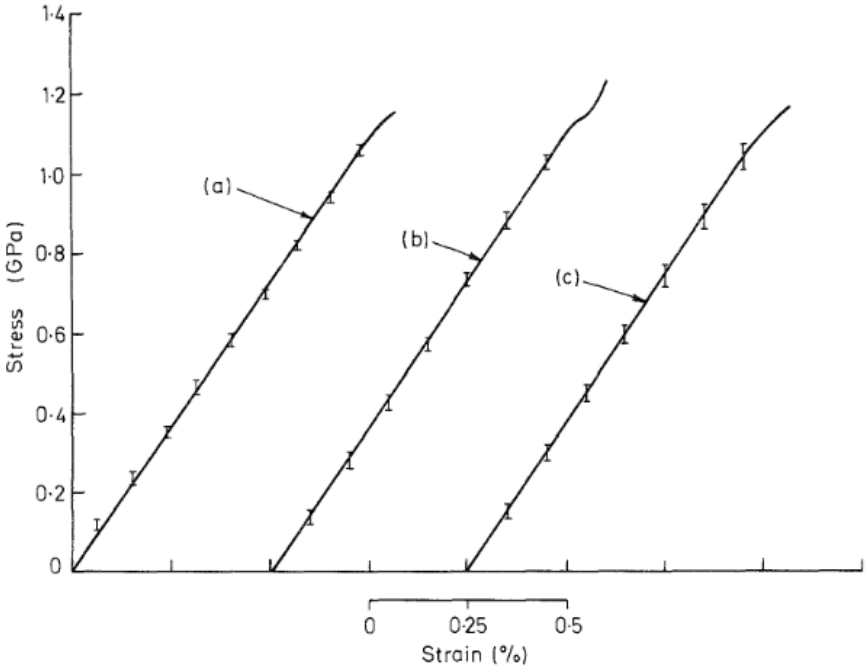

Figure 13 Tensile stress–strain curves for CFRP specimens (a) $\dot{\epsilon} = 5 \times 10^{-4}$ sec^{-1}, $E = 145$ GPa, $\sigma_f = 1.21 \pm 0.07$ GPa (mean of 5 tests). (b) $\dot{\epsilon} = 7$ sec^{-1}, $E = 145$ GPa, $\sigma_f = 1.26 \pm 0.07$ GPa (mean of 4 tests). (c) $\dot{\epsilon} = 450$ sec^{-1}, $E = 149$ GPa, $\sigma_f = 1.14 \pm 0.05$ GPa (mean of 4 tests).

Figure 2.11: Strain-rate Influence on Unidirectional CFRP Stress-strain Relationships (Harding and Welsh, 1983).

Chapter 3. Experimental Program

3.1. General

The experimental program involved the construction and simulated blast testing of thirteen reinforced concrete wall and slab members. No reinforced concrete beam specimens were tested as it was felt that the results of one-way walls and slabs would be equally applicable to flexure dominant beams. Specimens were designed to investigate the benefits of using externally bonded FRP laminates as a retrofit to improve blast resistance by increasing flexural capacity. The details of test specimens, material properties, instrumentation, test setup, and test procedure are described in this chapter.

3.2. Description of Test Specimens

Thirteen large scale reinforced concrete specimens were designed, built and tested as part of this research study. These thirteen specimens may be broadly lumped into two categories of specimen based on their size and reinforcing arrangement: one-way reinforced concrete wall strip panels and two-way reinforced concrete slab plates. Due to the similarities in construction and geometry, the one-way reinforced concrete members were considered to effectively simulate typical one-way wall elements. Due to the activation of a second bending plane, the two-way members were considered to effectively represent the behaviour of two-way slab plates subject to blast loading.

3.2.1 One-way Reinforced Concrete Panels

Seven one-way reinforced concrete wall strip panels were constructed. Each panel was *2440 mm* long, *440 mm* wide and either *80 mm* or *120 mm* thick. Four *80 mm* thick panels (companion set 1) and three *120 mm* thick panels (companion set 2) were constructed. The clear span of each of the specimens was *2232 mm*.

All one-way panels were doubly reinforced with four *6.3 mm* diameter non-deformed steel reinforcement, with yield strength of *580 MPa*. 180-degree hooks, with an exterior hook diameter of *63 mm* and hook length of *150 mm*, were provided on either end of the wires to ensure adequate reinforcement anchorage in the support regions. The reinforcing ratio was selected to satisfy minimum code requirements and was *0.35%* for the *80 mm* thick panels and *0.24%* for the *120 mm* thick panels. Clear cover to reinforcement was maintained at *6 mm*. The geometry and reinforcing details of the one-way specimens is shown in Figure 3.1.

The specified 28-day concrete strength for all panels was *40 MPa*, however the panels were not cast or tested concurrently and concrete strength on the day of testing varied. Material properties are discussed in Section 3.5.

3.2.2 Two-way Reinforced Concrete Plates

Four large-scale, two-way reinforced concrete slab plates were constructed. These plates had nominal dimensions of *2440 mm x 2440 mm x 75 mm*. To facilitate mounting of specimens to the shock tube, twenty *15.8 mm* diameter bolt holes, formed with small sections of *19 mm* PVC tubing, were installed in the slab formwork. These matched locations of existing bolt holes in the shock tube testing frame. The clear span of the two-way plates varied depending on the boundary conditions; specimens tested with simply-supported supports had a clear span of *2232 mm* while specimens tested with clamped supports had a clear span of *2132 mm*. Details of specimen support conditions are described in Section 3.3.

The slab plates were doubly reinforced with eleven *6.3 mm* diameter non-deformed steel reinforcement evenly spaced in each principle direction and in both top and bottom mats. The resulting reinforcing ratio was *0.2%* and satisfied minimum design code requirements. Clear cover to reinforcing was maintained at *6 mm*. 180-degree hooks with an exterior hook diameter of *63 mm* and hook length of *150 mm* were provided on either ends of the reinforcement to ensure sufficient development within the support region. A *150 mm* wide strip of expanded steel diamond mesh was provided along the entire length of the support region to reinforce the region around the bolt holes. Geometry and reinforcing details of the two-way reinforced concrete plates is shown in Figure 3.2.

The specified 28-day concrete strength for all plates was *40 MPa*. However, the plates were not cast concurrently and concrete strength on the day of testing varied. Material properties are discussed in Section 3.5.

3.3. Description of Companion Sets

The thirteen specimens – seven one-way panels and six two-way plates – were divided into five companion sets; CS1 to CS5. Generally, each companion set consisted of at least one unretrofitted control specimen and one CFRP retrofitted specimen. Additionally, companion sets CS1, and CS2 also contained a specimen that was retrofitted with externally bonded CFRP sheets and incorporated FRP anchors. The details of each of the companion sets and corresponding blast retrofits are described in subsequent subsections.

3.3.1 Companion Set 1 (CS1)

Companion set 1 consisted of four one-way reinforced concrete panels of *80 mm* thickness. Specimens were simply-supported under one-way bending with a clear span of *2232 mm*. Specimen CS1-C served as the un-strengthened control. Specimens CS1-R1, CS1-R2 and CS1-A were each retrofitted on the unloaded face with one layer of externally bonded Fyfe Co. Tyfo SCH-41 CFRP/epoxy laminate. The retrofit was applied over the entire clear span of the panels. CS1-A also incorporated FRP fan anchors intended to prevent or delay premature debonding failure of FRP laminates. Five anchors were installed in two rows at each end of the FRP sheets. Anchor diameter and embedment depth was *12.5 mm* and *70 mm*, respectively. The bonded length of the FRP anchors to the externally bonded FRP laminate was approximately *125 mm*. CFRP retrofit details for companion set 1 are illustrated in Figure 3.3. FRP material properties are discussed in Section 3.5 and FRP anchor preparation and installation is described in Section 3.6.3.

3.3.2 Companion Set 2 (CS2)

Companion set 2 consisted of three one-way reinforced concrete panels of *120 mm* thickness. Specimens were simply-supported under one-way bending with a clear span of *2232 mm*. Specimen CS2-C served as the un-strengthened control slab. Specimen CS2-R and CS2-A

were each retrofitted with one layer of externally bonded Fyfe Co. Tyfo SCH-41 CFRP/epoxy laminate. The retrofit was applied over the full width and length of the clear span of the slabs. Specimen CS2-A also incorporated FRP anchors to prevent or delay premature debonding failure of FRP laminates. Five anchors were installed in two rows at each end of the FRP sheets. Anchor diameter and embedment depth was *12.5 mm* and *70 mm*, respectively. The bonded length of the FRP anchors to the externally bonded FRP laminate was approximately *125 mm*. CFRP retrofit details for companion set 2 are illustrated in Figure 3.3.

3.3.3 Companion Set 3 (CS3)

Companion set 3 consisted of two nominally identical two-way reinforced concrete plates. The specimens were subjected to shock wave loading under simply-supported one-way bending with a clear span of *2232 mm*. Specimen CS3-C remained unstrengthened, while slab CS3-R was retrofitted with the WABO MBRACE CF-130 carbon/epoxy fibre reinforced polymer system. An externally bonded *[0°/90°]* cross-ply retrofit configuration was applied to both faces of the slab. The CFRP sheets covered the entire surface of each face between the centerlines of the bolts holes, *2232 mm,* in both principle directions. CFRP sheets were extended into the support region to the exterior edges of the specimen. Retrofit details for specimen CS3-R are illustrated in Figure 3.4.

3.3.4 Companion Set 4 (CS4)

Companion set 4 consisted of two nominally identical two-way reinforced concrete plates tested under simply supported, two-way bending with a clear span of *2232 mm*. No control specimen was tested as a part of companion set 4. Specimen CS4-R1 was retrofitted with an externally bonded *[0°/90°]* cross-ply retrofit configuration of WABO MBRACE CF-130 CFRP. The CFRP sheets covered the entire surface between the centerlines of the bolts holes, *2232 mm*, in both principle directions. CFRP sheets were extended into the support region to the exterior edges of the specimen. Retrofit details for specimen CS4-R1 are illustrated in Figure 3.4.

Specimen CS4-R2 was retrofitted with *200 mm* wide strips of externally bonded Fyfe Co. Tyfo SCH-41 CFRP laminate. A total of ten strips were bonded to the inbound face only,

five of which were applied in each principle direction of bending. The retrofit was centered about the centerline of the slabs and center-to-center spacing of the strips was *446 mm*. CFRP retrofit details for specimen CS4-R2 are shown in Figure 3.5.

3.3.5 Companion Set 5 (CS5)

Companion set 5 consisted of two nominally identical two-way reinforced concrete plates tested under fully-clamped two-way bending with a clear span of *2132 mm*. Specimen CS5-C served as an unretrofitted control specimen, while specimen CS5-R was retrofitted with an externally bonded *[0°/90°]* cross-ply retrofit configuration of WABO MBRACE CF-130 CFRP. The CFRP sheets covered the entire surface between the centerlines of the bolts holes, *2232 mm*, in both principle directions and on both faces. CFRP sheets were extended into the support region to the exterior edges of the specimen. Retrofit details for specimen CS5-R are illustrated in Figure 3.4.

Retrofitted specimens CS3-R, CS4-R and CS5-R are in fact the same specimen. This retrofitted specimen was first tested under two-way bending with fully-fixed supports (CS5-R). However, the specimen remained undamaged after testing and the support conditions were changed to two-way bending with simple supports (CS4-R). Once again, the specimen remained undamaged after testing and supports were modified to one-way bending with simply supported boundary conditions (CS3-R). For the sake of convenience, this specimen (tested with three different support configurations) is considered to be three individual specimens in this thesis.

3.4. Description of Test Setup

3.4.1 Shock Tube

The University of Ottawa's Shock Tube Testing Facility is capable of simulating the shock waves produced by the distant detonation of high explosives. A summary of the operation and capabilities of the shock tube are described below. For more detailed information, the reader is directed to the references by Lloyd (2010) and Lloyd et al. (2010).

Operation

The pneumatically driven shock tube, shown in Figure 3.6 and Figure 3.7, is composed of three main components: a variable length driver section, spool section and expansion section. Shock wave energy is generated in the driver section. Shock tube firing is controlled with the spool section. Shock wave expansion and specimen testing occur in the expansion section.

The driver section is comprised a series of *12.5 mm* thick steel pipes, each with an inner diameter of *597 mm* and outer diameter of *812 mm.* The shock tube has six pipe sections of various length; two *1525 mm* lengths, one *915 mm* length, one *610 mm* length and two *305 mm* lengths. Combinations of pipes may be selected such that driver length varies from *305 mm* to *5185 mm* in *305 mm* increments. Individual segments of pipe are bolted together with twenty *31.75 mm* diameter bolts. A synthetic gasket is placed between pipe sections to ensure the driver section is properly sealed when pressurized. A *12.5 mm* thick steel plate is bolted to the end of the driver section assembly, while the other end of the driver section is bolted to the spool section. The entire driver section sits on an inverted steel C-section tray.

The *90 mm* long spool section is bolted between the driver section and the expansion section. Combinations of *Grade 1100* aluminum diaphragms are placed between the driver-spool section and the spool-expansion section. For each desired driver pressure, combinations of aluminum diaphragms are selected such that the differential pressure gradient across the driver-spool and spool-expansion sections is less than the specified rupture strength of the diaphragms. Known as a "double diaphragm firing system," this firing mechanism allows for safe and accurate control of shock tube firing. The rupture strength of the diaphragms used during testing is shown in Table 3.2.

Shock tube operation is monitored and controlled from a remote control station located above the shock tube on the main floor of the Structures Laboratory. Static pressure gauges monitor the pressure within the driver and spool sections. Pressurization of the driver and spool sections follows a sequence that ensures the differential pressure across both sections is less than the rupture strength of the diaphragms at all times. When the desired driver pressure has been achieved, shock tube firing is initiated by venting pressure in the spool-expansion section, causing the driver-spool diaphragm to rupture, followed immediately by the rupture of the spool-expansion diaphragm.

Immediately following the rupture of both diaphragms, a shock wave is formed as high pressure air in the driver section attempts to equalize with the atmospheric pressure in the expansion section. The *6096 mm* long expansion section transitions from a *597 mm* diameter circular opening at the spool section to a *2032 mm x 2032 mm* square opening at the testing frame. The shock front then propagates down the length of the expansion section where it interacts with structural specimens mounted to the shock tube testing frame. The testing frame is a *203 mm* wide, *12.5 mm* thick steel flange which runs along the perimeter of the shock tube opening. Twenty *19 mm* diameter circular bolt holes are distributed along the length of the flange to allow for specimens to be mounted to the testing frame.

Twelve pressure relief vents are located at the end of the expansion section, adjacent to the test frame. These vents are opened by the reflected pressure wave and serve two purposes: they allow for the development of a negative pressure phase and they help reduce the magnitude of tertiary peaks caused by subsequent reflection of the shock wave within the shock tube.

Range of Operation

The shock tube can effectively simulate the reflected pressure, reflected impulse and positive phase duration of the first positive pressure wave caused by the detonation of high-explosive material. A typical reflected pressure-time history and reflected impulse-time history generated during shock tube testing is shown in Figure 3.8. The duration of the first positive phase is considered to be the time to the first local maxima of the impulse-time history curve. Although negative pressures may be developed during testing, the shock tube was not designed to simulate negative pressures generated by high explosive blast. Depending on the degree of venting and the initial driver pressure and driver length, tertiary peaks are noticed in the pressure-time history. Tertiary peaks are formed when the shock front reflects back and forth within the shock tube and will eventually damp themselves out of the system.

Lloyd (2010) reported that reflected pressure is controlled by selecting an appropriate driver pressure, while positive phase duration is controlled by driver length. As reflected impulse is the area under the pressure-time history curve, reflected impulse is controlled by selecting an appropriate combination of driver pressure and driver length. Figure 3.9 shows the relationship between reflected pressure and driver pressure, for various driver lengths. Similarly,

Figure 3.10 shows the relationship between reflected impulse and driver pressure for various driver lengths. Lloyd et al. (2010) reported that reflected pressure increases with driver pressure, while positive phase duration (and hence, reflected impulse) increases as driver length increases. Approximate maximum capabilities of the shock tube are shown in Table 3.3.

Lloyd et al. (2010) discussed shock wave planarity. They reported that the shock tube was effectively planar at the location of the testing frame, with a deviation of *8%* in the arrival time of the shock front. Furthermore, Lloyd et al. (2010) found that the wave front velocity was weakly coupled to driver pressure, with typical wave front velocities between *340 m/s* and *410 m/s*, increasing with increasing pressure. Lloyd et al. (2010) also noted that the shock tube is not suited to diffraction loading as a result of low particle velocities associated with the shock wave.

3.4.2 Support Conditions

Companion Set 1 and 2 (CS1 and CS2)

The *440 mm* wide one-way panels in companion set 1 and 2 were tested with simply supported end conditions. The top and bottom of the slabs were clamped between a *440 mm* long *19 mm* diameter steel rod welded to a *2440 mm* long *152 mm x 152 mm x 6.4 mm* square hollow steel section on the front face and another *19 mm* diameter steel rod welded to a *500 mm* long *51 mm x 51 mm x 6.4 mm* built-up hollow steel section on the back face. *19 mm* diameter threaded steel rods were used to bolt the entire support assembly to the shock tube testing frame. This system allowed the supports to rotate freely but prevented lateral movement of the specimens during testing. The details of this support condition are illustrated in Figure 3.11, and a close-up of the supports is shown in Figure 3.12.

Companion Set 3 and 4 (CS3 and CS4)

The two-way reinforced concrete plates from companion set 3 and 4 were tested under simply supported end conditions. Knife edged supports were simulated by clamping the slabs between a set of star shaped equal leg angles: a *38 mm x 38 mm x 4.8 mm* angle on the front face and a *50 mm x 50 mm x 4.8 mm* angle on the back face. Holes were drilled in the angles corresponding to the locations of bolt holes in the flange of the shock tube test frame. Slabs were clamped in place by bolting the slab specimens between the back-to-back angles and the shock tube test frame. The star shaped back-to-back angles were only placed along the

top and bottom edge of the specimens in companion set 3 to allow for one-way behaviour, while they were placed on all four edges of the specimens in companion set 4 to allow for two-way bending. Details of the support knife edged support conditions are illustrated in Figure 3.13 and Figure 3.14.

Companion Set 5 (CS5)

The two-way reinforced concrete plates of companion set 5 were tested under fully-fixed two-way bending. This degree of fixity was provided by bolting the specimens between the shock tube testing frame and a specially constructed built-up steel frame assembled from four *152 mm x 152 mm x 6.4 mm* hollow steel sections. Three of the hollow sections were welded to form a "U"-shape. The vertical legs of the "U"-shape were capped with a *6.35 mm* thick steel plate through which four *6.35 mm* diameter threaded bolt holes were drilled and tapped. A matching set of unthreaded bolt holes were drilled into the ends of the fourth hollow HSS "top beam," such that the "U"-shape and the top beam could be bolted together to form one rigid frame. Holes were drilled in the frame corresponding to the locations of bolt holes in the flange of the shock tube testing frame. Specimens were clamped between the shock tube test frame and the rigid frame composed of the "U"-shape and the top beam. Details of this support condition are illustrated in Figure 3.15 and Figure 3.16.

3.4.3 Load Transfer Device (for Companion Sets CS1 and CS2)

A load transfer device was used to transfer shock wave loading from the entire shock tube opening to the face of the specimens. The load transfer device, seen in Figure 3.11, was first used by Lloyd (2010) to test reinforced concrete columns subjected to simulated blast loading using a shock tube. The load transfer device consisted of fifteen rigid out-of-plane steel beams (*76.2 mm x 76.2 mm x 4.8 mm x 2440 mm* long) equally distributed over the height of the shock tube opening. Attached to these beams was a light gauge steel sheet metal skin covering the entire height of the shock tube opening and running the entire width of the shock tube test frame (*2032 mm x 2440 mm*). Shock tube reflected pressures were transferred from the sheet metal skin to the rigid beams which applied a series of discrete point loads to the face of the specimens. These point loads effectively simulated uniformly distributed load acting over the entire clear span of the specimens. The load transfer device was supported at the top to prevent the apparatus from falling and was friction supported between the speci-

mens and the shock tube testing frame. The load transfer device was free to move laterally, restrained only by the displacements of the specimens.

The main advantage of the load transfer device is it increases the capacity of the shock tube. This increase in capacity is directly related to the ratio of the width of the shock tube opening to the width of the specimen being tested. For the case of the one-way specimens with width of *440 mm* and load transfer width *2440 mm*, the reflected pressure capacity of the shock tube is increased by a factor of *5.54*. However, the disadvantage of using a load transfer device is that it adds considerable mass (approximately *394 kg*) to the system which must be accounted for during analytical calculations of dynamic response. Furthermore, negative pressures developed during shock wave loading are not transferred to the slab specimens as the load transfer device was not connected to the slabs. Another disadvantage of the load transfer device is that rebound displacements cannot occur as the rigid out-of-plane beams prevent negative displacement of the specimens into the shock tube.

3.5. Material Properties

3.5.1 Concrete

Slabs were constructed and cast in three separate batches. Each batch was specified to have a 28-day compressive strength of *40 MPa*, using *10 mm* crushed limestone aggregate and a slump of *100 mm*. However, the concrete strength for the specimens at the time of testing was approximately *50-60 MPa*. The compressive strength, f_c', of concrete at the time of testing is summarized in Table 3.1. Concrete strength was determined from an average of at least three standard cylinders.

3.5.2 Steel

All specimens were constructed with *6.3 mm* diameter undeformed steel wire with a yield strength of *580 MPa* at a yield strain of *0.0028 mm/mm*. The stress-strain relationship of the longitudinal reinforcement, shown in Figure 3.17, was determined using an average of four tensile coupon tests. Ultimate strength of the steel reinforcing was *670 MPa* at an ultimate strain of *0.196 mm/mm*.

3.5.3 CFRP

Due to availability of materials, two types of carbon fibre reinforced polymer retrofit systems were used; the MBRACE CF-130 Fibre System and the Tyfo SCH-41S-1 Composite System. Slabs CS3-R, CS4-R and CS5-R were retrofitted with the MBRACE CF 130 Fibre System, while all remaining retrofitted slabs were retrofitted with the Tyfo SCH-41S-1 Composite System. All FRP anchors were constructed using Tyfo SCH-41S-1 CFRP material.

MBRACE CF 130 Fibre System

The MBRACE CF-130 Fibre System, manufactured by BASF Construction Chemicals, is composed of unidirectional tow sheet carbon fibres with a glass fibre cross-weave. CF-130 sheets had a width of *500 mm* and an assumed laminate thickness of *0.8 mm* when saturated with epoxy. The manufacturer's specifications for ultimate tensile strength and tensile modulus were *781 MPa* and *47.5 GPa*, respectively (BASF, 2007; Ozbakkaloglu and Saatcioglu, 2005). Similarly, the manufacturer's specification for ultimate strength and tensile modulus of the dry carbon fibres was *4960 MPa* and *296.4 GPa*, respectively. The ultimate strain of the bare fibres and composite laminate was reported to be *1.67%*. Two-part MBRACE Epoxy Saturant was used to bond fibre sheets to the specimens. A summary of mechanical properties of the MBRACE CF-130 Fibre System may be found in Table 3.4. Dry fibre properties in the *0°* orientation are listed in Table 3.5. The *0°* tensile stress-strain relationship for the composite laminate is illustrated in Figure 3.18.

Fyfe Co. Tyfo SCH-41S-1 Composite System

The Tyfo SCH-41S-1 system was a unidirectional carbon fibre fabric with glass cross-fibres. The fibres were saturated with two-part Tyfo S Epoxy. According to manufacturer's specifications, the composite laminate had a tensile strength of *876 MPa*, tensile modulus of *72.4 GPa* and ultimate strain of *1.2%* (Fyfo Co. LLC, 2009). The tensile strength, tensile modulus and ultimate strain of the dry carbon fibres was reported to be *3790 MPa*, *230 GPa* and *1.7%*, respectively. Composite laminate thickness was *1.0 mm* and the width of carbon fibre sheets was *500 mm*. Gross composite laminate properties in the *0°* orientation of the Tyfo SCH-41S-1 CFRP are listed in Table 3.4. Dry fibre properties in the *0°* orientation are listed in Table 3.5. The *0°* tensile stress-strain relationship for the composite laminate is illustrated in Figure 3.18.

3.6. Construction of Test Specimens

All test specimens were constructed at the University of Ottawa's Civil Engineering Structures Laboratory. In general, the construction of all specimens was divided into four phases:

1. Construction and instrumentation of steel reinforcement cages
2. Construction of formwork
3. Casting and curing of slabs
4. As required, application of externally bonded CFRP retrofit, with or without FRP fan anchors

3.6.1 General Construction

All slab reinforcement was fabricated from *6096 mm* lengths of *6.3 mm* diameter undeformed steel wire supplied by a local distributor. The bars were cut to approximate length and bent by hand with a jig to form 180-degree hooks with a hook diameter of *63 mm* and a *150 mm* hook length on each end. Prior to assembly of the reinforcing cages, the bars were instrumented with *350Ω* strain gauges. Strain gauge locations are discussed in Section 3.7.

The steel reinforcing cages for the one-way reinforced concrete panels from companion set 1 and 2 were constructed from eight lengths of longitudinal reinforcement. Five *400 mm* long *6.3 mm* diameter undeformed steel wires were evenly spaced along both the top and bottom mats as transverse reinforcement to facilitate tying and to ensure proper spacing of longitudinal wires. Two *6.3 mm* diameter steel wire hooks were installed in each slab to facilitate transportation by the overhead crane in the Civil Engineering Structures Laboratory. Finally, the strain gauges wires were neatly bundled to reduce the likelihood of damage during construction and testing.

Construction of the two-way reinforced concrete plates from companion sets 3, 4, and 5 followed a similar procedure. A jig constructed from *2"x4"*s was used to ensure proper spacing of reinforcement during construction. To reinforce the support regions of the slabs, *1220 mm x 125 mm* sheets of expanded steel mesh were placed within the support regions of the slabs between the upper and lower mats. Holes were provided in the sheets of mesh to accommo-

date the *75 mm* long sections of *19 mm* diameter PVC tubing required to bolt the slabs to the shock tube. Four 10M hooks, properly anchored within the support regions, were provided to facilitate transportation by the overhead crane. A typical two-way slab reinforcement cage prior to casting is shown in Figure 3.19.

Wooden formwork for all slabs was constructed from *4'x8'* sheets of *3/4"* plywood and *2"x4"*s. Bolt holes for the panels of companion set 3, 4 and 5 were formed from *75 mm* long lengths of *19 mm* diameter PVC tubing. The final step in formwork preparation was the application of motor oil with a brush to facilitate formwork removal after casting. Slab reinforcing cages were then lowered into position within the formwork. Clear cover to the top mat of reinforcing was maintained using plastic chairs and clear cover of the bottom mat was maintained using small lengths of *6 mm* diameter undeformed steel wire. Clear cover to reinforcing for all slabs was maintained at *6 mm*. Finally, the PVC tubing, expanded wire mesh, bars, hooks and strain gauges wires were adjusted prior to casting.

A bucket attached to an overhead crane and wheel barrows were used to place concrete in the formwork. Special care was taken during hand finishing to ensure a smooth finish to facilitate the FRP retrofit. Lab personnel assisted with concrete placement and finishing. A sufficient number of standard concrete cylinders were cast to determine the mechanical strength properties of concrete at the time of testing. Slabs were covered with burlap and/or plastic tarps and kept wet for the first week to promote concrete curing. A typical two-way plate during concrete casting is shown in Figure 3.20.

3.6.2 Externally Bonded CFRP Retrofit Procedure

The application of externally bonded FRP laminates was performed using a wet lay-up technique following the manufacturers' recommendations. A summary of the procedure followed during retrofitting is outlined below:

1. Concrete surfaces were prepared by removing any loose debris, dust, dirt, etc.

2. Surface irregularities greater than *1 mm* in height were removed using an angle grinder with a masonry grinding disk. A belt sander was then used to produce a smooth slab surface.

3. Slab surfaces with excessive irregularities were treated with a layer of high-viscosity epoxy putty filler. Specimens with epoxy putty treatment were left to cure for at least two days.

4. Any remaining irregularities in the epoxy putty were then removed using a belt sander.

5. Epoxy resin was mixed according to the manufacturers recommendations and applied to the surface of the slabs using a paint roller.

6. CFRP sheets were then saturated with epoxy resin using a roller. Saturated CFRP sheets were applied to the surface of the slabs.

7. A final layer of epoxy resin was applied over the first layer of CFRP using a paint roller.

8. Air voids and excess epoxy saturant were removed using a ribbed steel roller.

9. As required, additional layers of CFRP were applied by repeating steps 5 through 8.

10. Specimens were left to cure for at least a week prior to testing.

Typical externally bonded CFRP retrofitted two-way and one-way specimens are shown in Figure 3.16 (b) and Figure 3.21, respectively.

3.6.3 FRP Fan Anchor Preparation and Installation

CFRP fan anchors were incorporated into the retrofit of slabs CS1-A and CS2-A. CFRP fan anchors can prevent or delay premature retrofit failure by debonding of externally bonded CFRP sheets and concrete substrate. The construction of FRP anchors is described in detail by Ozbakkaloglu and Saatcioglu (2009), but has been summarized below for completeness.

FRP fan anchors were prepared exclusively from the Fyfe Co. Tyfo SCH-41 composite system. A typical CFRP fibre anchor is shown in Figure 3.22, while an illustration of an anchor with nomenclature is shown in Figure 3.23. All anchors had a diameter of *12.7 mm*, embedment depth of *70 mm* and fan radius of approximately *125 mm*. Anchors were produced by

cutting rectangular sections of CFRP sheets *440 mm* long running parallel to the principle direction of the fibres and *90 mm* wide. A small bead of glue from a glue gun was applied along the width of the CFRP sections to prevent fraying of the anchors during construction. To allow for the expansion of the fan blades, a utility knife was used to cut the glass cross fibres running parallel to the length of the CFRP sheet at *15 mm* increments between the exterior of the sheet and the inner edge of the embedment length. The CFRP sections were then folded in *15 mm* increments along the width of the sheet to form a nearly circular tube. The nearly circular tube was then folded in half, and fishing wire was wrapped around the embedment length of the circular CFRP anchor. CFRP anchor production was completed by removing or trimming stray or excess fibres. No breakage of fibres was observed during manufacturing.

After the preparation of the concrete substrate, holes were drilled in the specimens at the locations of the FRP anchors. These holes had a diameter of *12.7 mm* and a depth of *70 mm*. The holes were cleaned using compressed air. FRP laminates were then externally bonded to the surface of the specimens following the steps outlined in the preceding section. The FRP anchors were placed immediately following the application of the laminate, while the epoxy was still "wet." The longitudinal FRP fibres were displaced around the anchor holes and a small dropper was used to saturate the hole with epoxy. The anchors themselves were then saturated with epoxy, ensuring that the embedment region of the anchors was completely saturated. The anchors were then placed into the holes and the fan lengths were "fanned" out and bonded to the surface of the longitudinal FRP sheets. A ribbed roller was used to remove excess epoxy and eliminate any air voids. The entire retrofitted specimen was then left to cure for at least a week prior to testing. A typical one-way wall strip retrofitted with FRP and incorporating FRP anchors is shown in Figure 3.24

3.7. Instrumentation

Experimental data was recorded by a Yokogawa SL1000 High-Speed Data Acquisition Unit recording at *100 kilo-samples per second* (*kS/s*) resulting in a sample being recorded every *10 μs*. The data acquisition unit was triggered when one of the pressure sensors recorded a pressure greater than a predetermined threshold level. Data was recorded for *1 s* with a pre-

trigger time of *0.1 s*. The SL1000 was configured to record ten strain channels and six low-voltage channels. Excitation was supplied by a Kistler *24V* 16 channel power supply unit. Experimental data from the SL1000 was saved to a Windows PC while another PC was used to run the high speed camera.

Specimen displacements were generally monitored using three Celesco CLWG-300 linear variable displacement transducers (LVDT's) with a stroke of *312 mm*. LVDT's were typically mounted at member mid-span, along yield lines, and near supports. The LVDT's were mounted to the slabs using aluminum brackets and were supported on rigid shoring jacks. Each LVDT was calibrated prior to testing each specimen. Wire gauges were used whenever there was a possibility of damaging the LVDT's (i.e. for large, destructive shots). Two Celesco SP1-25 spring loaded wire gauges, each with a range of *635 mm*, and one Celesco SP1-50 spring loaded wire gauge, with a range of *1270 mm*, were used. LVDT positioning for companion sets 1 and 2, companion set 3 and companion sets 4 and 5 are illustrated in Figure 3.25, Figure 3.26, Figure 3.27, respectively.

Shock wave reflected pressure-time histories were recorded using two PCB Piezotronics Model #112A22 piezoelectric pressure sensors. The two pressure sensors were located along the bottom and side walls of the expansion section, *50 mm* away from the specimens.

Strain in longitudinal reinforcement and CFRP laminates was recorded using Tokyo Sokki Kenkyujo Co., Ltd. FLA-6-350-11 *350Ω* electrical resistance strain gauges. Strain gauge locations varied between companion sets. However, strain gauges were typically located at regions of maximum strain, along yield lines, on both the inbound and rebound tension steel and on FRP. Strain gauge locations for companion sets 1 and 2 are illustrated in Figure 3.25. Strain gauge locations for companion set 3 are illustrated in Figure 3.26. Strain gauge locations for companion sets 4 and 5 are illustrated in Figure 3.27, with additional FRP strain gauge locations for specimen CS4-R2 shown in Figure 3.28. Not shown in the figures are the strain gauge locations for specimen CS5-R. This retrofitted panel had one FRP strain gauge located at mid-span on the unloaded face and another FRP strain gauge located at the maximum moment region near the supports on the loaded face.

One PCB Piezotronics Model #355B12 piezoelectric shear accelerometer was used to record mid-span slab acceleration-time history for all slabs in companion sets 1 and 2, and slabs CS3-C. The accelerometer was mounted to the same aluminum bracket as the mid-span LVDT.

A high-speed video camera was used to record member response to blast loading. An AOS Technologies X-PRI full color camera recording at a maximum of *1000 frames per second* with a resolution of *800 x 600* pixels was used. For smaller shots, the camera was placed such that the profile of the specimens was recorded, while for destructive shots the camera was typically located slightly off to the front of the shock tube. The camera was triggered by the SL1000 data acquisition unit. Three *1000W* studio lights were used to illuminate the specimens. A Windows PC was used to setup and monitor the high-speed camera.

Typical specimen instrumentation (strain gauges, LVDT's, accelerometers, etc) for each companion set is shown in Figure 3.25 to Figure 3.28.

3.8. Test Procedure and Blast Loading Program

Prior to mounting the specimens into position, supports and the load transfer device (if required) were installed. The specimens were then positioned at the mouth of the shock tube and the installation of the support conditions was completed. Specimen instrumentation was installed, the high speed camera and studio lights were adjusted, and the data acquisition system was calibrated. Photographs were taken of the specimens before and after each shot to document damage progression. To ensure the data acquisition system was properly configured, a trigger check was performed prior to testing each specimen. Finally, the appropriate driver length and aluminum foils were selected according to the desired reflected pressure and reflected impulse. On average, two to three days were required to install and configure a virgin specimen. Performing one simulated explosion required two people approximately two hours. A specimen was considered destroyed when the maximum support rotation exceeded *10°*, residual displacement exceeded *50 mm*, FRP retrofit had failed or the maximum capacity of the shock tube had been achieved.

The objective of the research program was to directly compare the blast performance of structures with and without CFRP retrofits. Accordingly, the blast loading program used throughout the research was controlled by the as-built specimen of each companion set. At minimum, two shots were performed on each control specimen; the first shot was selected to such that member response was in the elastic range, while the second shot was selected to generate a relatively inelastic response without exceeding the capabilities of the corresponding retrofitted specimens. The retrofitted specimens were then subjected to the same simulated explosions. As required, additional shots were performed with a strict focus on matching shots within each companion set to facilitate direct comparison of results.

Table 3.1: Summary of Test Specimens and Companion Sets.

Companion Set	Bending; Thickness	Support Conditions	Specimen Type	Specimen Designation	f'_c MPa	Retrofit Details
1	One-way *80 mm*	Simply Supported	One-way RC panel	CS1-C	59.5	Control (as-built)
				CS1-R1	59.5	One layer SCH-41 CFRP applied over the entire unloaded face
				CS1-R2	60	One layer SCH-41 CFRP applied over the entire unloaded face
				CS1-A	60	One layer SCH-41 CFRP applied over the entire unloaded face with five FRP fan anchors at each end of the laminate
2	One-way *120 mm*	Simply Supported	One-way RC panel	CS2-C	59.5	Control (as-built)
				CS2-R	59.5	One layer SCH-41 CFRP applied over the entire unloaded face
				CS2-A	60	One layer SCH-41 CFRP applied over the entire unloaded face with five FRP fan anchors at each end of the laminate
3	One-way *75 mm*	Simply Supported	Two-way RC plate	CS3-C	60	Control (as-built)
				CS3-R	49.5	One layer MBRACE CF-130 CFRP applied to each face and each principle direction
4	Two-way *75 mm*	Simply Supported	Two-way RC plate	CS4-R1	49.5	One layer MBRACE CF-130 CFRP applied to each face and in each principle direction
				CS4-R2	60	Strips of SCH-41 CFRP applied to inbound face in each principle direction
5	Two-way *75 mm*	Fixed	Two-way RC plate	CS5-C	49.5	Control (as-built)
				CS5-R	49.5	One layer MBRACE CF-130 CFRP applied to each face and in each principle direction

Table 3.2: Rupture Strength of Aluminum Diaphragms Used in Shock Tube Operation.

Aluminum Diaphragm Thickness		Rupture Strength	
Inches	**mm**	**psi**	**kPa**
3/1000"	0.0762	5	34.47
5/1000"	0.127	8	55.15
8/1000"	0.2032	13	89.63
12/1000"	0.3048	20	137.89

Table 3.3: Approximate Maximum Shock Tube Capabilities (based on Lloyd et al., 2010).

Driver length L_d mm	Reflected pressure P_r kPa	Reflected impulse I_r kPa-ms	Equivalent mass of TNT* W kg	Stand-off* R m
305	78	217	8	12
915	92	410	42	18
1830	100	840	290	33
3355	103	1760	2500	67
4880	104	2690	10000	106

* - based on hemi-spherical surface burst

Table 3.4: 0° Composite Gross Laminate Tensile Properties of CFRP Laminates.

	Nominal thickness t_f mm/ply	Ultimate tensile strength f_{fu} MPa	Elastic Modulus E_f MPa	Rupture strain ε_f %
MBRACE CF-130	0.8	781	47.5	1.67
Tyfo SCH-41	1	876	72.4	1.2

Table 3.5: 0° Dry Fibre Properties of CFRP Laminates.

	Ultimate tensile strength MPa	Elastic Modulus GPa	Rupture strain %
MBRACE CF-130	4950	296.4	1.67
Tyfo SCH-41	3790	230	1.7

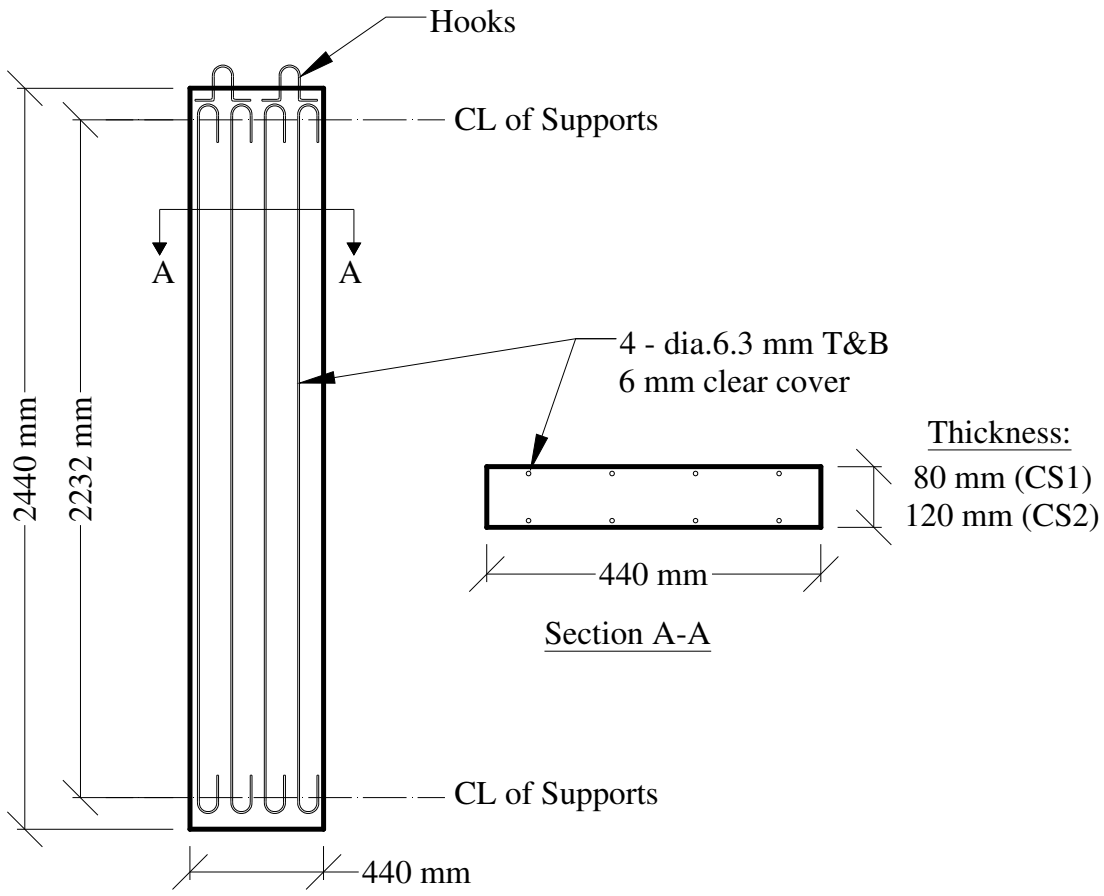

Figure 3.1: Reinforcement Details for One-way Reinforced Concrete Wall Panels.

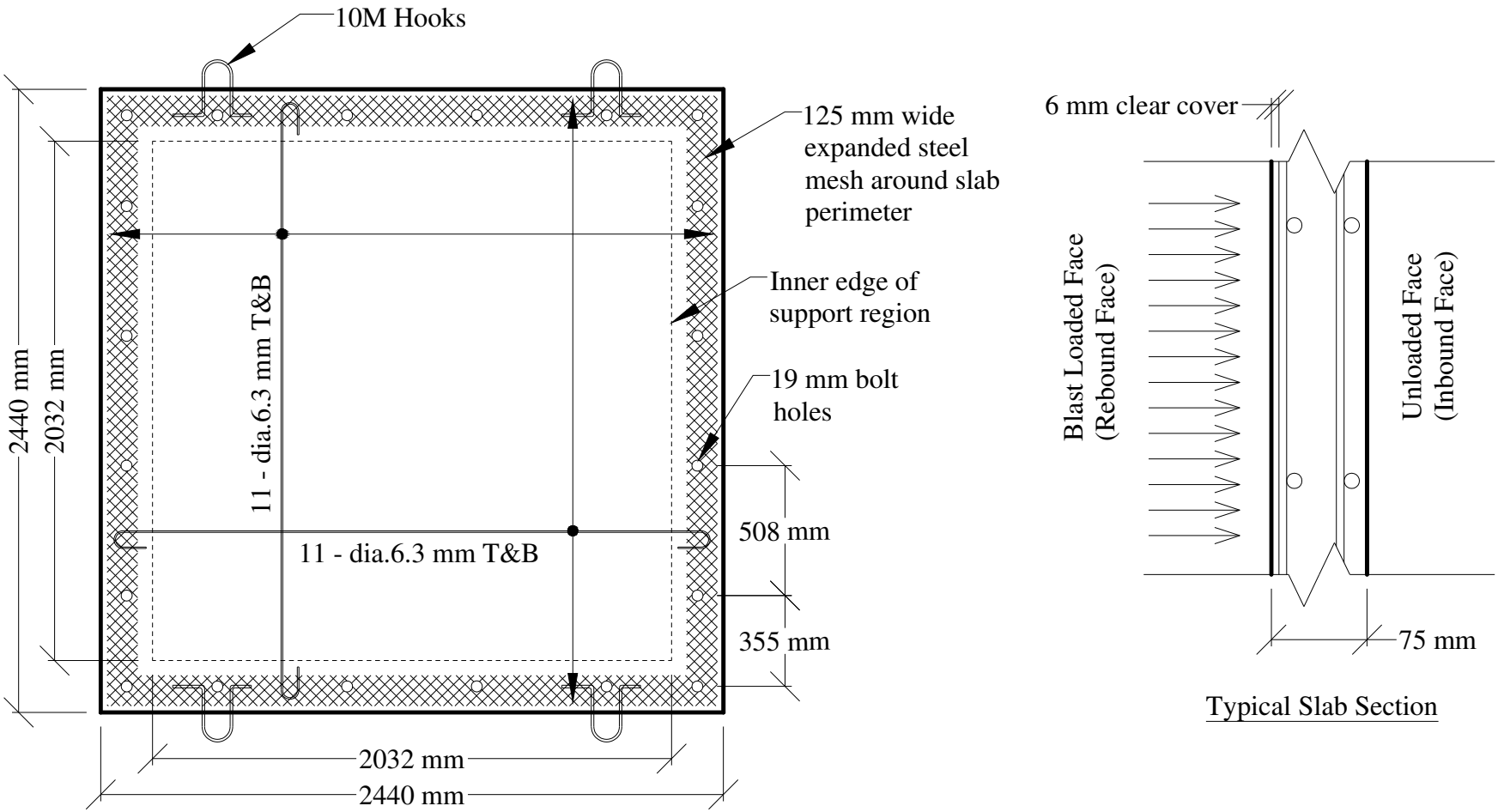

Figure 3.2: Reinforcement Details for Two-way Reinforced Concrete Slab Plates.

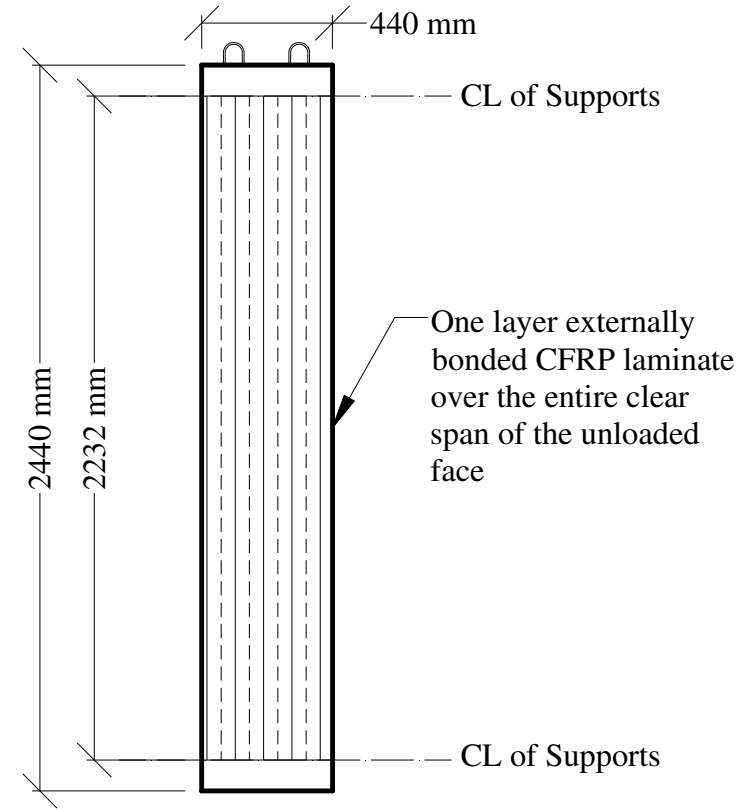

(a) Externally bonded CFRP retrofit for panels without FRP anchors (CS1-R1, CS1-R2, CS2-R)

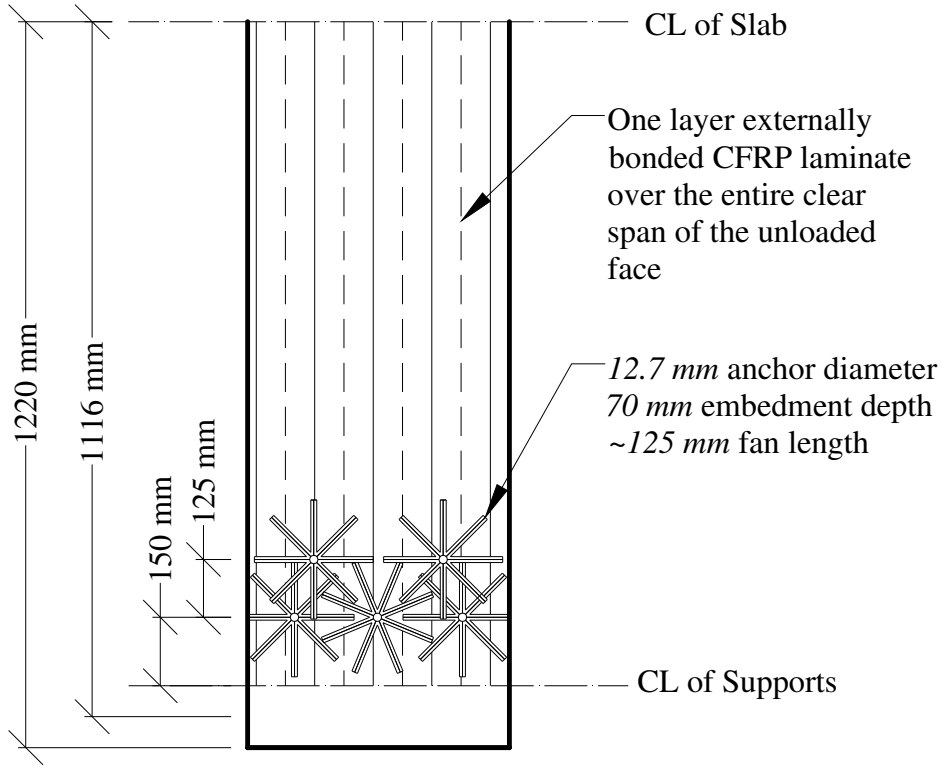

(b) Externally bonded CFRP retrofit for panels with FRP anchors (CS1-A, CS2-A)

Figure 3.3: CFRP Retrofit Details for Companion Sets 1 and 2.

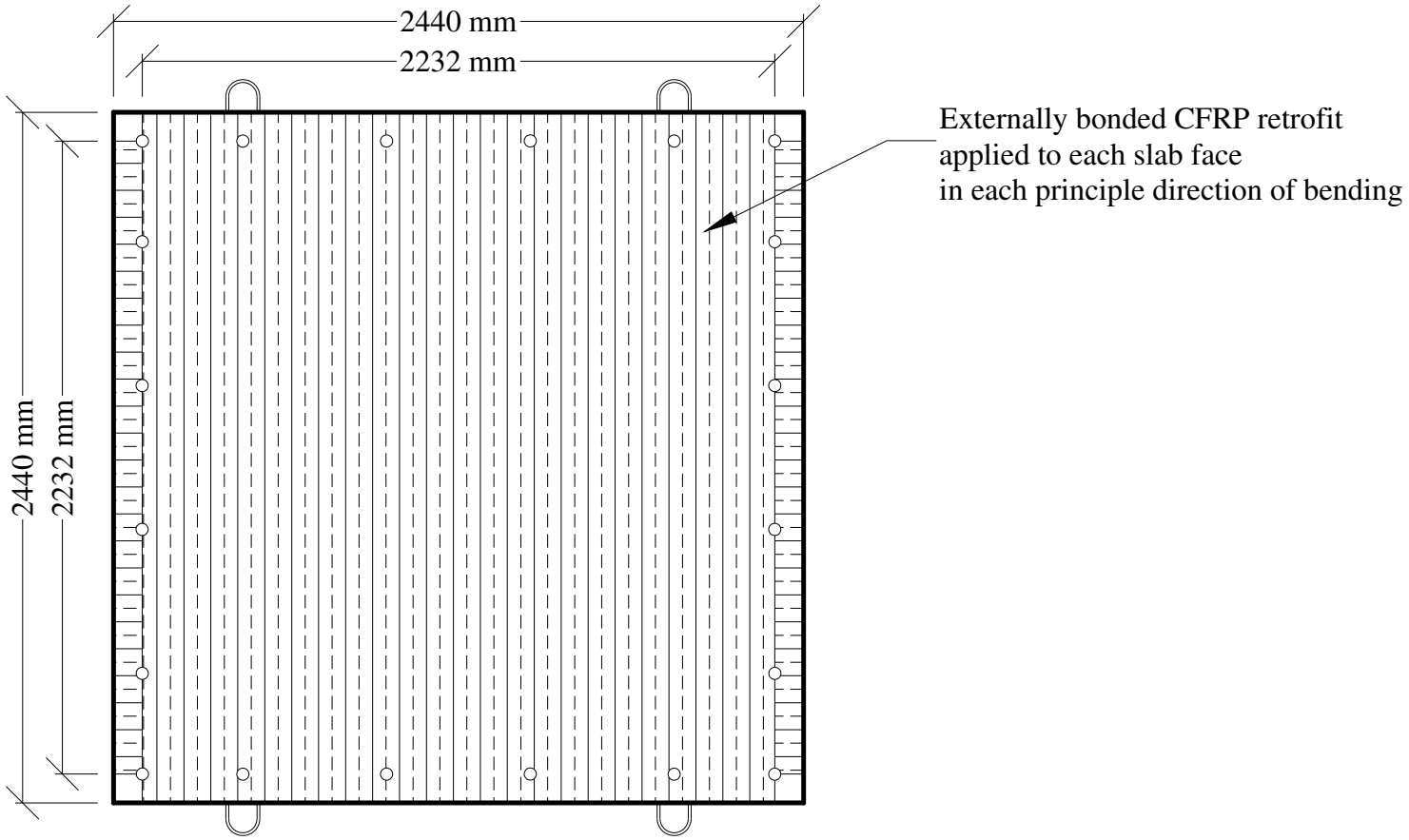

Figure 3.4: CFRP Retrofit Details for Specimens CS3-R, CS4-R1 and CS5-R.

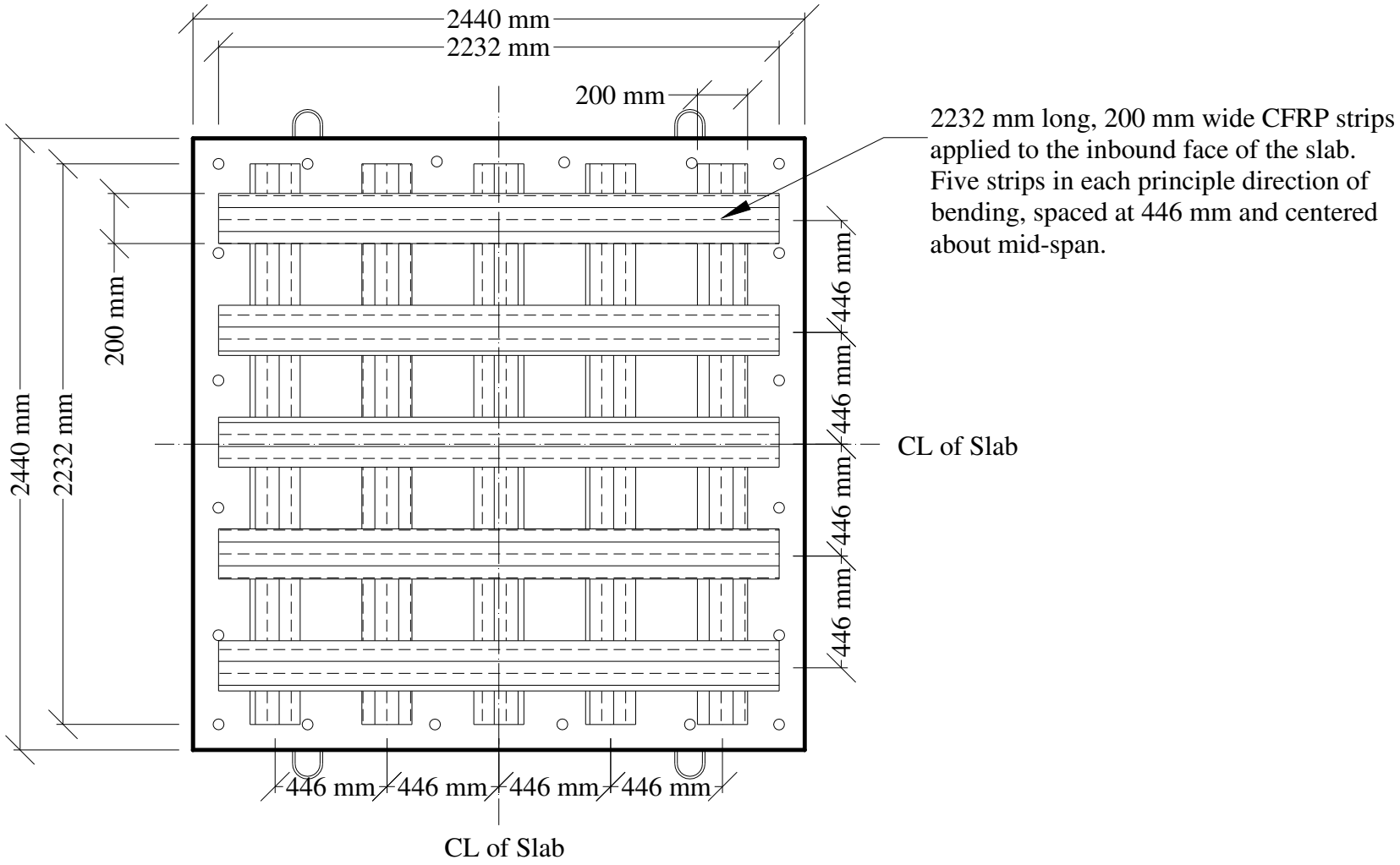

Figure 3.5: CFRP Retrofit Details for Specimen CS4-R2.

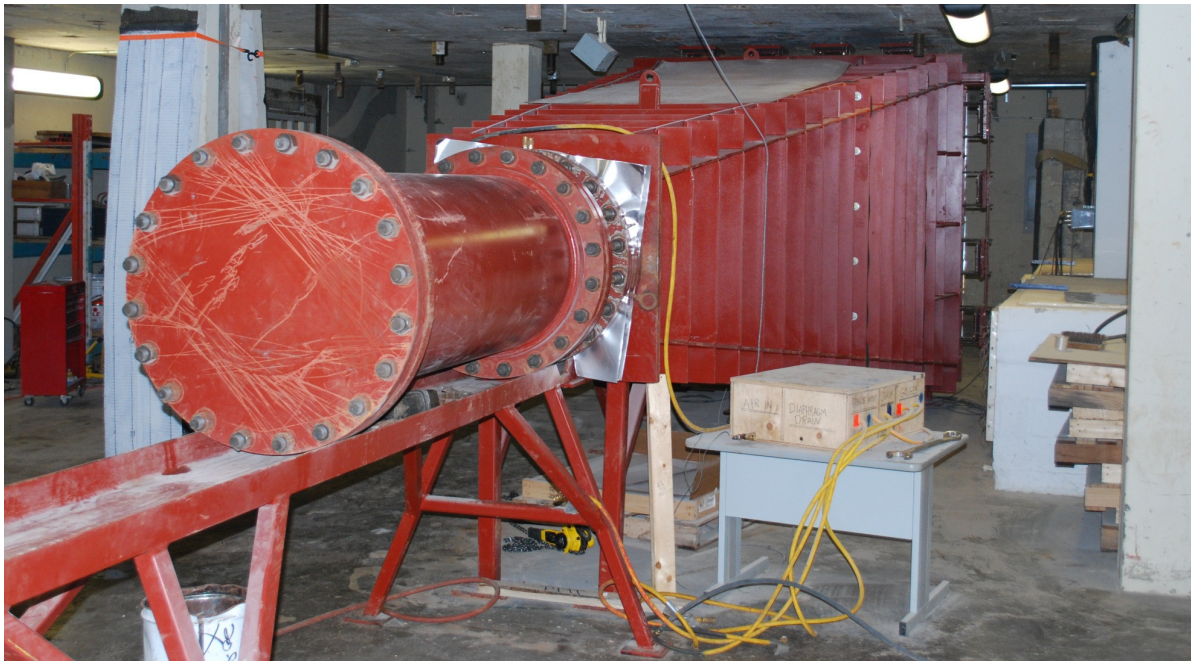

Figure 3.6: Rear View of the Shock Tube Driver Section with *1830 mm* Driver.

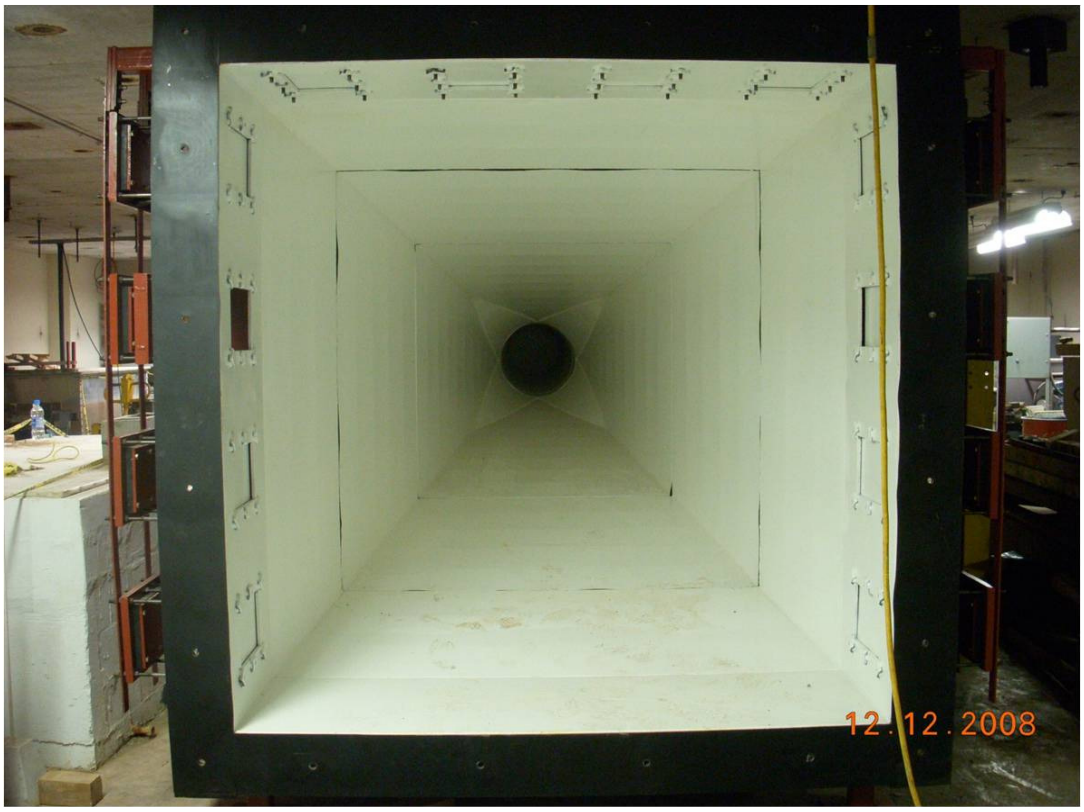

Figure 3.7: Front View of the Shock Tube Testing Frame.

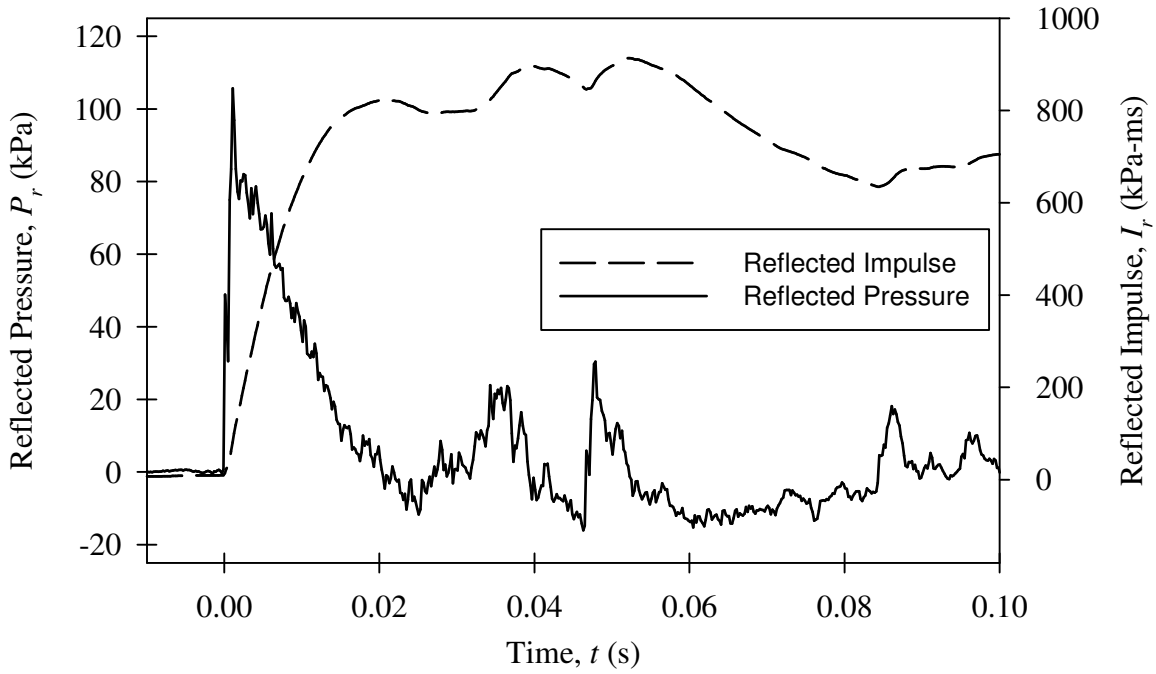

Figure 3.8: Typical Shock Wave Time History Generated by the Shock Tube.

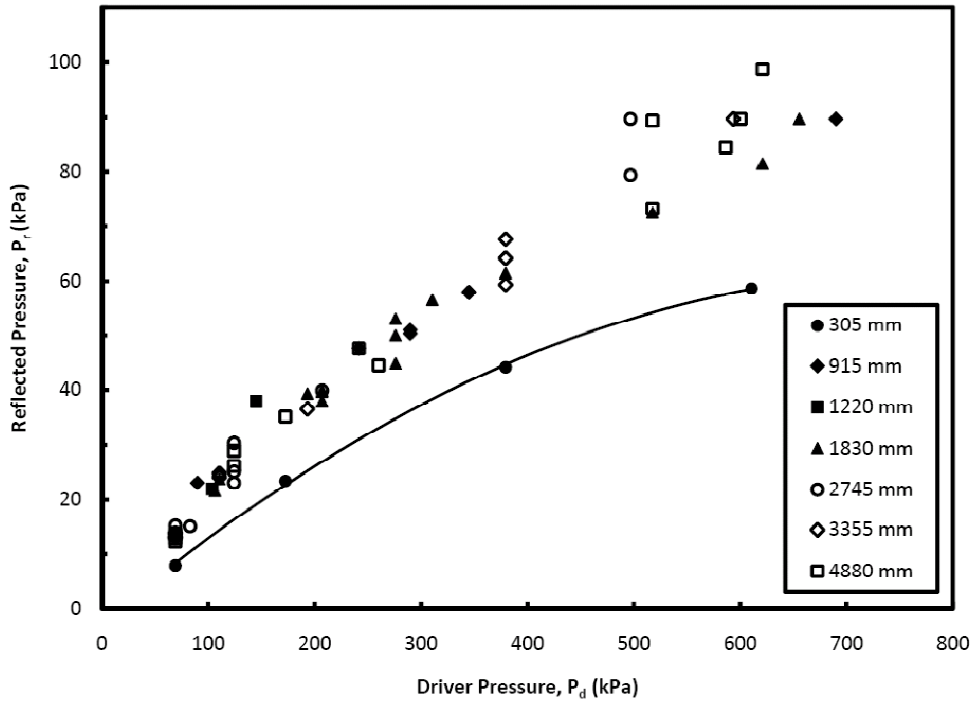

Figure 3.9: Shock Tube Reflected Pressures as a Function of Driver Pressure for Various Driver Lengths (Reproduced from Lloyd et al., 2010).

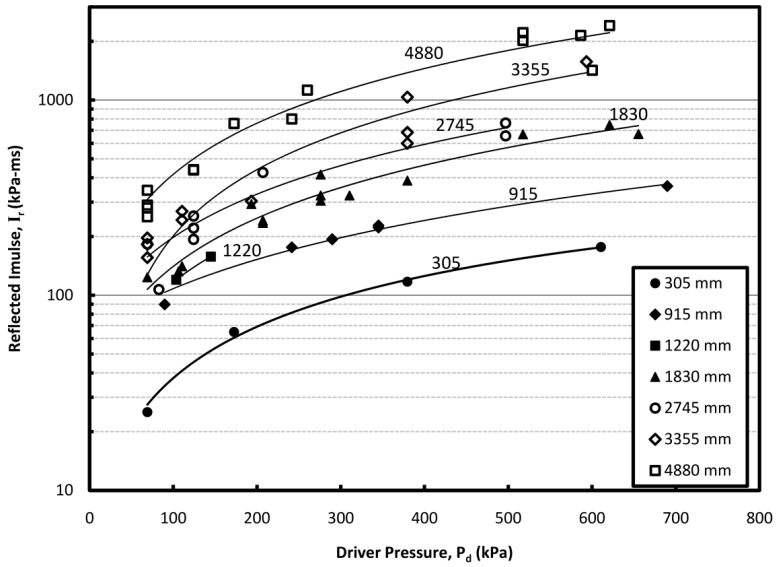

Figure 3.10: Shock Tube Reflected Impulses Over the Positive Phase as a Function of Driver Pressure for Various Driver Lengths (Reproduced from Lloyd et al., 2010).

(a) Front view (b) Side view

Figure 3.11: Load Transfer Device and Support Conditions for Companion Set 1 and 2.

Figure 3.12: Close-up of Support Conditions for Companion Set 1 and 2.

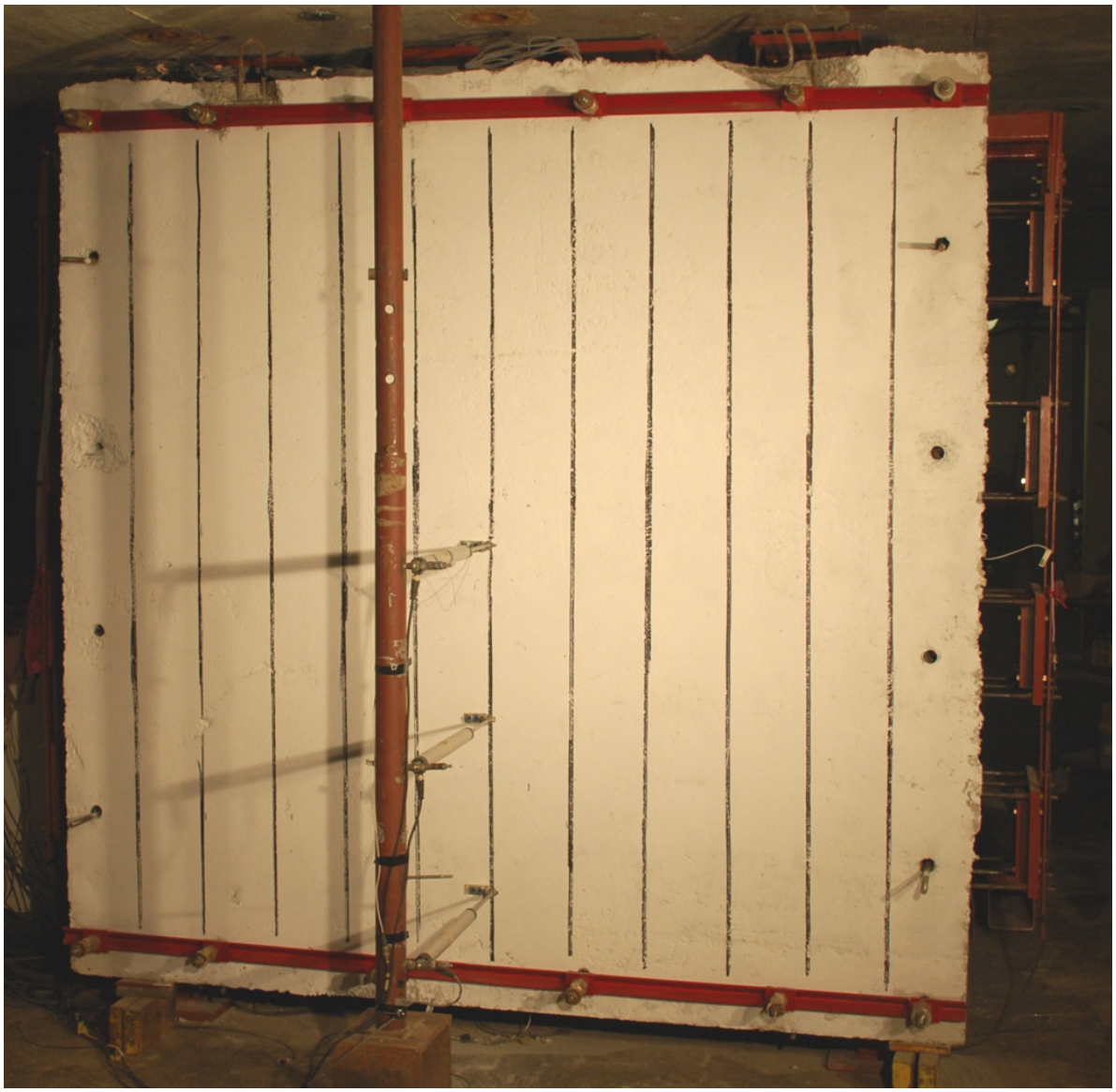

Figure 3.13: Typical Knife-Edged Support Conditions for Companion Sets 3 and 4.

Figure 3.14: Close-up of Back-to-Back Angles Used for Knife Edge Supports in Companion Set 3 and 4.

Figure 3.15: Close-up of Support Conditions for Companion Set 5.

(a) Specimen CS5-C (b) Specimen CS5-R

Figure 3.16: Experimental Setup and Support Conditions for Companion Set 5.

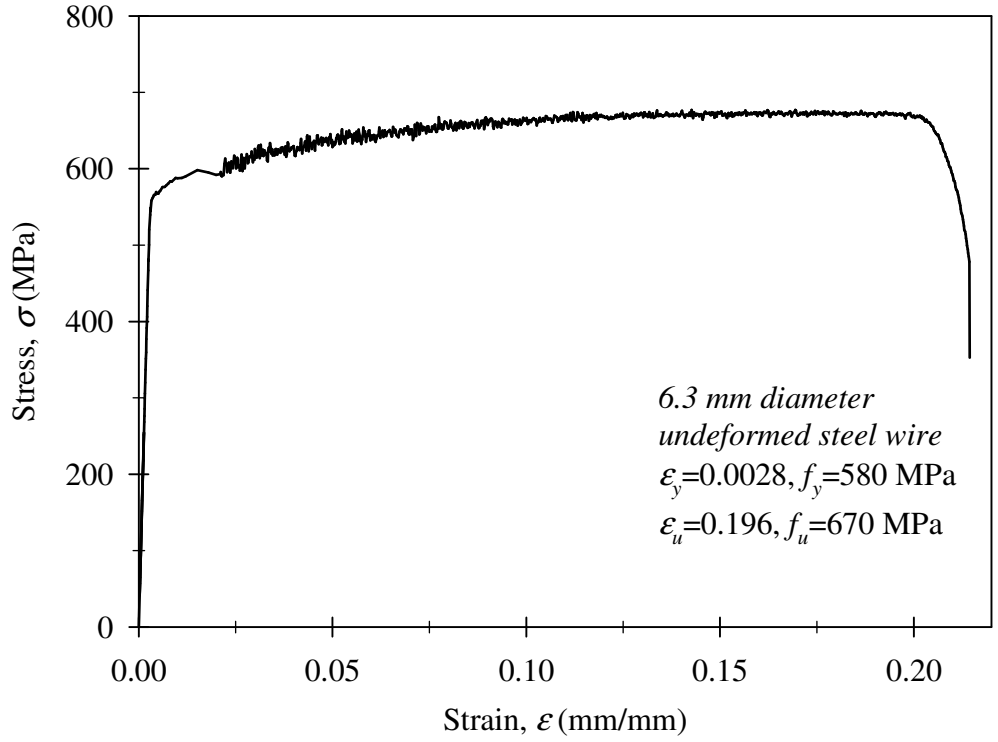

Figure 3.17: Stress-Strain Relationship of Longitudinal Reinforcing Steel.

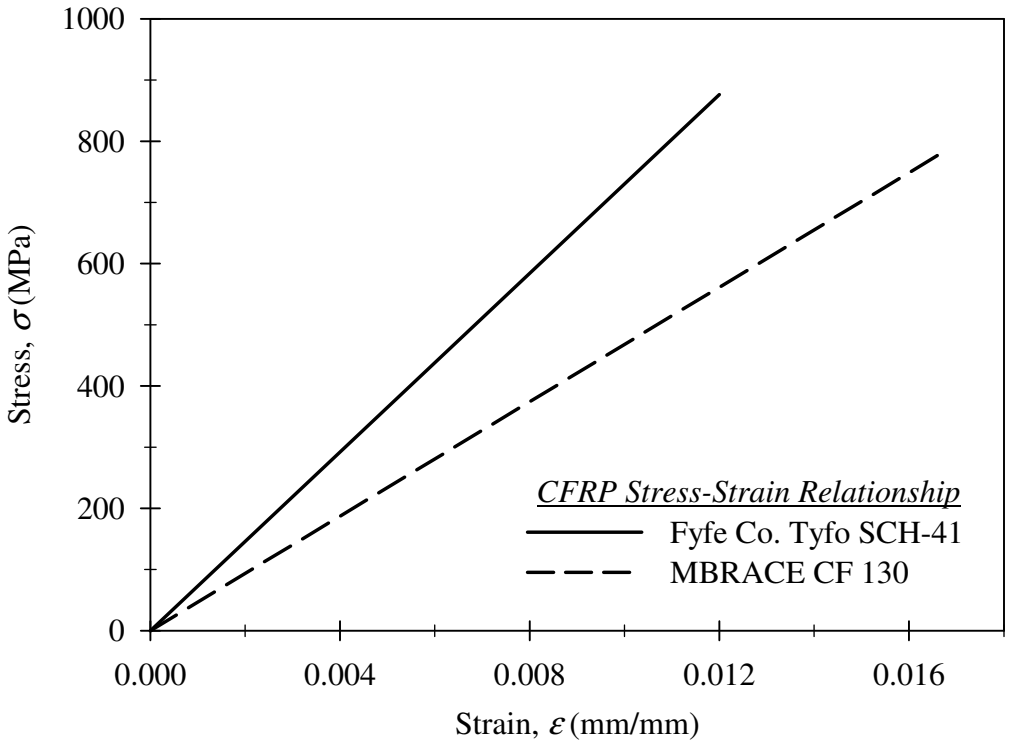

Figure 3.18: Composite Gross Laminate 0° Tensile Properties of CFRP Materials.
(Based on an assumed thickness of* 0.8 mm *for MBRACE CF 130
and* 1.0 mm *for Fyfe Co. Tyfo SCH-41 CFRP)

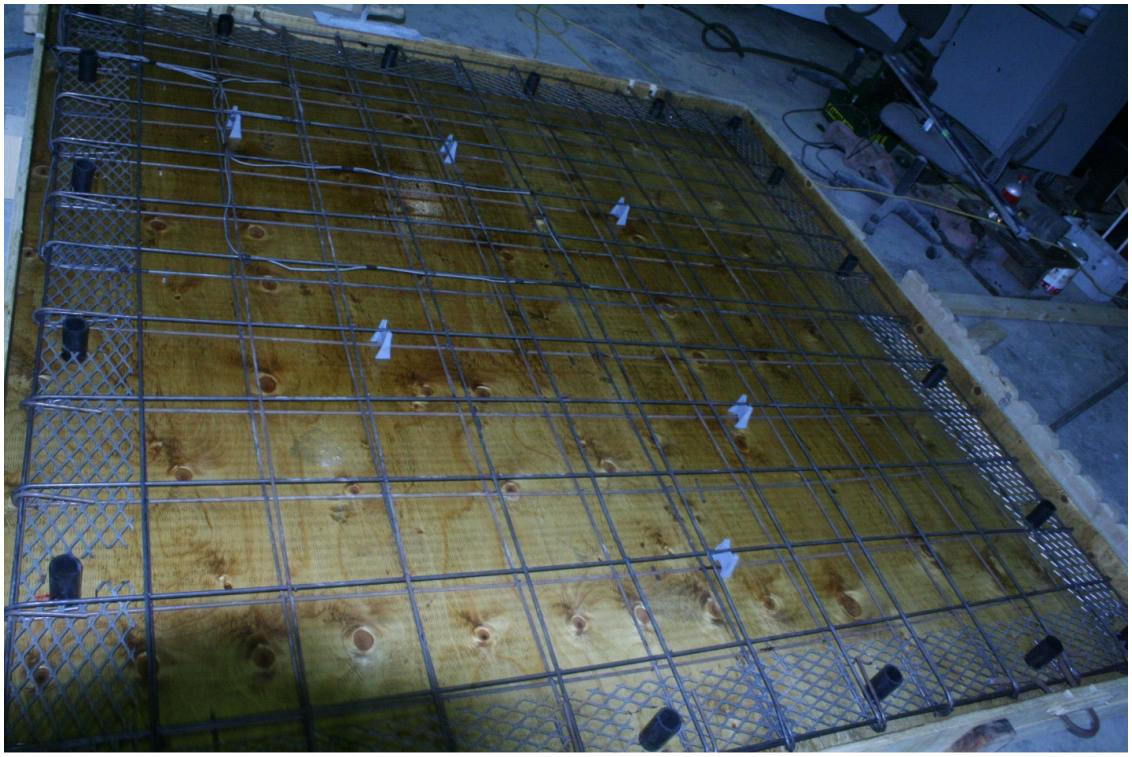

Figure 3.19: Typical Two-way Slab Reinforcement Cage Prior to Casting.

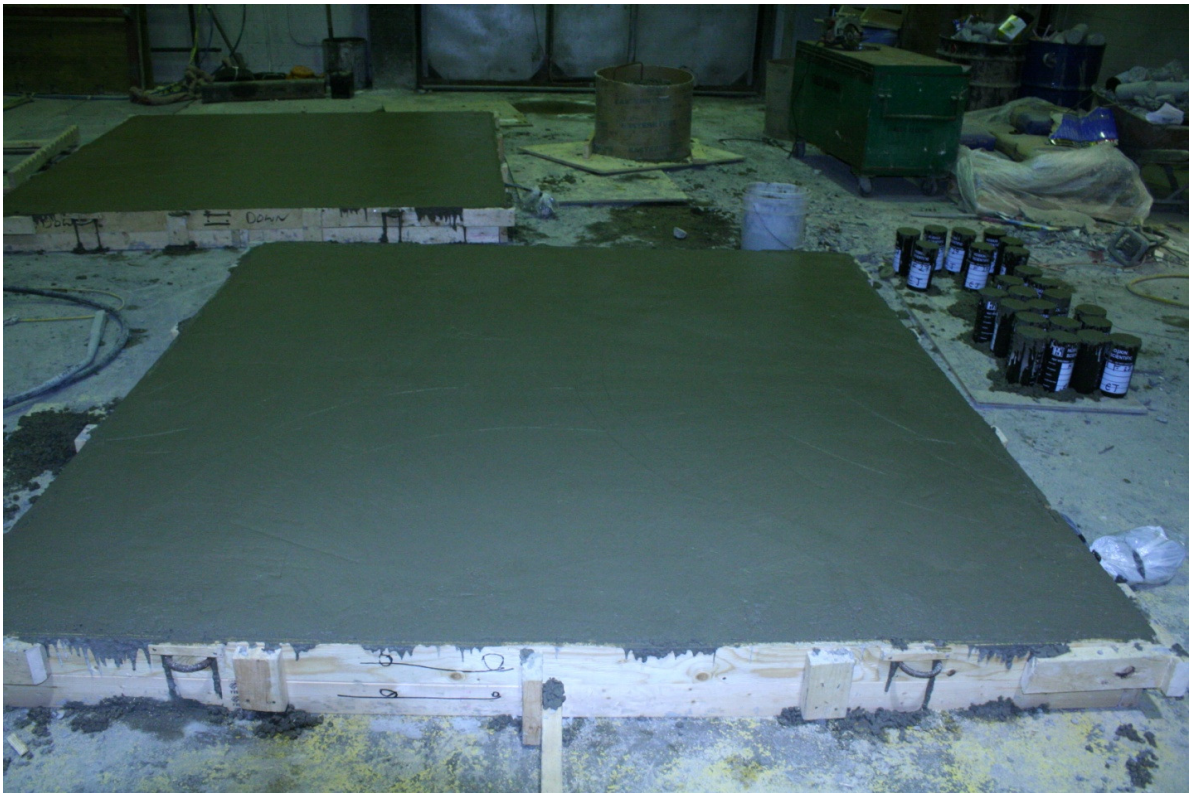

Figure 3.20: Typical Two-way Slab During Casting.

Figure 3.21: Typical One-way Reinforced Concrete Panel with Externally Bonded CFRP Retrofit Prior to Testing.

Figure 3.22: Typical FRP Anchor.

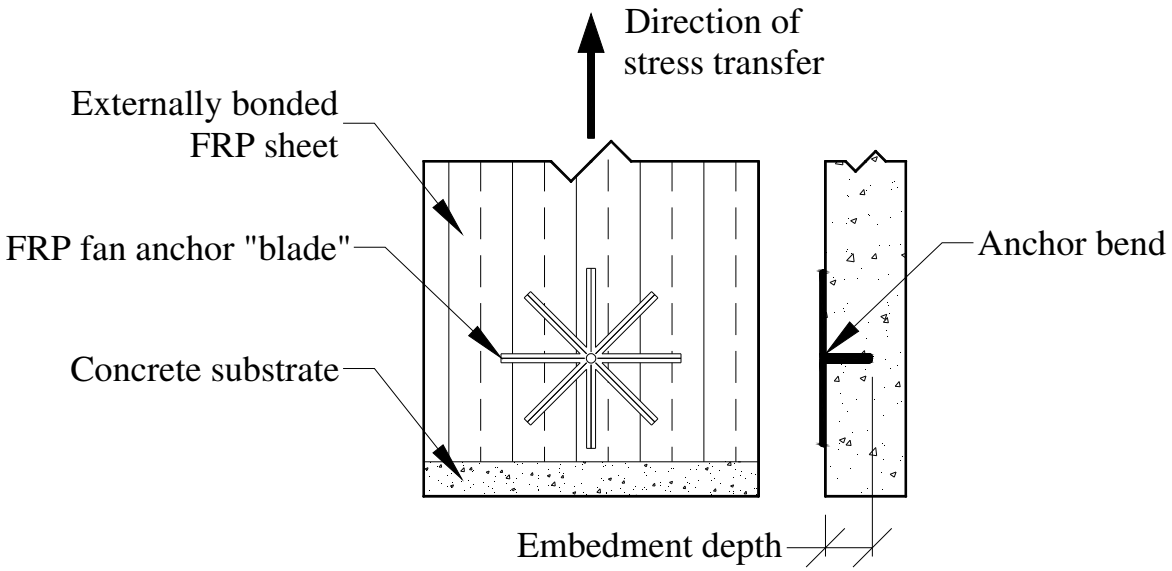

Figure 3.23: FRP Fan Anchor Details.

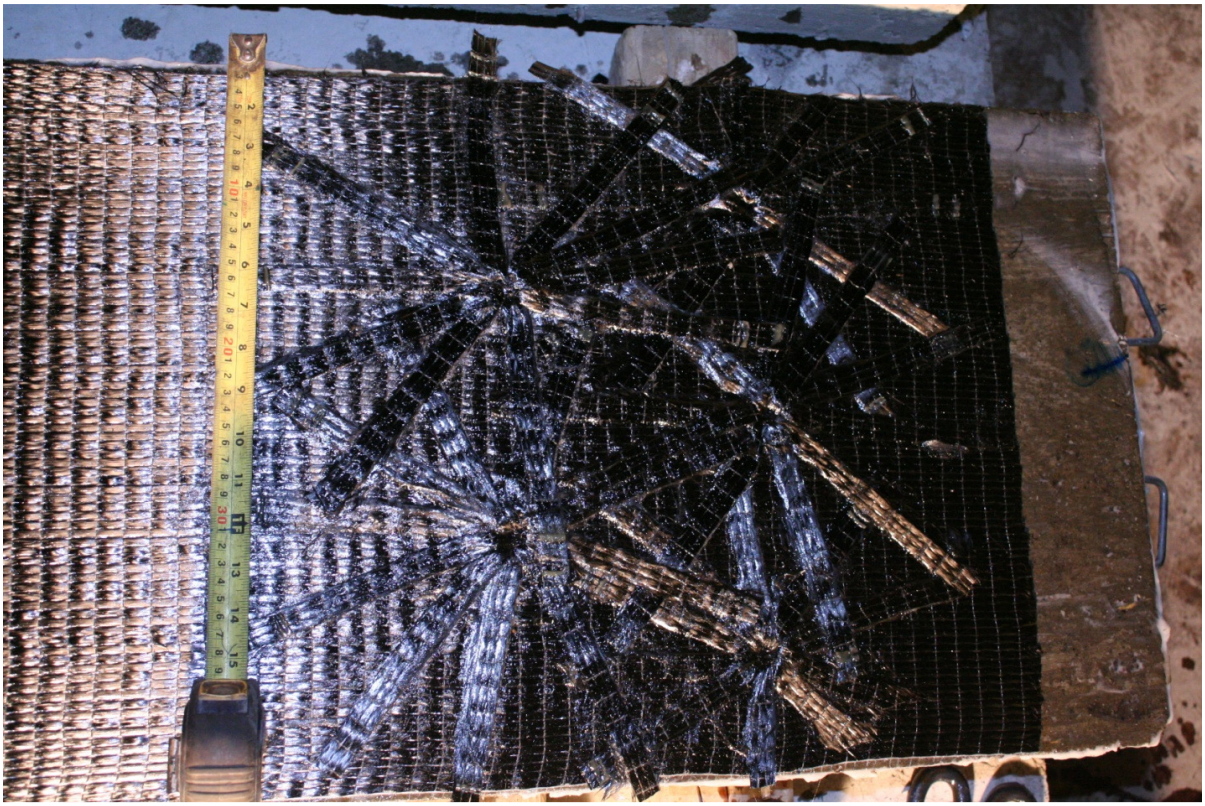

Figure 3.24: Typical FRP Anchor Placement.

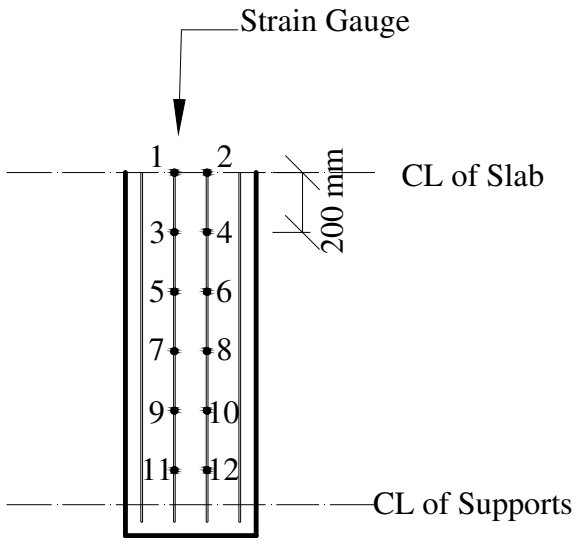

Top Mat (Inbound) Reinforcing Steel Strain Gauge Locations

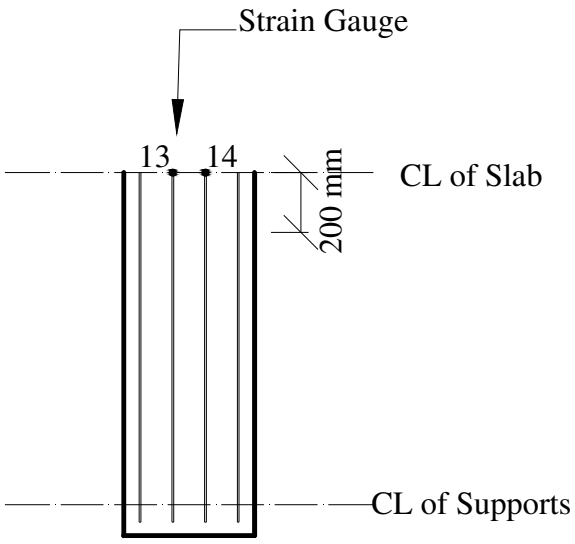

Bottom Mat (Rebound) Reinforcing Steel Strain Gauge Locations

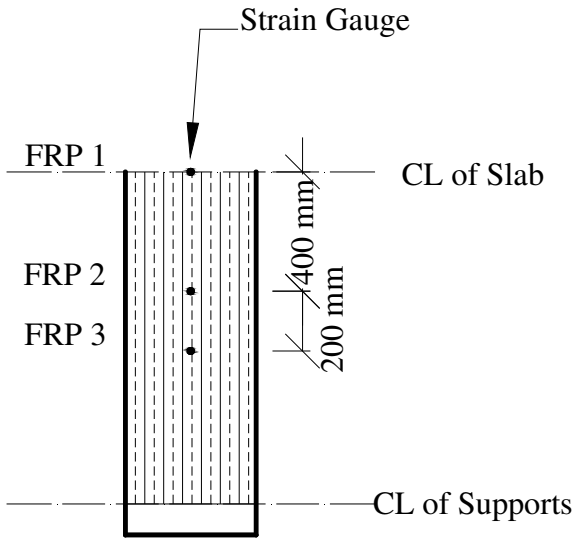

FRP Strain Gauge Locations Inbound Face

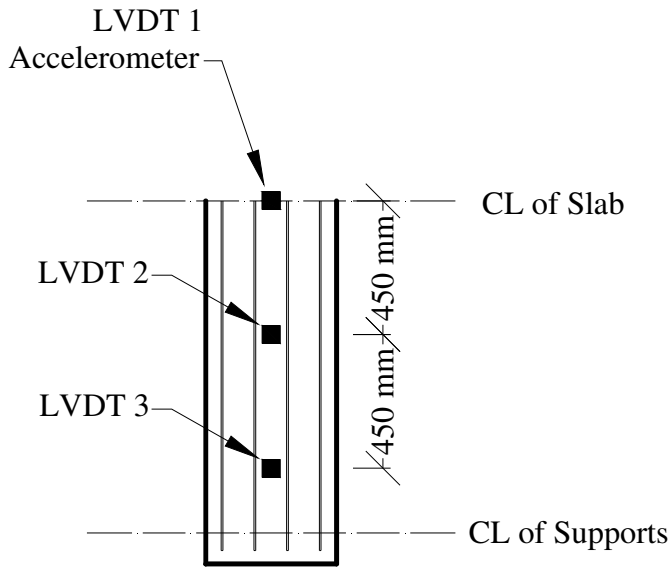

LVDT and Accelerometer Locations Inbound Face

Figure 3.25: Typical Instrumentation for Companion Set 1 and 2.

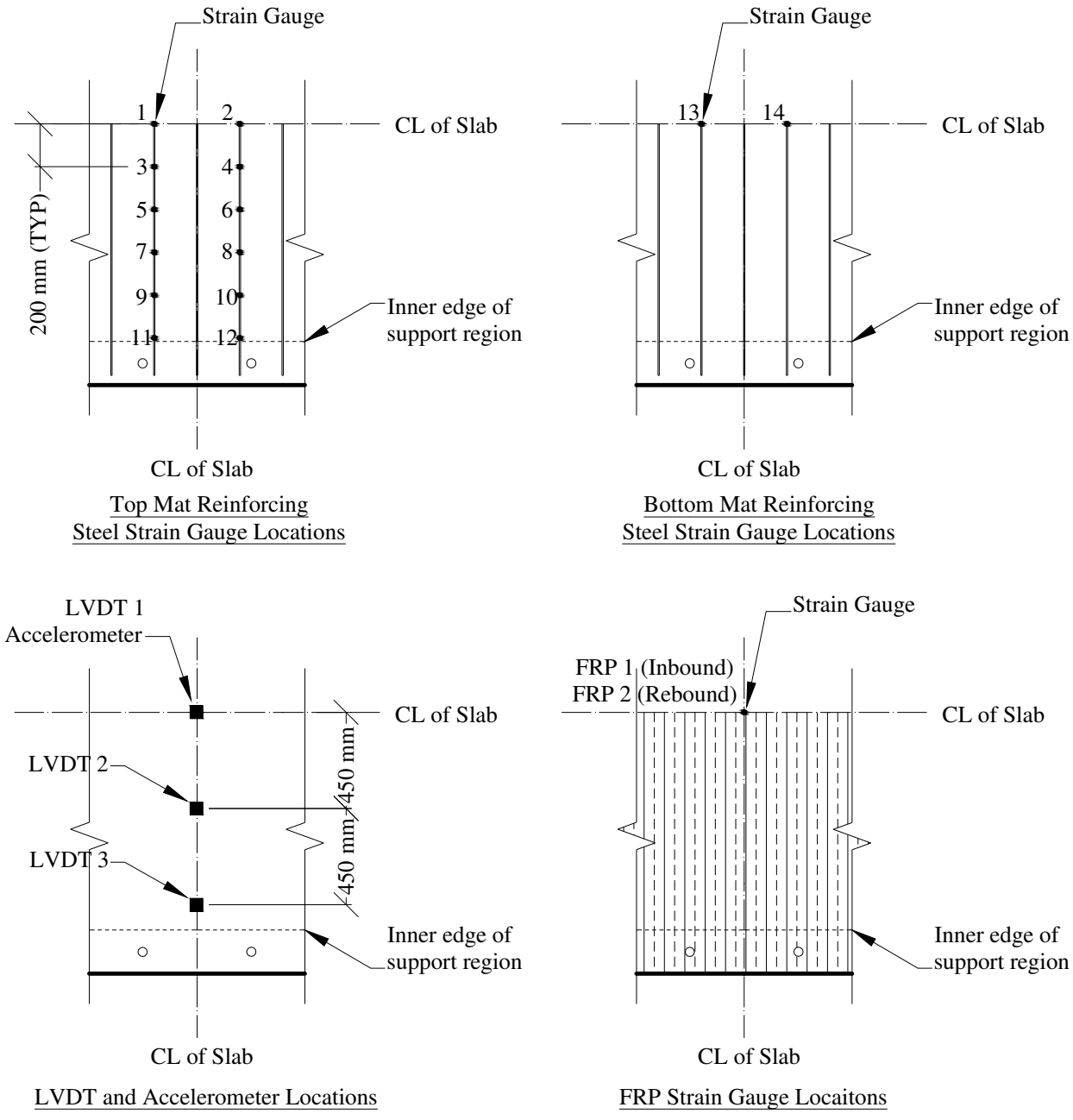

Figure 3.26: Typical Instrumentation for Companion Set 3.

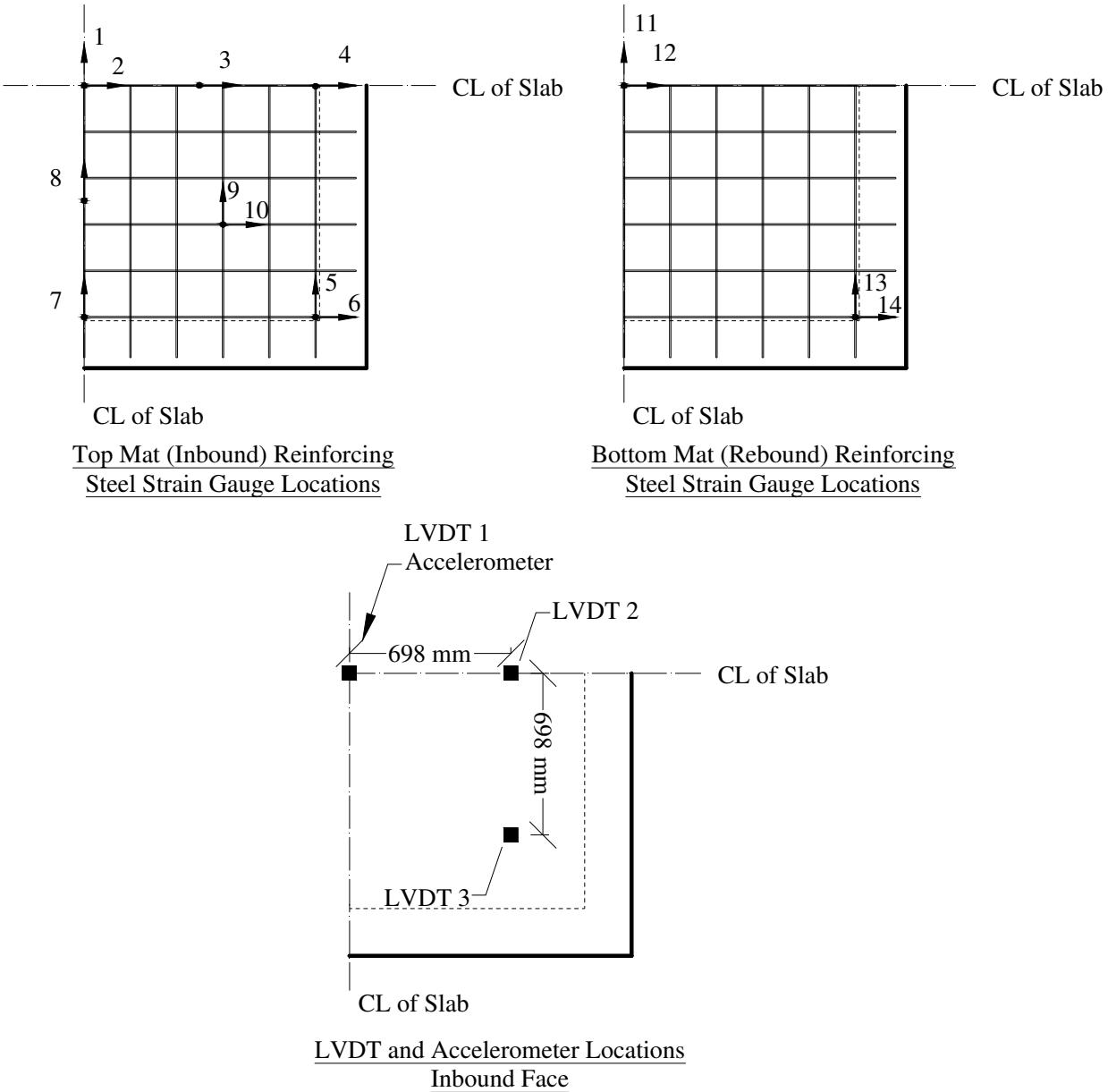

Figure 3.27: Typical Instrumentation for Companion Set 4 and 5.

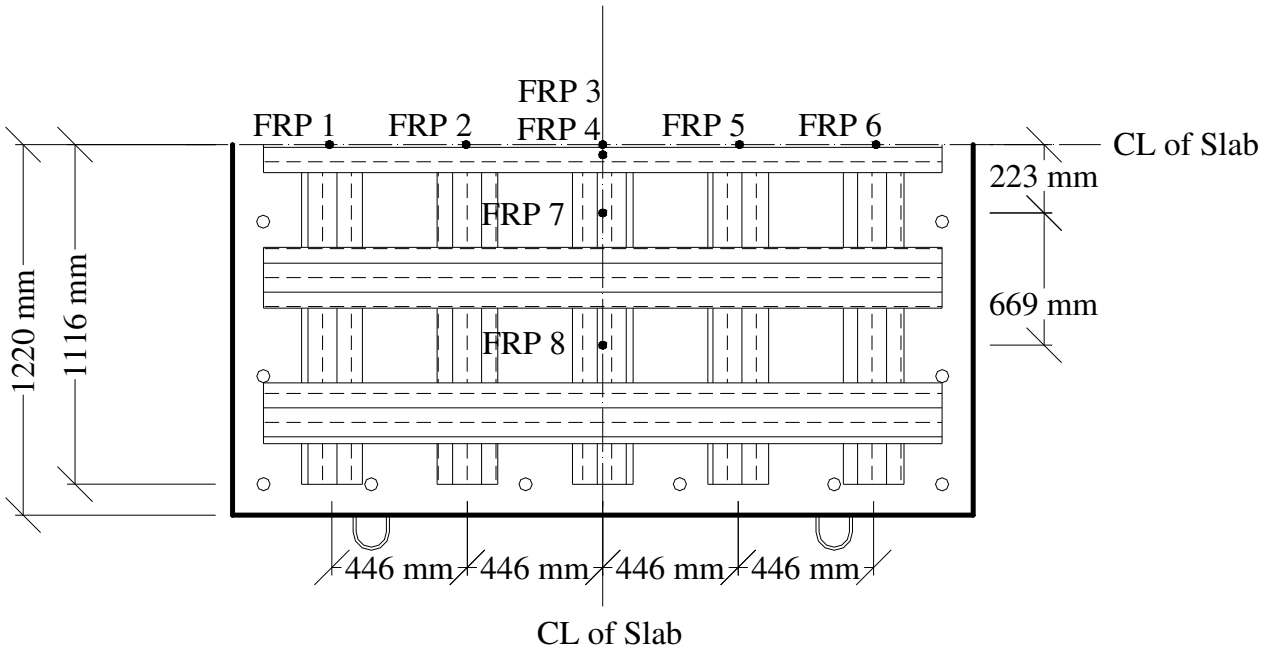

Figure 3.28: FRP Strain Gauge Locations for Specimen CS4-R2.

Chapter 4. Test Results and Evaluation of Data

4.1. General

The experimental results obtained from the shock wave loading of thirteen reinforced concrete wall panels and slab plates incorporating various CFRP retrofit configurations are presented in this chapter. Shock wave properties, maximum displacement, support rotations (given in parenthesis), time-to-maximum displacement and steel and CFRP strains for each of the sixty simulated explosions are discussed. Wherever possible, displacement time-history plots for each companion set have been grouped according to driver length and driver pressure to facilitate direct comparison of retrofitted and unretrofitted specimen response. These experimental displacement time-history comparisons are presented in Appendix A.

4.2. Companion Set 1 (CS1)

Companion set 1, consisted of four one-way, *80 mm* thick reinforced concrete wall panels. A load transfer device was used to transfer shock wave loading to the face of the members. A total of sixteen shots were performed as part of CS1. A summary of the experimental results for this companion set, including shock tube firing parameters, shock wave properties and displacements, may be found in Table 4.1. A summary of pertinent strain information may be found in Table 4.5. A comparison of the experimental displacement time-histories for all specimens of companion set 1 may be found in Figure A-1 to Figure A-5.

4.2.1 Specimen CS1-C

Specimen CS1-C served as an unretrofitted control for companion set 1 and was subjected to two simulated explosions of increasing destructiveness. The extent of damage progression for CS1-C is illustrated in Figure 4.1.

CS1-C – 1

Test CS1-C – 1 used a driver length of *1830 mm* and a driver pressure of *60.7 kPa*. The resulting shock wave had a peak pressure of *12.5 kPa*, reflected impulse of *95.7 kPa-ms* and positive phase duration of *13 ms*. Maximum deflection was *26.1 mm* (*1.3°*) which occurred at a time of *65.6 ms*. Residual displacement was *7.3 mm*. The displacement time-history plot for test CS1-C – 1 may be seen in Figure A-1.

The maximum strain in mid-span tension gauge SG1 was *0.112%* at a time of *69 ms*, corresponding to a strain-rate of *0.016* s^{-1}. There was no residual strain in tension gauge SG1. The maximum strain in mid-span tension gauge SG2 was *0.106%* at a time of *70 ms*, corresponding to a strain-rate of *0.015* s^{-1}. The residual strain in tension gauge SG2 was *0.058%*. The strain in mid-span compression gauge SG13 at a time of *70 ms* was *-0.02%*.

Minor cracking was observed at the locations of transverse reinforced, as illustrated in Figure 4.1 (b).

CS1-C – 2

Test CS1-C – 2 used a driver length of *1830 mm* and a driver pressure of *241.3 kPa*. The resulting shock wave had a peak pressure of *42.6 kPa*, reflected impulse of *301.6 kPa-ms* and positive phase duration of *16.3 ms*. Maximum deflection was *167.8 mm* (*8.6°*) which occurred at a time of *89.8 ms*. Residual displacement was *140.0 mm* (*147.3 mm* cumulative). A comparison of the displacement time-history for all specimens of companion set 1 with similar shock wave properties may be seen in Figure A-2.

The final strain reading in mid-span tension gauge SG1 was *0.197%* at a time of *42.5 ms*, corresponding to a strain-rate of *0.046* s^{-1}. Gauge SG1 was destroyed and no residual strain was recorded. The final strain reading in mid-span tension gauge SG2 was *0.129%* at a time of *26.2 ms*, corresponding to a strain-rate of *0.049* s^{-1}. Gauge SG2 was destroyed and no residual strain was recorded. The strain in mid-span compression gauge SG13 at a time of *26.2 ms* and *42.5 ms* was *-0.027%*.

The extent of damage after testing is illustrated in Figure 4.1 (c). Cracking was predominately focused at mid-span with crushing of concrete on the compression face of the maxi-

mum moment region. The residual displaced shape closely resembled that of rigid body motion of the two halves of the panel.

4.2.2 Specimen CS1-R1

Specimen CS1-R1 was one of two specimens retrofitted with one layer of externally bonded CFRP applied over the entire clear span of the inbound tensile face. CS1-R1 was subjected to two simulated explosions of increasing destructiveness. The extent of damage progression for CS1-R1 is illustrated in Figure 4.2.

CS1-R1 – 1

Test CS1-R1 – 1 used a driver length of *1830 mm* and a driver pressure of *61.4 kPa*. The resulting shock wave had a peak pressure of *12.9 kPa*, reflected impulse of *83.6 kPa-ms* and positive phase duration of *12.7 ms*. Maximum deflection was *11.6 mm* (*0.6°*) which occurred at a time of *26.1 ms*. Residual displacement was *1.4 mm*, although this was likely caused by the test setup settling. The displacement time-history plot for test CS1-R1 – 1 may be seen in Figure A-1.

No strain data was recorded for this shot.

The specimen remained elastic and no visible damage was observed.

CS1-R1 – 2

Test CS1-R1 – 2 used a driver length of *1830 mm* and a driver pressure of *241.3 kPa*. The resulting shock wave had a peak pressure of *46.4 kPa*, reflected impulse of *300.0 kPa-ms* and positive phase duration of *16.3 ms*. Maximum deflection was *146.9 mm* (*7.5°*) which occurred at a time of *85 ms*. Residual displacement was *118.6 mm* (*120 mm* cumulative). The displacement time-history plot for test CS1-R1 – 2 may be seen in Figure A-2.

The final strain reading in mid-span tension gauge SG1 was *0.234%* at a time of *28 ms*, corresponding to a strain-rate of *0.084* s^{-1}. Gauge SG1 was destroyed and no residual strain was recorded. The maximum strain in mid-span tension gauge SG2 was *0.213%* at a time of *61.5 ms*, corresponding to a strain-rate of *0.034* s^{-1}. Residual strain was *0.17%*. Mid-span FRP gauge 1 and compression gauge SG13 were destroyed and did not record any data.

The extent of damage progression during testing may be seen in Figure 4.2. CS1-R1 failed by debonding of CFRP and concrete substrate. Upon inspection of the CFRP-concrete interface after debonding, the concrete substrate remained essentially intact and failure of the retrofit was entirely limited to the epoxy binder. It was determined that the premature failure of CS1-R1 was caused by poor workmanship resulting from insufficient saturation of the CFRP sheet with epoxy. Despite the high level of damage, little debris was generated as a result of specimen failure.

4.2.3 Specimen CS1-R2

Specimen CS1-R2 was the second of two specimens retrofitted with one layer of externally bonded CFRP applied over the entire clear span of the inbound tensile face. CS1-R2 was subjected to six simulated explosions of increasing destructiveness. The extent of damage progression for CS1-R2 is illustrated in Figure 4.3.

CS1-R2 – 1

Test CS1-R2 – 1 used a driver length of *1830 mm* and a driver pressure of *57.9 kPa*. The resulting shock wave had a peak pressure of *11.1 kPa*, reflected impulse of *89.3 kPa-ms* and positive phase duration of *14 ms*. Maximum deflection was *8.1 mm* (*0.4°*) which occurred at a time of *23.8 ms*. Residual displacement was *1.7 mm*, although this is likely due to the test setup settling. The displacement time-history plot for test CS1-R2 – 1 may be seen in Figure A-1.

The maximum strain in mid-span FRP gauge 1 was *0.127%* at a time of *22.8 ms*, corresponding to a strain-rate of *0.056* s^{-1}. No residual strain was recorded. The strain in mid-span compression steel gauge SG13 was *-0.035%* at a time of *22.8 ms*. Based on this strain profile, the strain in mid-span tension steel was calculated to be *0.106%* corresponding to a strain-rate of *0.047* s^{-1}.

CS1-R2 – 2

Test CS1-R2 – 2 used a driver length of *1830 mm* and a driver pressure of *238.6 kPa*. The resulting shock wave had a peak pressure of *44.8 kPa*, reflected impulse of *331.2 kPa-ms* and positive phase duration of *16.1 ms*. Maximum deflection was *42.5 mm* (*2.2°*) which occurred

at a time of *29.7 ms*. There was no residual displacement. The displacement time-history plot for test CS1-R2 – 2 may be seen in Figure A-2.

The maximum strain in mid-span FRP gauge 1 was *0.459%* at a time of *29.7 ms*, corresponding to a strain-rate of *0.154* s^{-1}. No residual strain was recorded. The strain in mid-span compression steel gauge SG13 was *-0.097%* at a time of *29.7 ms*. Based on this strain profile, the strain in mid-span tension steel was calculated to be *0.388%* corresponding to a strain-rate of *0.131* s^{-1}.

No visible cracking or damage was noted.

CS1-R2 – 3

Test CS1-R2 – 3 used a driver length of *1830 mm* and a driver pressure of *273.7 kPa*. The resulting shock wave had a peak pressure of *49.0 kPa*, reflected impulse of *336.9 kPa-ms* and positive phase duration of *15.7 ms*. Maximum deflection was *40.4 mm* (*2.1°*) which occurred at a time of *28.9 ms*. There was no residual displacement.

The maximum strain in mid-span FRP gauge 1 was *0.459%* at a time of *27.8 ms*, corresponding to a strain-rate of *0.165* s^{-1}. No residual strain was recorded. The strain in mid-span compression steel gauge SG13 was *-0.152%* at a time of *27.8 ms*. Based on this strain profile, the strain in mid-span tension steel was calculated to be *0.398%* corresponding to a strain-rate of *0.143* s^{-1}.

Minor cracking in the mid-span region was noted, but the retrofit system was otherwise undamaged.

CS1-R2 – 4

Test CS1-R2 – 4 used a driver length of *1830 mm* and a driver pressure of *353.0 kPa*. The resulting shock wave had a peak pressure of *64.7 kPa*, reflected impulse of *444.3 kPa-ms* and positive phase duration of *15.7 ms*. Maximum deflection was *62.6 mm* (*3.2°*) which occurred at a time of *30.7 ms*. There was no residual displacement. The displacement time-history plot for test CS1-R2 – 4 may be seen in Figure A-3.

The maximum strain in mid-span FRP gauge 1 was *0.690%* at a time of *29.8 ms*, corresponding to a strain-rate of *0.231* s^{-1}. No residual strain was recorded. The strain in mid-span com-

pression steel gauge SG13 was *-0.170%* at a time of *29.8 ms*. Based on this strain profile, the strain in mid-span tension steel was calculated to be *0.6%* corresponding to a strain-rate of *0.201* s^{-1}.

Few new cracks were noted and the specimen remained elastic.

CS1-R2 – 5

Test CS1-R2 – 5 used a driver length of *1830* mm and a driver pressure of *415.8 kPa*. The resulting shock wave had a peak pressure of *72.9 kPa*, reflected impulse of *510.9 kPa-ms* and positive phase duration of *16.6 ms*. Maximum deflection was *84.6 mm* (*4.3°*) which occurred at a time of *34.1 ms*. Residual displacement was *17.1 mm* (*18.7 mm* cumulative). The displacement time-history plot for test CS1-R2 – 5 may be seen in Figure A-4.

The maximum strain in mid-span FRP gauge 1 was *0.854%* at a time of *34.5 ms*, corresponding to a strain-rate of *0.248* s^{-1}. No residual strain was recorded. Mid-span compression steel gauge SG13 was destroyed, but the strain at a time of *29.8 ms* was at least *-0.25%*.

More distributed cracking was noticed along the length of the specimen over a region approximately *500 mm* on either side of mid-span. Furthermore, a *50 mm* wide strip of CFRP located along the edge of the specimen at mid-span ruptured. This rupture was caused by a fabrication defect in the CFRP fibres at this location which went unnoticed during construction. However, the rest of the specimen remained undamaged so the ruptured section of CFRP was removed and testing continued. The extent of cracking and the ruptured CFRP strip are illustrated in Figure 4.3 (b).

CS1-R2 – 6

Test CS1-R2 – 6 used a driver length of *1830 mm* and a driver pressure of *489.5 kPa*. The resulting shock wave had a peak pressure of *79.6 kPa*, reflected impulse of *595.1 kPa-ms* and positive phase duration of *17.7 ms*. Maximum deflection was *224.6 mm* (*11.4°*) which occurred at a time of *118.5 ms*. Residual displacement was *188.1 mm* (*206.9 mm* cumulative). The displacement time-history plot for test CS1-R2 – 6 may be seen in Figure A-5.

The strain in mid-span FRP gauge 1 at debonding failure was *1.0%* at *27.1 ms*, corresponding to a strain-rate of *0.365* s^{-1}. Mid-span compression steel gauge SG13 was destroyed on the previous shot.

Plate-end interfacial debonding, initiated at the top of the sheet, was the cause of specimen failure. Pieces of failed concrete cover, approximately *5-15 mm* in size, were projected a distance up to *2 m* away from the specimen. Concrete cracking was distributed evenly over the length of the specimen. Although a plastic hinge had clearly formed at the mid-span, the top and bottom halves of the specimen were markedly bowed. This indicates that inelasticity was relatively distributed over the length of the member, as opposed to being focused at the hinge as was the case for specimen CS1-C. The extent of damage in specimen CS1-R2 at different stages of testing is illustrated in Figure 4.3.

4.2.4 Specimen CS1-A

Specimen CS1-A was retrofitted with one layer of externally bonded CFRP applied to the inbound tensile face of the member. Additional mechanical end anchorage was provided with 5 FRP fan anchors installed on either end of the composite sheet. CS1-A was subjected to six shots of increasing destructiveness resulting in failure of the member by FRP anchor failure leading to CFRP debonding. The extent of damage progression for CS1-A is illustrated in Figure 4.4.

CS1-A – 1

Test CS1-A – 1 used a driver length of *1830 mm* and a driver pressure of *62.1 kPa*. The resulting shock wave had a peak pressure of *13.3 kPa*, reflected impulse of *99.9 kPa-ms* and positive phase duration of *13.2 ms*. Maximum deflection was *9.4 mm* (*0.5°*) which occurred at a time of *24.3 ms*. Residual displacement was *1.4 mm*, although this is likely due to the test setup settling. The displacement time-history plot for test CS1-A – 1 may be seen in Figure A-1.

The maximum strain in mid-span FRP gauge 1 was *0.11%* at a time of *24.3 ms*, corresponding to a strain-rate of *0.045* s^{-1}. No residual strain was recorded. The strain in mid-span compression steel gauge SG13 was *-0.039%* at a time of *24.3 ms*. Based on this strain profile, the strain in mid-span tension steel was calculated to be *0.091%* corresponding to a strain-rate of *0.037* s^{-1}.

No visible damage or cracking was observed.

CS1-A – 2

Test CS1-A – 2 used a driver length of *1830 mm* and a driver pressure of *241.3 kPa*. The resulting shock wave had a peak pressure of *51.3 kPa*, reflected impulse of *335.3 kPa-ms* and positive phase duration of *16.5 ms*. Maximum deflection was *42.3 mm* (*2.2°*) which occurred at a time of *30 ms*. There was no residual displacement. The displacement time-history plot for test CS1-A – 2 may be seen in Figure A-2.

The maximum strain in mid-span FRP gauge 1 was *0.370%* at a time of *27.6 ms*, corresponding to a strain-rate of *0.134* s^{-1}. No residual strain was recorded. The strain in mid-span compression steel gauge SG13 was *-0.090%* at a time of *27.6 ms*. Based on this strain profile, the strain in mid-span tension steel was calculated to be *0.312%* corresponding to a strain-rate of *0.112* s^{-1}.

Very slight cracks were observed in the maximum moment region.

CS1-A – 3

Test CS1-A – 3 used a driver length of *1830 mm* and a driver pressure of *351.6 kPa*. The resulting shock wave had a peak pressure of *67.4 kPa*, reflected impulse of *460.6 kPa-ms* and positive phase duration of *16.1 ms*. Maximum deflection was *68.4 mm* (*3.5°*) which occurred at a time of *33.6 ms*. There was no residual displacement. The displacement time-history plot for test CS1-A – 3 may be seen in Figure A-3.

The maximum strain in mid-span FRP gauge 1 was *0.630%* at a time of *29.2 ms*, corresponding to a strain-rate of *0.216* s^{-1}. No residual strain was recorded. The strain in mid-span compression steel gauge SG13 was *-0.185%* at a time of *29.2 ms*. Based on this strain profile, the strain in mid-span tension steel was calculated to be *0.527%* corresponding to a strain-rate of *0.180* s^{-1}.

The size and magnitude of flexural cracks increased noticeably after this test. The cracked region extended approximately *600 mm* on either side of mid-span. No damage to the externally bonded CFRP sheets or FRP fan anchors was noted.

CS1-A – 4

Test CS1-A – 4 used a driver length of *1830 mm* and a driver pressure of *416.4 kPa*. The resulting shock wave had a peak pressure of *70.9 kPa*, reflected impulse of *511.8 kPa-ms* and

positive phase duration of *17.1 ms*. Maximum deflection was *83.6 mm* (*4.3°*) which occurred at a time of *36 ms.* There was no residual displacement. The displacement time-history plot for test CS1-A – 4 may be seen in Figure A-8.

The maximum strain in mid-span FRP gauge 1 was *0.729%* at a time of *32.1 ms*, corresponding to a strain-rate of *0.227* s^{-1}. No residual strain was recorded. The strain in mid-span compression steel gauge SG13 was *-0.230%* at a time of *32.1 ms*. Based on this strain profile, the strain in mid-span tension steel was calculated to be *0.607%* corresponding to a strain-rate of *0.189* s^{-1}.

No damage to the retrofit system was observed, although the cracked region had expended to approximately *800 mm* on either side of the mid-span of the member.

CS1-A – 5

Test CS1-A – 5 used a driver length of *1830 mm* and a driver pressure of *482.6 kPa*. The resulting shock wave had a peak pressure of *74.7 kPa*, reflected impulse of *511.7 kPa-ms* and positive phase duration of *15.8 ms*. Maximum deflection was *85.5 mm* (*4.4°*) which occurred at a time of *36.3 ms*. There was no residual displacement. The displacement time-history plot for test CS1-A – 5 may be seen in Figure A-4.

The maximum strain in mid-span FRP gauge 1 was *0.730%* at a time of *31.1 ms*, corresponding to a strain-rate of *0.235* s^{-1}. No residual strain was recorded. The strain in mid-span compression steel gauge SG13 was *-0.239%* at a time of *31.1 ms*. Based on this strain profile, the strain in mid-span tension steel was calculated to be *0.607%* corresponding to a strain-rate of *0.195* s^{-1}.

The first signs of impending failure of the retrofit were noticed in the two innermost FRP anchors located in the bottom group of anchors. The ends of the fan blades had begun to debond from the rest of the laminate. This debonding extended for a length of approximately *15 mm* from the tip of the blades. No other new damage was observed.

CS1-A – 6

Test CS1-A – 6 used a driver length of *1830 mm* and a driver pressure of *487.5 kPa*. The resulting shock wave had a peak pressure of *82.6 kPa*, reflected impulse of *603.0 kPa-ms* and positive phase duration of *17.5 ms*. Maximum deflection was *132.8 mm* (*6.8°*) which oc-

curred at a time of *74.2 ms*. Residual displacement was *92.0 mm* (*93.4 mm* cumulative). The displacement time-history plot for test CS1-A – 6 may be seen in Figure A-5.

The strain in mid-span FRP gauge 1 at retrofit failure was *0.804%* at a time of *31.9 ms*, corresponding to a strain-rate of *0.252* s^{-1}. No residual strain was recorded. The strain in mid-span compression steel gauge SG13 was *-0.260%* at a time of *31.9 ms*. Based on this strain profile, the strain in mid-span tension steel was calculated to be *0.669%* corresponding to a strain-rate of *0.210* s^{-1}.

Failure of the specimen was by plate-end interfacial debonding of the CFRP sheet, followed by failure of the bottom group of anchors. The extent of damage in specimen CS1-A at different stages of testing is illustrated in Figure 4.4. Stress concentrations at the anchor bends resulted in fibre rupture and loss of anchorage. A photograph of the failed FRP anchors is shown in Figure 4.4 d). Failure of the anchors resulted in a loss of composite action and the complete debonding of the CFRP laminate from concrete substrate. The surface of the member was pitted and rough where both aggregate and cement binder had failed in tension and remained bonded to the composite sheet. The debris pattern was such that the small pieces of concrete were strewn across the floor up to *2 m* away. Despite experiencing large inelastic deformations, the final displaced shaped of CS1-A, shown in Figure 4.4 c), was characterised by a gradual curve, as opposed to a distinct plastic hinge at mid-span. The distributed nature of the crack pattern, also shown in Figure 4.4 c), is indicative of smeared inelasticity of the member at failure.

4.3. Companion Set 2 (CS2)

Companion set 2 consisted of three one-way, *120 mm* thick reinforced concrete wall panels. A load transfer device was used to transfer shock wave loading to the face of the members. A total of eleven shots were performed as part of CS2. A summary of the experimental results for this companion set, including shock tube firing parameters, shock wave properties and displacements, may be found in Table 4.2. A summary of pertinent strain information may be found in Table 4.6. A comparison of the experimental displacement time-histories for all specimens of companion set 2 may be found in Figure A-6 to Figure A-9.

4.3.1 Specimen CS2-C

Specimen CS2-C served as an unretrofitted control for companion set 2 and was subjected to two simulated explosions of increasing destructiveness. The extent of damage progression for CS2-C is illustrated in Figure 4.5.

CS2-C – 1

Test CS2-C – 1 used a driver length of *1830 mm* and a driver pressure of *84.1 kPa*. The resulting shock wave had a peak pressure of *17.7 kPa*, reflected impulse of *143 kPa-ms* and positive phase duration of *13.8 ms*. Maximum deflection was *16.3 mm* (*0.8°*) which occurred at a time of *31.5 ms*. Residual displacement was *5.7 mm*. The displacement time-history plot for test CS2-C – 1 may be seen in Figure A-6.

The maximum strain in mid-span tension gauge SG1 was *0.900%* at a time of *39.2 ms*, corresponding to a strain-rate of *0.023* s^{-1}. Residual strain was *0.078%*. The maximum strain in mid-span tension gauge SG2 was *0.098%* at a time of *39.2 ms*, corresponding to a strain-rate of *0.025* s^{-1}. The residual strain in tension gauge SG2 was *0.086%*. The strain in mid-span compression gauge SG13 was too small to be recorded.

Minor cracking was observed at the locations of transverse reinforced, as illustrated in Figure 4.5 (b).

CS2-C – 2

Test CS2-C – 2 used a driver length of *1830 mm* and a driver pressure of *311.6 kPa*. The resulting shock wave had a peak pressure of *57.8 kPa*, reflected impulse of *383 kPa-ms* and positive phase duration of *17.4 ms*. Maximum deflection was *148.9 mm* (*7.6°*) which occurred at a time of *80.7 ms*. Residual displacement was *120.6 mm* (*126.3 mm* cumulative). The displacement time-history plot for test CS2-C – 2 may be seen in Figure A-7.

The maximum strain in mid-span tension gauge SG1 was *0.190%* at a time of *42 ms*, corresponding to a strain-rate of *0.045* s^{-1}. Cumulative residual strain was *0.102%*. The maximum strain in mid-span tension gauge SG2 was *0.190%* at a time of *57.2 ms*, corresponding to a strain-rate of *0.033* s^{-1}. The cumulative residual strain in tension gauge SG2 was *0.086%*. The strain in mid-span compression gauge SG13 was too small to be recorded.

The extent of damage after testing is illustrated in Figure 4.5 (c). Specimen CS2-C was considered as being failed after this test. A single, large crack had formed at the mid-span allowing for rigid body rotation of the top and bottom panel. Crushing of concrete was also noted on the compressive face of mid-span of the member.

4.3.2 Specimen CS2-R

Specimen CS2-R was retrofitted with one layer of externally bonded CFRP applied over the entire clear span of the inbound tensile face. CS2-R was subjected to four simulated explosions of increasing destructiveness. The extent of damage progression for CS2-R is illustrated in Figure 4.6.

CS2-R – 1

Test CS2-R – 1 used a driver length of *1830 mm* and a driver pressure of *82.7 kPa*. The resulting shock wave had a peak pressure of *17.1 kPa*, reflected impulse of *128.3 kPa-ms* and positive phase duration of *13.6 ms*. Maximum deflection was *7.0 mm* (*0.4°*) which occurred at a time of 1*8.5 ms*. There was no residual displacement. The displacement time-history plot for test CS2-R2 – 1 may be seen in Figure A-6.

The maximum strain in mid-span tension gauge SG1 was *0.008%* at a time of *17.5 ms*, corresponding to a strain-rate of *0.005* s^{-1}. There was no residual strain in tension gauge SG1. The maximum strain in mid-span tension gauge SG2 was *0.012%* at a time of *17.5 ms*, corresponding to a strain-rate of *0.007* s^{-1}. There was no residual strain. The strain in mid-span compression gauge SG13 at a time of *17.5 ms* was *-0.009%*. Based on this relationship between maximum FRP strain and mid-span displacement for specimen CS2-A, the average strain in mid-span CFRP gauge 1 was calculated to be *0.153%* corresponding to a strain-rate of *0.087* s^{-1}.

CS2-R – 2

Test CS2-R – 2 used a driver length of *1830 mm* and a driver pressure of *306.1 kPa*. The resulting shock wave had a peak pressure of *59 kPa*, reflected impulse of *371.3 kPa-ms* and positive phase duration of *17.7 ms*. Maximum deflection was *31.4 mm* (*1.6°*) which occurred at a time of *24.7 ms*. There was no residual displacement. The displacement time-history plot for test CS2-R2 – 2 may be seen in Figure A-7.

The maximum strain in mid-span tension gauge SG1 was *0.180%* at a time of *26.7 ms*, corresponding to a strain-rate of *0.067* s^{-1}. Residual strain was *0.050%*. The maximum strain in mid-span tension gauge SG2 was *0.193%* at a time of *25.2 ms*, corresponding to a strain-rate of *0.076* s^{-1}. Residual strain was *0.040%*. The strain in mid-span compression gauge SG13 at a time of *17.5 ms* and *25.2 ms* was *-0.048%*. Based on this relationship between maximum FRP strain and mid-span displacement for specimen CS2-A, the average strain in mid-span CFRP gauge 1 was calculated to be *0.473%* corresponding to a strain-rate of *0.188* s^{-1}.

Minor cracking was noted near the maximum moment region of the specimen.

CS2-R – 3

Test CS2-R – 3 used a driver length of *1830 mm* and a driver pressure of *359.2 kPa*. The resulting shock wave had a peak pressure of *64 kPa*, reflected impulse of *424.4 kPa-ms* and positive phase duration of *18 ms*. Maximum deflection was *42.9 mm* (*2.2°*) which occurred at a time of *26.8 ms*. There was no residual displacement. The displacement time-history plot for test CS2-R2 – 3 may be seen in Figure A-8.

Mid-span tension gauge SG1 was lost during this test, however the final recorded strain was *0.195%* at a time of *24 ms*, corresponding to a strain-rate of *0.081* s^{-1}. Mid-span tension gauge SG2 was also lost however the final strain reading was *0.250%* at a time of *19.8 ms*, corresponding to a strain-rate of *0.126* s^{-1}. The corresponding strain in mid-span compression gauge SG13 was *-0.056%*. Based on this relationship between maximum FRP strain and mid-span displacement for specimen CS2-A, the average strain in mid-span CFRP gauge 1 at debonding was calculated to be *0.600%* corresponding to a strain-rate of *0.274* s^{-1}.

This shot resulted in a critical diagonal crack debonding failure with concrete cover separation at the high shear and low moment region at the bottom support. However, only the very on-set of CFRP debonding was achieved after this shot. The debonded region, seen as the shaded zone in Figure 4.6 (b) and (c), was located at the bottom of the specimen and extended over the entire width of the specimen. The fact that the specimen registered no residual displacement indicates that this shot just achieved failure of the retrofit system. The specimen was considered failed at this point as composite action between the retrofit and the

member was lost due to debonding. However, it was decided to perform a fourth shot for the sake of an interesting and destructive high-speed video.

CS2-R – 4

Test CS2-R – 4 used a driver length of *1830 mm* and a driver pressure of *750.1 kPa*. The resulting shock wave had a peak pressure of *106.7 kPa*, reflected impulse of 738.1 *kPa-ms* and positive phase duration of *18.7 ms*. There was no discernable maximum displacement as the specimen slipped free from the bottom support and rotated about the top support. The displacement time-history plot for test CS2-R2 – 4 may be seen in Figure A-9.

No strain data was recorded for this shot as the CFRP had already debonded and the mid-span tension steel strain gauges were destroyed.

Significant yielding of steel and crushing of concrete occurred during this shot. As illustrated in Figure 4.6 (d), failure of the specimen occurred at the location of CFRP debonding at the bottom of the panel. Concrete debris travelled a distance of *3 m* away from the specimen.

4.3.3 Specimen CS2-A

Specimen CS2-A was retrofitted with one layer of externally bonded CFRP applied to the inbound tensile face of the member over the entire clear span. Additional mechanical end anchorage was provided with 5 FRP fan anchors installed on either end of the composite sheet. CS2-A was subjected to five shots of increasing destructiveness resulting in failure of the member by FRP anchor failure leading to CFRP debonding. The extent of damage progression for CS2-A is illustrated in Figure 4.7.

CS2-A – 1

Test CS2-A – 1 used a driver length of *1830 mm* and a driver pressure of *82.7 kPa*. The resulting shock wave had a peak pressure of *16 kPa*, reflected impulse of *126.2 kPa-ms* and positive phase duration of *13.7 ms*. Maximum deflection was *6.1 mm* (*0.3°*) which occurred at a time of *19.8 ms*. There was no residual displacement. The displacement time-history plot for test CS2-A – 1 may be seen in Figure A-6.

The maximum strain in mid-span FRP gauge 1 was *0.148%* at a time of *19.8 ms*, corresponding to a strain-rate of *0.075* s^{-1}. No residual strain was recorded. Mid-span compression strain gauges were damaged/destroyed prior to testing and no data was recorded.

No visible damage or cracking was observed.

CS2-A – 2

Test CS2-A – 2 used a driver length of *1830 mm* and a driver pressure of *310.3 kPa*. The resulting shock wave had a peak pressure of *51.3 kPa*, reflected impulse of *329.9 kPa-ms* and positive phase duration of *15.1 ms*. Maximum deflection was *29.1 mm* (*1.5°*) which occurred at a time of *24.9 ms*. Residual displacement was *2.4 mm*, although this was likely caused by the test setup settling. The displacement time-history plot for test CS2-A – 2 may be seen in Figure A-7.

The maximum strain in mid-span FRP gauge 1 was *0.420%* at a time of *23.1 ms*, corresponding to a strain-rate of *0.182* s^{-1}. No residual strain was recorded. Mid-span compression strain gauges were damaged/destroyed prior to testing and no data was recorded.

Slight flexural cracking at mid-span was noted but no other damage was observed.

CS2-A – 3

Test CS2-A – 3 used a driver length of *1830 mm* and a driver pressure of *362.7 kPa*. The resulting shock wave had a peak pressure of *60.1 kPa*, reflected impulse of *422.8 kPa-ms* and positive phase duration of *16.2 ms*. Maximum deflection was *38.7 mm* (*2.0°*) which occurred at a time of *26.4 ms*. There was no residual displacement. The displacement time-history plot for test CS2-A – 3 may be seen in Figure A-8.

The maximum strain in mid-span FRP gauge 1 was *0.563%* at a time of *24.1 ms*, corresponding to a strain-rate of *0.234* s^{-1}. No residual strain was recorded. Mid-span compression strain gauges were damaged/destroyed prior to testing and no data was recorded.

Some new flexure cracks were identified but the specimen remained elastic and no other damage was recorded.

CS2-A – 4

Test CS2-A – 4 used a driver length of *1830 mm* and a driver pressure of *431.6 kPa*. The resulting shock wave had a peak pressure of *69 kPa*, reflected impulse of *493.8 kPa-ms* and positive phase duration of *18.1 ms*. Maximum deflection was *45.9 mm* (*2.6°*) which occurred at a time of *26.5 ms*. There was no residual displacement.

The maximum strain in mid-span FRP gauge 1 was *0.663%* at a time of *24.2 ms*, corresponding to a strain-rate of *0.274* s^{-1}. No residual strain was recorded. Mid-span compression strain gauges were damaged/destroyed prior to testing and no data was recorded.

No new cracks or damage was observed after this test.

CS2-A – 5

Test CS2-A – 5 used a driver length of *1830 mm* and a driver pressure of *618.5 kPa*. The resulting shock wave had a peak pressure of *91.2 kPa*, reflected impulse of *670.8 kPa-ms* and positive phase duration of *19.8 ms*. Maximum deflection was *122 mm* (*6.2°*) which occurred at a time of *82.2 ms*. Residual displacement was *76.7 mm* (*79.1 mm* cumulative). The displacement time-history plot for test CS2-A – 5 may be seen in Figure A-9.

The strain in mid-span FRP gauge 1 at retrofit failure was *0.9%* at a time of *21.1 ms*, corresponding to a strain-rate of *0.426* s^{-1}.

Retrofit failure was caused by critical diagonal crack debonding of the CFRP sheet and FRP anchor failure due to stress concentrations in the anchor bends of the bottom group of anchors. The extent of damage in specimen CS2-A at different stages of testing is illustrated in Figure 4.7. No concrete cover separation occurred although the surface of the member was pitted and rough where both aggregate and cement binder had failed in tension and remained bonded to the composite sheet. The debris pattern was such that small pieces of concrete and aggregate were strewn across the floor up to approximately *2 m* away. Despite experiencing large inelastic deformations, the final displaced shaped of CS2-A lacked a distinct plastic hinge at mid-span. The final displaced shaped, shown in Figure 4.7 e), was characterised by a gradual curve as opposed to a distinct plastic hinge at mid-span. The distributed nature of the crack pattern is indicative of the smeared inelasticity of the member at failure.

4.4. Companion Set 3 (CS3)

Companion set 3 consisted of two *75 mm* thick reinforced concrete wall strip plates under simply-supported one-way bending. A total of seven shots were performed as part of CS3. A summary of the experimental results for companion set 3, including shock tube firing parameters, shock wave properties and displacements, may be found in Table 4.2. A summary of pertinent strain information may be found in Table 4.7. A comparison of the experimental displacement time-histories for all specimens of companion set 3 may be found in Figure A-10 to Figure A-13.

4.4.1 Specimen CS3-C

Specimen CS3-C served as an unretrofitted control specimen for companion set 3 and was subjected to three simulated explosions of increasing destructiveness. The extent of damage progression for CS3-C is illustrated in Figure 4.8.

CS3-C – 1

Test CS3-C – 1 used a driver length of *1830 mm* and a driver pressure of *75.8 kPa*. The resulting shock wave had a peak pressure of *15.4 kPa*, reflected impulse of *123.3 kPa-ms* and positive phase duration of *13.8 ms*. Maximum deflection was *6.9 mm* (*0.4°*) which occurred at a time of *23.9 ms*. Residual displacement was *1.8 mm*. The displacement time-history plot for test CS3-C – 1 may be seen in Figure A-10.

The maximum strain in mid-span tension gauge SG1 was *0.102%* at a time of *19.9 ms*, corresponding to a strain-rate of *0.051* s^{-1}. Residual strain in tension gauge SG1 was *0.036%*. The maximum strain in mid-span tension gauge SG2 was *0.079%* at a time of *19.9 ms*, corresponding to a strain-rate of *0.040* s^{-1}. Residual strain in tension gauge SG2 was *0.027%*. The strain in mid-span compression gauge SG13 at a time of *19.9 ms* was *-0.02%*.

A small flexure crack formed which ran approximately along mid-span of the plate. No other damage was observed.

CS3-C – 2

Test CS3-C – 2 used a driver length of *1830 mm* and a driver pressure of *133.1 kPa*. The resulting shock wave had a peak pressure of *28.2 kPa*, reflected impulse of *204.2 kPa-ms* and

positive phase duration of *14.7 ms*. Maximum deflection was *16.3 mm* (*0.8°*) which occurred at a time of *30.2 ms*. Residual displacement was *5.2 mm* (*7.0 mm* cumulative). The displacement time-history plot for test CS3-C – 2 may be seen in Figure A-11.

The maximum strain in mid-span tension gauge SG1 was *0.180%* at a time of *29 ms*, corresponding to a strain-rate of *0.062* s^{-1}. Residual strain in tension gauge SG1 was *0.011%*. The maximum strain in mid-span tension gauge SG2 was *0.182%* at a time of *29 ms*, corresponding to a strain-rate of *0.063* s^{-1}. Residual strain in tension gauge SG2 was *0.044%*. Mid-span compression steel strain gauge SG13 was damaged during this test and no data was registered.

A minor crack was formed which extended along the mid-span of the plate for two-thrids of the width and then extending upwards towards the top-right corner on an angle *~30°* from horizontal for the remaining one-third of the width. This unusual crack pattern, shown in Figure 4.8 (b), was likely influenced by existing cracks which were formed prior to testing.

CS3-C – 3

Test CS3-C – 3 used a driver length of *1830 mm* and a driver pressure of *678.4 kPa*. The resulting shock wave had a peak pressure of *100.6 kPa*, reflected impulse of *811.2 kPa-ms* and positive phase duration of *19.5 ms*. Maximum deflection was *197.5 mm* (*10°*) which occurred at a time of *63.7 ms*. Residual displacement was *134.5 mm* (*141.5 mm* cumulative). The displacement time-history plot for test CS3-C – 3 may be seen in Figure A-12.

Mid-span tension gauge SG1 was lost during this test, however the final recorded strain was *1.7%* at a time of *34.8 ms*. The strain-rate in gauge SG1 based on time to yield of reinforcing was *0.229* s^{-1}. Mid-span tension gauge SG2 was also lost however the final strain reading was *0.349%* at a time of *24.4 ms*. The strain-rate in gauge SG2 based on time to yield of reinforcing was *0.156* s^{-1}.

The final displaced shape, seen in Figure 4.8 (c) and (d), shows characteristics of significant rigid body rotation and the formation of a plastic region located approximately at mid-span. After testing, the concrete around the maximum moment region was removed to allow for visual inspection of the tension steel. Approximately *50-60%* of the tension steel reinforce-

ment had ruptured and the remainder were well into the strain hardening region evidenced by significant necking.

4.4.2 Specimen CS3-R

Specimen CS3-R served as the CFRP retrofitted specimen for companion set 3. The externally bonded CFRP retrofit was applied over the entire clear span in the principle direction over the entire width of both sides of the plate. CS3-R was subjected to four simulated explosions of increasing destructiveness. The extent of damage progression for CS3-R may be seen in Figure 4.9. The specimen remained elastic throughout the first three shots with no visible damage and no recorded permanent deformations. However, the fourth shot resulted in debonding of CFRP from concrete substrate.

CS3-R – 1

Test CS3-R – 1 used a driver length of *1830 mm* and a driver pressure of *80 kPa*. The resulting shock wave had a peak pressure of *16.5 kPa*, reflected impulse of *131.3 kPa-ms* and positive phase duration of *14.5 ms*. Maximum deflection was *6.0 mm* (*0.3°*) which occurred at a time of *19.3 ms*. There was no residual displacement. The displacement time-history plot for test CS3-R – 1 may be seen in Figure A-10.

The maximum strain in mid-span tension gauge SG1 was *0.040%* at a time of *18 ms*, corresponding to a strain-rate of *0.022* s^{-1}. There was no residual strain in tension gauge SG1. The maximum strain in mid-span FRP gauge 1 was *0.089%* at a time of *19.3 ms*, corresponding to a strain-rate of *0.046* s^{-1}. No residual strain was recorded. Mid-span steel compression strain gauges were damaged/destroyed and no data was recorded.

The specimen remained elastic after testing and no damage or cracking was observed.

CS3-R – 2

Test CS3-R – 2 used a driver length of *1830 mm* and a driver pressure of *131.7 kPa*. The resulting shock wave had a peak pressure of *27 kPa*, reflected impulse of *193.9 kPa-ms* and positive phase duration of *15.2 ms*. Maximum deflection was *9.2 mm* (*0.5°*) which occurred at a time of *19.7 ms*. There was no residual displacement. The displacement time-history plot for test CS3-R – 2 may be seen in Figure A-11.

The maximum strain in mid-span tension gauge SG1 was *0.059%* at a time of *17.8 ms*, corresponding to a strain-rate of *0.033* s^{-1}. Residual strain in tension gauge SG1 was *-0.02%*. The maximum strain in mid-span FRP gauge 1 was *0.140%* at a time of *17.8 ms*, corresponding to a strain-rate of *0.079* s^{-1}. No residual strain was recorded. Mid-span steel compression strain gauges were damaged/destroyed and no data was recorded.

The specimen remained elastic after testing and no damage or cracking was observed.

CS3-R – 3

Test CS3-R – 3 used a driver length of *1830 mm* and a driver pressure of *648.8 kPa*. The resulting shock wave had a peak pressure of *93 kPa*, reflected impulse of *738.2 kPa-ms* and positive phase duration of *21.2 ms*. Maximum deflection was *44.8 mm* (*2.3°*) which occurred at a time of *26.4 ms*. There was no residual displacement, although LVDT 1 did become detached from the specimen during the test preventing a complete displacement time history from being recorded. The displacement time-history plot for test CS3-R – 3 may be seen in Figure A-12.

No useable strain data was recorded as the mid-span tension and compression steel strain gauges, as well as mid-span FRP gauge 1, were damaged. However, extrapolating from the strain profile generated from the previous two tests, the maximum strain in mid-span FRP gauge 1 was *0.7%* at a time of *44.8 ms*, corresponding to a strain-rate of *0.265* s^{-1}.

The specimen remained elastic after testing and no damage or cracking was observed.

CS3-R – 4

Test CS3-R – 4 used a driver length of *3660 mm* and a driver pressure of *718.4 kPa*. The resulting shock wave had a peak pressure of *99.3 kPa*, reflected impulse of *2535 kPa-ms* and positive phase duration of *48.9 ms*. Maximum deflection was *155.8 mm* (*7.9°*) which occurred at a time of *61.7 ms*. Residual displacement was *82.8 mm*. The displacement time-history plot for test CS3-R – 4 may be seen in Figure A-13.

No useable strain data was recorded as the mid-span tension and compression steel strain gauges, as well as mid-span FRP gauge 1, were damaged. From the high-speed video, bonding occurred *24 ms* after the shock wave impacted the specimen. The mid-span displacement at debonding was *54.6 mm*. Extrapolating for the debonding strain from the strain profile

generated from the first two shots, the strain at debonding in mid-span FRP gauge 1 was *0.86%* at a time of *24 ms*, corresponding to a strain-rate of *0.192* s^{-1}.

The CFRP retrofitted specimen failed by plate-end interfacial debonding of the composite laminate from the concrete substrate. Analysis of the high speed video indicates that the debonding began at the top in the middle of the slab, near the supports, and propagated outwards. The debonded region extended over the entire top half of the specimen, from the maximum moment region to the supports. The debonded surface of the laminate sheet was relatively smooth, with very few pieces of concrete remaining bonded to the sheet. In fact, besides extensive transverse cracking within the maximum moment region, the concrete surface was relatively free of damage, with very little concrete having failed in tension during debonding. This indicates that the failure path was likely through the plane of the epoxy-concrete interfacial matrix. The extent of damage to CS3-R after shot 4 is illustrated in Figure 4.9.

4.5. Companion Set 4 (CS4)

Companion set 4 consisted of two *75 mm* thick reinforced concrete slab plates under simply-supported two-way bending. One specimen was retrofitted with the entire face of each principle direction covered with CFRP while the other specimen was retrofitted with CFRP strips on the inbound face only. No control specimen was considered for companion set 4. A total of thirteen shots were performed as part of CS4. A summary of the experimental results for companion set 4, including shock tube firing parameters, shock wave properties and displacements, may be found in Table 4.3. A summary of pertinent strain information may be found in Table 4.7. A comparison of the experimental displacement time-histories for all specimens of companion set 4 may be found in Figure A-14 to Figure A-20.

4.5.1 Specimen CS4-R1

Specimen CS4-R1 was retrofitted with an externally bonded *[0°/90°]* cross-ply retrofit configuration of WABO MBRACE CF-130 CFRP applied to both faces. The CFRP sheets covered the entire surface between the centerlines of the bolts holes, *2232 mm*, in both principle directions. CS4-R1 was subjected to seven simulated explosions of increasing destructive-

ness. Specimen CS4-R1, seen in Figure 4.10, remained elastic throughout testing with no residual displacement and no damage being observed.

CS4-R1 – 1

Test CS4-R1 – 1 used a driver length of *1830 mm* and a driver pressure of *80.7 kPa*. The resulting shock wave had a peak pressure of *16.6 kPa*, reflected impulse of *125.9 kPa-ms* and positive phase duration of *14.4 ms*. Maximum deflection was *3.6 mm* (*0.2°*) which occurred at a time of *14.4 ms*. There was no residual displacement. The displacement time-history plot for test CS4-R1 – 1 may be seen in Figure A-14.

The maximum strain in mid-span tension gauge SG1 was *0.025%* at a time of *13.5 ms*, corresponding to a strain-rate of *0.019* s^{-1}. No useful residual strains were recorded for SG1. The maximum strain in mid-span tension gauge SG2 was *0.027%* at a time of *13.5 ms*, corresponding to a strain-rate of *0.020* s^{-1}. There was no residual strain in SG2. The maximum strain in mid-span FRP gauge 1 was *0.047%* at a time of *14.4 ms*, corresponding to a strain-rate of *0.033* s^{-1}.

The specimen remained elastic after testing and no damage or cracking was observed.

CS4-R1 – 2

Test CS4-R1 – 2 used a driver length of *1830 mm* and a driver pressure of *135.8 kPa*. The resulting shock wave had a peak pressure of *29 kPa*, reflected impulse of *214.1 kPa-ms* and positive phase duration of *15.3 ms*. Maximum deflection was *6.6 mm* (*0.3°*) which occurred at a time of *14.8 ms*. There was no residual displacement. The displacement time-history plot for test CS4-R1 – 2 may be seen in Figure A-15.

The maximum strain in mid-span tension gauge SG1 was *0.041%* at a time of *14.8 ms*, corresponding to a strain-rate of *0.028* s^{-1}. No useful residual strains were recorded for SG1. The maximum strain in mid-span tension gauge SG2 was *0.045%* at a time of *14.8 ms*, corresponding to a strain-rate of *0.031* s^{-1}. Residual strain in SG2 was *0.012%*. The maximum strain in mid-span FRP gauge 1 was *0.084%* at a time of *14.8 ms*, corresponding to a strain-rate of *0.057* s^{-1}.

The specimen remained elastic after testing and no damage or cracking was observed.

CS4-R1 – 3

Test CS4-R1 – 3 used a driver length of *1830 mm* and a driver pressure of *215.8 kPa*. The resulting shock wave had a peak pressure of *43 kPa*, reflected impulse of *315.1 kPa-ms* and positive phase duration of *16.2 ms*. Maximum deflection was *10 mm* (*0.5°*) which occurred at a time of *15.2 ms*. There was no residual displacement. The displacement time-history plot for test CS4-R1 – 3 may be seen in Figure A-16.

The maximum strain in mid-span tension gauge SG1 was *0.067%* at a time of *14.8 ms*, corresponding to a strain-rate of *0.045* s^{-1}. No useful residual strains were recorded for SG1. The maximum strain in mid-span tension gauge SG2 was *0.071%* at a time of *14.8 ms*, corresponding to a strain-rate of *0.048* s^{-1}. Residual strain in SG2 was *0.035%*. The maximum strain in mid-span FRP gauge 1 was *0.137%* at a time of *14.7 ms*, corresponding to a strain-rate of *0.093* s^{-1}.

The specimen remained elastic after testing and no damage or cracking was observed.

CS4-R1 – 4

Test CS4-R1 – 4 used a driver length of *1830 mm* and a driver pressure of *377.8 kPa*. The resulting shock wave had a peak pressure of *65.2 kPa*, reflected impulse of *511.5 kPa-ms* and positive phase duration of *22 ms*. Maximum deflection was *16.1 mm* (*0.8°*) which occurred at a time of *15.4 ms*. There was no residual displacement. The displacement time-history plot for test CS4-R1 – 4 may be seen in Figure A-17.

The maximum strain in mid-span tension gauge SG1 was *0.109%* at a time of *14.8 ms*, corresponding to a strain-rate of *0.073* s^{-1}. No useful residual strains were recorded for SG1. The maximum strain in mid-span tension gauge SG2 was *0.119%* at a time of *14.8 ms*, corresponding to a strain-rate of *0.080* s^{-1}. Residual strain in SG2 was *0.042%*. The maximum strain in mid-span FRP gauge 1 was *0.244%* at a time of *14.8 ms*, corresponding to a strain-rate of *0.165* s^{-1}.

The specimen remained elastic after testing and no damage or cracking was observed.

CS4-R1 – 5

Test CS4-R1 – 5 used a driver length of *1830 mm* and a driver pressure of *615.7 kPa*. The resulting shock wave had a peak pressure of *91.4 kPa*, reflected impulse of *825.3 kPa-ms* and

positive phase duration of *27.7 ms*. Maximum deflection was *23.7 mm* (*1.2°*) which occurred at a time of *16.1 ms*. There was no residual displacement. The displacement time-history plot for test CS4-R1 – 5 may be seen in Figure A-18.

The maximum strain in mid-span tension gauge SG1 was *0.212%* at a time of *15.6 ms*, corresponding to a strain-rate of *0.136* s^{-1}. No useful residual strains were recorded for SG1. The maximum strain in mid-span tension gauge SG2 was *0.185%* at a time of *15.6 ms*, corresponding to a strain-rate of *0.119* s^{-1}. Residual strain in SG2 was *0.042%*. The maximum strain in mid-span FRP gauge 1 was *0.389%* at a time of *15.6 ms*, corresponding to a strain-rate of *0.249* s^{-1}.

The specimen remained elastic after testing and no damage or cracking was observed.

CS4-R1 – 6

Test CS4-R1 – 6 used a driver length of *2745 mm* and a driver pressure of *679.1 kPa*. The resulting shock wave had a peak pressure of *99.7 kPa*, reflected impulse of *1316 kPa-ms* and positive phase duration of *34.8 ms*. Maximum deflection was *33.4 mm* (*1.7°*) which occurred at a time of *18.7 ms*. There was no residual displacement. The displacement time-history plot for test CS4-R1 – 6 may be seen in Figure A-19.

No useful strain data was recorded for SG1 on this shot. The maximum strain in mid-span tension gauge SG2 was *0.353%* at a time of *18.7 ms*. The strain-rate in gauge SG1 based on time to yield of reinforcing was *0.206* s^{-1}. Residual strain in SG2 was *0.042%*. The maximum strain in mid-span FRP gauge 1 was *0.540%* at a time of *18.7 ms*, corresponding to a strain-rate of *0.289* s^{-1}.

The specimen remained elastic after testing and no damage or cracking was observed.

CS4-R1 – 7

Test CS4-R1 – 7 used a driver length of *4880 mm* and a driver pressure of *613.6 kPa*. The resulting shock wave had a peak pressure of *87.4 kPa*, reflected impulse of *2386.9 kPa-ms* and positive phase duration of *61.5 ms*. Maximum deflection was *35.1 mm* (*1.8°*) which occurred at a time of *20.4 ms*. There was no residual displacement. The displacement time-history plot for test CS4-R1 – 6 may be seen in Figure A-20.

No useful strain data was recorded for mid-span tension steel strain gauges SG1 or SG2 on this shot. The maximum strain in mid-span FRP gauge 1 was *0.591%* at a time of *19.6 ms*, corresponding to a strain-rate of *0.302* s^{-1}.

CS4-R1 remained elastic and undamaged after testing as the strength enhancement provided by the CFRP retrofit was greater than the maximum capacity of the shock tube.

4.5.2 Specimen CS4-R2

Specimen CS4-R2 was retrofitted with *200 mm* wide strips of externally bonded Fyfe Co. Tyfo SCH-41 CFRP laminate. A total of ten strips were bonded to the inbound face only, five of which were applied in each principle direction of bending. This specimen was subjected to six simulated explosions of increasing destructiveness and was intended to study the effect of rebound on specimens with FRP retrofits on the inbound face only. The extent of damage progression of CS4-R2 at various stages of testing may be seen in Figure 4.11

CS4-R2 – 1

Test CS4-R2 – 1 used a driver length of *1830 mm* and a driver pressure of *78.6 kPa*. The resulting shock wave had a peak pressure of *16.5 kPa*, reflected impulse of *136.7 kPa-ms* and positive phase duration of *14.9 ms*. Maximum deflection was *3.5 mm* (*0.2°*) which occurred at a time of *12.8 ms*. There was no residual displacement. The displacement time-history plot for test CS4-R2 – 1 may be seen in Figure A-14.

No useful strain data was obtained from mid-span steel tension gauge SG1. The maximum strain in mid-span FRP gauge 4 was *0.020%* at a time of *12.5 ms*, corresponding to a strain-rate of *0.016* s^{-1}.

The specimen remained elastic after testing and no damage or cracking was observed.

CS4-R2 – 2

Test CS4-R2 – 2 used a driver length of *1830 mm* and a driver pressure of *135.1 kPa*. The resulting shock wave had a peak pressure of *27.5 kPa*, reflected impulse of *223.8 kPa-ms* and positive phase duration of *15.9 ms*. Maximum deflection was *6.1 mm* (*0.3°*) which occurred at a time of *13.7 ms*. There was no residual displacement. The displacement time-history plot for test CS4-R2 – 2 may be seen in Figure A-14.

No useful strain data was obtained from mid-span steel tension gauge SG1.The maximum strain in mid-span FRP gauge 4 was *0.047%* at a time of *13.8 ms*, corresponding to a strain-rate of *0.034* s^{-1}.

The specimen remained elastic after testing and no damage or cracking was observed.

CS4-R2 – 3

Test CS4-R2 – 3 used a driver length of *1830 mm* and a driver pressure of *217.9 kPa*. The resulting shock wave had a peak pressure of *42.4 kPa*, reflected impulse of *346.9 kPa-ms* and positive phase duration of *16.7 ms*. Maximum deflection was *10.3 mm* (*0.5°*) which occurred at a time of *15.0 ms*. There was no residual displacement. The displacement time-history plot for test CS4-R2 – 3 may be seen in Figure A-16.

No useful strain data was obtained from mid-span steel tension gauge SG1.The maximum strain in mid-span FRP gauge 4 was *0.100%* at a time of *14.7 ms*, corresponding to a strain-rate of *0.068* s^{-1}.

The first signs of the expected simply-supported two-way yield line crack pattern were observed on the inbound face of the specimen. These cracks were very slight. Conversely, two large cracks had formed on the rebound face; one crack ran the entire horizontal length of the specimen along the centerline, while the other had formed along the vertical centerline of the specimen. The orientation of both the cracks on the rebound face was likely influenced by existing cracks which had formed prior to testing.

CS4-R2 – 4

Test CS4-R2 – 4 used a driver length of *1830 mm* and a driver pressure of *382.7 kPa*. The resulting shock wave had a peak pressure of *68.0 kPa*, reflected impulse of *542.1 kPa-ms* and positive phase duration of *18.1 ms*. Maximum deflection was *17.7 mm* (*0.9°*) which occurred at a time of *15.6 ms*. Residual displacement was *2.1 mm* (*2.1 mm cumulative*). The displacement time-history plot for test CS4-R2 – 4 may be seen in Figure A-17.

The maximum strain in mid-span tension gauge SG1 was *0.114%* at a time of *14.9 ms*, corresponding to a strain-rate of *0.077* s^{-1}. Cumulative residual strain in tension gauge SG1 was *0.002%*.. The maximum strain in mid-span FRP gauge 1 was *0.238%* at a time of *15.9 ms*, corresponding to a strain-rate of *0.149* s^{-1}.

Cracks continued to propagate and expand on the inbound face of the specimen, and were clearly visible. Diagonal cracks had formed on the rebound face as well. Otherwise, the specimen appeared undamaged.

CS4-R2 – 5

Test CS4-R2 – 5 used a driver length of *1830 mm* and a driver pressure of *624.0 kPa*. The resulting shock wave had a peak pressure of *88.4 kPa*, reflected impulse of *862.8 kPa-ms* and positive phase duration of *24.1 ms*. Maximum deflection was *35.9 mm* (*1.8°*) which occurred at a time of *18.4 ms*. Residual displacement was *2.1 mm* (*4.2 mm cumulative*). The displacement time-history plot for test CS4-R2 – 5 may be seen in Figure A-18.

The maximum strain in mid-span tension gauge SG1 was *0.178%* at a time of *16.0 ms*, corresponding to a strain-rate of *0.111* s^{-1}. Cumulative residual strain in tension gauge SG1 was *-0.001%*. The maximum strain in mid-span FRP gauge 1 was *0.456%* at a time of *18.6 ms*, corresponding to a strain-rate of *0.246* s^{-1}.

Cracking continued to propagate on both faces of the specimen, although the slab remained otherwise undamaged.

CS4-R2 – 6

Test CS4-R2 – 6 used a driver length of *2745 mm* and a driver pressure of *697.1 kPa*. The resulting shock wave had a peak pressure of *95.7 kPa*, reflected impulse of *1374.7 kPa-ms* and positive phase duration of *28.7 ms*. Maximum deflection was *57.1 mm* (*2.9°*) which occurred at a time of *20.5 ms*. Residual displacement was *3.1 mm* (*7.3 mm cumulative*). The displacement time-history plot for test CS4-R2 – 6 may be seen in Figure A-19.

The maximum strain in mid-span tension gauge SG1 was *0.301%* at a time of *20.1 ms*, corresponding to a strain-rate of *0.150* s^{-1}. Cumulative residual strain in tension gauge SG1 was *-0.002%*. The maximum strain in mid-span FRP gauge 1 was *0.703%* at a time of *20.1 ms*, corresponding to a strain-rate of *0.351* s^{-1}.

As a result of this pressure-impulse combination, the CFRP retrofit system experienced localized debonding and composite rupture. The failed areas are denoted by dark hatching as illustrated in Figure 4.11 (b). It was observed that the outermost (e.g. horizontal) CFRP strips were most likely to debond at the location where they extended over the innermost (e.g. ver-

tical) CFRP strips. This suggests that the presence of a slight transition, no greater than the thickness of a composite FRP sheet (*1 mm* in this case) may be enough to promote debonding failures. However, the debonding failures were localized and the retrofit was otherwise well anchored to the concrete substrate.

Rupture of a *100 mm* wide section of the central vertical CFRP strip was observed during this test. The rupture was located where a horizontal strip passes over the vertical strips, as illustrated in Figure 4.11 (b). It is believed that the rupture of the retrofit was caused by stress concentrations in the sheet influenced by the formation of a large crack in the concrete substrate and restraint provided by the outermost horizontal sheet.

Unlike other CFRP retrofitted two-way slab plates, CS4-R2 was retrofitted only on the inbound face. Therefore, kinetic energy of the specimen during the inbound displacement phase would be converted into elastic strain energy in FRP. This elastic strain energy would be released during the rebound displacement phase resulting in relatively large initial rebound displacements compared with specimens retrofitted on both faces. This phenomenon was observed during testing where the initial maximum rebound displacement varied from 89% of the initial maximum inbound displacement for Shot 1 to 38% for Shot 6. This suggests that externally bonded FRP retrofits are required for structures with insufficient reinforcement to resist moment reversal caused by rebound displacements.

4.6. Companion Set 5 (CS5)

Companion set 5 consisted of two *75 mm* thick reinforced concrete slab plates under fully-fixed two-way bending. Specimen CS5-C served as an unretrofitted control specimen, while specimen CS5-R was retrofitted with an externally bonded *[0°/90°]* cross-ply CFRP retrofit extending over the entire clear span on both sides of the specimen. A total of thirteen shots were performed as a part of CS5. A summary of the experimental results for companion set 5, including shock tube firing parameters, shock wave properties and displacements, may be found in Table 4.4. A comparison of the experimental displacement time-histories for the two specimens of companion set 5 may be found in Figure A-21 to Figure A-26.

4.6.1 Specimen CS5-C

Specimen CS5-C served as a control for companion set 5 and was subjected to seven simulated explosions of increasing destructiveness. A photograph of specimen CS5-C prior to testing may be seen in Figure 4.12. The extent of damage for CS5-C after testing is illustrated in Figure 4.13.

CS5-C – 1

Test CS5-C – 1 used a driver length of *305 mm* and a driver pressure of *61.4 kPa*. The resulting shock wave had a peak pressure of *8.2 kPa*, reflected impulse of *24.7 kPa-ms* and positive phase duration of *5 ms*. Maximum deflection was *0.6 mm* (*0°*) which occurred at a time of *8.6 ms*. There was no residual displacement.

No damage or cracking was identified.

CS5-C – 2

Test CS5-C – 2 used a driver length of *1830 mm* and a driver pressure of *77.2 kPa*. The resulting shock wave had a peak pressure of *17.2 kPa*, reflected impulse of *142.7 kPa-ms* and positive phase duration of *14 ms*. Maximum deflection was *3.5 mm* (*0.2°*) which occurred at a time of *15.9 ms*. Residual displacement was *1.6 mm*, although this was likely caused by the test setup settling. The displacement time-history plot for test CS5-C – 2 may be seen in Figure A-21.

Small cracks began to appear on the surface of the specimen, although these appeared to be random in nature. No other damage was observed.

CS5-C – 3

Test CS5-C – 3 used a driver length of *1830 mm* and a driver pressure of *137.9 kPa*. The resulting shock wave had a peak pressure of *26.7 kPa*, reflected impulse of *219.6 kPa-ms* and positive phase duration of *15.4 ms*. Maximum deflection was *6.7 mm* (*0.4°*) which occurred at a time of *14.2 ms*. There was no residual displacement (*1.6 mm* cumulative). The displacement time-history plot for test CS5-C – 3 may be seen in Figure A-22.

No new cracking or damage was identified after this shot.

CS5-C – 4

Test CS5-C – 4 used a driver length of *1830 mm* and a driver pressure of *217.9 kPa*. The resulting shock wave had a peak pressure of *44 kPa*, reflected impulse of *335.4 kPa-ms* and positive phase duration of *16 ms*. Maximum deflection was *12.6 mm* (*0.7°*) which occurred at a time of *17.2 ms*. Residual displacement was *3.6 mm* (*5.2 mm* cumulative). The displacement time-history plot for test CS5-C – 4 may be seen in Figure A-23.

The first signs of the expected two-way yield line crack pattern were observed following this test. Small diagonal cracks in the corners of the slab near the supports, typical of corner lever cracking with corners restrained, were noticed on the unloaded face. No other damage was identified.

CS5-C – 5

Test CS5-C – 5 used a driver length of *1830 mm* and a driver pressure of *356.5 kPa*. The resulting shock wave had a peak pressure of *60.2 kPa*, reflected impulse of *514 kPa-ms* and positive phase duration of *17.3 ms*. Maximum deflection was *21.0 mm* (*1.2°*) which occurred at a time of *18.4 ms*. Residual displacement was *4.0 mm* (*9.2 mm* cumulative). The displacement time-history plot for test CS5-C – 5 may be seen in Figure A-24.

The first positive moment yield line cracks were formed during this shot. These cracks extended diagonally from the corners into the mid-span region of the plate. However, these cracks were closed after testing and overall damage to the specimen remained negligible.

CS5-C – 6

Test CS5-C – 6 used a driver length of *2745 mm* and a driver pressure of *710.2 kPa*. The resulting shock wave had a peak pressure of *100.9 kPa*, reflected impulse of *1396.3 kPa-ms* and positive phase duration of *29.5 ms*. Maximum deflection was *67.8 mm* (*3.8°*) which occurred at a time of *24.5 ms*. Residual displacement was *17.5 mm* (*26.7 mm* cumulative). The displacement time-history plot for test CS5-C – 6 may be seen in Figure A-25.

Positive moment yield line cracking was clearly noticeable after this shot. Additionally, negative moment cracking near the supports around the perimeter of the specimen on the unloaded face was observed for the first time. The presence of this type of cracking was the

first sign of moment reversal during free vibration response. Additionally, some cover concrete along the yield lines was lost during shot 6 on both faces of the slab.

CS5-C – 7

Test CS5-C – 7 used a driver length of *4880 mm* and a driver pressure of *689.5 kPa*. The resulting shock wave had a peak pressure of *91.9 kPa*, reflected impulse of *2620.9 kPa-ms* and positive phase duration of *63.3 ms*. Maximum deflection was *79.0 mm* (*4.4°*) which occurred at a time of *29.5 ms*. Residual displacement was *26.1 mm* (*52.8 mm* cumulative). The displacement time-history plot for test CS5-C – 7 may be seen in Figure A-26.

Shot 7, at maximum driver length and driver pressure (e.g. maximum shock tube capacity), was the final test performed on specimen CS5-C. Despite inelastic response and significant cracking, qualitative observation the specimen indicated it likely had significant reserve capacity. The extent of damage to the loaded and unloaded faces of specimen CS5-C is illustrated in Figure 4.13. The crack pattern was in general agreement with the theoretical yield line pattern of a two-way fixed reinforced concrete plate. The formation of negative and positive moment yield lines, along with fan shaped corner cracking, was clearly visible in high-speed videos of blast response. Upon closer inspection of the cracking pattern, both the unloaded and loaded faces show evidence of reversal of moments caused by slab rebound during the free-vibration phase.

4.6.2 Specimen CS5-R

Specimen CS5-R was retrofitted with an externally bonded *[0°/90°]* cross-ply retrofit configuration of WABO MBRACE CF-130 CFRP. The CFRP sheets covered the entire surface between the centerlines of the bolts holes, *2232 mm*, in both principle directions on both faces. CS5-R was subjected to six simulated explosions of increasing destructiveness. Specimen CS5-R, seen in Figure 4.14, remained elastic throughout testing as no residual displacement and no damage was observed.

CS5-R – 1

Test CS5-R – 1 used a driver length of *1830 mm* and a driver pressure of *77.2 kPa*. The resulting shock wave had a peak pressure of *16.1 kPa*, reflected impulse of *142 kPa-ms* and positive phase duration of *14.3 ms*. Maximum deflection was *1.3 mm* (*0.1°*) which occurred

at a time of *9 ms*. There was no residual displacement. The displacement time-history plot for test CS5-R – 1 may be seen in Figure A-21.

No damage or cracking was identified.

CS5-R – 2

Test CS5-R – 2 used a driver length of *1830 mm* and a driver pressure of *115.8 kPa*. The resulting shock wave had a peak pressure of *25.3 kPa*, reflected impulse of *193.9 kPa-ms* and positive phase duration of *14.3 ms*. Maximum deflection was *1.8 mm* (*0.1°*) which occurred at a time of *9 ms*. There was no residual displacement. The displacement time-history plot for test CS5-R – 2 may be seen in Figure A-22.

The specimen remained elastic and no damage to the retrofit was observed.

CS5-R – 3

Test CS5-R – 3 used a driver length of *1830 mm* and a driver pressure of *215.8 kPa*. The resulting shock wave had a peak pressure of *42 kPa*, reflected impulse of *317.1 kPa-ms* and positive phase duration of *16 ms*. Maximum deflection was *3.2 mm* (*0.2°*) which occurred at a time of *8.9 ms*. There was no residual displacement. The displacement time-history plot for test CS5-R – 3 may be seen in Figure A-23.

The specimen remained undamaged.

CS5-R – 4

Test CS5-R – 4 used a driver length of *1830 mm* and a driver pressure of *355.8 kPa*. The resulting shock wave had a peak pressure of *62 kPa*, reflected impulse of *493 kPa-ms* and positive phase duration of *18.1 ms*. Maximum deflection was *6 mm* (*0.3°*) which occurred at a time of *11.6 ms*. There was no residual displacement. The displacement time-history plot for test CS5-R – 4 may be seen in Figure A-24.

The specimen remained undamaged.

CS5-R – 5

Test CS5-R – 5 used a driver length of *2745 mm* and a driver pressure of *698.4 kPa*. The resulting shock wave had a peak pressure of *97.1 kPa*, reflected impulse of *1365.1 kPa-ms* and positive phase duration of *32.8 ms*. Maximum deflection was *20.3 mm* (*1.1°*) which occurred

at a time of *17.8 ms*. Residual displacement was *1.7 mm*, although this was likely caused by the test setup settling. The displacement time-history plot for test CS5-R – 5 may be seen in Figure A-25.

The specimen remained elastic and undamaged after testing.

CS5-R – 6

Test CS5-R – 6 used a driver length of *4880 mm* and a driver pressure of *637.1 kPa*. The resulting shock wave had a peak pressure of *87.5 kPa*, reflected impulse of *2379.1 kPa-ms* and positive phase duration of *60.5 ms*. Maximum deflection was *25.3 mm* (*1.4°*) which occurred at a time of *18.8 ms*. Residual displacement was *0.6 mm* (*2.3 mm* cumulative). The displacement time-history plot for test CS5-R – 6 may be seen in Figure A-26.

Shot CS5-R-6, performed at maximum driver length and driver pressure (e.g. maximum shock tube capacity), was not powerful enough to generate any observable damage or inelasticity in the retrofitted specimen.

4.7. Performance of Walls vs Slab Specimens

Based on the results of the experimental research program, it is not unreasonable to conclude that reinforced concrete wall panel performance is more critical than reinforced concrete slab performance when designing structures to resist the effects of high explosive blast. Reasons for this include:

- Exterior walls will likely experience larger reflected pressures than reinforced concrete slabs when subjected to an explosion with a point of detonation located outside of the building envelope.

- Reinforced concrete walls are generally more lightly reinforced than doubly reinforced concrete slabs. Additionally, walls generally do not possess the same level of reinforcement continuity as reinforced concrete slabs.

- Wall end restraints are generally not designed to sustain large in-elastic rotations. Slabs are inherently more capable of dissipating blast energy by redistribution of in-

ternal forces by the formation of typical yield lines through plastic hinging and tensile membrane action.

- Qualitatively, slabs have greater shear resistance than walls as the thickness of the concrete section is greater. Slabs may also have additional shear reinforcement at critical locations to resist punching shear around columns.

- Slabs may also have sufficient reinforcement and support continuity to develop catenary action – i.e. tension membrane behaviour – once the ultimate flexural resistance has been achieved.

4.8. Performance of As-built vs Retrofitted Specimens

As much as possible, specimens of the same companion set were subjected to the same pressure-impulse combinations to facilitate direct comparison of results. The repeatability of the reflected pressures and impulses for each companion set were determined by first normalizing the results based on the average pressure and impulse for a particular companion test. The pressure and impulse ratios within each companion set were then compared. The normalized pressure and impulse ratios for each companion set are plotted against their corresponding percentile in Figure 4.15. The linearity of the results, coupled with the clustering of data points around the mean, indicate that the shock wave parameters were consistent and repeatable.

Bar charts have been prepared to illustrate the effect of utilizing CFRP retrofits to reduce mid-span displacements and time-to-maximum displacements. These charts are shown in Figure 4.16 to Figure 4.20. Without exception, a significant reduction in maximum displacement and time-to-maximum displacement for all specimens retrofitted with externally bonded CFRP was observed over corresponding as-built members. At failure, the maximum support rotation for as-built one-way wall panel strips was between *7°* and *10°*. The corresponding CFRP retrofitted wall strips were able to survive the same simulated explosions and sustain elastic support rotations of approximately *2°*. The externally bonded CFRP retrofit resulted in a reduction in displacement level of approximately *3.5* to *5* times the as-built response. Prior to failure, the CFRP retrofitted wall strips were able to sustain elastic support

rotations of between *2°* and *4°*. Although the capacity of the shock tube was not sufficient enough to generate large inelastic behaviour of the slab plates, a similar reduction is support rotations was observed for two-way companion tests.

It was observed that retrofitted specimens consistently remained elastic prior to failure. During the inbound displacement phase, kinetic energy of the specimens is stored as elastic strain energy in the externally bonded CFRP. This adds considerable elastic strength and stiffness to the member, resulting in an overall reduction in response levels. However, as the traditional mechanisms of energy dissipation have been eliminated through retrofitting (i.e. no crushing of concrete and no yielding of steel), elastic strain energy is violently released as kinetic energy during the rebound phase. This phenomenon was particularly noticeable for tests performed on the one-way reinforced concrete panels for CS1 and CS2 which were retrofitted on one face only. These retrofitted panels interacted violently with the transverse beams of the load transfer device during rebound. Although the load transfer device greatly reduced negative displacement of the specimens, rebound of the retrofitted specimens *bent* many of the transverse beams. The displacement time-history plot for specimen CS1-A, shown in Figure A-4, is an excellent example of the interaction between the load transfer device and the response of the retrofitted members. Had the load transfer device not prevented rebound, it is likely that the specimens retrofitted on one face only would have survived the first inbound displacement, only to suffer extensive damage during the rebound displacement phase as a result of moment reversal. Furthermore, the debonding failure of CS4-R2 was almost certainly influenced by damage to, and cracking of, the concrete substrate on the retrofitted faced during the rebound displacement face. Based on these observations, it is recommended that FRP retrofits be applied to both faces of the member to reduce the likelihood of failure due to moment reversal during rebound.

Debonding of CFRP from the concrete substrate was the sole mode of failure for all retrofitted specimens. It was observed that the retrofitted one-way wall strips with thickness of *75 mm* (CS3-R) and *80 mm* (CS1-R2 and CS1-A) failed by interfacial plate end debonding. However, the *120 mm* thick retrofitted specimens (CS2-R and CS2-A) failed by critical diagonal crack debonding. The flexural stiffness of specimens CS2-R and CS2-A was increased to such an extent that flexure-shear interaction became the primary cause of retrofit

failure mode. This indicates that shear capacity could limit the effectiveness of blast resistant externally bonded FRP retrofits by increasing the likelihood of intermediate crack debonding.

The efficacy of FRP anchors at preventing or delaying premature debonding failure depends on the anticipated failure mode. It was observed that FRP anchors had no impact on retrofit performance when plate-end interfacial debonding triggered by flexural action was the primary failure mode. As presented in Table 4.5, the retrofitted specimens with and without anchors failed at approximately the same strain level in FRP; *1.0%* for CS1-R2 versus *0.8%* for CS1-A. However, when the observed failure mode was dominated by diagonal crack debonding, FRP anchors improved the effectiveness of FRP sheets by delaying debonding (in specimen CS2-A), and resulting in an increased FRP strain of *0.9%* at failure, versus the specimen without the anchors (CS2-R) debonding at *0.6%* strain (presented in Table 4.6). Therefore, the direction of debonding propagation – either away from the plate-end (*e.g.* plate-end debonding) or towards the plate-end (*e.g.* critical diagonal crack debonding) – had an impact on FRP anchor performance. Regardless of the anticipated debonding mode, specimens with FRP anchors always developed a minimum strain of approximately *0.8%* at failure, whereas those without the anchors could develop a minimum FRP strain of approximately *0.6%* due to premature debonding.

FRP anchors were incorporated into two specimens – CS1-A and CS2-A – to investigate the potential of these mechanical anchorages to prevent debonding failure. Bar charts comparing the effect of FRP anchors on maximum FRP strain for each companion shot for CS1 and CS2 are shown in Figure 4.21 and Figure 4.22, respectively. Differential slip between the FRP sheet and concrete substrate at the location of anchorage is required to activate the FRP anchors. As expected, FRP anchors had no impact on response of companion tests performed prior to failure as there was no relative slip between the FRP and concrete. However, upon slip of the FRP sheet, the anchors are assumed to contribute to member response. Unexpectedly, the use of FRP anchors did not appear to have any effect on the performance of companion set 1. Whereas both specimens failed at the same pressure-impulse combination, a higher level of CFRP capacity was mobilized for the specimen retrofitted without anchors, CS1-R2, (*83%* of CFRP tensile capacity) than the corresponding retrofitted specimen with

anchors, CS1-A (*67%* of CFRP tensile capacity). However, the results for companion set 2 were the opposite; Specimen CS2-R utilized approximately *50%* of CFRP tensile capacity prior to debonding, while the corresponding specimen with anchors, CS2-A, mobilized *75%* of the retrofit capacity and failed at approximately double the pressure-impulse combination. It is believed that the contradictory results are related to the relative stiffness of the members and corresponding debonding failure modes. The results are encouraging and more research is required in this area.

At failure, the FRP anchors consistently sheared at the locations of anchor bends caused by stress concentrations. One solution to mitigate this failure mode, shown in Figure 4.23, would be to insert the anchors into the concrete at a shallow angle relative to the concrete surface, as opposed to perpendicular to the concrete surface: *45°* would be one possible angle of inclination. Another possible improvement would be to countersink the holes slightly to further reduce stress concentrations: *120°* for a depth of *12.5 mm*, as an example. The arrangement of the anchor blades could be further optimized as well. As opposed to bonding the anchor blades in a circular pattern in all directions, a more useful arrangement would be to bond the blades in the direction of expected tensile stress transfer. In this way, a greater proportion of the fibre material would be mobilized during response. It is clear that FRP anchors have the ability to prevent or delay debonding failures; however more research is required to be able to effectively rely on this type of supplemental anchorage.

Table 4.1: Shock Tube Firing Parameters, Shock Wave Properties and Experimental Results for Companion Set 1.

Name		Driver Length L_d mm	Driver Pressure P_d kPa	Reflected Pressure P_r kPa	Positive Phase Duration t_d ms	Reflected Impulse I_r kPa-ms	Max. Deflection δ_{max} mm	Max. Support Rotation θ_{max} degree	Time to Max. t_{max} ms	Residual Deflection δ_{res} mm
CS1-C	- 1	1830	60.7	12.5	13.0	95.7	26.1	1.3	65.5	7.3
CS1-C	- 2	1830	241.3	42.6	16.3	301.6	167.8	8.6	89.8	140.0
CS1-R1	- 1	1830	61.4	12.9	12.7	83.6	11.6	0.6	26.1	1.4
CS1-R1	- 2	1830	241.3	46.4	16.3	300.0	146.9	7.5	85.0	118.6
CS1-R2	- 1	1830	57.9	11.1	14.0	89.3	8.1	0.4	23.8	1.7
CS1-R2	- 2	1830	238.6	44.8	16.1	331.2	42.5	2.2	29.7	0.0
CS1-R2	- 3	1830	273.7	49.0	15.7	336.9	40.4	2.1	28.9	0.0
CS1-R2	- 4	1830	353.0	64.7	15.7	444.3	62.6	3.2	30.7	0.0
CS1-R2	- 5	1830	415.8	72.9	16.6	510.9	84.6	4.3	34.1	17.1
CS1-R2	- 6	1830	489.5	79.6	17.7	595.1	224.6	11.4	118.5	188.1
CS1-A	- 1	1830	62.1	13.3	13.2	99.9	9.4	0.5	24.3	1.4
CS1-A	- 2	1830	241.3	51.3	16.5	335.3	42.3	2.2	30.0	0.0
CS1-A	- 3	1830	351.6	67.4	16.1	460.6	68.4	3.5	33.6	0.0
CS1-A	- 4	1830	416.4	70.9	17.1	511.8	83.6	4.3	36.0	0.0
CS1-A	- 5	1830	482.6	74.7	15.8	511.7	85.5	4.4	36.3	0.0
CS1-A	- 6	1830	487.5	82.6	17.5	603.0	132.8	6.8	74.2	92.0

Table 4.2: Shock tube Firing Parameters, Shock Wave Properties and Experimental Results for Companion Set 2 and 3.

Name		Driver Length L_d mm	Driver Pressure P_d kPa	Reflected Pressure P_r kPa	Positive Duration t_d ms	Reflected Impulse I_r kPa-ms	Max. Deflection δ_{max} mm	Support Rotation θ_{max} degree	Time to Max. t_{max} ms	Residual Deflection δ_{res} mm
CS2-C	- 1	1830	84.1	17.7	13.8	143.0	16.3	0.8	31.5	5.7
CS2-C	- 2	1830	311.6	57.8	17.4	383.0	148.9	7.6	80.7	120.6
CS2-R	- 1	1830	82.7	17.1	13.6	128.3	7.0	0.4	18.5	0
CS2-R	- 2	1830	306.1	59.0	17.7	371.3	31.4	1.6	24.7	0.0
CS2-R	- 3	1830	359.2	64.0	18.0	424.4	42.9	2.2	26.8	0.0
CS2-R	- 4	1830	750.1	106.7	18.7	738.1	No Discernable Maximum – Specimen Destroyed			
CS2-A	- 1	1830	82.7	16.0	13.7	126.2	6.1	0.3	19.8	0.0
CS2-A	- 2	1830	310.3	51.3	15.1	329.9	29.1	1.5	24.9	2.4
CS2-A	- 3	1830	362.7	60.1	16.2	422.8	38.7	2.0	26.4	0.0
CS2-A	- 4	1830	431.6	69.0	18.1	493.8	45.9	2.6	26.5	0.0
CS2-A	- 5	1830	618.5	91.2	19.8	670.8	122.0	6.2	82.2	76.7
CS3-C	- 1	1830	75.8	15.4	13.8	123.3	6.9	0.4	23.9	1.8
CS3-C	- 2	1830	133.1	28.2	14.7	204.2	16.3	0.8	30.2	5.2
CS3-C	- 3	1830	678.4	100.6	19.5	811.2	197.5	10.0	63.7	134.5
CS3-R	- 1	1830	80.0	16.5	14.5	131.3	6.0	0.3	19.3	0.0
CS3-R	- 2	1830	131.7	27.0	15.2	193.9	9.2	0.5	19.7	0.0
CS3-R	- 3	1830	648.8	93.0	21.2	783.2	44.8	2.3	26.4	0.0
CS3-R	- 4	3660	718.4	99.3	48.9	2535.0	155.8	7.9	61.7	82.8

Table 4.3: Shock Tube Firing Parameters, Shock Wave Properties and Experimental Results for Companion Set 4.

Name	Driver Length L_d mm	Driver Pressure P_d kPa	Reflected Pressure P_r kPa	Positive Phase Duration t_d ms	Reflected Impulse I_r kPa-ms	Max. Deflection δ_{max} mm	Max. Support Rotation θ_{max} degree	Time to Max. t_{max} ms	Residual Deflection δ_{res} mm
CS4-R1 - 1	1830	80.7	16.6	14.4	125.9	3.6	0.2	14.4	0.0
CS4-R1 - 2	1830	135.8	29.0	15.3	214.1	6.6	0.3	14.8	0.0
CS4-R1 - 3	1830	215.8	43.0	16.2	315.1	10.0	0.5	15.2	0.0
CS4-R1 - 4	1830	377.8	65.2	22.0	511.5	16.1	0.8	15.4	0.0
CS4-R1 - 5	1830	615.7	91.4	27.7	825.3	23.7	1.2	16.1	0.0
CS4-R1 - 6	2745	679.1	99.7	34.8	1316.0	33.4	1.7	18.7	0.0
CS4-R1 - 7	4880	613.6	87.4	61.5	2386.9	35.1	1.8	20.4	0.0
CS4-R2 - 1	1830	78.6	16.5	14.9	136.7	3.5	0.2	12.8	0.0
CS4-R2 - 2	1830	135.1	27.5	15.9	223.8	6.1	0.3	13.7	0.0
CS4-R2 - 3	1830	217.9	42.4	16.7	346.9	10.3	0.5	15.0	0.0
CS4-R2 - 4	1830	382.7	68.0	18.1	542.1	17.7	0.9	15.6	2.1
CS4-R2 - 5	1830	624.0	88.4	24.1	862.8	35.9	1.8	18.4	2.1
CS4-R2 - 6	2745	697.1	95.7	28.7	1374.7	57.1	2.9	20.5	3.1

Table 4.4: Shock Tube Firing Parameters, Shock Wave Properties and Experimental Results for Companion Set 5.

Name		Driver Length L_d mm	Driver Pressure P_d kPa	Reflected Pressure P_r kPa	Positive Phase Duration t_d ms	Reflected Impulse I_r kPa-ms	Max. Deflection δ_{max} mm	Max. Support Rotation θ_{max} degree	Time to Max. t_{max} ms	Residual Deflection δ_{res} mm
CS5-C	- 1	305	61.4	8.2	5.0	24.7	0.6	0.0	8.6	0.0
CS5-C	- 2	1830	77.2	17.2	14.0	142.7	3.5	0.2	15.9	1.6
CS5-C	- 3	1830	137.9	26.7	15.4	219.6	6.7	0.4	14.2	0.0
CS5-C	- 4	1830	217.9	44.0	16.0	335.4	12.6	0.7	17.2	3.6
CS5-C	- 5	1830	356.5	60.2	17.3	514.0	21.0	1.2	18.4	4.0
CS5-C	- 6	2745	710.2	100.9	29.5	1396.3	67.8	3.8	24.5	17.5
CS5-C	- 7	4880	689.5	91.9	63.3	2620.9	79.0	4.4	29.5	26.1
CS5-R	- 1	1830	77.2	16.1	14.3	142.0	1.3	0.1	9.0	0.0
CS5-R	- 2	1830	115.8	25.3	14.3	193.9	1.8	0.1	9.0	0.0
CS5-R	- 3	1830	215.8	42.0	16.0	317.1	3.2	0.2	8.9	0.0
CS5-R	- 4	1830	355.8	62.0	18.1	493.0	6.0	0.3	11.6	0.0
CS5-R	- 5	2745	698.4	97.1	32.8	1365.1	20.3	1.1	17.8	1.7
CS5-R	- 6	4880	637.1	87.5	60.5	2379.1	25.3	1.4	18.8	0.6

Table 4.5: Experimental Strain Data for Companion Set 1.

Name	Mid-span Tension Gauge SG1				Mid-span Tension Gauge SG2				Mid-span FRP Gauge 1			Mid-span Compression Gauge SG13
	ε_{max} %	t_{max} ms	$\dot{\varepsilon}_{SG1}$ s^{-1}	$\Sigma\varepsilon_{res.}$ %	ε_{max} %	t_{max} ms	$\dot{\varepsilon}_{SG2}$ s^{-1}	$\Sigma\varepsilon_{res.}$ %	ε_{max} %	t_{max} ms	$\dot{\varepsilon}_{FRP1}$ s^{-1}	ε_{SG13} %
CS1-C - 1	0.112	69	0.016	0	0.106	70	0.015	0	No CFRP Retrofit			-0.020
CS1-C - 2	0.197	42.5	0.046	-	0.129	26.2	0.049	-				-0.027
CS1-R1 - 1	No data				No data				No data			No data
CS1-R1 - 2	0.234	28	0.084	-	0.213	61.5	0.034	0.170				
CS1-R2 - 1	0.106†	22.8	0.047	-	No data				0.127	22.8	0.056	-0.035
CS1-R2 - 2	0.388†	29.7	0.131	-					0.459	29.7	0.154	-0.097
CS1-R2 - 3	0.398†	27.8	0.143	-					0.459	27.8	0.165	-0.152
CS1-R2 - 4	0.600†	29.8	0.201	-					0.690	29.8	0.231	-0.170
CS1-R2 - 5	No data								0.854	34.5	0.248	> -0.25
CS1-R2 - 6									1.0	27.1	0.365	No data
CS1-A - 1	0.091†	24.3	0.037	-	No data				0.110	24.3	0.045	-0.039
CS1-A - 2	0.312†	27.6	0.113	-					0.370	27.6	0.134	-0.090
CS1-A - 3	0.527†	29.2	0.180	-					0.630	29.2	0.216	-0.185
CS1-A - 4	0.607†	32.1	0.189	-					0.729	32.1	0.227	-0.230
CS1-A - 5	0.607†	31.1	0.195	-					0.730	31.1	0.235	-0.239
CS1-A - 6	0.669†	31.9	0.210	-					0.804	31.9	0.252	-0.260

† – Strain data for mid-span tension gauge SG1 for specimens CS1-R2 and CS1-A was interpolated from the strain profile generated from FRP gauge 1 and mid-span compression gauge SG13.

Table 4.6: Experimental Strain Data for Companion Set 2.

Name	Mid-span Tension Gauge SG1				Mid-span Tension Gauge SG2				Mid-span FRP Gauge 1			Mid-span Compression Gauge SG13
	ε_{max} %	t_{max} ms	$\dot{\varepsilon}_{SG1}$ s^{-1}	$\Sigma\varepsilon_{res.}$ %	ε_{max} %	t_{max} ms	$\dot{\varepsilon}_{SG2}$ s^{-1}	$\Sigma\varepsilon_{res.}$ %	ε_{max} %	t_{max} ms	$\dot{\varepsilon}_{FRP1}$ s^{-1}	ε_{SG13} %
CS2-C - 1	0.090	39.2	0.023	0.078	0.098	39.2	0.025	0.086	No CFRP Retrofit			No data
CS2-C - 2	0.190	42	0.045	0.102	0.190	57.2	0.033	0.086				
CS2-R - 1	0.008	17.5	0.005	0.000	0.012	17.5	0.007	0.000	0.153†	17.5	0.087	-0.009
CS2-R - 2	0.180	26.7	0.067	0.050	0.193	25.2	0.076	0.040	0.473†	25.2	0.188	-0.048
CS2-R - 3	0.195	24	0.081	-	0.250	19.8	0.126	-	0.600†	21.9	0.274	-0.056
CS2-R - 4	No data				No data				No data			-
CS2-A - 1	No data				No data				0.148	19.8	0.075	No data
CS2-A - 2									0.420	23.1	0.182	
CS2-A - 3									0.563	24.1	0.234	
CS2-A - 4									0.663	24.2	0.274	
CS2-A - 5									0.900	21.1	0.427	

† – Strain data for FRP gauge 1 for specimen CS2-R was interpolated from the strain profile results for specimen CS2-A.

Table 4.7: Experimental Strain Data for Companion Set 3.

Name	Mid-span Tension Gauge SG1				Mid-span Tension Gauge SG2				Mid-span FRP Gauge 1			Mid-span Compression Gauge SG13
	ε_{max} %	t_{max} ms	$\dot{\varepsilon}_{SG1}$ s^{-1}	$\Sigma\varepsilon_{res.}$ %	ε_{max} %	t_{max} ms	$\dot{\varepsilon}_{SG2}$ s^{-1}	$\Sigma\varepsilon_{res.}$ %	ε_{max} %	t_{max} ms	$\dot{\varepsilon}_{FRP1}$ s^{-1}	ε_{SG13} %
CS3-C - 1	0.102	19.9	0.051	0.036	0.079	19.9	0.040	0.027				-0.02
CS3-C - 2	0.180	29.0	0.062	0.011	0.182	29.0	0.063	0.044	No CFRP Retrofit			-
CS3-C - 3	1.700	34.8	0.229	-	0.349	24.4	0.156	-				-
CS3-R - 1	0.040	18.0	0.022	0					0.089	19.3	0.046	
CS3-R - 2	0.059	17.8	0.033	-0.020					0.140	17.8	0.079	
CS3-R - 3					No data				0.700†	26.4	0.265	No data
CS3-R - 4	No data								0.860†	44.8	0.192	

† – Strain data for FRP gauge 1 for was interpolated from the strain profile generated from Shot 1 and 2 for specimen CS3-R.

Table 4.8: Experimental Strain Data for Companion Set 4.

Name	Mid-span Tension Gauge SG1				Mid-span Tension Gauge SG2				Mid-span FRP Gauge 1			Mid-span Compression Gauge SG13
	ε_{max} %	t_{max} ms	$\dot{\varepsilon}_{SG1}$ s^{-1}	$\Sigma\varepsilon_{res.}$ %	ε_{max} %	t_{max} ms	$\dot{\varepsilon}_{SG2}$ s^{-1}	$\Sigma\varepsilon_{res.}$ %	ε_{max} %	t_{max} ms	$\dot{\varepsilon}_{FRP1}$ s^{-1}	ε_{SG13} %
CS4-R1 - 1	0.025	13.5	0.019	-	0.027	13.5	0.020	0	0.047	14.4	0.033	
CS4-R1 - 2	0.041	14.8	0.028	-	0.045	14.8	0.031	0.012	0.084	14.8	0.057	
CS4-R1 - 3	0.067	14.8	0.045	-	0.071	14.8	0.048	0.035	0.137	14.7	0.093	
CS4-R1 - 4	0.109	14.8	0.073	-	0.119	14.8	0.080	0.042	0.244	14.8	0.165	No data
CS4-R1 - 5	0.212	15.6	0.136	-	0.185	15.6	0.119	0.042	0.389	15.6	0.249	
CS4-R1 - 6	No data				0.353	18.7	0.206	0.042	0.540	18.7	0.289	
CS4-R1 - 7					No data				0.591	19.6	0.302	
CS4-R2 - 1									0.020%	12.53	0.016	
CS4-R2 - 2	No data								0.047%	13.8	0.034	
CS4-R2 - 3									0.100%	14.7	0.068	
CS4-R2 - 4	0.114	14.9	0.002	0.002	No data				0.238%	15.9	0.149	No data
CS4-R2 - 5	0.178	16.0	-0.003	-0.001					0.456%	18.6	0.246	
CS4-R2 - 6	0.301	20.1	-0.002	-0.002					0.703%	20.1	0.351	

(a) Prior to testing

(b) After shot 1
P_r = 12.5 kPa
I_r = 95.7 kPa-ms

(c) After shot 2
P_r = 42.6 kPa
I_r = 301.6 kPa-ms

Figure 4.1: Extent of Damage in Specimen CS1-C at Different Stages of Testing.

(a) Prior to testing

(b) After shot 2
P_r = 12.9 kPa
I_r = 83.6 kPa-ms

(c) After shot 2
P_r = 46.4 kPa
I_r = 300.0 kPa-ms

Figure 4.2: Extent of Damage in Specimen CS1-R1 at Different Stages of Testing.

(a) Prior to testing

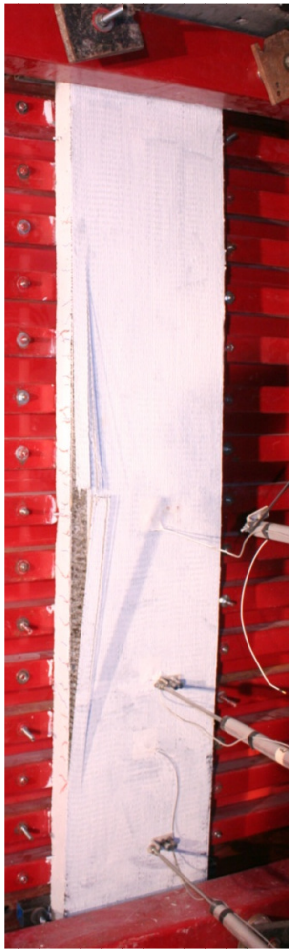

(b) After shot 5
P_r = 72.9 kPa
I_r = 510.9 kPa-ms

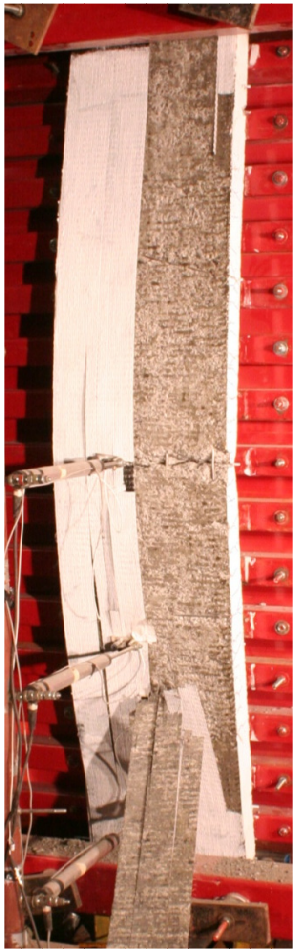

(c) After shot 6
P_r = 79.6 kPa
I_r = 595.1 kPa-ms

(d) After shot 6
$1P_r$ = 79.6 kPa
I_r = 595.1 kPa-ms

Figure 4.3: Extent of Damage in Specimen CS1-R2 at Different Stages of Testing.

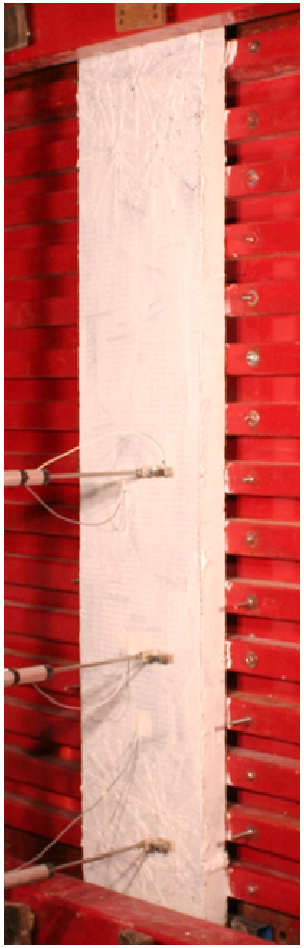

(a) Prior to testing

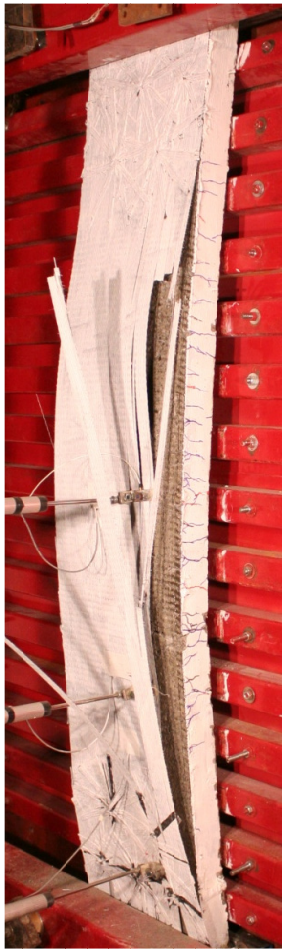

(b) After shot 6
P_r = 82.6 kPa
I_r = 603.0 kPa-ms

(c) After shot 6
P_r = 82.6 kPa
I_r = 603.0 kPa-ms

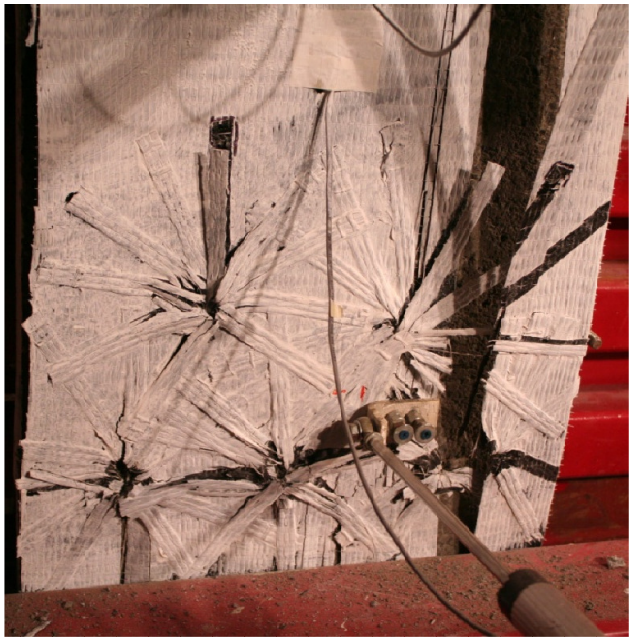

(d) After shot 6
P_r = 82.6 kPa
I_r = 603.0 kPa-ms
Anchor failure

Figure 4.4: Extent of Damage in Specimen CS1-A at Different Stages of Testing.

(a) Prior to testing

(b) After shot 1
P_r = 17.7 kPa
I_r = 143.0 kPa-ms

(c) After shot 2
P_r = 57.8 kPa
I_r = 383.0 kPa-ms

Figure 4.5: Extent of Damage in Specimen CS2-C at Different Stages of Testing.

(a) Prior to testing

(b) After shot 2
P_r = *59.0 kPa*
I_r = *371.3 kPa-ms*

(c) After shot 3
P_r = *64.0 kPa*
I_r = *424.4 kPa-ms*

(d) After shot 3
P_r = *64.0 kPa*
I_r = *424.4 kPa-ms*

(e) After shot 4
P_r = *106.7 kPa*
I_r = *738.1 kPa-ms*

Figure 4.6: Extent of Damage in Specimen CS2-R at Different Stages of Testing.

(a) Prior to testing

(b) After shot 2
P_r = 51.3 kPa
I_r = 329.9 kPa-ms

(c) After shot 4
P_r = 69.0 kPa
I_r = 493.8 kPa-ms

(d) After shot 5
P_r = 91.2 kPa
I_r = 670.8 kPa-ms

(e) After shot 5
P_r = 91.2 kPa
I_r = 670.8 kPa-ms

Figure 4.7: Extent of Damage in Specimen CS2-A at Different Stages of Testing.

(a) Prior to testing

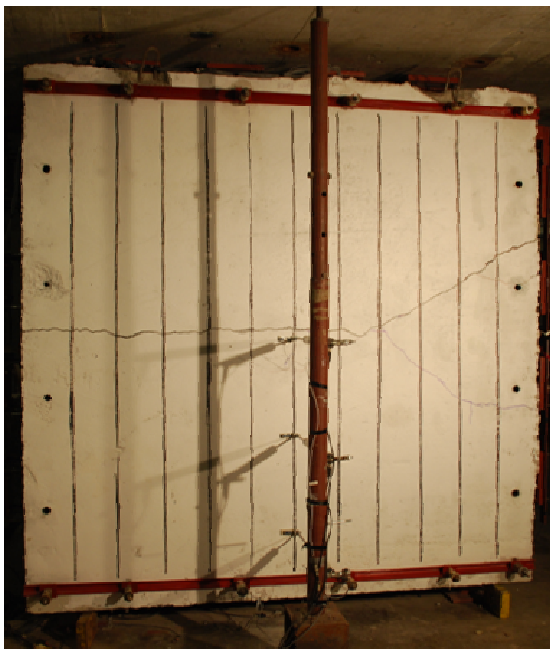

(b) After shot 2
P_r = *28.2 kPa*
I_r = *204.2 kPa-ms*

(c) After shot 3
P_r = *100.6 kPa*
I_r = *811.2 kPa-ms*

(d) After shot 3
P_r = *100.6 kPa*
I_r = *811.2 kPa-ms*

Figure 4.8: Extent of Damage in Specimen CS3-C at Different Stages of Testing.

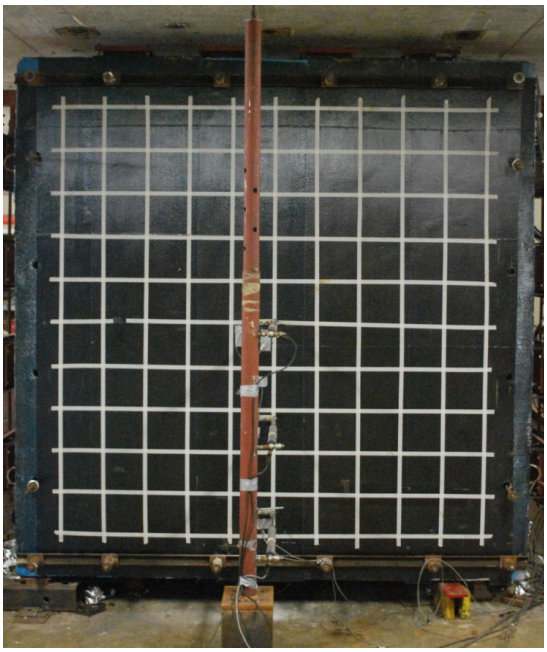

(a) Prior to testing

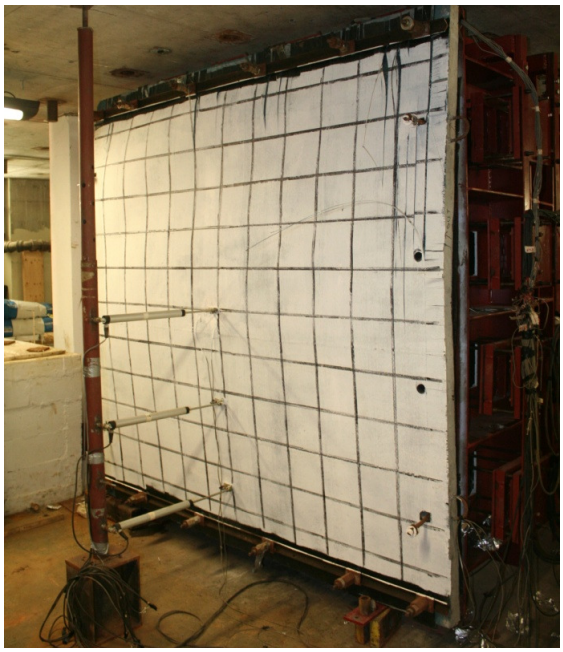

(b) After shot 4
P_r = *99.3 kPa*
I_r = *2535.0 kPa-ms*

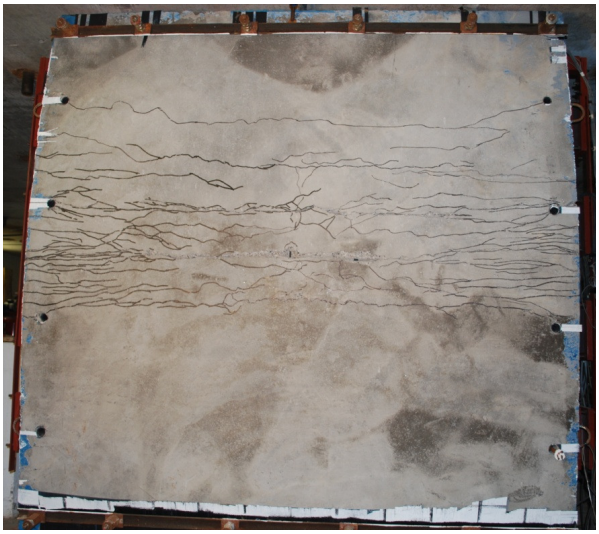

(c) After shot 4
P_r = *99.3 kPa*
I_r = *2535.0 kPa-ms*

(CFRP removed to expose crack pattern)

(d) After shot 4
P_r = *99.3 kPa*
I_r = *2535.0 kPa-ms*

Figure 4.9: Extent of Damage in Specimen CS3-R at Different Stages of Testing.

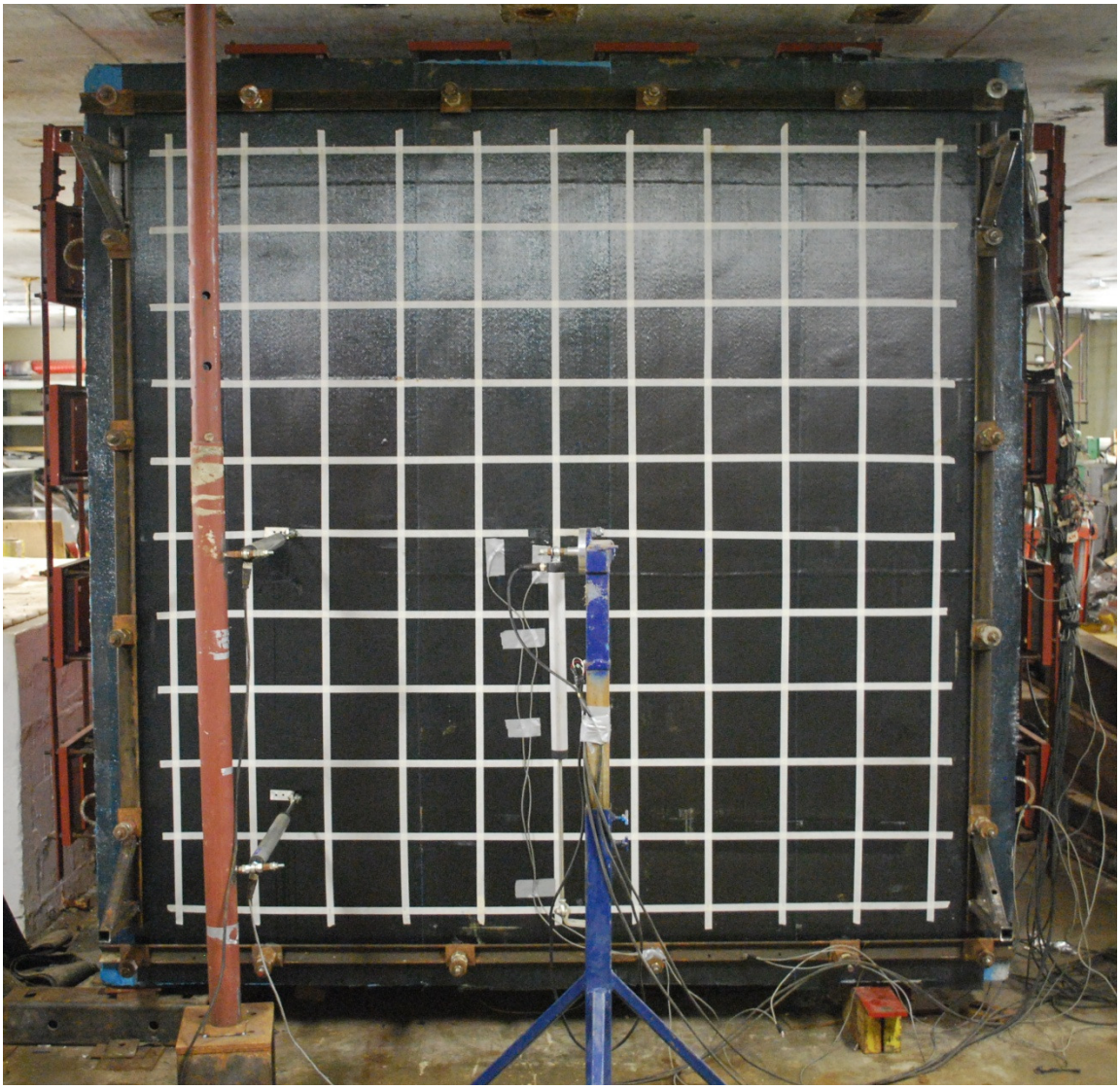

Figure 4.10: Extent of Damage in Specimen CS4-R1 at Different Stages of Testing.

(a) Prior to testing

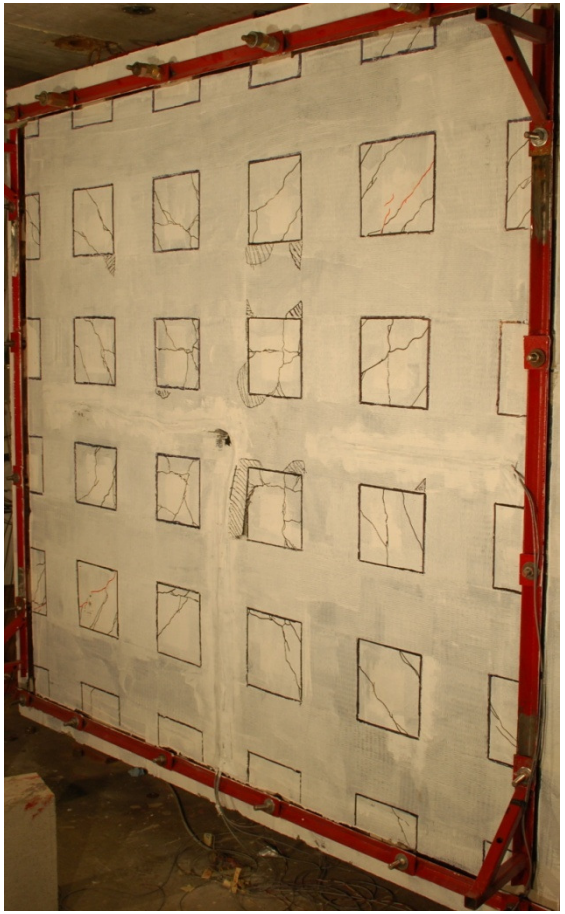

(b) Inbound face
After shot 6
P_r = 95.7 kPa
I_r = 1374.7 kPa-ms

(c) Rebound face
After shot 6
P_r = 95.7 kPa
I_r = 1374.7 kPa-ms

Figure 4.11: Extent of Damage in Specimen CS4-R2 at Different Stages of Testing.

Figure 4.12: Specimen CS5-C Prior to Testing.

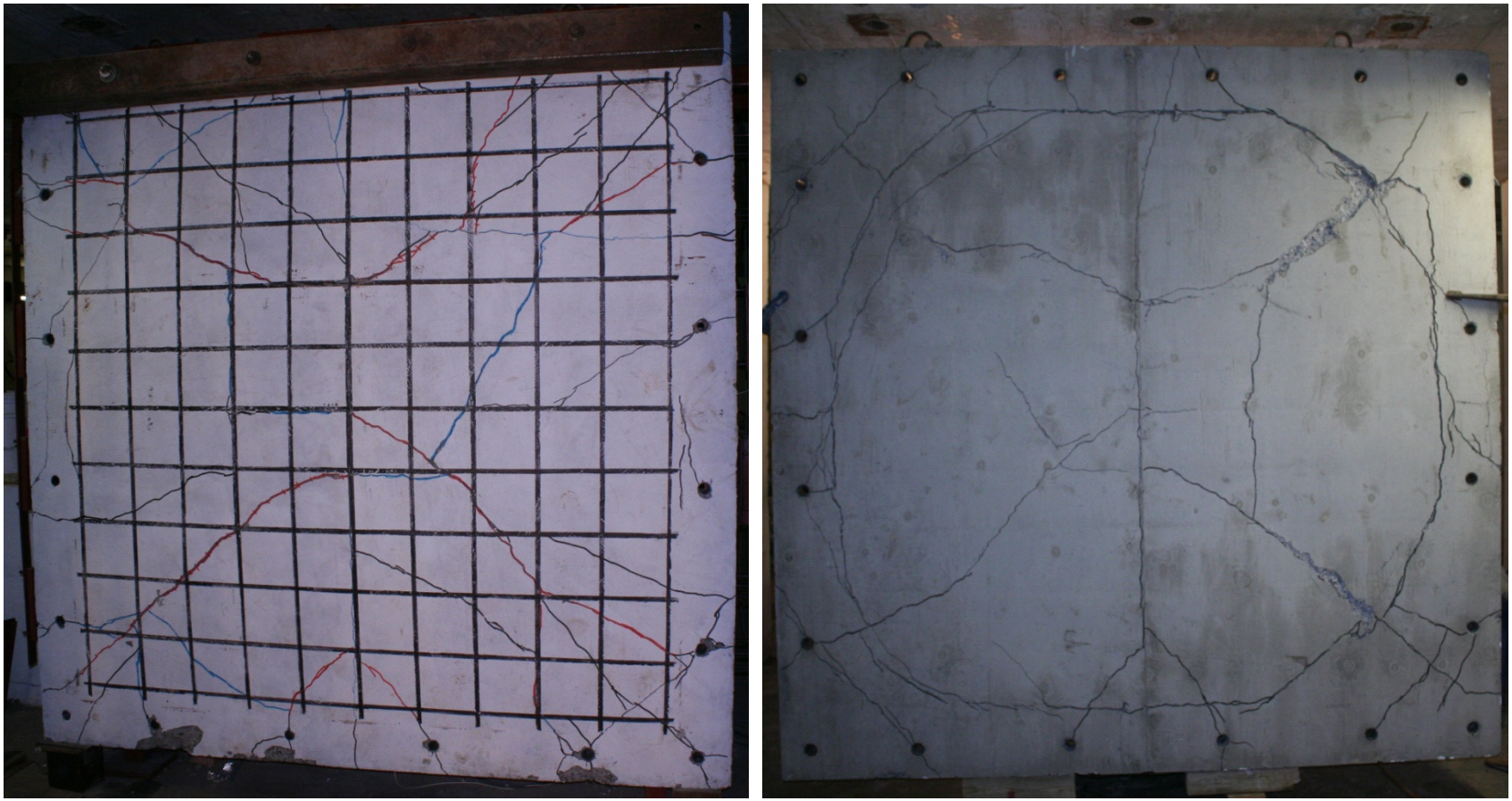

(a) After shot 7
Inbound face crack pattern
P_r = 91.9 kPa
I_r = 2620.9 kPa-ms

(b) After shot 7
Rebound face crack pattern
P_r = 91.9 kPa
I_r = 2620.9 kPa-ms

Figure 4.13: Extent of Damage in Specimen CS5-C at Different Stages of Testing.

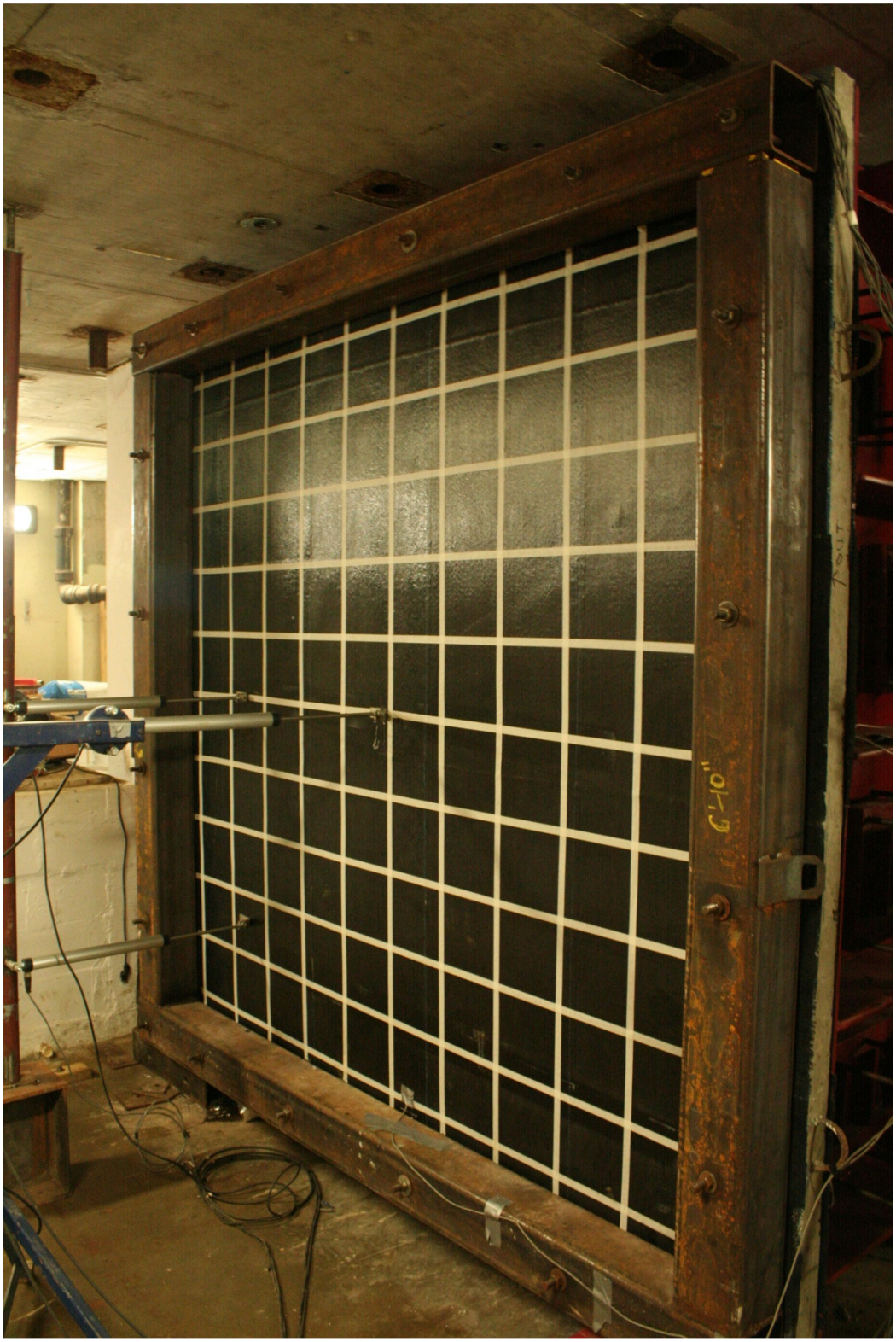

Figure 4.14: Extent of Damage in Specimen CS5-R at Different Stages of Testing.

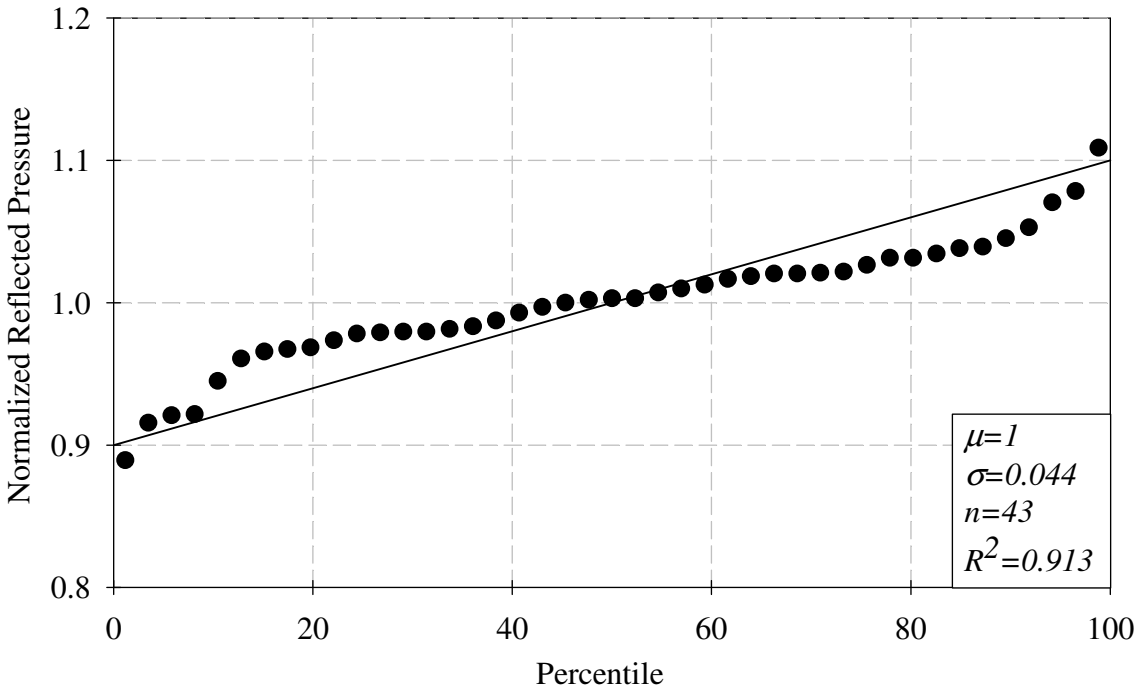

(a) Repeatability of reflected pressure, P_r

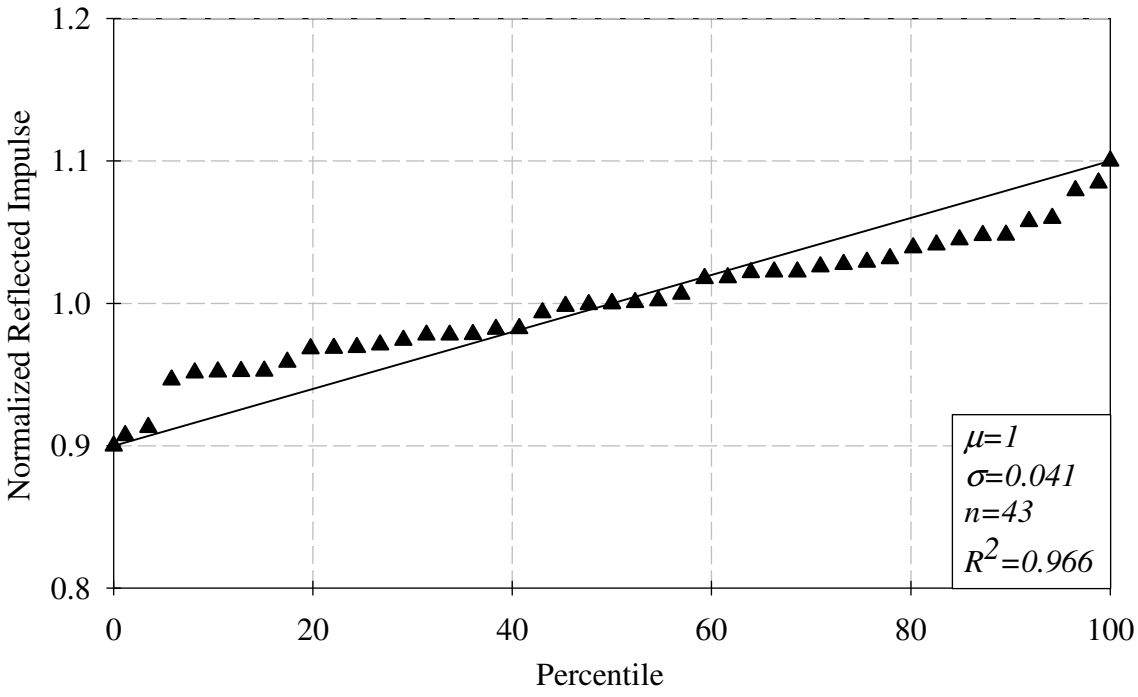

(b) Repeatability of reflected impulse, I_r

Figure 4.15: Repeatability of Reflected Pressure and Reflected Impulse Parameters Generated by the Shock Tube.

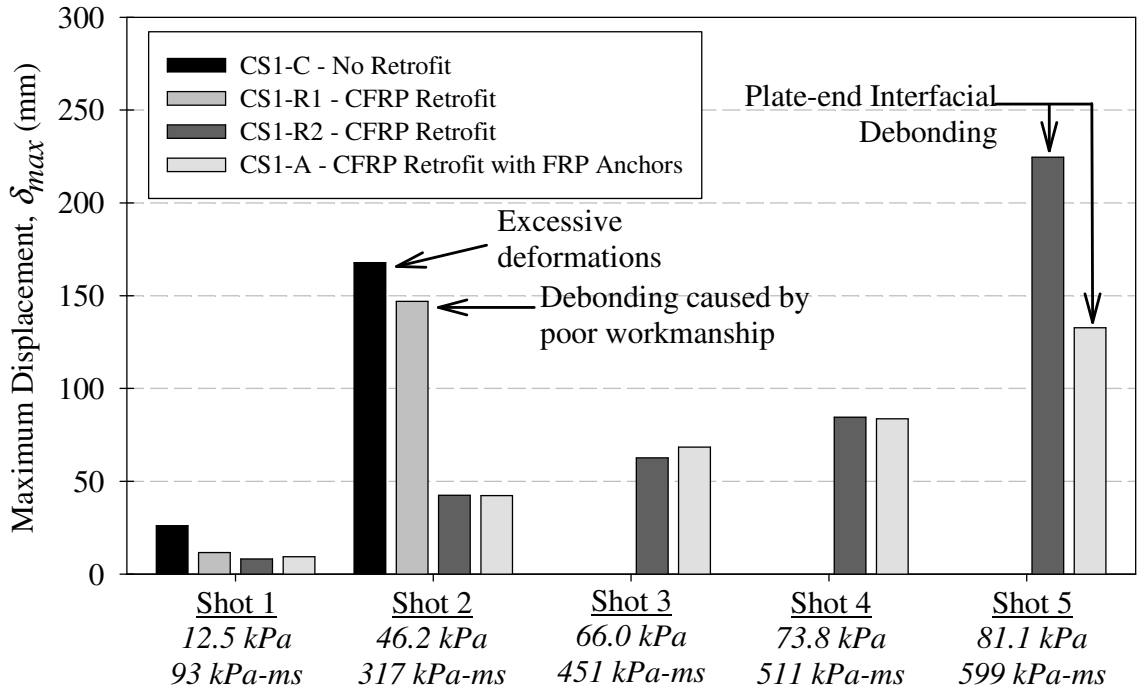

(a) Comparison of maximum displacements

(Companion shots grouped by reflected pressure, P_r, and reflected impulse, I_r)

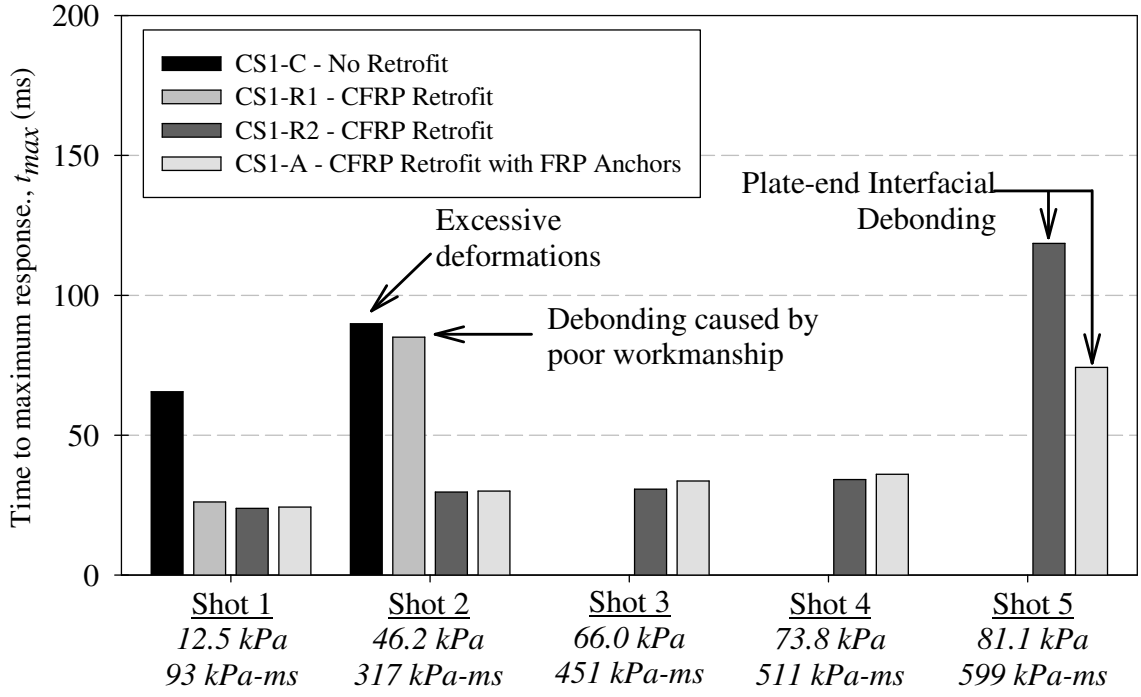

(b) Comparison of time-to-maximum displacements

(Companion shots grouped by reflected pressure, P_r, and reflected impulse, I_r)

Figure 4.16: Comparison of Experimental Results for Companion Set 1.

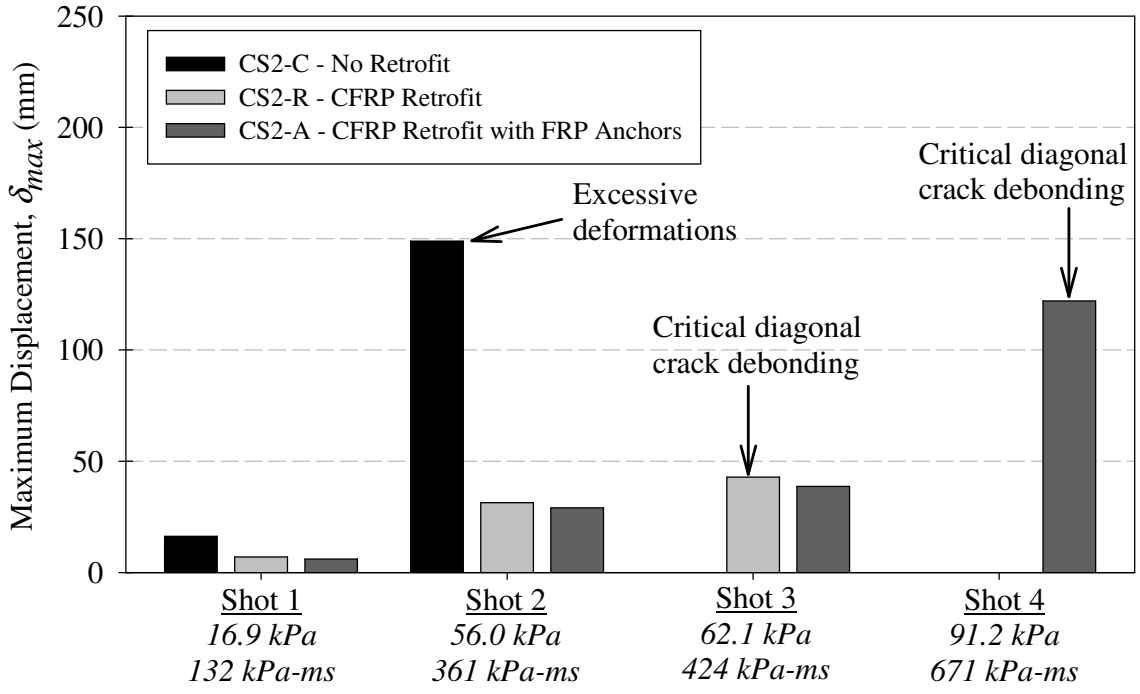

(a) Comparison of maximum displacements

(Companion shots grouped by reflected pressure, P_r, and reflected impulse, I_r)

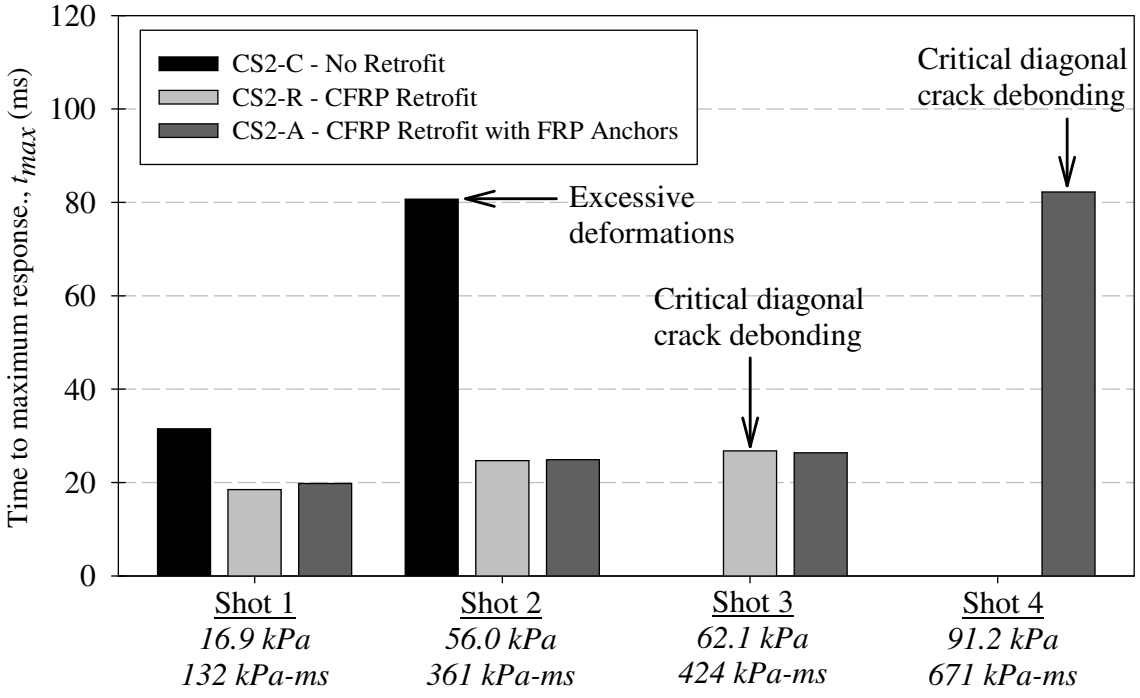

(b) Comparison of time-to-maximum displacements

(Companion shots grouped by reflected pressure, P_r, and reflected impulse, I_r)

Figure 4.17: Comparison of Experimental Results for Companion Set 2.

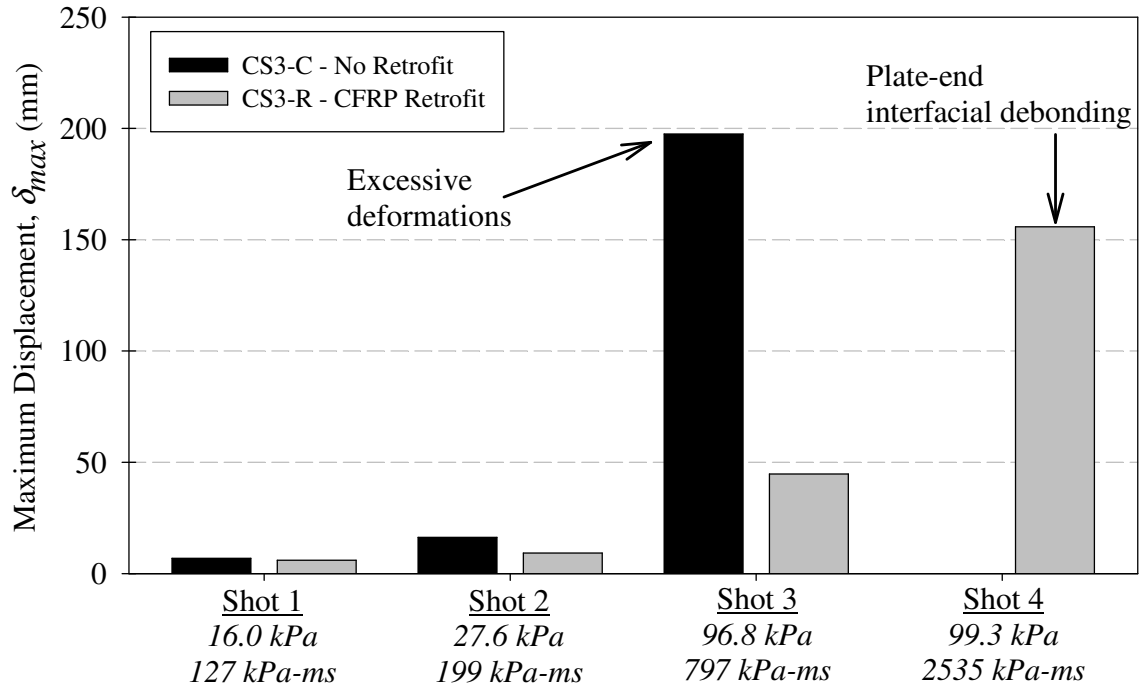

(a) Comparison of maximum displacements

(Companion shots grouped by reflected pressure, P_r, and reflected impulse, I_r)

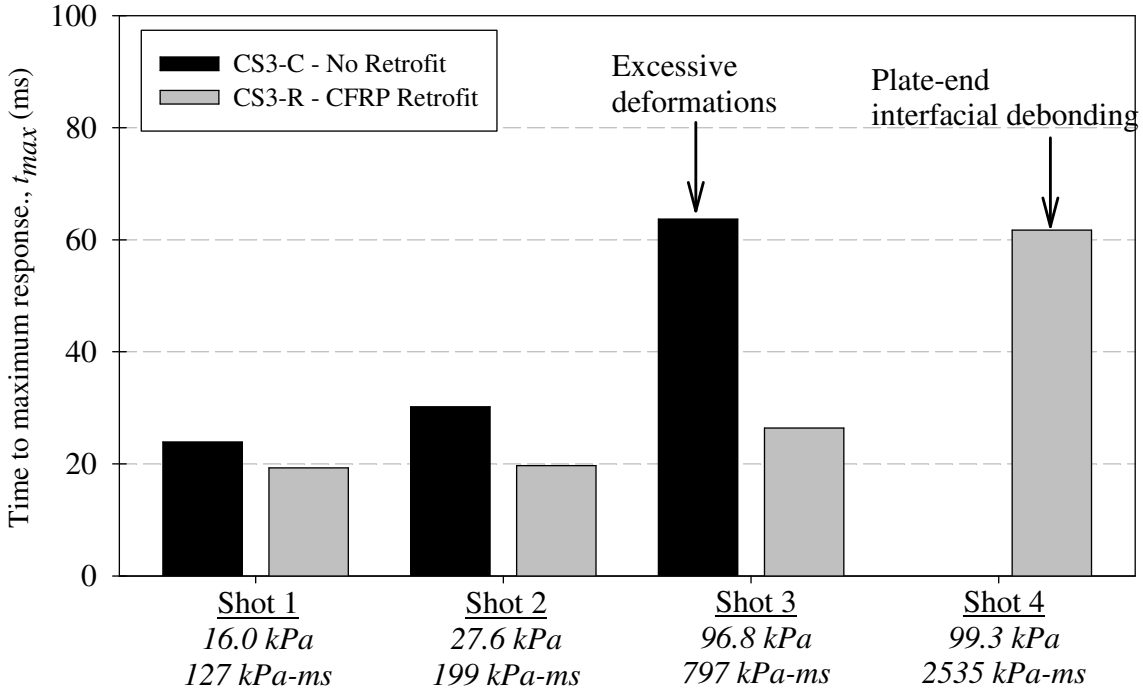

(b) Comparison of time-to-maximum displacements

(Companion shots grouped by reflected pressure, P_r, and reflected impulse, I_r)

Figure 4.18: Comparison of Experimental Results for Companion Set 3.

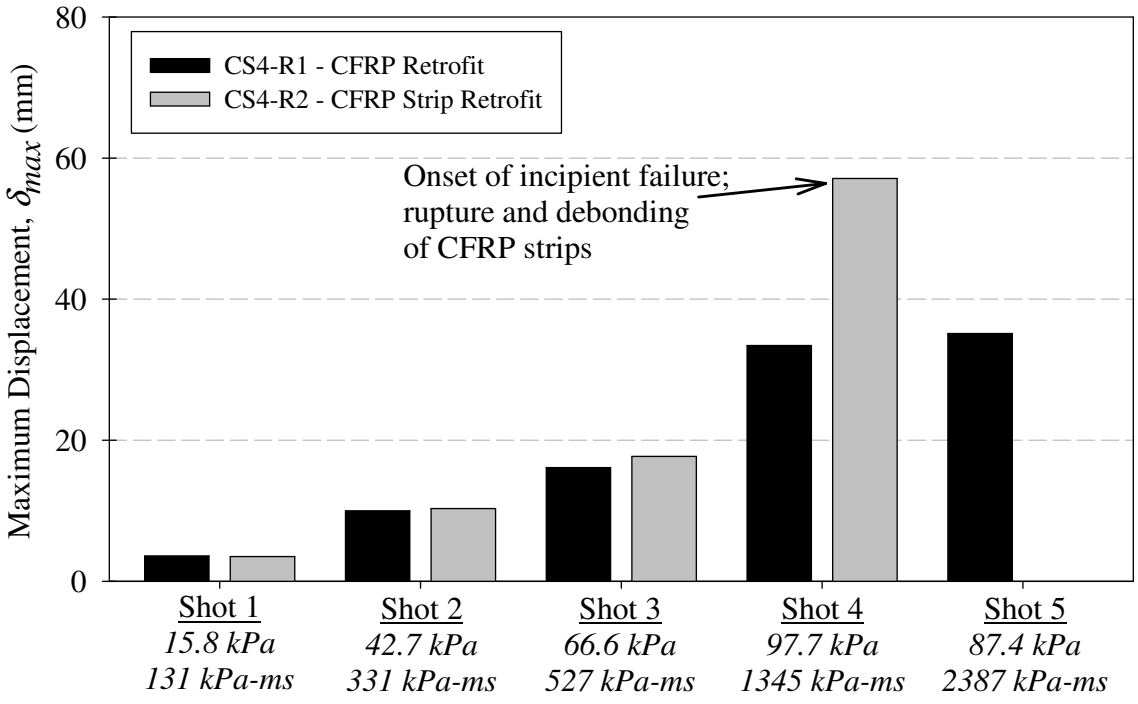

(a) Comparison of maximum displacements

(Companion shots grouped by reflected pressure, P_r, and reflected impulse, I_r)

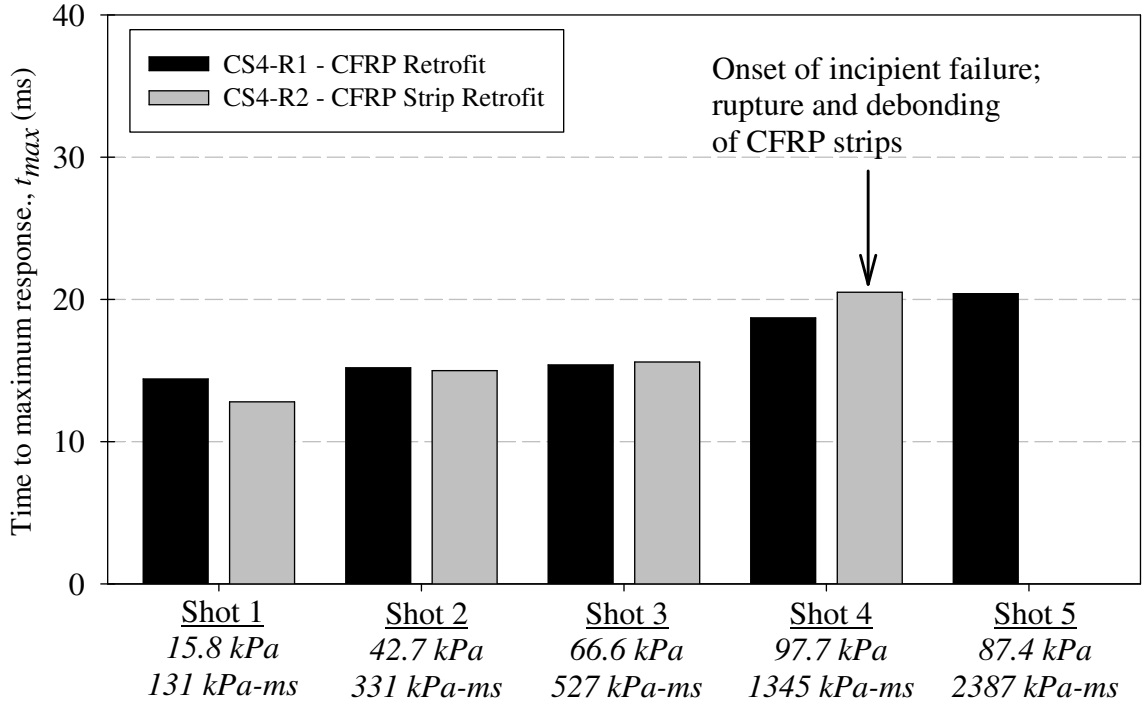

(b) Comparison of time-to-maximum displacements

(Companion shots grouped by reflected pressure, P_r, and reflected impulse, I_r)

Figure 4.19: Comparison of Experimental Results for Companion Set 4.

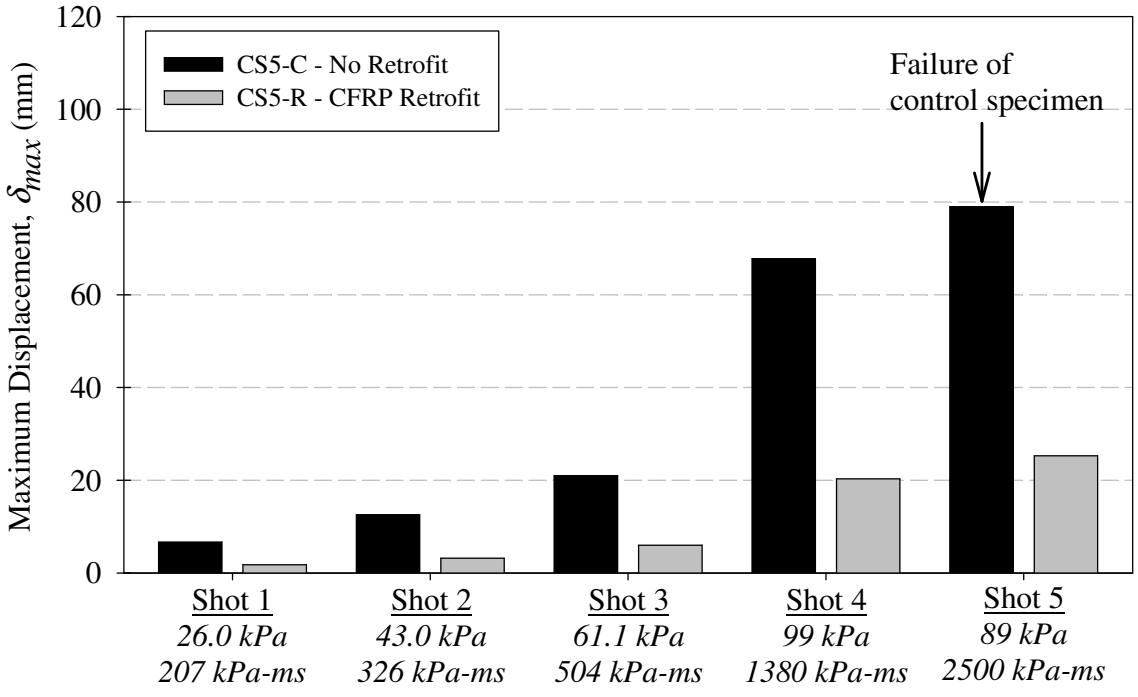

(a) Comparison of maximum displacements

(Companion shots grouped by reflected pressure, P_r, and reflected impulse, I_r)

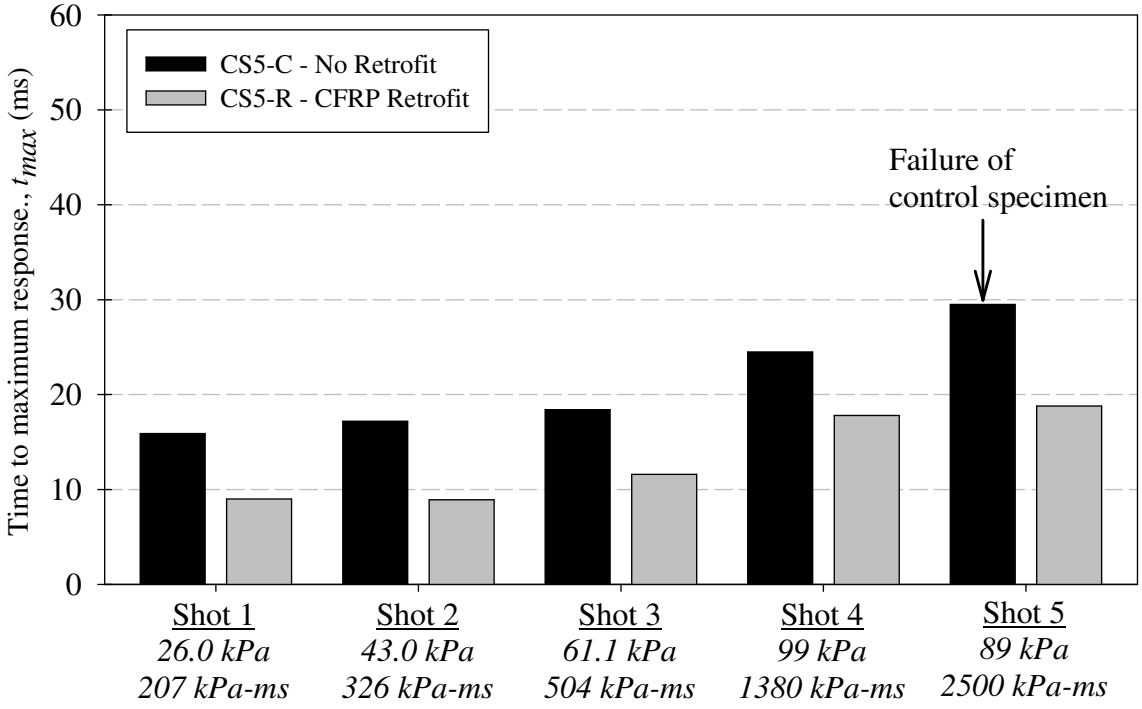

(b) Comparison of time-to-maximum displacements

(Companion shots grouped by reflected pressure, P_r, and reflected impulse, I_r)

Figure 4.20: Comparison of Experimental Results for Companion Set 5.

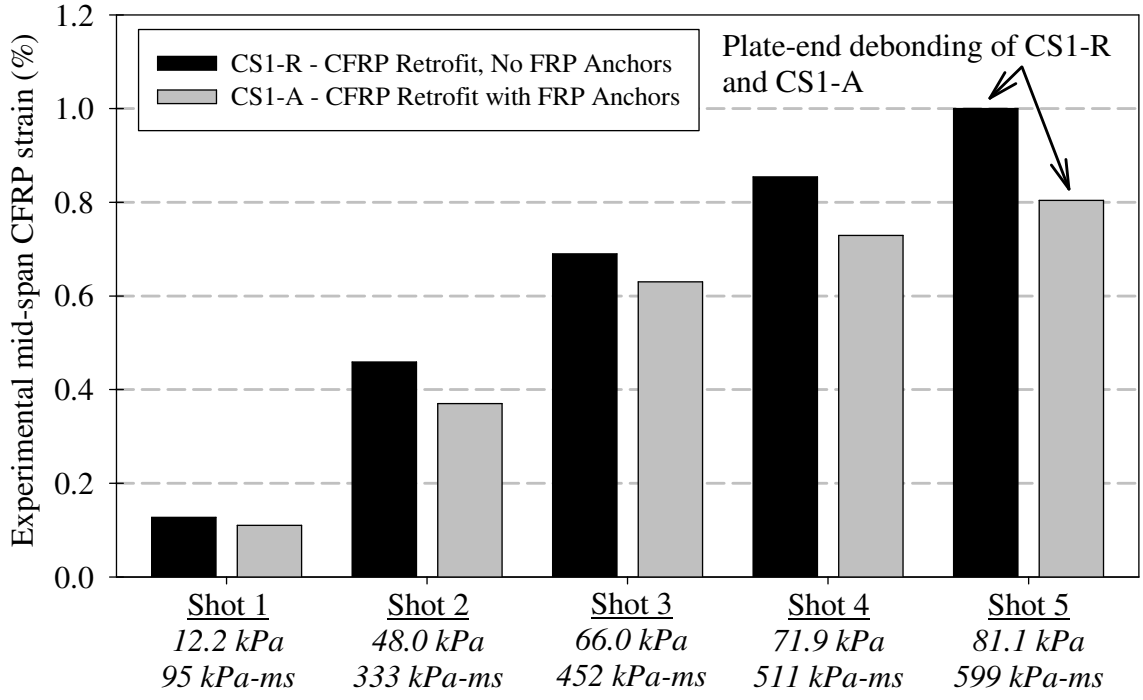

Figure 4.21: Effect of FRP Anchors on CFRP Retrofit Strain for Companion Set CS1.
(Companion shots grouped by reflected pressure, P_r, and reflected impulse, I_r)

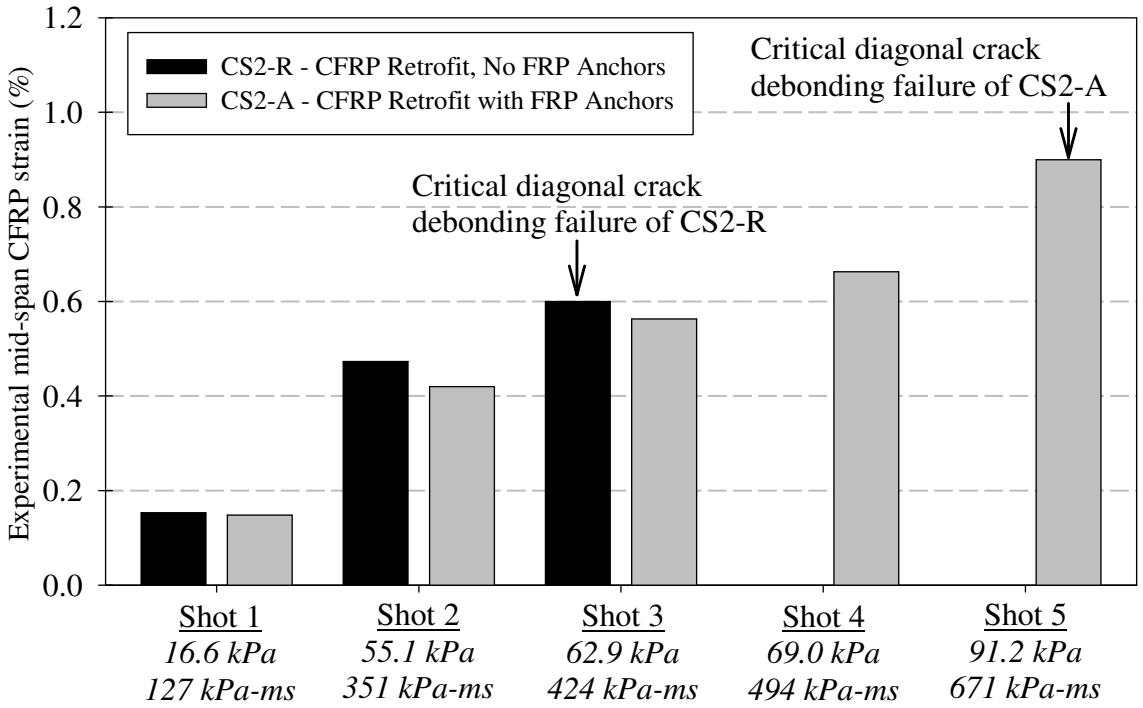

Figure 4.22: Effect of FRP Anchors on CFRP Retrofit Strain for Companion Set CS2.
(Companion shots grouped by reflected pressure, P_r, and reflected impulse, I_r)

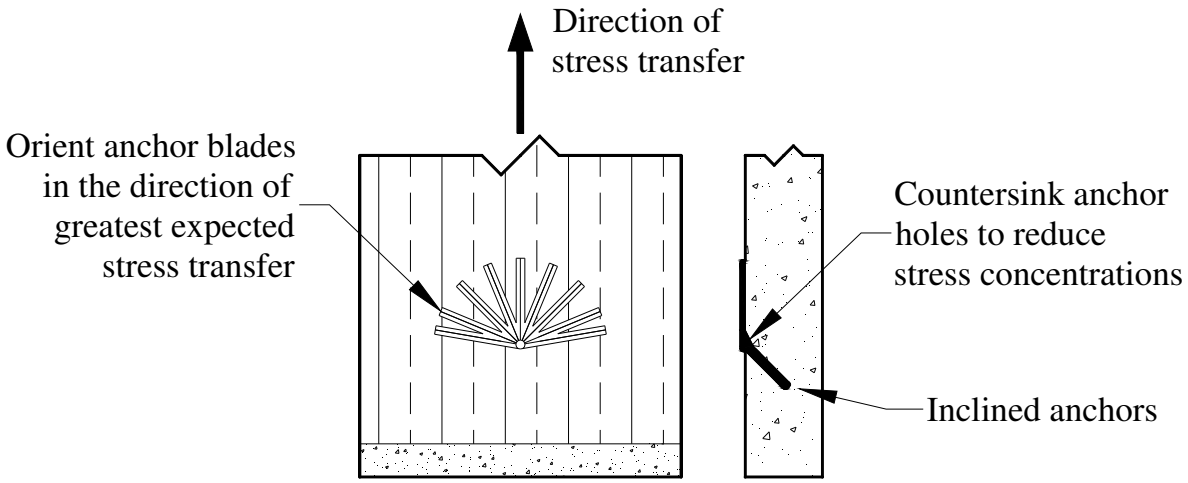

Figure 4.23: Proposed Modifications to FRP Anchors to Increase Performance.

Chapter 5. Theoretical Analyses of Slab Response

5.1. General

The experimental test data was used to verify analytical techniques to model the behaviour of reinforced concrete walls and slabs subjected to blast loading. The force-deformation characteristics of one-way wall strips were established using inelastic sectional and member analyses. The force-deformation characteristics of two-way slab plates were established using commonly accepted design approximations. The response of all specimens was computed by explicit solution of the single degree of freedom dynamic equation of motion. An equivalent static force procedure was used to analyze the response of shots performed on elastic, CFRP retrofitted specimens. The predicted maximum displacements and time-to-maximum displacements were compared against experimental results. The analysis indicates that the modelling procedures accurately describe the response characteristics of both retrofitted and unretrofitted specimens observed during the experiment.

5.2. Analytical Calculation of Force-Deformation Characteristics

5.2.1 General

Theoretical force-deformation characteristics were calculated for each of the thirteen specimens tested. These theoretical relationships were developed using well established static analysis techniques and incorporated dynamic material strength increase factors to account for high strain-rate effects. A computer program was written to generate the theoretical force-displacement relationships and SDOF load-mass factors for one-way members (CS1, CS2 and CS3), incorporating an algorithm to describe the progression of plastic hinge formation in maximum moment regions. Force-displacement relationships and SDOF transformation factors for two-way members (CS4 and CS5) were developed based on the simplified bilinear resistance curves – e.g. the methods prescribed by Biggs (1964) and UFC 03-340-02

(2008). The details of the methods and results predictions are described in the following sections.

5.2.2 Material Modelling

The material models used to describe the strength characteristics of concrete, steel and CFRP are discussed in the following sections.

Concrete

The constitutive model for the static compressive strength of concrete used in the analysis was developed by Hognestad (1951). The ascending branch of the stress-strain relationship, when $0 \leq \varepsilon_c \leq \varepsilon_o$, is described by

$$f_c = f_c' \left[\frac{2\varepsilon_c}{\varepsilon_o} - \left(\frac{\varepsilon_c}{\varepsilon_o} \right)^2 \right] \qquad [5.1]$$

and the descending branch, when $\varepsilon_c > \varepsilon_o$, is a straight line connecting the peak to $0.85 f_c'$ at a strain of *0.0038*. The peak strain, ε_o, was assumed to be *0.002* and the ultimate strain, ε_{cu}, was assumed to be *0.004*.

The contribution of concrete tensile strength was conservatively ignored in the analysis.

To account for the strength enhancement caused by high strain-rate loading, the dynamic increase factor model for concrete in compression proposed by the CEB Model Code (CEB, 1990) was incorporated into the analysis. The dynamic stress-strain curve for concrete in compression was determined by defining Hognestad's parabola and then applying the dynamic increase factor to the concrete stress, f_c, defined by equations [2.22] to [2.25] in Section 2.4.2.

Steel

The experimental static stress-strain relationship of the *6.3 mm* diameter undeformed steel wires, discussed in Section 3.5.2, was used in the analysis. It was assumed that this relationship was equally valid for the full range of compressive strains as well as tensile strain. The dynamic material increase factors for yield stress and ultimate stress, defined by Malvar (1998b), were used to account for high strain-rate effects. The static stress-strain relationship

was modified to account for strain-rate effects using equations [2.26] to [2.28] presented in Section 2.4.2.

CFRP

A linear stress-strain relationship for CFRP was used, based on the manufacturer's gross composite laminate properties for both the Tyfo SCH-41S and Wabo MBRACE CF 130 CFRP retrofit materials. CFRP material properties were discussed in Section 3.5.3.

No dynamic increase factor was applied to the composite properties used in the analysis as the material properties of CFRP were found to be independent of strain-rate (Harding and Welsh, 1983).

5.2.3 Prediction of FRP Debonding Strain

Due to the inherent difficulty and variability associated with predicting FRP debonding strains (ACI 440, 2008), no attempt was made to predict the strain level at which the composite retrofit systems would debond. Accordingly, the experimental FRP debonding failure strains were directly used in the analysis.

5.2.4 Detailed Analysis for One-way Members

Sectional Analysis

The first step in the derivation of the force-displacement relationship for one-way members was a plane section analysis. Strain-rate dependent material stress-strain curves were computed for an assumed strain-rate of $0.1\ s^{-1}$. The choice of an assumed strain-rate will be discussed in subsequent sections.

An initial extreme compressive fibre strain was selected and a corresponding neutral axis depth assumed. The strain profile within the section was then generated and internal forces in reinforcing steel, concrete and FRP (if applicable) were computed. Cover concrete was assumed to have spalled off when the compressive strain exceeded the crushing strain of concrete, ε_{cu}, defined in the stress-strain relationship. Additionally, concrete internal forces were computed by summing the force within a number of strips of finite height within the compressive region, allowing for numerical integration of the concrete stress-strain diagram. Equilibrium of internal forces was then verified against a convergence criterion. The bisec-

tion method was used to select a revised neutral axis and the procedure was repeated until convergence. The internal moment and corresponding curvature were then computed. Another incremental extreme compressive fibre strain was selected and the procedure was repeated. The analysis continues until a predetermined failure criterion was satisfied. Figure 5.2 shows a typical cross-section with corresponding strain profile and internal forces.

The sectional analysis was terminated when one of two failure criteria was satisfied. Section failure was defined as the reinforcing steel strain exceeding the rupture strain or when strain in the FRP exceeded a predetermined maximum value. The rupture strain of steel was defined in the stress-strain relationship, while the maximum strain in FRP was specified by the analyst. FRP failure strain was defined based on the expected failure mode. For the purpose of this analysis, FRP failure strains were always defined based on the maximum FRP strain observed during experimental testing. Experimental FRP failure strains for each test were discussed in Chapter 4. Failure of concrete is not an explicit failure mode as redistribution of compressive force is accounted for by allowing cover concrete to crush and spall.

The above procedure was used to generate dynamic moment-curvature relationships for each one-way wall strip of companion sets CS1, CS2, and CS3.

Member Analysis

The results of the sectional analysis were used to calculate the force-deformation characteristics of the one-way reinforced concrete wall panels. The post-peak behaviour of unconfined reinforced concrete is characterized by a decrease in moment resistance with increasing curvatures prior to failure. This post-peak behaviour cannot be accounted for by directly interpolating from the moment-curvature diagram. An algorithm was used to describe the formation and progression of plastic hinging during response. This analytical procedure was developed by Razvi and Saatiocglu (1999) to model the formation and progression of plastic hinging in reinforced concrete columns subjected to lateral loading. It has been modified to model large inelastic displacement of simply-supported beams subjected to distributed loading, as shown in Figure 5.3 (a).

The algorithm used in the analysis was as follows:

1. Establish the moment-curvature relationship of the section.

2. Assume an initial incremental distributed load, w_i.

3. The incremental moment distribution is computed using, $M_i = \frac{w_i x}{2}(L - x)$, and the corresponding curvature distribution along the length of the member is determined.

    a. When M_i remains less than the maximum moment capacity of the section, M_{max}, the curvature distribution is determined by interpolating directly from the moment-curvature relationship (Figure 5.3 (b)). The on-set of plastic behaviour is assumed to occur as the applied moment approaches the maximum moment capacity of the section.

    b. When the maximum incremental moment, M_i, reaches or exceeds the maximum moment capacity, M_{max}, a plastic hinge forms with constant curvature, ϕ_i, corresponding to the incremental moment, M_i, at the location of the critical section (Figure 5.3 (c)). The length of the plastic hinge, L_{pl}, is defined as either the distance between the incremental maximum moment, M_i, and the maximum moment, M_{max}, along the curvature distribution or by an empirical equation describing hinge length, whichever is less. In this case, the plastic hinge length, L_{pl} was defined according to the expression described by Sawyer (1964),

$$L_{pl} = 0.25d + 0.075z \qquad [5.2]$$

where d is the effective depth and z is the shear span. Curvatures outside of the plastic hinge region are interpolated directly from the moment-curvature diagram.

4. The resistance at the current load increment is computed by $R_i = w_i L$, and the corresponding mid-span displacement, δ_i, is computed by numerical integration of the moment of the area of the curvature distribution.

5. The normalized displaced shape, $\Phi_i(x)$, is computed by numerical integration of the moment of the area under the curvature distribution. The load-mass factor, k_{LMi}, at the particular load increment is computed by numerical integration of the

displaced shape along the length of the member. The load-mass factor is computed by equations [2.13] and [2.14] in Section 2.3.2.

6. Another incremental distributed load, w_i, is selected and the procedure is repeated until the ultimate curvature in the critical section has been achieved.

    a. The incremental load, w_i, is increased with each successive iteration prior to achieving maximum moment capacity, M_{max}, of the section (pre-peak member behaviour).

    b. The incremental load, w_i, is decreased with each successive iteration after achieving maximum moment capacity, M_{max}, of the section (post-peak strength decay).

Following the procedure outlined above, the complete force-deformation characteristics of the retrofitted and unretrofitted reinforced concrete wall panels were predicted and used in the dynamic analysis.

A composite resistance curve was generated for FRP retrofitted members. The first portion of the composite resistance curve was assumed to follow that of the retrofitted specimen, up to the point of retrofit failure (either by debonding, anchor failure, or fibre rupture). After the point of retrofit failure, the resistance curve was assumed to follow the backbone curve of the unretrofitted specimens. A composite load-mass transformation factor was defined in a similar manner.

Resistance curves and load-mass factors used in the dynamic analysis for members in companion sets CS1, CS2 and CS3, are shown in Figure 5.4 to Figure 5.11.

5.2.5 Simplified Analysis for Two-way Members

In lieu of a more detailed analysis, the force-deformation characteristics of the two-way reinforced concrete plates were calculated using the method described by Biggs (1964). This analysis methodology has been accepted by UFC 03-340-02 (2008) to define the resistance curves and load-mass transformation factors of reinforced concrete structures. The force-deformation characteristics for the simply-supported two-way specimens of CS4 were de-

fined based on Table 5.4 of Biggs (1964). Similarly, the force-deformation characteristics for the fully-fixed two-way specimens of CS5 were defined according to Table 5.5 of Biggs (1964). The resistance curves were calculated assuming that the moment capacity – and hence bending stiffness – was the same in both orthogonal directions of bending. In reality, this assumption was not the case but was reasonable given all the other assumptions inherent to using such a simplified method of analysis.

Resistance curves and load-mass factors using the in dynamic analysis for members in companion sets CS4, CS5, are shown in Figure 5.12 to Figure 5.15.

5.3. Dynamic SDOF Analysis

A VB.NET computer program was written to calculate SDOF displacement time-histories and generate PI diagrams of blast loaded structures. The program was developed on the basis of the average acceleration method, which is unconditionally stable for any time-step. A graphical user interface was developed to streamline the analysis process. All variables in the dynamic equation of motion may be modified by the user. The software has the ability to process piecewise linear functions as inputs for member resistance, load-mass transformation factors and reflected pressure time-histories. Results are plotted to the screen, and the software has the capability to overlay experimental results and theoretical predictions to facilitate data analysis. Finally, the program gives the analyst the ability to save/load analysis sessions and export results to comma delimited text files *(*.csv)*. Screenshots of the program running in SDOF and PI diagram mode are shown in Figure 5.16 and Figure 5.17.

5.3.1 Equation of Motion

The equation of motion used to describe the dynamic response of the reinforced concrete flexure members subjected to simulated shock wave loading is given in equation [2.16].

5.3.2 Iterating for Strain-rate

The default strain-rate used to calculate dynamic increase factors in the analysis was $0.1\ s^{-1}$. This is the assumed strain-rate for design of blast resistant structures subjected to distant ex-

plosions in UFC 03-340-02 (2008). This assumption is appropriate as Lloyd (2010) has shown that the shock tube effectively simulates distant explosions.

Generating strain-rate dependent resistance curves should be an iterative procedure, whereby an initial strain-rate is assumed, single degree of freedom analysis is performed, new strain-rate calculated based on dynamic response, and iterated until strain-rate convergence. However, the computational effort required by such an iterative procedure is generally not warranted as the procedure will usually converge on the second iteration (UFC 03-340-02, 2008). This assumption is appropriate given that the relative change in the dynamic increase factor for concrete and steel is negligible in the anticipated range of strain-rates. Furthermore, there is inherent uncertainty built-in to the static material properties. This uncertainty may be larger than the anticipated strength increase caused by high strain-rates. Finally, strain-rate varies as a function of: time; the relative position along the length of the specimens; depth relative to the neutral axis. As the distribution of strain-rate is assumed to be constant along the length of the member and for the duration of response, using an assumed strain-rate which lies within the expected range of actual strain-rates is appropriate.

Consider the strain-rate dependent resistance curves, shown in Figure 5.18, for specimen CS1-C. These resistance curves were generated by solving the dynamic equation of motion and iterating for strain-rate. Blast loading was simulated by a linearly decreasing function with peak reflected pressure of *100 kPa* and positive phase duration of *10 ms*. The strain-rate dependent displacement time-histories are shown in Figure 5.19. The difference in both maximum displacement and time-to-maximum displacement based on iteration 1 (static resistance curve) and iteration 3 ("true" dynamic strain-rate $0.3\ s^{-1}$) is approximately *10%*. This difference becomes approximately *4%* when comparing iteration 2 (assumed "correct" dynamic strain-rate $0.1\ s^{-1}$) and iteration 3. However, the significant increase in effort required to increase accuracy of the solution by such a small margin is not warranted in lieu of all the other uncertainties, unknowns and assumptions inherent to analysis and design of blast resistant structures.

It is for these reasons that all analyses were performed with an assumed high strain-rate of $0.1\ s^{-1}$, as recommended by UFC 03-340-02 (2008) for explosions in the far design range.

5.3.3 Degree of freedom

The degree-of-freedom for all analyses was consistently taken as mid-span displacement of all members.

5.3.4 Resistance Curves

As described in the preceding sections, piecewise linear resistance curves, $R(u)$, were generated with material dynamic increase factors corresponding to an assumed strain-rate of $0.1\ s^{-1}$. As necessary, a constant post-ultimate resistance of 5% of ultimate capacity was arbitrarily added to the resistance curves to facilitate convergence of the equation of motion when developing PI diagrams.

No attempt was made to model the reduction in strength and stiffness of the specimens when subjected to progressively increasing pressure-impulse combinations. This would require the use of a hysteretic model which was considered beyond the scope of this project. Accordingly, the resistance curves generated for virgin (*i.e.* undamaged specimens) were used throughout the analysis.

5.3.5 Transformation Factors

The piecewise linear load-mass transformation factors, $k_{LM}(u)$, generated from the detailed analysis of one-way members (CS1, CS2 and CS3), along with the load-mass transformation factors defined as step functions based on the Biggs analysis of two-way members (CS4 and CS5), were used in the dynamic analysis.

5.3.6 System Mass

Specimen mass was calculated based on the volume of the specimen that was within the clear span of the members; the participation of mass located outside of the clear span was assumed to be negligible. The unit weight, γ_c, of all specimens was assumed to be $2400\ kg/m^3$. The mass of the one-way reinforced concrete panels of CS1 and CS2 was *188.5 kg* and *282 kg*, respectively. However, the load transfer device adds approximately *394 kg* to the mass of the dynamic system, which is assumed to act up to the time of maximum response. Therefore, the system mass, m_s, for CS1 and CS2 was *582 kg* and *676 kg*, respectively. The mass of the

simply-supported two-way reinforced concrete plates of CS3 and CS4 was *896.7 kg*, while the mass of the clamped two-way reinforced concrete plates of CS5 was *818.2 kg*.

5.3.7 Loaded Area

The area impacted by the reflected pressure wave is known as the loaded area, A_{LTD}. For tests which did not require a load transfer device, this area was calculated based on the area demarcated by the clear span of bending. The loaded area for companion set CS3 was *4.53* m^2. The loaded area for companion set CS4 and CS5 was *4.98* m^2 and *4.13* m^2, respectively.

Selecting an appropriate loaded area for tests requiring a load transfer device (i.e. companion sets CS1 and CS2) was more difficult due to the construction of the load transfer device. Prior to the arrival of the shock front, the loaded area of the load transfer device was *4.13* m^2. However, as the specimen began to displace laterally, the theoretical loaded area could be as large as *4.98* m^2. To account for the effects of increased loaded area and shock wave venting, an empirical pressure-dependent loaded area was used in the analysis. The loaded area for one-way members with load transfer device (i.e. companion sets CS1 and CS2) was *4.13* m^2 when the peak reflected pressure was less than *40 kPa* and the loaded area was *4.53* m^2 when the peak reflected pressure was greater than *40 kPa*. The smaller loaded area was based on the area of the test frame opening, while the larger loaded area was based on the area between the centerline of the test frame flange and the height of the load transfer device.

Consider Figure 5.20 comparing the SDOF displacement ratio for tests performed on CS1 and CS2 versus reflected pressure for two different loaded areas, *4.13* m^2 and *4.53* m^2, respectively. Undoubtedly, using a loaded area equal to the area of the test frame, *4.13* m^2, yields results which are superior to those using a loaded area of *4.53* m^2 when the peak reflected pressure was less than *40 kPa*. However, when the peak reflected pressure was greater than *40 kPa*, the choice of which loaded area to use was less certain. The mean displacement ratio predicted using a loaded area of *4.13* m^2 for pressures greater than *40 kPa* was *0.953*, whereas the mean displacement ratio predicted using a loaded area of *4.53* m^2 was *1.116*. Therefore, using a loaded area of *4.53* m^2 when the reflected pressure was larger than *40 kPa reduces* the accuracy of the predictions by *15%* relative to using an area of *4.13*

m^2. Regardless, it is the opinion of this analyst that increasing or decreasing the loaded area by *9%* has little consequence on the overall analytical results at large reflected pressures.

5.3.8 Pressure-time history

For the sake of consistency, the reflected pressure time-history, P_r, recorded by one of two reflected pressure sensors was used as the load-time forcing function in the dynamic analysis. The side pressure gauge served as the primary source of the load-time function used in the dynamic analysis, while the bottom reflected pressure gauge was used as a backup. The difference in SDOF results when using either the side or bottom pressure gauge was generally negligible.

The use of a load transfer device for companion sets CS1 and CS2 meant that negative pressures would not be transferred to the surface of the specimens. This is a consequence of not attaching the load transfer device to the slabs themselves. Therefore, the pressure-time history used in the dynamic analysis of these specimens was modified by setting any negative pressure values to zero to account for this phenomenon.

5.3.9 Selection of time-step

A time step of 10^{-5} *s* (*0.01 ms*) was found to give acceptable and accurate results.

5.3.10 Extent of dynamic SDOF analysis

SDOF displacement time-histories were generated for each shock tube test up to the time of maximum displacement, primarily because design of blast resistant structures is most concerned with maximum response (i.e. displacement). Another reason for choosing not to continue the analysis past the time of maximum response was that the experimental setup interfered with post-peak vibration of most of the specimens. For the case of companion sets CS1 and CS2, negative displacements (i.e. rebound) were prevented by the presence of the transverse steel beams of the load transfer device. There was also uncertainty as to how negative pressures affected the interaction between the load transfer device and the specimens themselves. Therefore, the analysis was performed up to the time of maximum response to eliminate these uncertainties.

5.3.11 Generation of Pressure-Impulse Diagrams

Pressure-impulse diagrams were generated for each test performed on each specimen. Points along the PI curves were generated by assuming a positive phase duration, t_d, and iterating on reflected pressure, P_r, until the maximum single degree of freedom displacement was equal to a specified target value. A linearly decreasing load-time function was used to describe the blast wave reflected pressure time-history. Each PI curve was composed of thirteen points: the impulsive asymptote was calculated with a positive phase duration of *4%* the natural period, T_N, of the structure and the quasi-static asymptote with a positive phase duration of *1000%* of T_N. An automatic time step control algorithm was developed to ensure an acceptable level of accuracy for each iteration.

5.4. Dynamic Analysis by Equivalent Static Force

As discussed in Chapter 2.3.3, the application of an equivalent static force can be used to approximate the dynamic response of a structure to dynamic loading. The dynamic load factor is computed based on the closed-form solution of the equation of motion assuming idealized load-time and resistance functions. Therefore, the accuracy of the equivalent static force analysis is based on how closely the actual resistance and loading functions agree with the assumed idealizations.

The experimental results indicate that the CFRP retrofitted specimens remained elastic until debonding failure. Therefore, the analysis of these specimens by an equivalent static force procedure should yield results which are in agreement with both experimental results and those results predicted by explicit solution of the equation of motion, but at a fraction of the computation expense. The elastic stiffness and load-mass factors for the equivalent static force analysis were determined from the force-deformation characteristics shown in Figure 5.4 to Figure 5.17. The experimental reflected pressures and load durations, discussed in Chapter 4, were used to approximate the pressure-time history with a linearly decreasing load. Finally, the dynamic load factor and time-to-maximum response were determined from the response plots in Figure 2.3. The results of the equivalent static force procedure are discussed in subsequent sections.

5.5. Comparison of Analytical Results with Experimental Data

Predicted and experimental mid-span displacement time-histories are plotted in Figure B-1 to Figure B-60 in Appendix B. Experimental and predicted maximum displacement and time-to-maximum displacements for all tests are shown in Table 5.1. Summaries of experimental and predicted results are shown in Table 5.2. The analysis indicates that the predicted behaviour of all specimens is in general agreement with the behaviour observed during experimental testing. However, the precision and accuracy of the predictions was found to be proportional to the level of refinement incorporated into the derivation of the force-deformation characteristics.

5.5.1 Prediction of maximum displacements by SDOF methods

Single degree of freedom displacement ratios, defined as the ratio between the maximum displacement predicted by the SDOF method and the corresponding experimental displacement, $\delta_{SDOF}/\delta_{exp}$, are tabulated in Table 5.2. Experimental and predicted SDOF maximum displacements for all tests are plotted in Figure 5.21. The average SDOF displacement ratio for *57* compared tests was *1.215*, with a corresponding standard deviation of *0.356* and coefficient of variation of *29.3%.* However, these results are statistically unbalanced for two reasons: two analytical techniques were used to derive the force-deformation characteristics of the walls and slabs and the high number of elastic tests on retrofitted specimens damp out as-built results and the displacement levels of the tests varied greatly.

One-way Wall Panels (CS1, CS2 and CS3)

The prediction of maximum displacements for companion sets CS1, CS2 and CS3 was superior to those predicted for the two-way slab plates of CS4 and CS5. The mean SDOF displacement ratio for all tests performed on the one-way wall panels was *1.163* with a corresponding standard deviation of *0.254* and coefficient of variance of *21.8%,* based on *31* samples. No distinction can be made between predicting as-built and retrofitted specimen response. The mean SDOF displacement ratio for all tests performed on as-built one-way wall panels was *1.020* with a corresponding standard deviation of *0.192* and coefficient of variance of *18.8%,* based on *8* samples. The mean SDOF displacement ratio for all tests per-

formed on retrofitted one-way wall panels was *1.213* with a corresponding standard deviation of *0.257* and coefficient of variance of *21.2%,* based on *23* samples.

This level of accuracy is a consequence of the detailed resistance curves and load-mass factors used to describe the one-way members. The maximum displacement of small displacement shots for as-built specimens was predicted with an excellent level of accuracy. However, the maximum displacement of destructive tests of as-built specimens was generally under-predicted. This is related to the difficulty in accurately describing member behaviour at large, inelastic displacement levels. Furthermore, the strength decay exhibited by severely damaged members is poorly understood. The plastic hinge formation algorithm employed in this analysis may not adequately describe this behaviour for as-built flexure dominant reinforced concrete members. The predicted SDOF displacement time-histories, shown in Appendix B, generally follow the slope of the experimental displacement were a reasonable level of accuracy. This indicates that the force-deformation characteristics and mass used in the analysis are appropriate.

The use of a large amount of high strength/low modulus retrofit material (i.e. CFRP) resulted in structures which exhibited essentially elastic response up to retrofit failure. As the SDOF method is well suited to modelling elastic structures, the predictions for said retrofitted members are relatively good. Maximum displacement predictions for retrofitted specimen CS3-R were consistently larger than corresponding experimental displacements. It is believed that this consistent over-prediction was caused by differences between actual MBRACE CF-130 composite material properties and those used in the analysis (based on manufacturer's specifications).

Two-way Slab Plates (CS4 and CS5)

The maximum displacements predicted by the SDOF method for the two-way slabs of CS4 and CS5 were consistently larger than corresponding experimental results. The mean SDOF displacement ratio for all tests performed on the two-way specimens was *1.276* with a corresponding standard deviation of *0.446* and coefficient of variance of *34.9%,* based on *26* tests. Statistically, no distinction can be made between predicting as-built and retrofitted specimen response. The mean SDOF displacement ratio for all tests performed on as-built two-way specimens was *1.344* with a corresponding standard deviation of *0.505* and coefficient of

variance of *37.6%,* based on *7* samples. The mean SDOF displacement ratio for all tests performed on retrofitted two-way specimens was *1.251* with a corresponding standard deviation of *0.434* and coefficient of variance of *34.7%,* based on *19* samples.

The analysis indicates that there is no statistical distinction between the consistency of predictions of as-built and retrofitted two-way specimens using simplified bi- and tri-linear resistance curves. The large difference between the predicted and experimental results can be linked to the choice of a simplified analytical model used to define the force-deformation characteristics of the members. It is accepted that these resistance curves generally yield conservative results and are acceptable for blast resistant design purposes (UFC 03-340-02, 2008). As expected, the approximate resistance curves and load-mass factors did not yield exact predictions of two-way member response to blast loading. However, the analysis did yield approximate and consistently over-predicted results. In this regard, these predictions are considered to be conservative and would be acceptable for design purposes.

One factor which contributed to the general trend of over-predicting displacements was the assumption that the contribution of concrete in tension to be negligible. However, this simplification likely only had an impact on small displacement predictions as the contribution of concrete tensile strength would only have significantly affected the initial pre-cracking stiffness of the members.

5.5.2 Prediction of time-to-maximum displacements by SDOF methods

SDOF time-to-maximum displacement ratios, defined as the ratio between the time-to-maximum displacement predicted by the SDOF method and the corresponding experimental time-to-maximum displacement, t_{SDOF}/t_{exp}, are tabulated in Table 5.2. Experimental and predicted SDOF time-to-maximum displacements for all tests are plotted in Figure 5.22. The average time-to-max ratio for all *57* compared tests was *1.061*, with a corresponding standard deviation of *0.177* and coefficient of variation of *16.7%*.

The time-to-max ratios predicted for the *31* tests on one-way wall panels (CS1, CS2 and CS3) have a mean of *1.124* with a corresponding standard deviation of *0.223* and coefficient of variation of *19.9%*. The analysis by the Biggs method for the two-way slab plates (CS4 and CS5) achieved a similar level of consistently, with a mean time-to-max ratio of *0.986*,

standard deviation of *0.167* and coefficient of variation of *16.9%,* based on *26* tests. However, it is difficult to directly compare the two methods, as the tests performed on the two-way specimens were well within the elastic range, whereas the analysis of one-way specimens included many large, inelastic displacement tests. Regardless, prediction of time-to-maximum displacement is thought to be less critical than prediction of maximum displacement. One reason for this is that blast resistant design is generally concerned with limiting maximum displacements, not the time to maximum displacement. Furthermore, due to the slope of the *DIF* curves for concrete and steel at moderately high strain-rates, over- or under-predicting time-to-maximum response should not have a significant impact on predicted response.

As the time-to-maximum displacement for each shot was computed using the same analytical methods as the maximum displacement, the same inaccuracies associated with predicting maximum displacements apply to predictions of time-to-maximum response.

5.5.3 Prediction of maximum displacement by ESF method

An equivalent static force procedure was used to predict the maximum displacement of the *39* shock tube tests performed on retrofitted specimens that remained elastic. Experimental and predicted ESF maximum displacements for these tests are plotted in Figure 5.23. A comparison of the predictions using an equivalent static force and numerical integration of the equation of motion is shown in Table 5.3. As expected, the predictions using an equivalent static force are consistent with the maximum displacements predicted by explicitly solution of the equation of motion using the complete force-deformation characteristics and actual pressure-time history.

The mean displacement ratio for predictions using explicit solution of the equation of motion was *1.210* with a corresponding standard of deviation of *0.340* and coefficient of variation of *28.1%.* The mean displacement ratio for predictions using the equivalent static force method was *1.312*, with a corresponding standard of deviation of *0.300* and coefficient of variation of *22.9%.* The numerical integration of the equation of motion and the analysis using an equivalent static force both consistently over-predict predicted maximum displacements. As the dynamic load factor for a perfectly elastic oscillator subjected to a linearly decreasing

load-time function is calculated based on the closed-form solution to the equation of motion, either analysis technique should yield the same response – provided the response remains elastic. In this case, the ESF method slightly over-predicts maximum displacement relative to the numerical integration of the equation of motion. This results from the idealized load-time function and member stiffness used in the derivation of the dynamic load factor.

It is important to point out that although the equivalent static force method does predict slightly higher displacements than those predicted by the solution of the equation of motion, the effort required to perform the ESF analysis is much less than that required to solve the equation of motion. This makes the use an equivalent static force particularly useful for design purposes or for preliminary analyses.

5.5.4 Prediction of time-to-maximum displacements by ESF method

An equivalent static force procedure was used to predict the time-to-maximum displacements of the *39* shock tube tests performed on retrofitted specimens that remained elastic. Experimental and predicted ESF time-to-maximum displacements for these tests are plotted in Figure 5.24. A comparison of the predictions using an equivalent static force and numerical integration of the equation of motion is shown in Table 5.3. As expected, the equivalent static force predictions are consistent with those predicted by explicit solution of the equation of motion using the complete force-deformation characteristics and actual pressure-time history. The mean time-to-max displacement ratio for predictions using explicit solution of the equation of motion was *1.044* with a corresponding standard of deviation of *0.192* and coefficient of variation of *18.4%*. The mean time-to-maximum displacement ratio for predictions using the equivalent static force method was *0.989*, with a corresponding standard of deviation of *0.170* and coefficient of variation of *17.2%*. Both SDOF methods yield results which consistently over-predict time-to-maximum displacements. However, these predictions are in agreement with experimental data.

5.5.5 Prediction of displaced shapes

The force-deformation characteristics of the one-way specimens of CS1, CS2 and CS3 were explicitly determined at various displacement levels throughout response. In this way, the

transition from elastic to plastic behaviour was described in detail by the analytical resistance-curves, predicted displaced shapes and theoretical load-mass transformation factors.

The predicted displaced shapes included the combined effects of elastic and inelastic member deformations caused by shock wave loading. The displaced shapes predicted by the analysis were compared against the experimental displaced shapes at four mid-span displacement levels for each test. The comparison was performed by computing the displaced shape corresponding to the theoretical mid-span displacement which matched the mid-span experimental displacement at each displacement comparison level. The experimental and predicted displacements of LVDT2 (located *450 mm* away from mid-span) and LVDT3 (located *900 mm* away from mid-span) were compared directly. A total of *112* displacement levels were compared, ranging from small elastic displacements to large, destructive tests.

The mean displacement ratio for LVDT2 was *1.071* with a corresponding standard deviation of *0.197* and coefficient of variation of *18.4%* for *112* samples. The mean displacement ratio for LVDT3 was *1.000* with a standard deviation of *0.166* and coefficient of variation of *16.5%* for *112* samples. A detailed summary of displaced shape predictions for LVDT2 and LVDT3, grouped by mid-span displacement level and retrofit, is shown in Table 5.4. The predicted displaced shapes are in good agreement with the experimental displaced shapes for as-built and retrofitted specimens, at all displacement levels. Therefore, the load-mass factors computed using the predicted displaced shapes are consistent with actual behaviour. As a simplification, it is generally assumed that the displaced shape – and hence load-mass factors – transitions from elastic to perfect plastic once member yield has been achieved (Biggs, 1964). The predicted load-mass factors in the elastic range, *0.788*, are in agreement with the load-mass factor computed based on the closed-form solution to equations [2.13] and [2.14] using the elastic displaced shape of a simply supported flexure member under distributed loading, *0.787*. However, the load-mass factor for the specimens at large displacement failure levels was approximately *0.7*, as opposed to *0.66* for the typically assumed rigid-body displaced shape. This indicates that the elastic deformation component, even at large, inelastic displacements, has a significant impact on the equivalent SDOF transformation factors. Ignoring the elastic contribution in displaced shape during response would result in less accurate results, as decreasing the load-mass factor during SDOF analysis results in decreased

maximum displacements and corresponding time-to-maximum. It is important to note that these load-mass factors have only been validated against experimental data up to maximum displacement: the effect of post-peak behaviour and rebound displacements on the single degree of freedom transformation factors may or may not include a significant elastic component.

5.5.6 Pressure-Impulse Diagrams

Iso-damage contour plots (i.e. pressure-impulse diagrams) were generated for each experimental maximum displacement for each specimen. These PI diagrams are shown in Appendix C from Figure C-1 to Figure C-13. Qualitatively, the level of accuracy of the predicted PI curves is comparable to the accuracy of the other analytical results. This is because all the analytical techniques employed in this thesis require the solution of the single degree of freedom equation of motion.

5.5.7 Experimental Sources of Error

Thus far, the discussion on discrepancies between experimental and predicted results has been primarily limited to the assumptions and idealizations associated with the various analytical methods. However, it is important to note that the experimental observations are subject to their own set of inaccuracies. The method used to attach the displacement gauges to the specimens resulted in a slight amount of lateral movement that may not have been registered by the LVDTs. The location of the critical section (i.e. location of maximum displacement) may not have corresponded exactly with the location of the mid-span LVDT. The calibration and resolution of the displacement gauges are also a source of inaccuracy. Settling of the supports and movement of the specimens within the supports certainly contributed to uncertainty in the experimental displacement readings. However, the contribution of these sources on the experimental results diminishes as the relative displacement of the specimens increases.

There is also some uncertainty associated with how the load transfer device interacted with the one-way specimens of CS1 and CS2 during the negative pressure phase; the assumption that no negative pressures act on the system may not be entirely appropriate. Two coupled SDOF equations could more accurately describe the interaction between the load transfer

device and the one-way specimens. There was also a slight gap between the load transfer device and the specimens, which may have contributed to uncertainty in the time-to-maximum response.

The use of smooth reinforcing bars introduced uncertainty into the analysis, particularly when predicting large displacement shots. Bar slip, caused by opening of the 180-degree hooks, was observed during testing of the one-way wall strips. The presence of bar slippage caused inelastic deformations which were not accounted for in the flexural analysis, thereby affecting the load-deformation characteristics. Furthermore, the equation used to compute plastic hinge length (Eq. [5.2]) incorporated into the member analysis was derived based on tests using deformed reinforcing steel.

The material properties used also introduce some uncertainty into the analysis and interpretation of results. Although an average of the compressive strengths f_c' of a number of tests on standard sized cylinders was used, large scatter was observed. Additionally, the use of Hognestad's model to describe the stress-strain characteristics of concrete may not have been the most appropriate choice given the relatively high strength concrete mix that was used. Furthermore, the composite properties for the MBRACE CF-130 CFRP and Fyfe Co. retrofit systems used in the analysis are based on the manufacturer's specifications. While the material properties used for all specimens retrofitted with the Fyfe Co. product (companion sets 1 and 2) yield excellent predictions of experimental behaviour, the behaviour of specimens retrofitted with the MBRACE product (retrofitted companion set 3, 4 and 5) are consistently over-predicted member response. It is possible that the actual composite properties of the MBRACE material differed significantly from specified values.

It is also important to acknowledge the uncertainties introduced by small construction defects on the strength and stiffness characteristics of the specimens; small errors in reinforcing steel placement, or the presence of voids could have a large impact on the actual physical properties of the system.

5.6. Summary of Analytical Results

The prediction of retrofitted and as-built reinforced concrete wall and slab behaviour subjected to shock wave loading using the single degree of freedom methods are in general agreement with experimental results. The degree of compatibility between predicted and experimental results is in direct proportion to the level of refinement associated with the derivation of the force-deformation characteristics used in the dynamic analysis. Accordingly, the detailed force-deformation characteristics generated for one-way wall panels of CS1, CS2 and CS3 generally predicted results which are in excellent agreement with experimental data. The idealized force-deformation characteristics used to analyze two-way slab plates of CS4 and CS5 yield results which consistently over-predict member response, but still adequately describe global member behaviour. Furthermore, the predicted behaviour using both analytical methods also describe the increase in strength and stiffness resulting from externally bonded CFRP retrofits observed during experimental testing.

Table 5.1: Reflected Shock Wave Properties, Maximum Displacement and Time-to-Maximum Displacement for Experimental Results and SDOF and ESF Predictions.

Name	Shock Wave Properties			Experimental		SDOF		ESF	
	P_r	t_d	I_r	δ_{exp}	t_{exp}	δ_{SDOF}	t_{SDOF}	δ_{ESF}	$t_{max,ESF}$
	kPa	ms	kPa-ms	mm	ms	mm	ms	mm	ms
CS1-C -1	12.5	13	95.7	26.1	65.5	30.3	65.4	-	-
CS1-C -2	42.6	16.3	301.6	167.8	89.8	137.3	87.1	-	-
CS1-R1 -1	12.9	12.7	83.6	11.6	26.1	11.2	30.7	11.5	30.8
CS1-R1 -2	46.4	16.3	300	146.9	85	140.1	89.4	-	-
CS1-R2 -1	11.1	14	89.3	8.1	23.8	9.36	30.2	11.6	31.4
CS1-R2 -2	44.8	16.1	331.2	42.5	29.7	51.7	32.4	59.2	32.2
CS1-R2 -3	49	15.7	336.9	40.4	28.9	62.8	35.8	60.6	31.9
CS1-R2 -4	64.7	15.7	444.3	62.6	30.7	75.9	37.5	82.6	31.1
CS1-R2 -5	72.9	16.6	510.9	84.6	34.1	94.3	39.3	-	-
CS1-R2 -6	79.6	17.7	595.1	224.6	118.5	No maximum predicted		No maximum predicted	
CS1-A -1	13.3	13.2	99.9	9.4	24.3	13	31.8	12.9	31.1
CS1-A -2	51.3	16.5	335.3	42.3	30	53.4	34.8	67.6	32.2
CS1-A -3	67.4	16.1	460.6	68.4	33.6	83.2	37.6	91.0	33.2
CS1-A -4	70.9	17.1	511.8	83.6	36	82.4	33.8	102.2	33.6
CS1-A -5	74.7	15.8	511.7	85.5	36.3	88	34.5	100.8	33.2
CS1-A -6	82.6	17.5	603.0	132.8	74.2	No maximum predicted		No maximum predicted	

Table 5.1: Reflected Shock Wave Properties, Maximum Displacement and Time-to-Maximum Displacement for Experimental Results and SDOF and ESF Predictions. (continued)

Name	Shock Wave Properties			Experimental		SDOF		ESF	
	P_r	t_d	I_r	δ_{exp}	t_{exp}	δ_{SDOF}	t_{SDOF}	δ_{ESF}	$t_{max,ESF}$
	kPa	ms	kPa-ms	mm	ms	mm	ms	mm	ms
CS2-C -1	17.7	13.8	143	16.3	31.5	16	32.8	-	-
CS2-C -2	57.8	17.4	383	148.9	80.7	105.7	69.1	-	-
CS2-R -1	17.1	13.6	128.3	7	18.5	5.7	21.4	10.4	23.4
CS2-R -2	59	17.7	371.3	31.4	24.7	34.2	31.8	43.7	23.9
CS2-R -3	64	18	424.4	42.9	26.8	38.6	24.6	47.4	23.9
CS2-R -4	106.7	18.7	738.1	Specimen Destroyed		No maximum predicted		-	-
CS2-A -1	16	13.7	126.2	6.1	19.8	10	23	8.9	22.4
CS2-A -2	51.3	15.1	329.9	29.1	24.9	30.2	23.7	34.7	22.9
CS2-A -3	60.1	16.2	422.8	38.7	26.4	37.9	24.4	44.5	23.9
CS2-A -4	69	18.1	493.8	45.9	26.5	44.7	25.2	51.1	23.9
CS2-A -5	91.2	19.8	670.8	122	82.2	191.9	104	-	-
CS3-C -1	15.4	13.8	123.3	6.9	23.9	8.9	29.8	-	-
CS3-C -2	28.2	14.7	204.2	16.3	30.2	18.6	31.9	-	-
CS3-C -3	100.6	19.5	811.2	197.5	63.7	217.8	69.5	-	-
CS3-R -1	16.5	14.5	131.3	6	19.3	7.3	23.6	8.8	24.0
CS3-R -2	27	15.2	193.9	9.2	19.7	13.7	24.4	15.1	24.2
CS3-R -3	93	21.2	783.2	44.8	26.4	58.1	27.9	59.4	25.5
CS3-R -4	99.3	48.9	2535	155.8	61.7	280	87.1	-	-

Table 5.1: Reflected Shock Wave Properties, Maximum Displacement and Time-to-Maximum Displacement for Experimental Results and SDOF and ESF Predictions. (continued)

Name	Shock Wave Properties			Experimental		SDOF		ESF	
	P_r kPa	t_d ms	I_r kPa-ms	δ_{exp} mm	t_{exp} ms	δ_{SDOF} mm	t_{SDOF} ms	δ_{ESF} mm	$t_{max,ESF}$ ms
CS4-R1 -1	16.6	14.4	125.9	3.6	14.4	5.5	15.3	5.3	14.8
CS4-R1 -2	29	15.3	214.1	6.6	14.8	9.31	15.4	9.3	14.8
CS4-R1 -3	43	16.2	315.1	10	15.2	13.6	15.4	13.8	14.8
CS4-R1 -4	65.2	22	511.5	16.1	15.4	21.4	15.6	29.3	17.0
CS4-R1 -5	91.4	27.7	825.3	23.7	16.1	31	16.2	41.0	17.0
CS4-R1 -6	99.7	34.8	1316	33.4	18.7	41	18.3	53.2	18.3
CS4-R1 -7	87.4	61.5	2386.9	35.1	20.4	40.5	19.7	50.9	19.0
CS4-R2 -1	16.5	14.9	136.7	3.5	12.8	4.6	13.5	4.1	12.8
CS4-R2 -2	27.5	15.9	223.8	6.1	13.7	7.2	13.4	6.9	12.8
CS4-R2 -3	42.4	16.7	346.9	10.3	15	11.1	13.4	10.6	12.8
CS4-R2 -4	68	18.1	542.1	17.7	15.6	18.0	13.6	19.4	13.5
CS4-R2 -5	88.4	24.1	862.8	35.9	18.4	25.0	13.6	25.2	13.5
CS4-R2 -6	95.7	28.7	1374.7	57.1	20.5	31.3	15.2	32.4	14.6

Table 5.1: Reflected Shock Wave Properties, Maximum Displacement and Time-to-Maximum Displacement for Experimental Results and SDOF and ESF Predictions. (continued)

Name	Shock Wave Properties			Experimental		SDOF		ESF	
	P_r kPa	t_d ms	I_r kPa-ms	δ_{exp} mm	t_{exp} ms	δ_{SDOF} mm	t_{SDOF} ms	δ_{ESF} mm	$t_{max,ESF}$ ms
CS5-C -1	8.2	5	24.7	0.6	8.6	0.35	7.7	-	-
CS5-C -2	17.2	14	142.7	3.5	15.9	7.7	17.5	-	-
CS5-C -3	26.7	15.4	219.6	6.7	14.2	11.4	18.1	-	-
CS5-C -4	44	16	335.4	12.6	17.2	17	18	-	-
CS5-C -5	60.2	17.3	514	21	18.4	27.5	19.4	-	-
CS5-C -6	100.9	29.5	1396.3	67.8	24.5	76.5	27.7	-	-
CS5-C -7	91.9	63.3	2620.9	79	29.5	89.7	32.5	-	-
CS5-R -1	16.1	14.3	142	1.3	9	2.7	11	2.0	9.1
CS5-R -2	25.3	14.3	193.9	1.8	9	3.7	10.8	3.2	9.1
CS5-R -3	42	16	317.1	3.2	8.9	5.6	10	5.3	9.1
CS5-R -4	62	18.1	493	6	11.6	8.7	10	9.2	9.8
CS5-R -5	97.1	32.8	1365.1	20.3	17.8	15.2	12	15.8	10.2
CS5-R -6	87.5	60.5	2379.1	25.3	18.8	13.8	11.1	16.2	10.8

Table 5.2: Summary of Experimental Response and Response Predicted by SDOF Analysis.

	SDOF Maximum Displacement Ratio, $\frac{\delta_{SDOF}}{\delta_{exp}}$					SDOF Time-to-Maximum Displacement Ratio, $\frac{t_{SDOF}}{t_{exp}}$					Tests
	Mean	**Std Dev**	**COV**	**Min**	**Max**	**Mean**	**Std Dev**	**COV**	**Min**	**Max**	**n**
Global	**1.215**	**0.356**	**29.3%**	**0.545**	**2.200**	**1.061**	**0.177**	**16.7%**	**0.590**	**1.585**	**57**
CS1, CS2 and CS3	**1.163**	**0.254**	**21.8%**	**0.71**	**1.80**	**1.124**	**0.223**	**19.9%**	**0.856**	**1.585**	**31**
As-built	1.020	0.192	18.8%	0.71	1.29	1.039	0.126	12.2%	0.856	1.247	8
Retrofits	1.213	0.257	21.2%	0.81	1.80	1.153	0.258	22.4%	0.814	1.639	23
CS4 and CS5	**1.276**	**0.446**	**34.9%**	**0.55**	**2.20**	**0.986**	**0.167**	**16.9%**	**0.590**	**1.275**	**26**
As-built	1.344	0.505	37.6%	0.58	2.20	1.086	0.113	10.4%	0.895	1.275	7
Retrofits	1.251	0.434	34.7%	0.55	2.08	0.949	0.170	17.9%	0.590	1.222	19

Table 5.3: Comparison of Predicted Response for Elastic Tests on Retrofitted Specimens Predicted using the SDOF and ESF Methods.

Analysis Method	Maximum Displacement Ratio					Time-to-Maximum Displacement Ratio					Tests
	Mean	Std Dev	COV	Min	Max	Mean	Std Dev	COV	Min	Max	n
SDOF	1.210	0.340	28.1%	0.55	2.08	1.044	0.192	18.4%	0.590	1.585	39
ESF	1.312	0.300	22.9%	0.57	1.82	0.989	0.170	17.2%	0.574	1.321	39

Table 5.4: Comparison of Predicted and Experimental Displacement Ratios for LVDT2 and LVDT3.

Mid-span Support Rotation	LVDT2 Displacement Ratio					LVDT3 Displacement Ratio					Tests
	Mean	Std Dev	COV	Min	Max	Mean	Std Dev	COV	Min	Max	n
All specimens	**1.071**	**0.197**	**18.4%**	**0.83**	**2.61**	**1.00**	**0.166**	**16.5%**	**0.70**	**1.52**	**112**
$\theta \leq 2°$	1.080	0.197	18.2%	0.83	2.61	1.001	0.178	17.8%	0.70	1.52	82
$2 < \theta \leq 4°$	1.001	0.072	7.2%	0.88	1.21	0.972	0.110	11.3%	0.78	1.17	17
$\theta > 4°$	1.110	0.129	11.7%	0.90	1.29	1.066	0.142	13.4%	0.93	1.35	13
All As-built	**1.129**	**0.131**	**11.6%**	**0.88**	**1.33**	**1.074**	**0.165**	**15.3%**	**0.84**	**1.44**	**28**
$\theta \leq 2°$	1.129	0.140	12.4%	0.88	1.33	1.119	0.186	16.6%	0.84	1.44	18
$2 < \theta \leq 4°$	1.103	0.094	8.6%	1.04	1.21	0.992	0.069	6.9%	0.88	1.08	3
$\theta > 4°$	1.139	0.136	11.9%	0.98	1.29	0.985	0.049	5.0%	0.93	1.05	7
All Retrofitted	**1.052**	**0.212**	**20.1%**	**0.83**	**2.61**	**0.981**	**0.161**	**16.4%**	**0.70**	**1.52**	**84**
$\theta \leq 2°$	1.066	0.237	22.2%	0.83	2.61	1.119	0.162	14.5%	0.70	1.52	64
$2 < \theta \leq 4°$	0.979	0.046	4.7%	0.88	1.06	0.992	0.154	15.6%	0.78	1.35	14
$\theta > 4°$	1.075	0.124	11.6%	0.90	1.23	0.985	0.161	16.3%	0.96	1.35	6

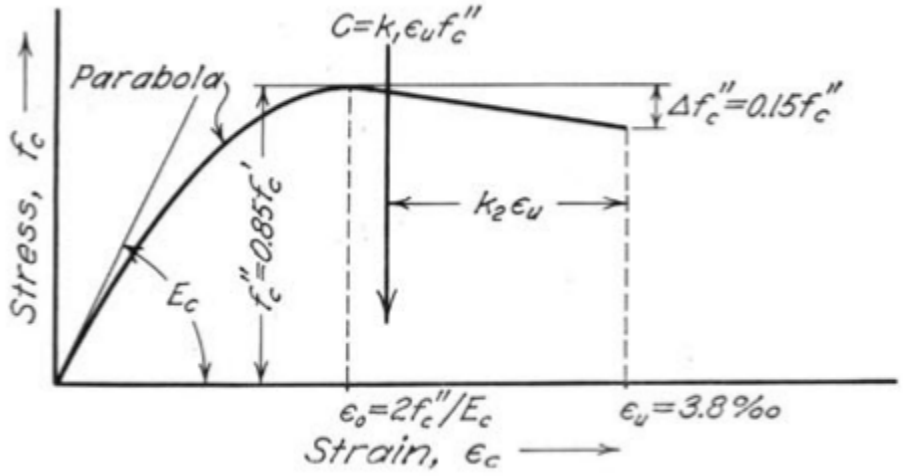

Figure 5.1: Static Stress-Strain Diagram for Concrete in Flexure (reproduced from Hognestad, 1951).

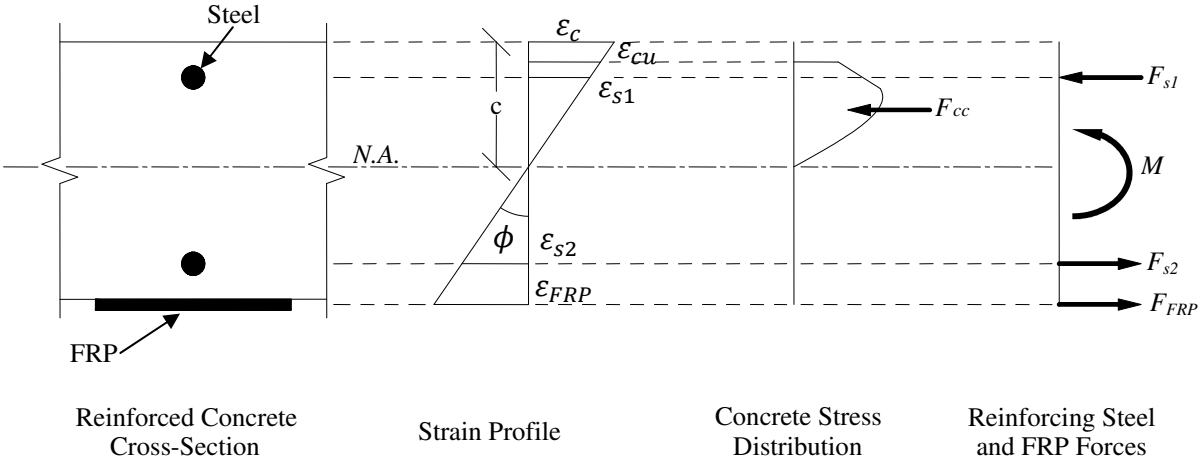

Figure 5.2: Sectional Analysis of One-way Members.

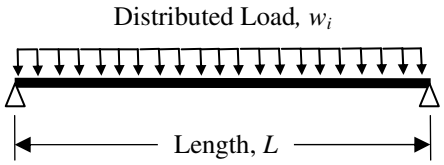

(a) Simply-supported beam under distributed loading

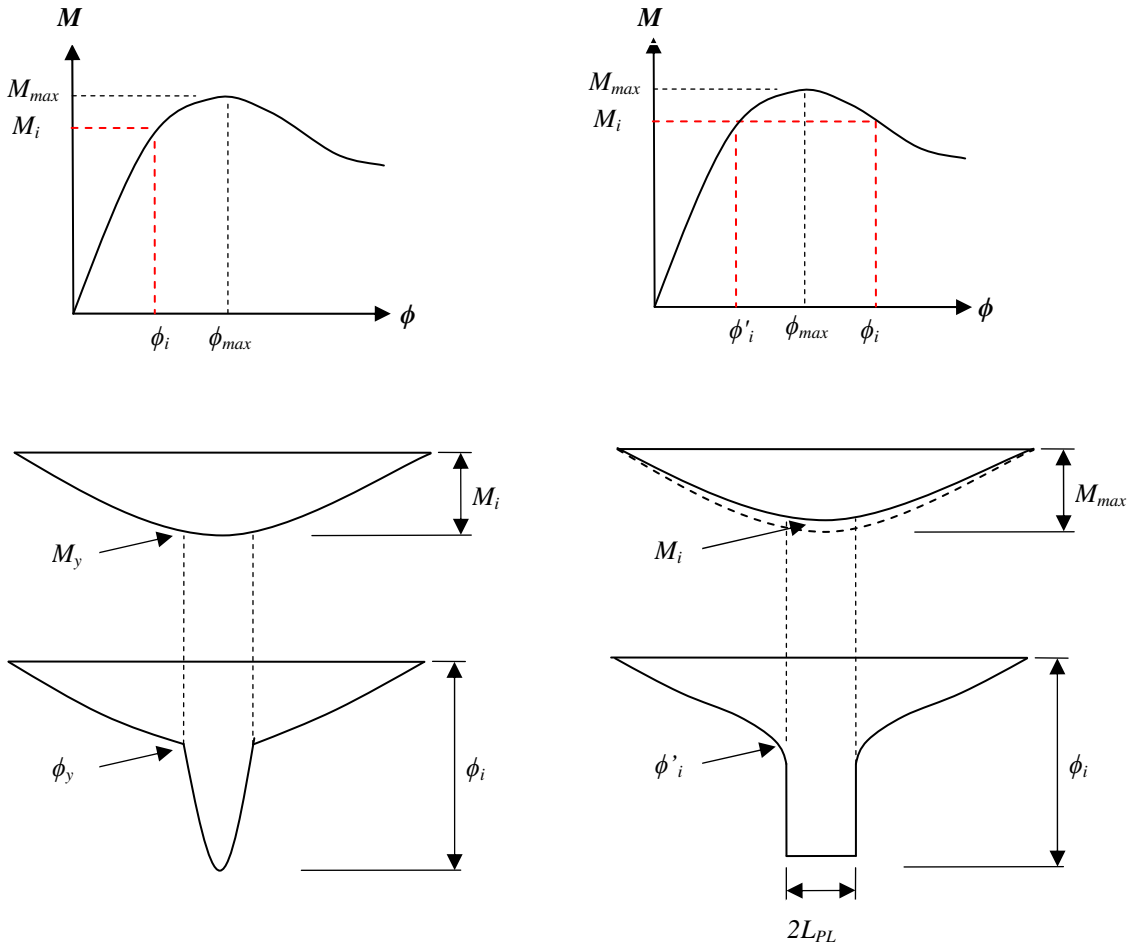

(b) Curvature definition in the loading phase

($M_i<M_{max}$; $\phi_i<\phi_{max}$)

(c) Curvature definition in the unloading phase

($M_i<M_{max}$; $\phi_i>\phi_{max}$)

Figure 5.3: Formation and Progression of Plastic Hinging.

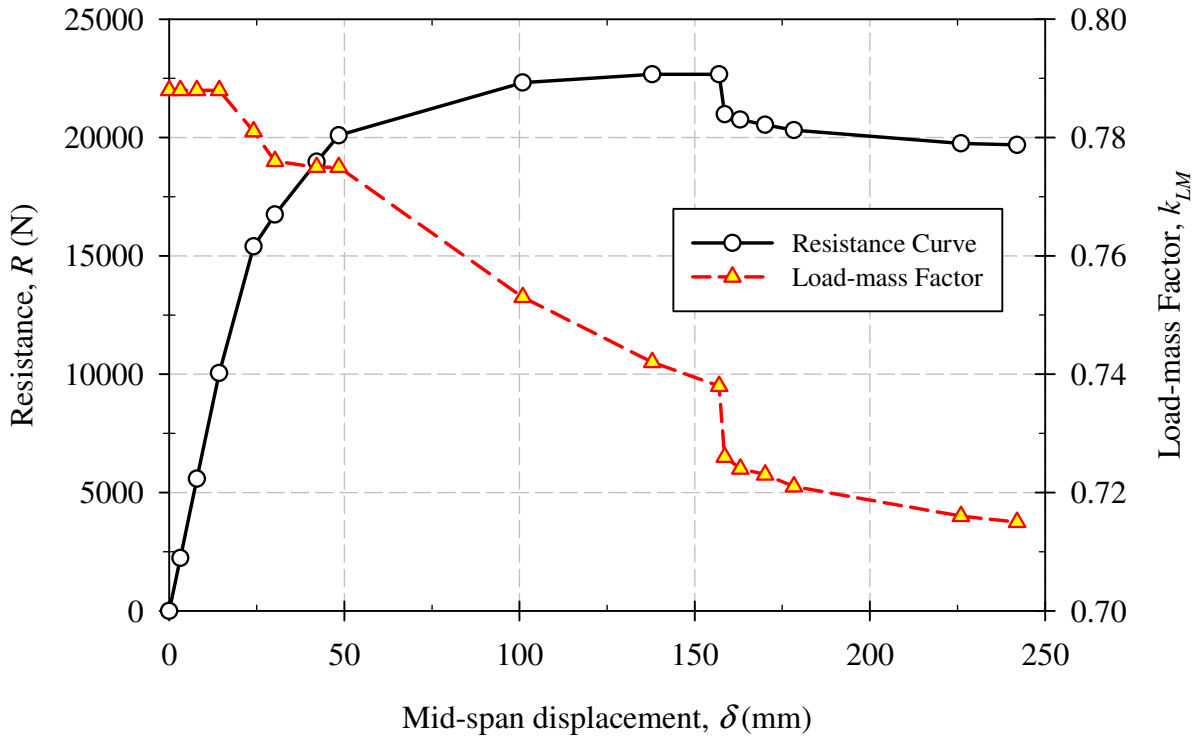

Figure 5.4: Resistance Curve and Load-mass Factors for Specimen CS1-C and CS1-R1 - Shot 2.

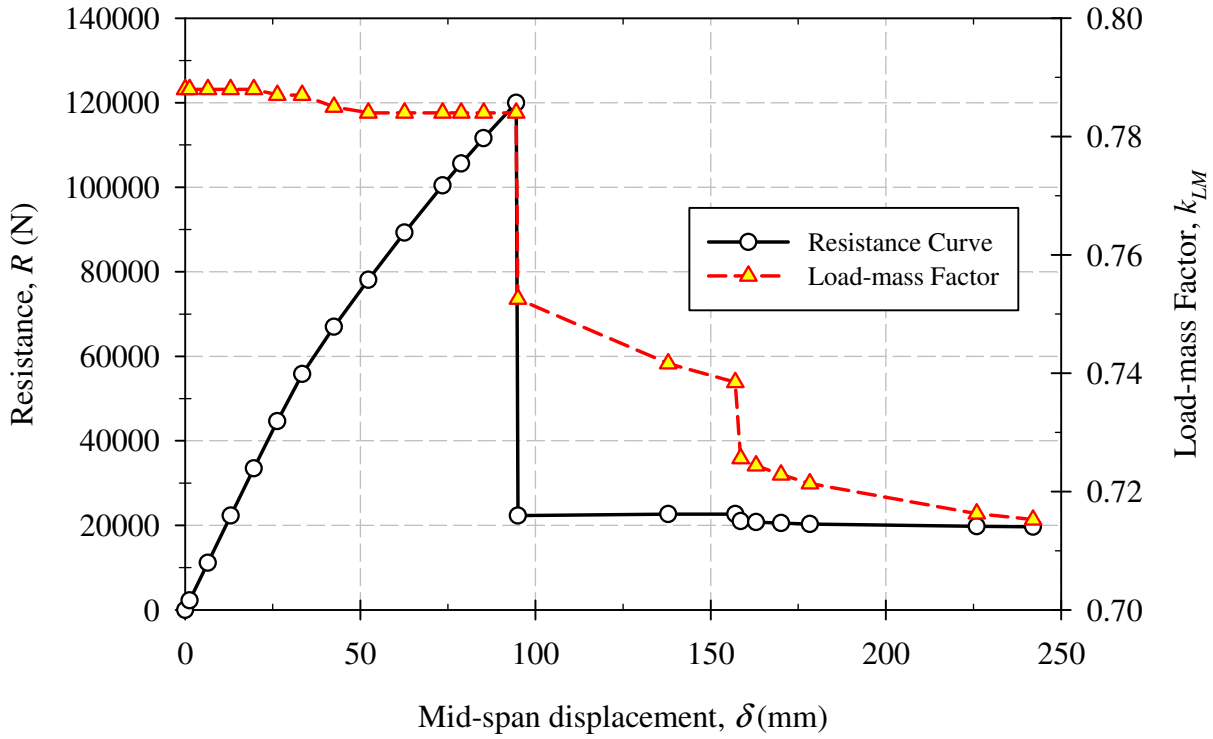

Figure 5.5: Resistance Curve and Load-mass Factors for Specimen CS1-R1 – Shot 1 and CS1-R2.

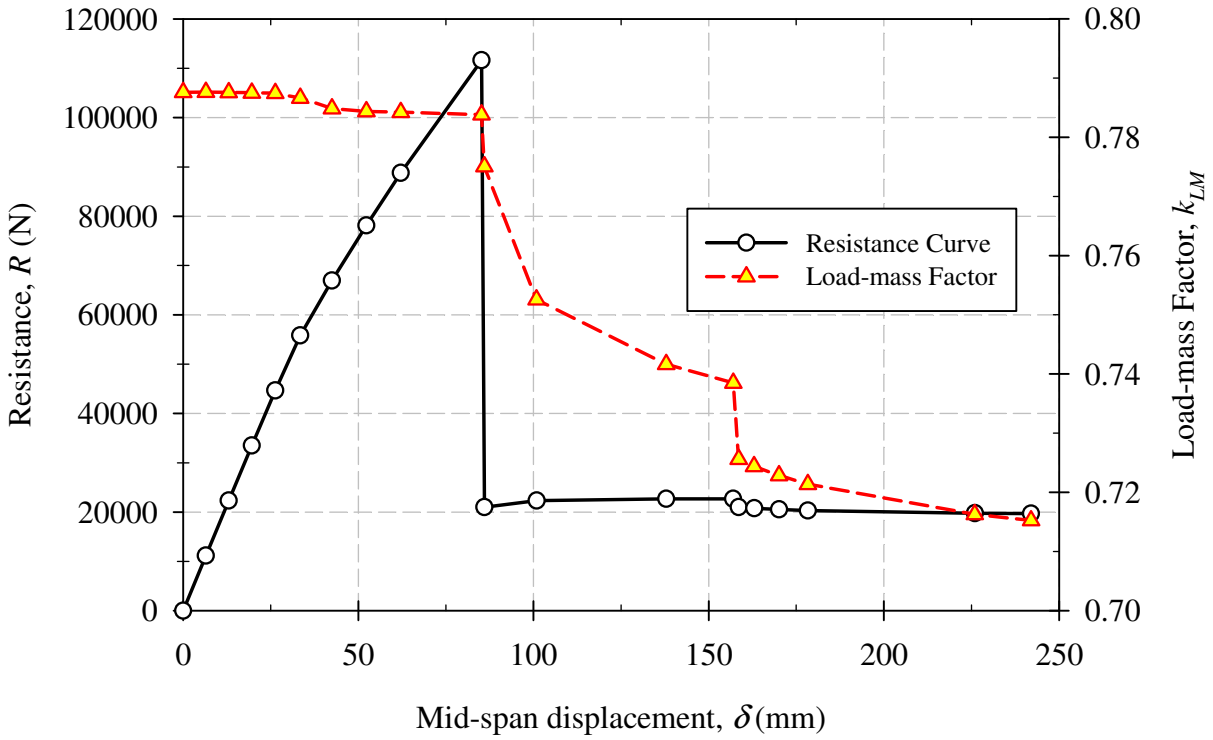

Figure 5.6: Resistance Curve and Load-mass Factors for Specimen CS1-A.

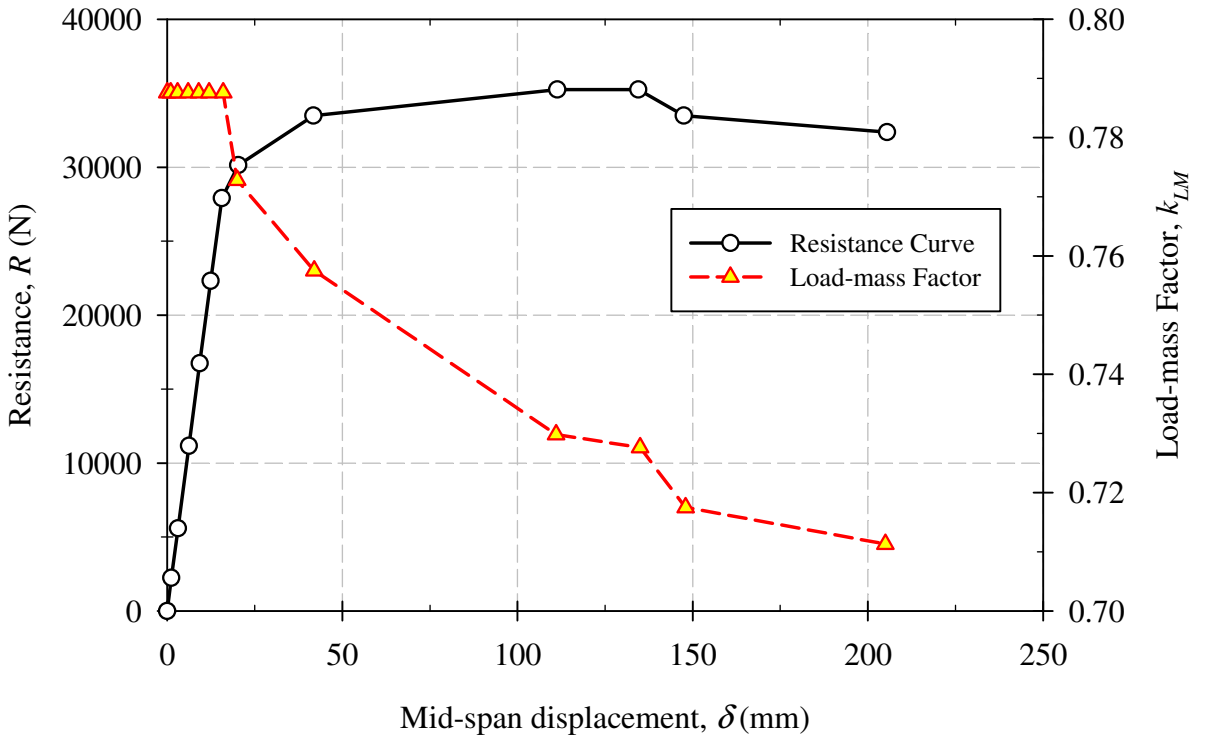

Figure 5.7: Resistance Curve and Load-mass Factors for Specimen CS2-C.

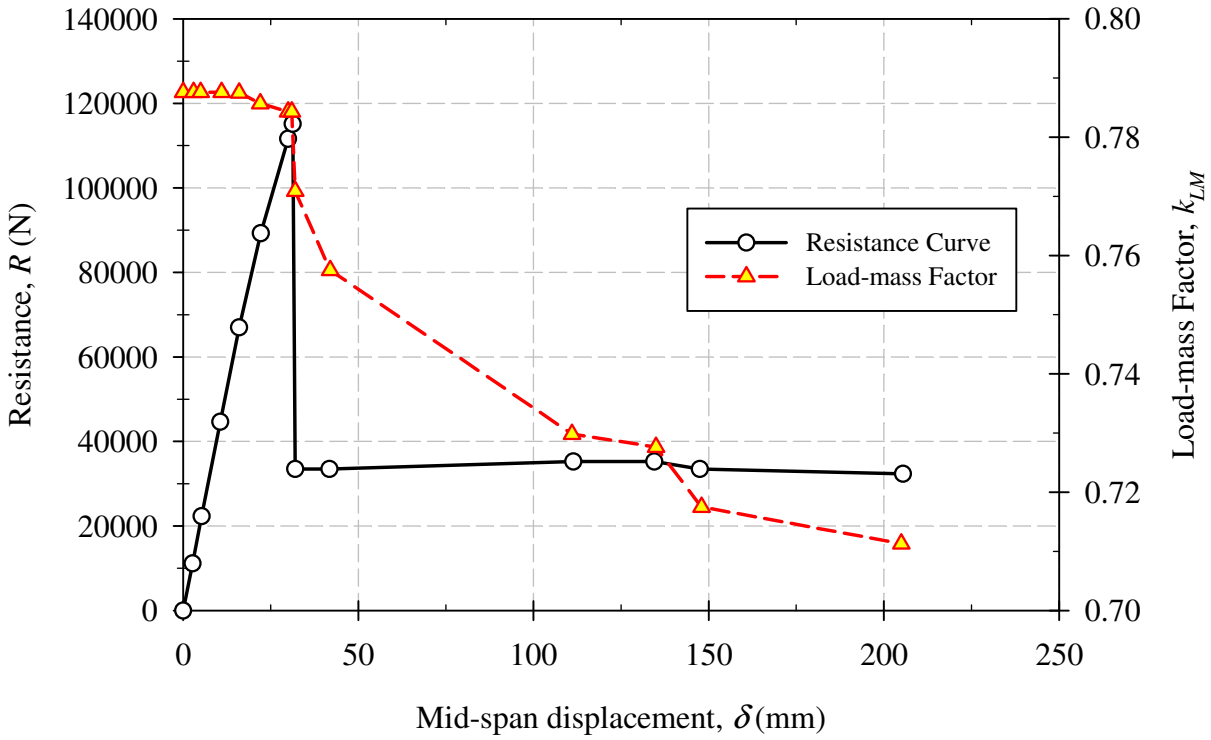

Figure 5.8: Resistance Curve and Load-mass Factors for Specimen CS2-R.

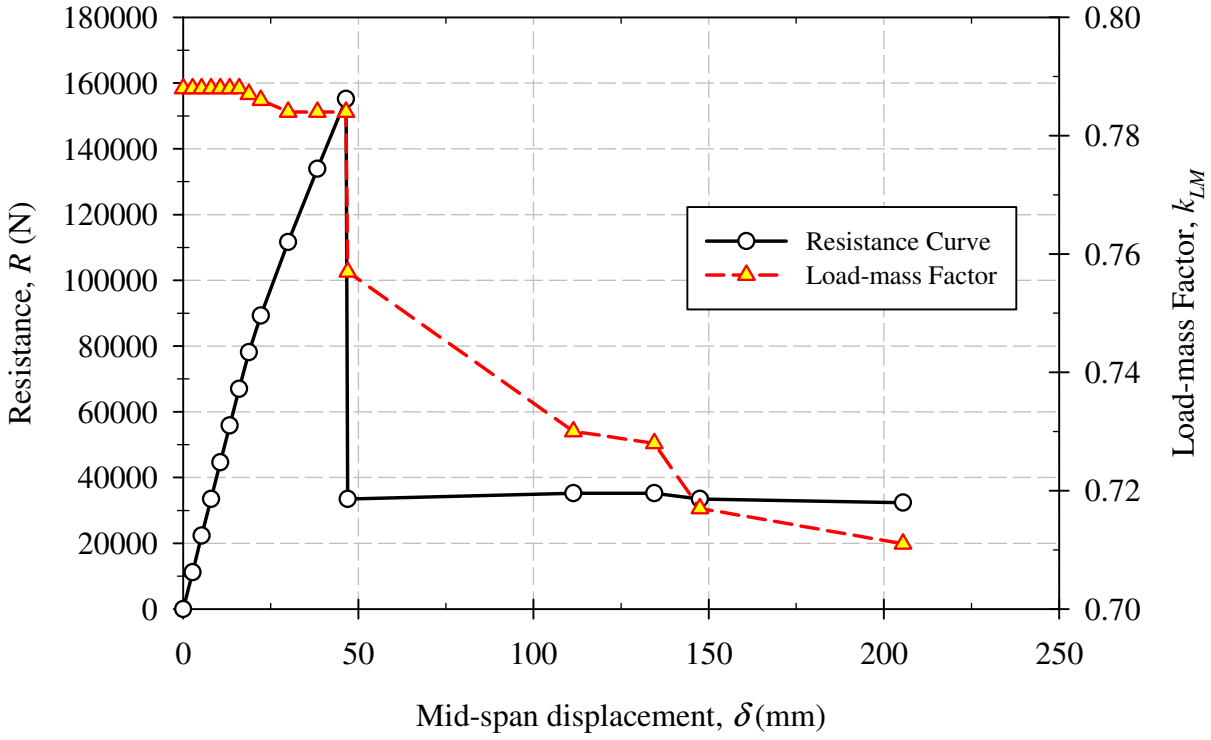

Figure 5.9: Resistance Curve and Load-mass Factors for Specimen CS2-A.

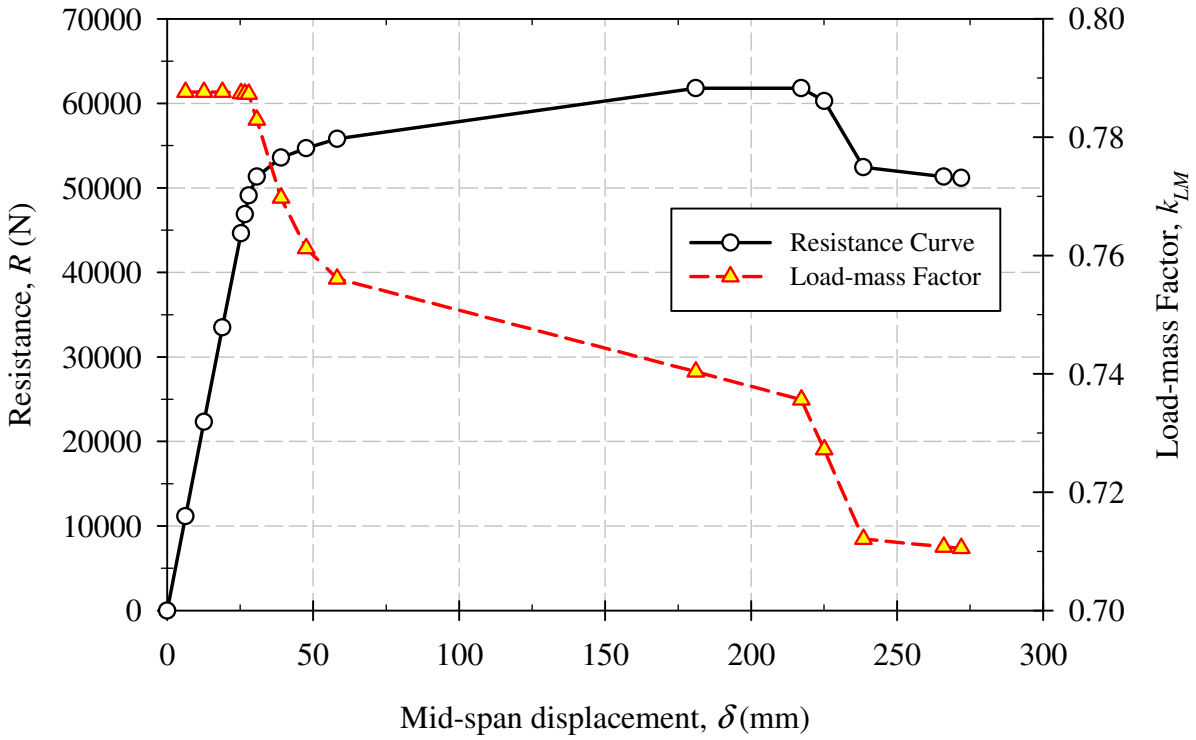

Figure 5.10: Resistance Curve and Load-mass Factors for Specimen CS3-C.

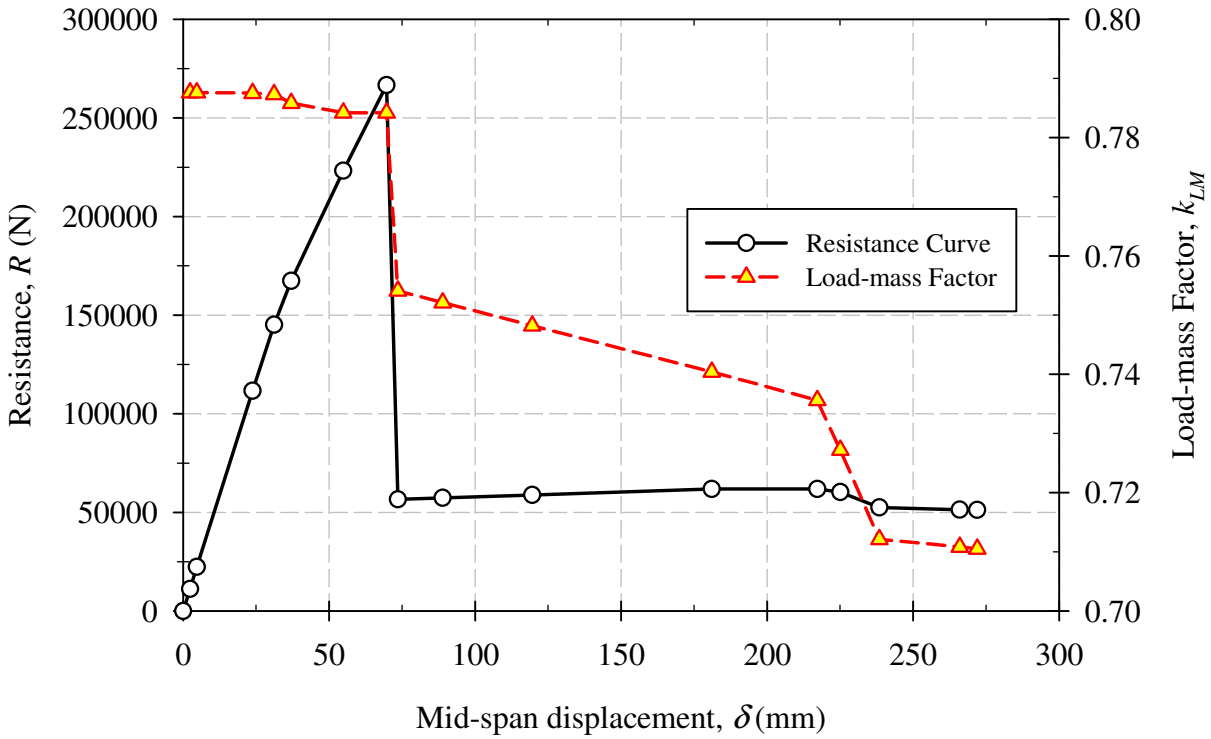

Figure 5.11: Resistance Curve and Load-mass Factors for Specimen CS3-R.

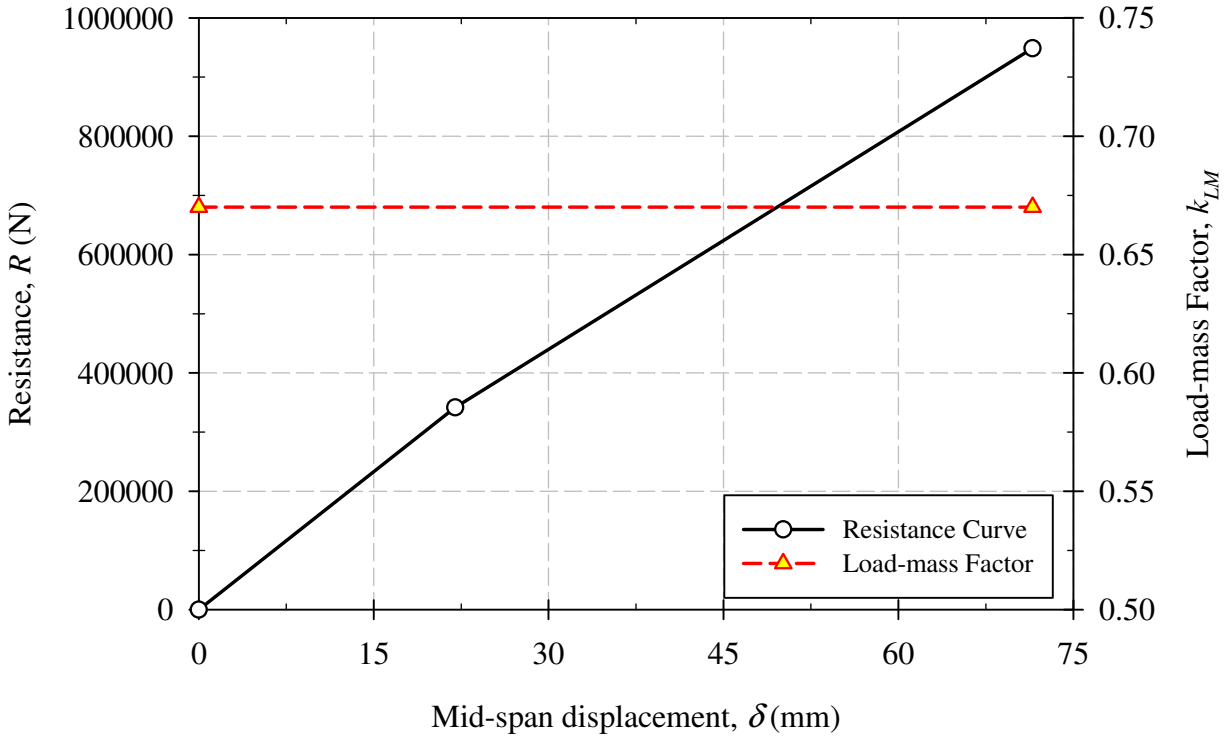

Figure 5.12: Resistance Curve and Load-mass Factors for Specimen CS4-R1.

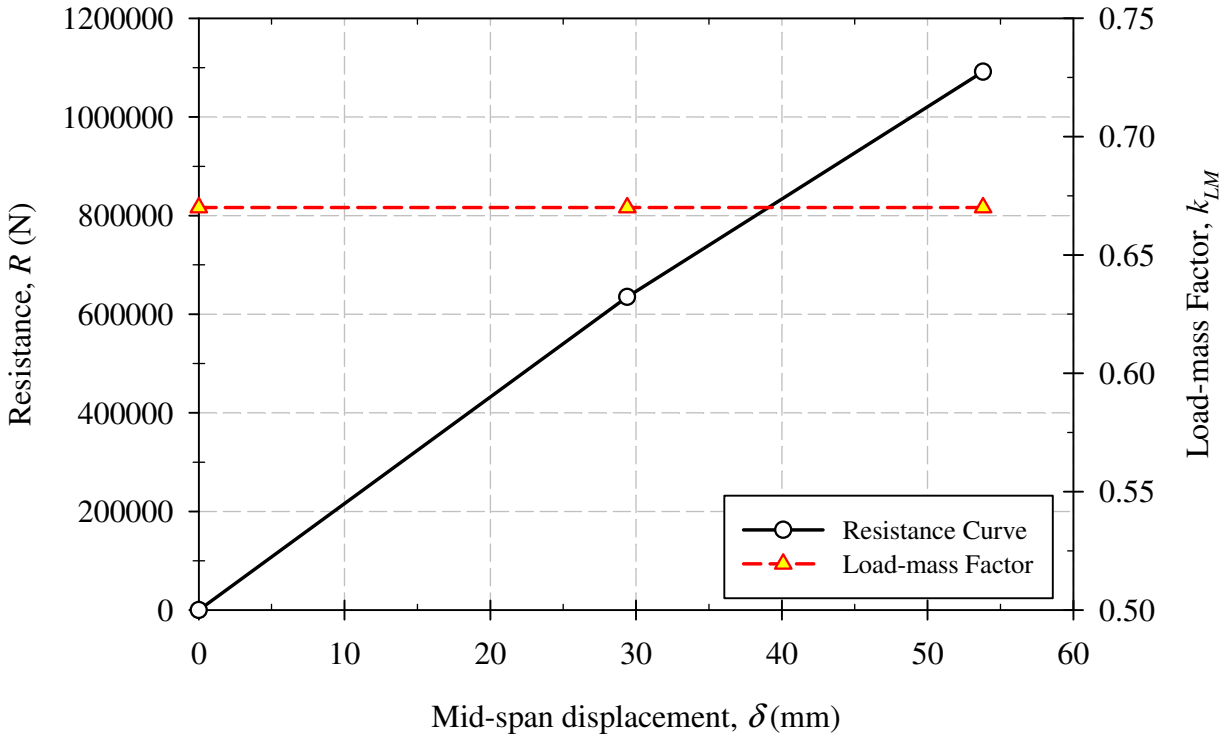

Figure 5.13: Resistance Curve and Load-mass Factors for Specimen CS4-R2.

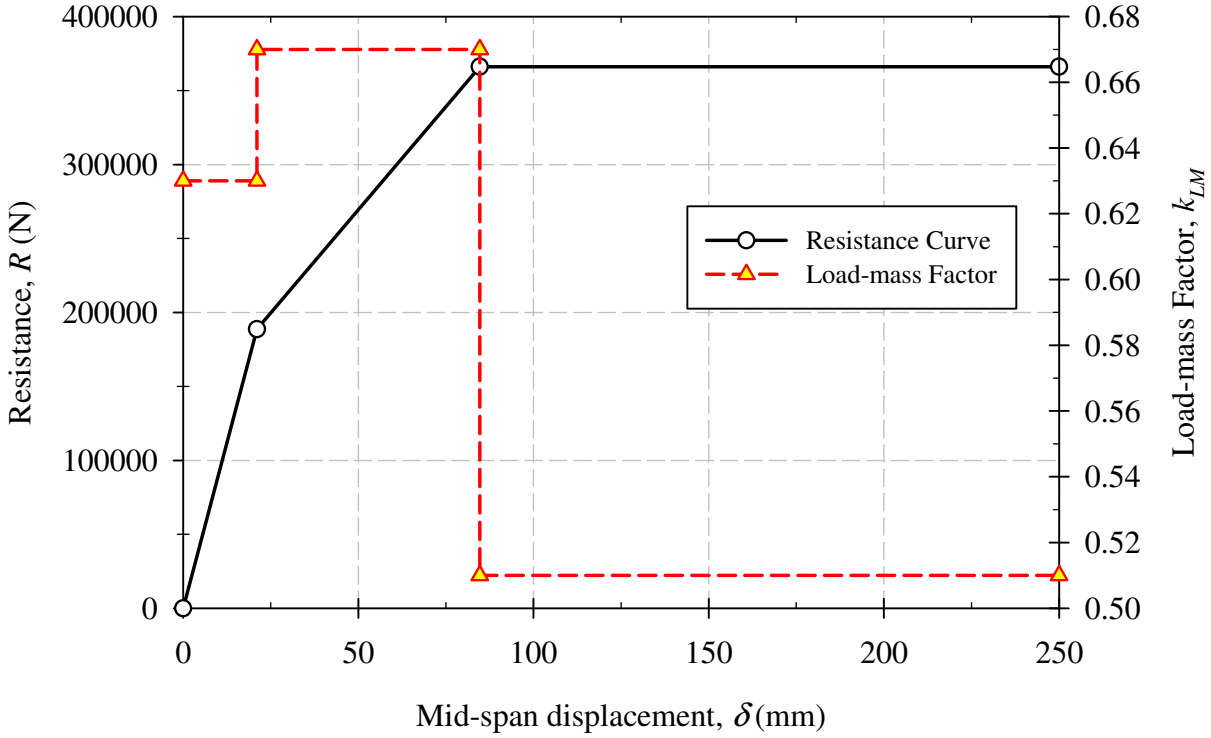

Figure 5.14: Resistance Curve and Load-mass Factors for Specimen CS5-C.

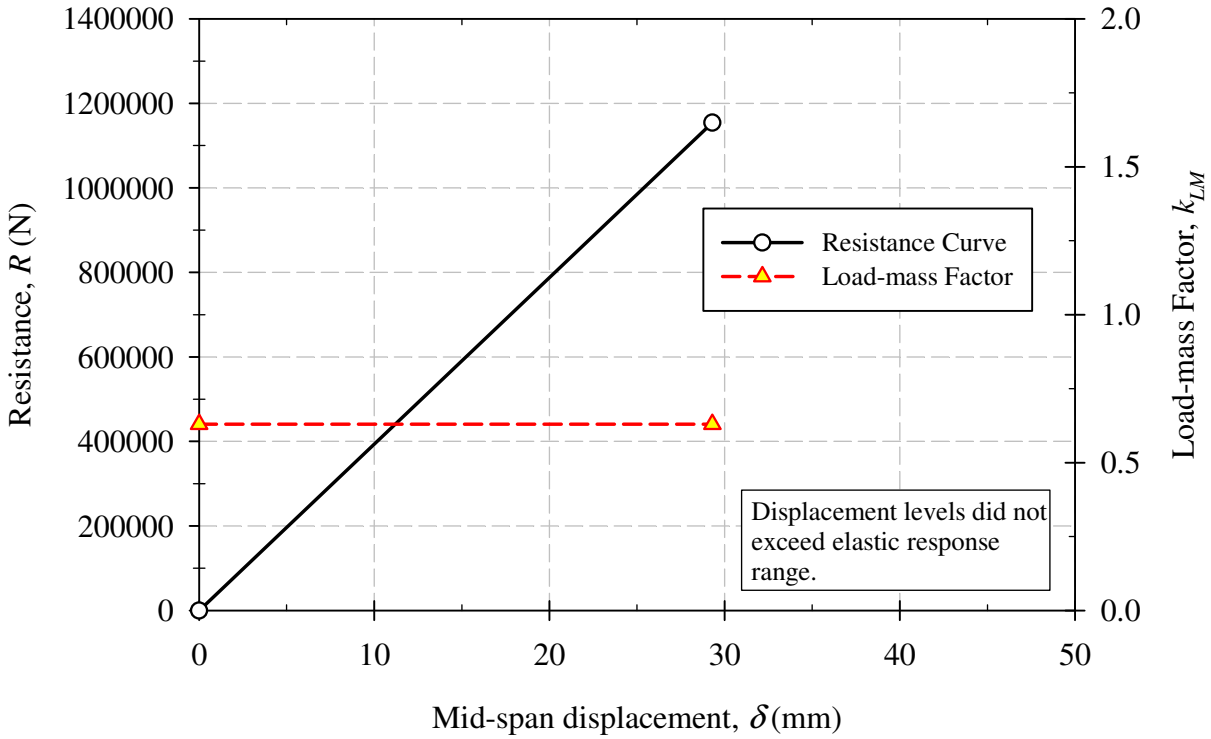

Figure 5.15: Resistance Curve and Load-mass Factors for Specimen CS5-R.

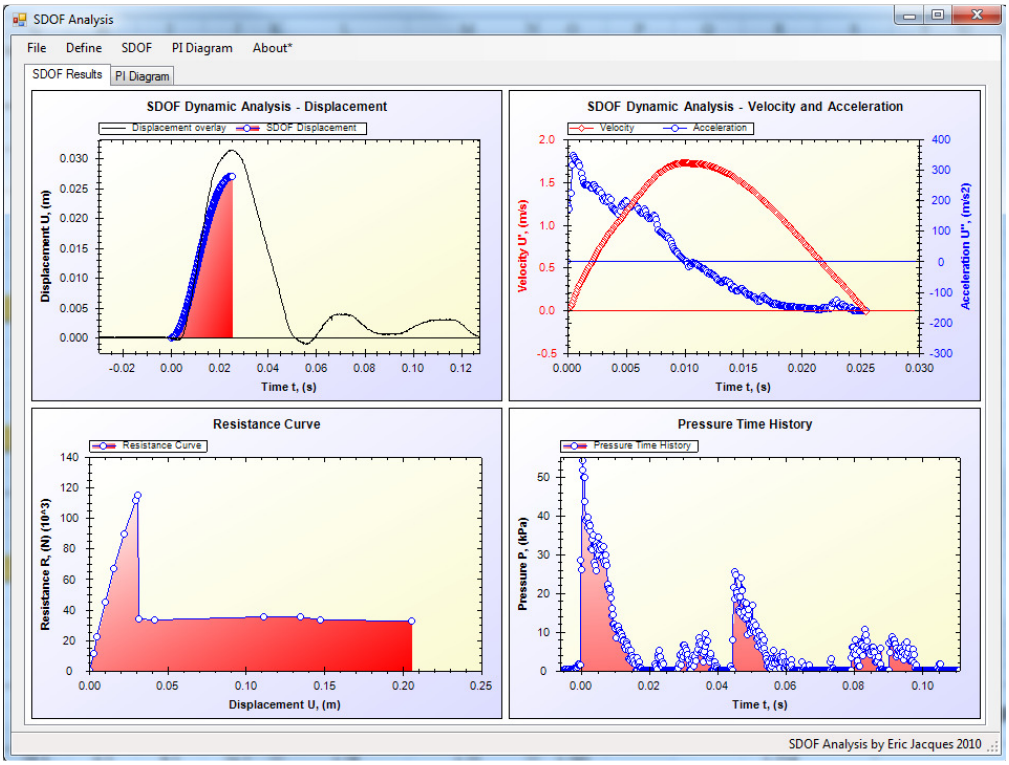

Figure 5.16: Screenshot of SDOF Analysis Program in Displacement Time-History Mode.

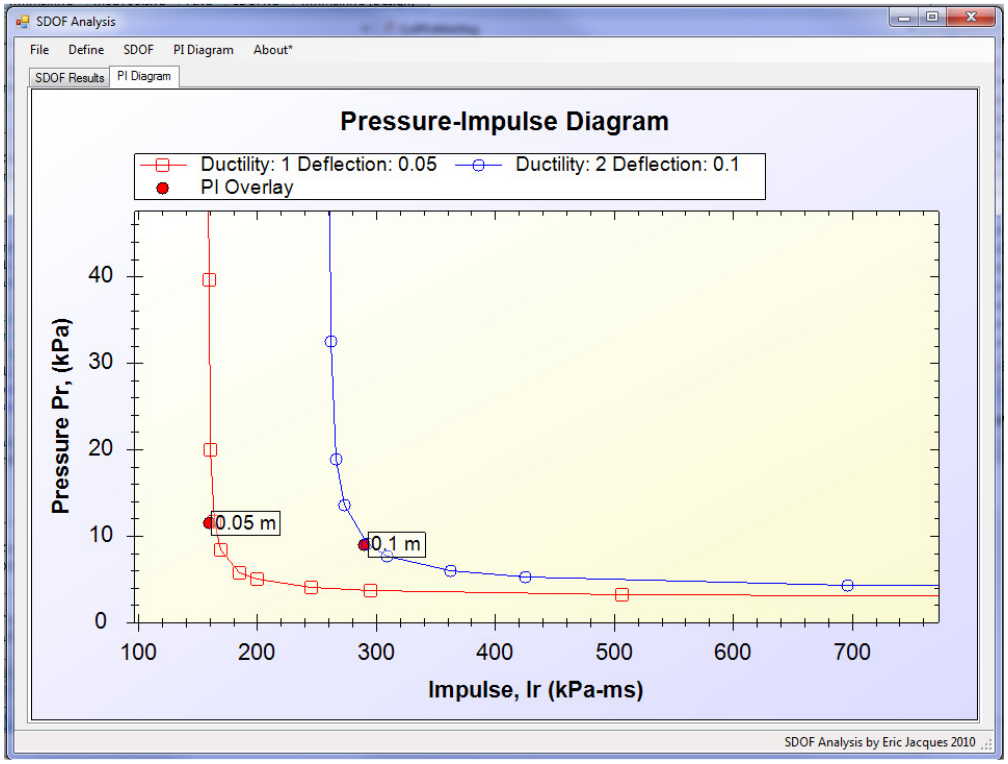

Figure 5.17: Screenshot of SDOF Analysis Program in PI Diagram Mode.

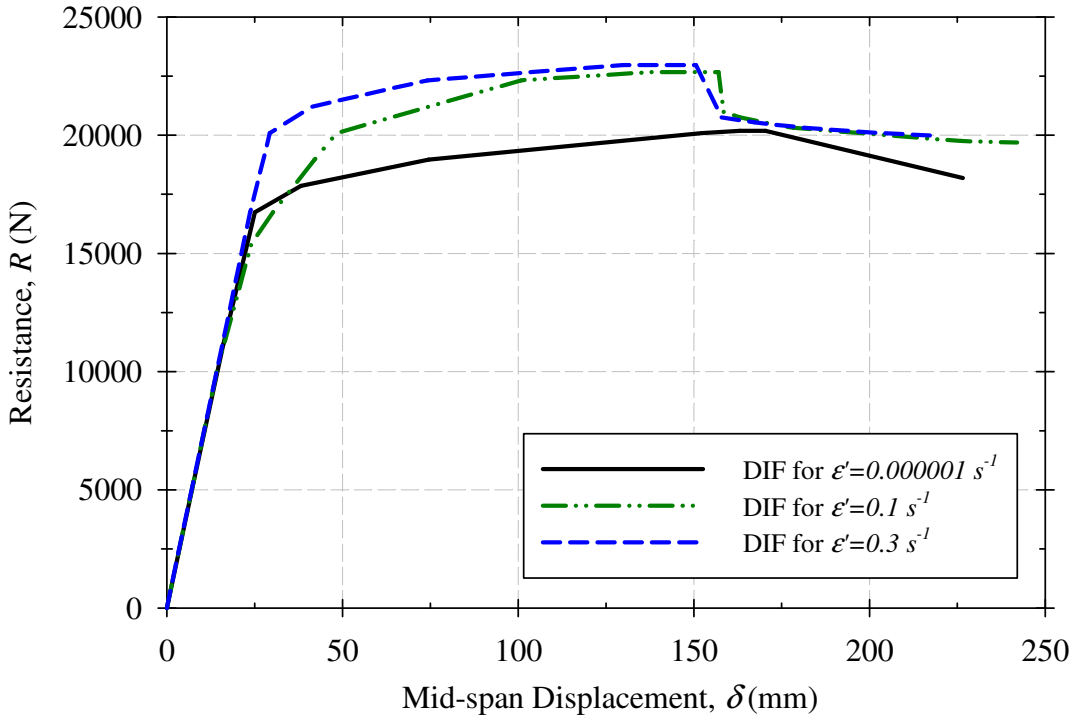

Figure 5.18: Sample Strain-rate Dependent Resistance Curves.

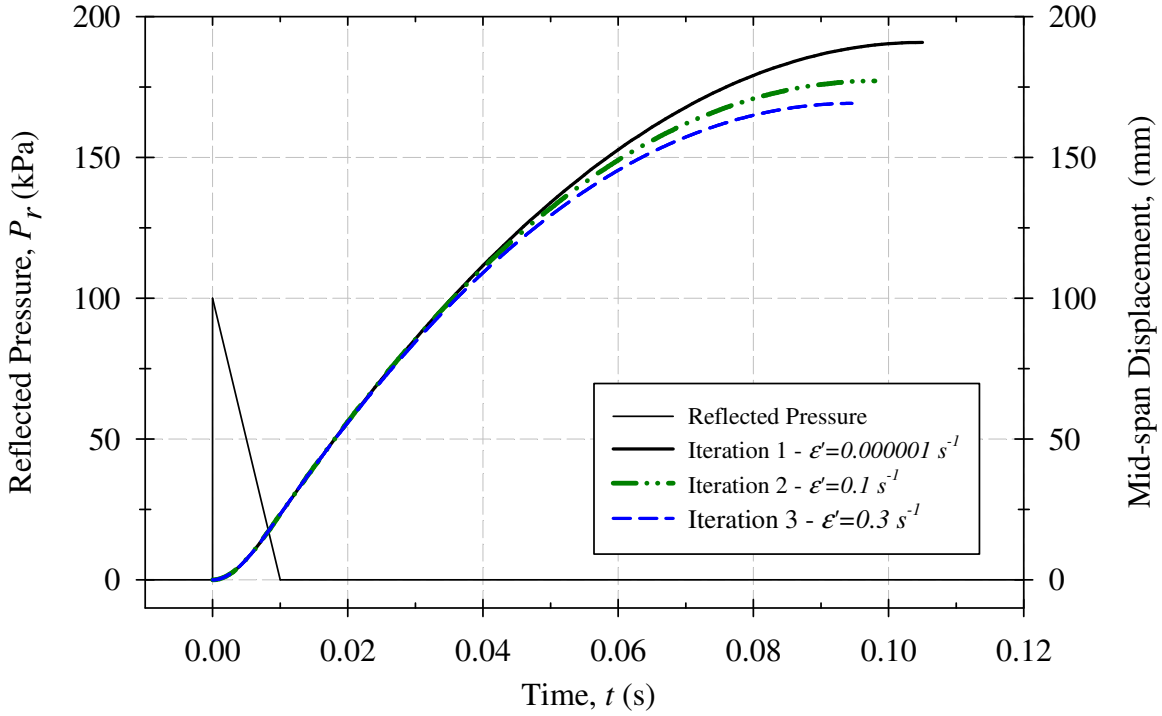

Figure 5.19: Comparison of Displacement Time-History Plots Using Strain-rate Dependent Resistance Curves.

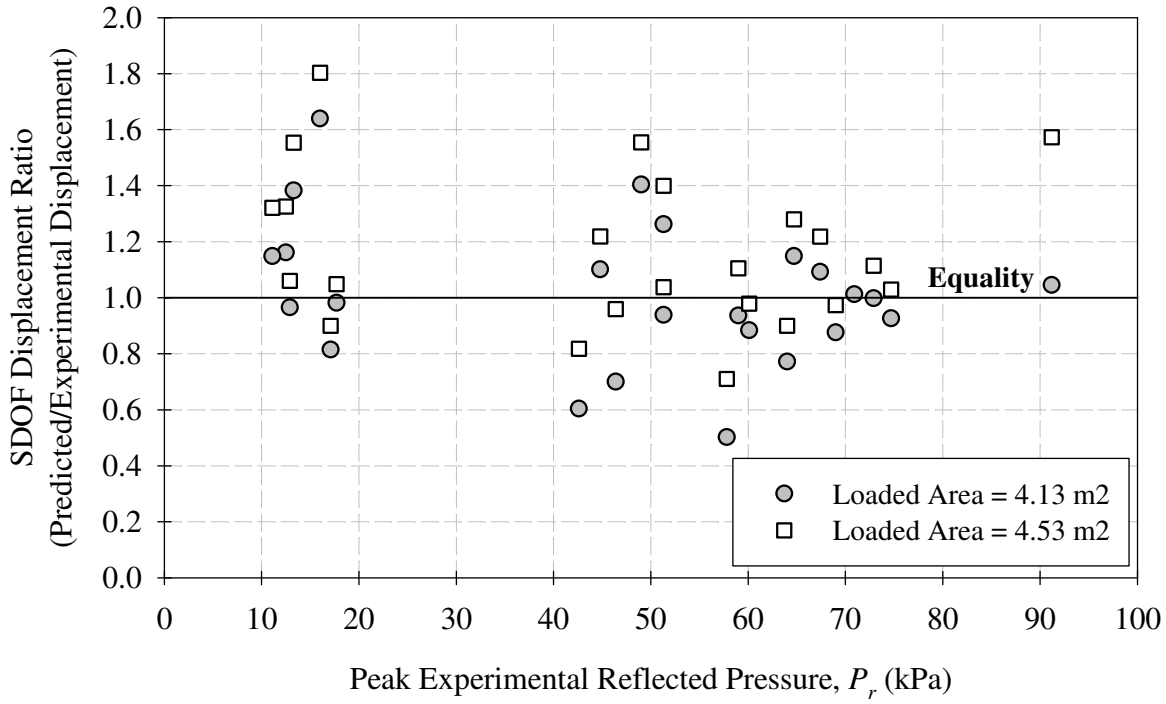

Figure 5.20: Effect of Loaded Area on SDOF Predictions for Tests Using a Load Transfer Device.

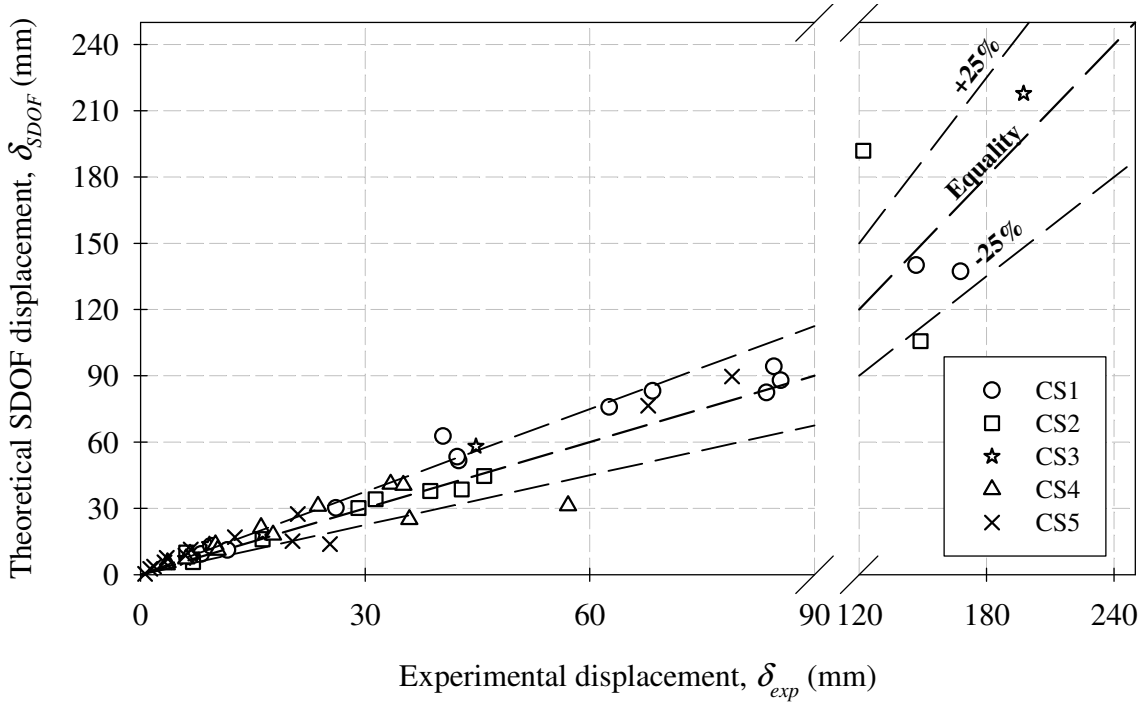

Figure 5.21: Maximum Experimental Displacements Compared Against those Calculated using the SDOF Method for All Tests.

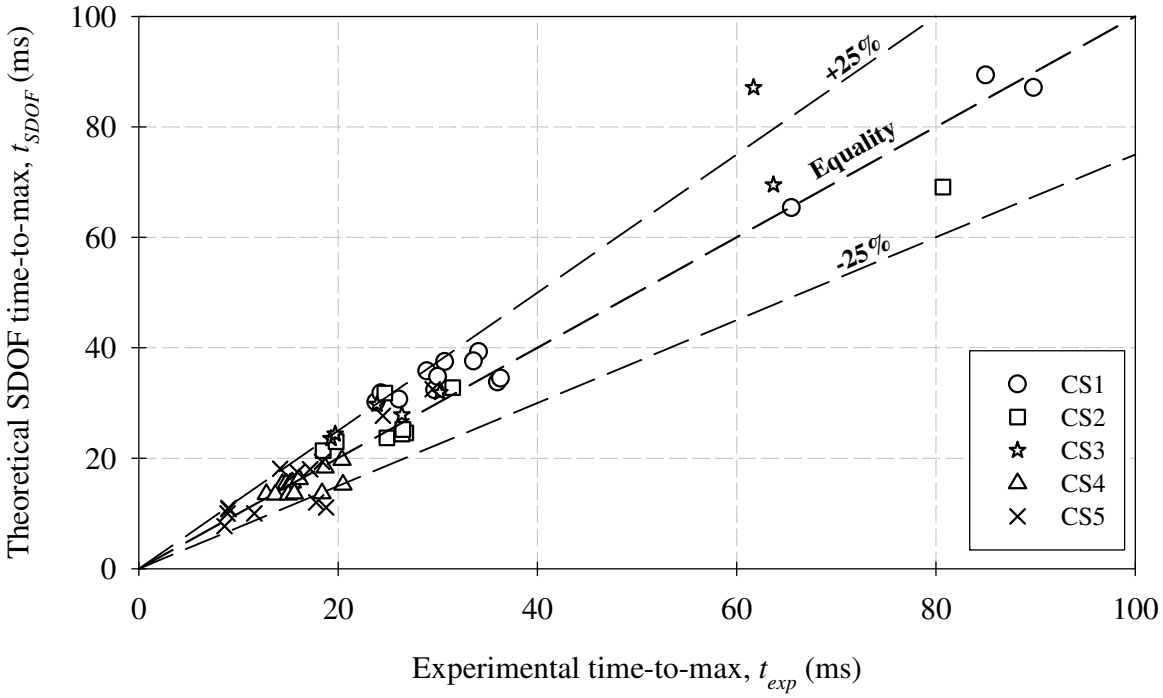

Figure 5.22: Maximum Experimental Time-to-Maximum Displacement Compared Against those Calculated using the SDOF Method for All Tests.

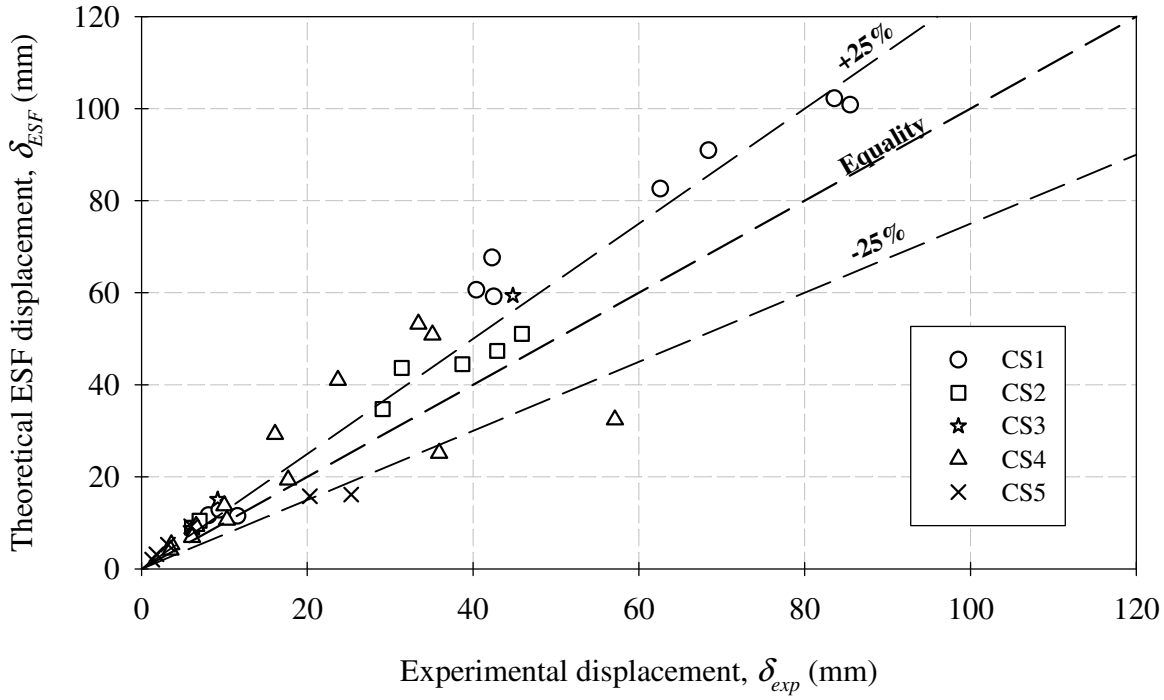

Figure 5.23: Maximum Experimental Displacements Compared Against those Calculated using the ESF Method for Elastic Shots Performed on Retrofitted Specimens.

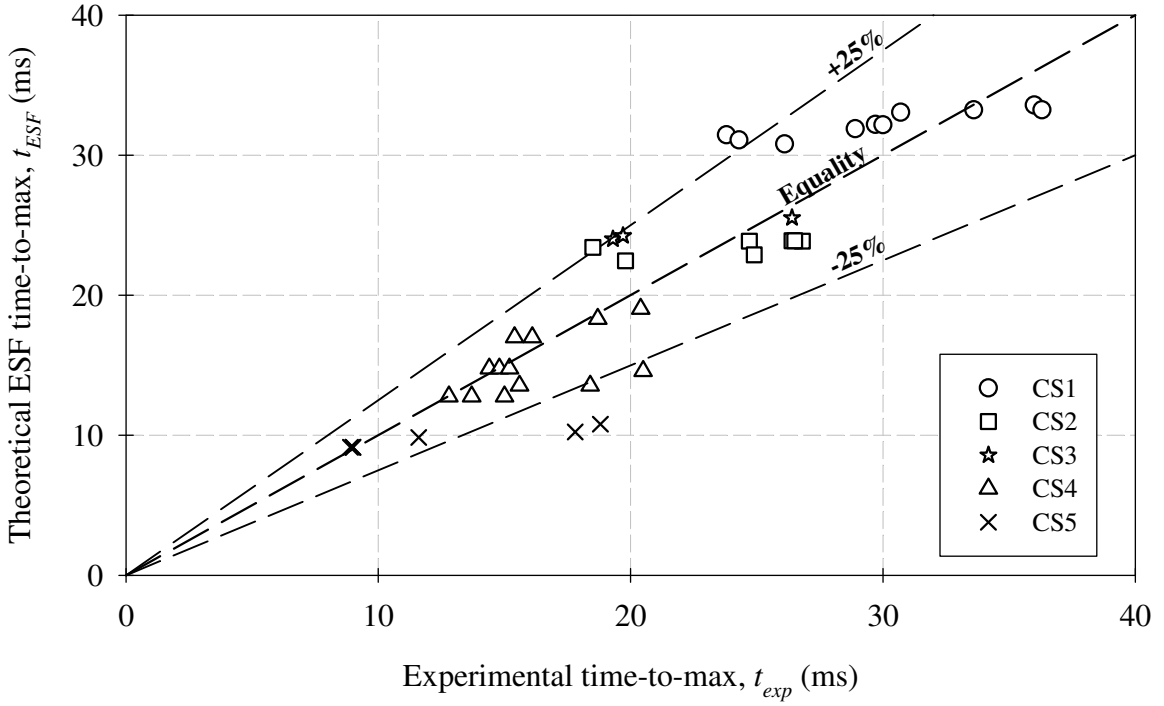

Figure 5.24: Maximum Experimental Time-to-Maximum Displacement Compared Against those Calculated using the ESF Method for Elastic Shots Performed on Retrofitted Specimens.

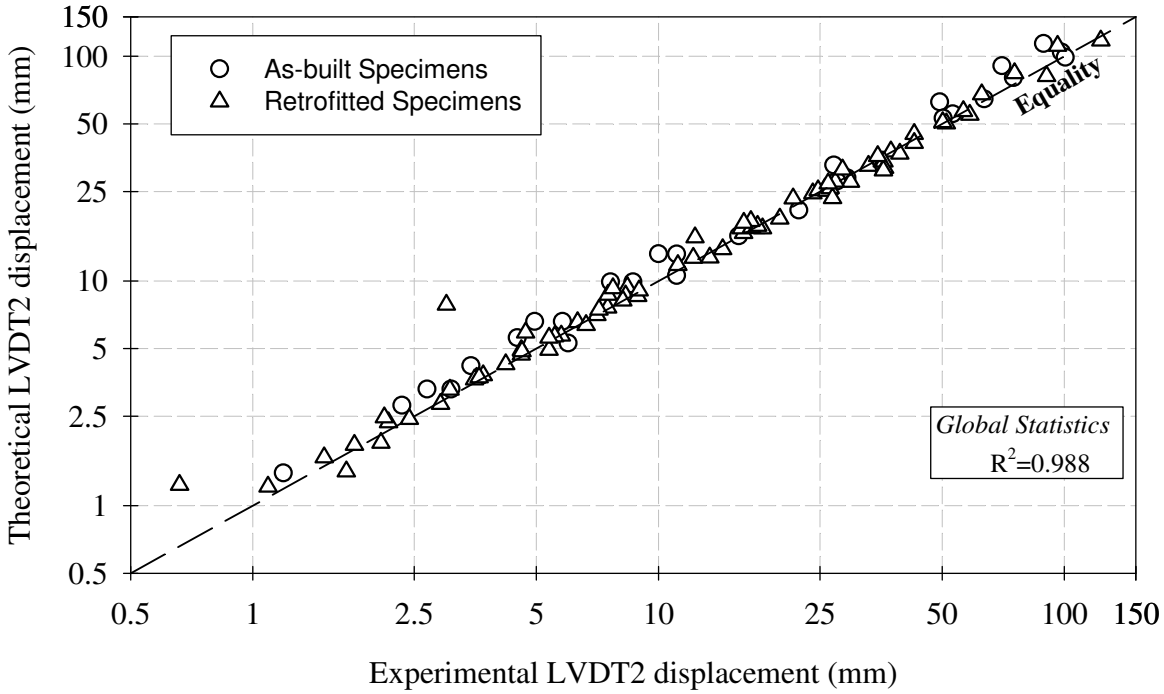

Figure 5.25: Experimental LVDT2 Displacements Compared Against the Theoretical Displacements Predicted for One-way Wall Panels.

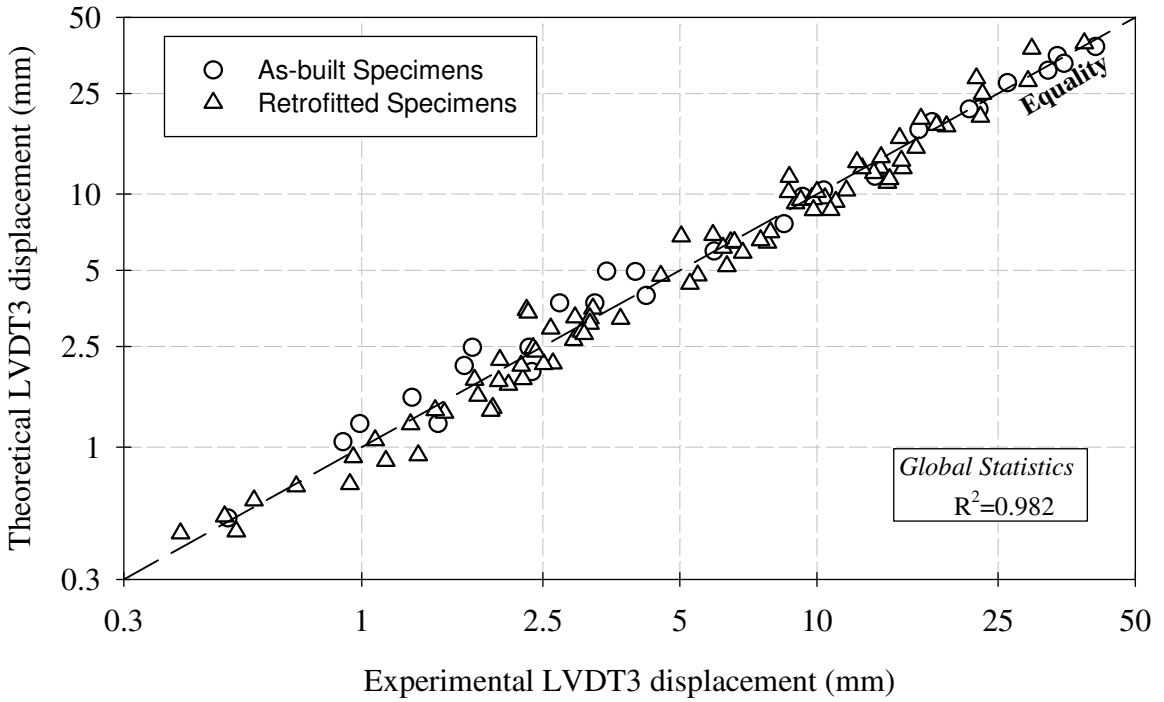

Figure 5.26: Experimental LVDT3 Displacements Compared Against the Theoretical Displacements Predicted for One-way Wall Panels.

Chapter 6. Conclusions

6.1. Summary

An experimental and analytical investigation was conducted to study the effect of using externally bonded fibre reinforced polymers as a retrofit technique to improve the blast resistance of reinforced concrete walls and slabs. The results of this study were extended to include blast retrofit of flexure dominant reinforced concrete beams. A total of 13 large scale one-way reinforced concrete wall panels and two-way reinforced concrete slab plates were tested under simulated blast loading. The specimens were subjected to sixty simulated explosions of various levels of destructiveness. A shock tube was used to simulate the shock waves produced by the detonation of high explosives. The performance of various configurations of externally bonded carbon fibre reinforced polymer retrofits was studied. Additionally, some retrofitted specimens incorporated FRP fibre anchors to prevent or delay premature debonding failures. Force-deformation characteristics of as-built and retrofitted specimens were discussed. Direct comparison of displacement and pressure time-histories for companion as-built and retrofitted specimens was performed. Reinforcing steel and FRP strains were recorded. A qualitative discussion on blast induced damage progression and behaviour augmented the experimental data. The effect of externally bonded FRP retrofits on improving blast resistance was assessed based on the experimental data and observations.

Theoretical analyses of the one- and two-way specimens were carried out to determine analytical displacement time-histories. Moment-curvature relationships for the one-way specimens were determined through plane section analysis, accounting for high strain-rate effects by incorporating dynamic material strength increase factors. Force-deformation characteristics of the one-way specimens were determined by a detailed inelastic analysis, predicting member resistance and displaced shapes at all stages of response. An algorithm was used to model the formation and progression of plastic hinge formation. Force-deformation characteristics of the two-way specimens were determined based on simplified relations commonly used in design of blast resistant structures. The force-deformation characteristics were used

to perform an equivalent single degree of freedom analysis to generate theoretical displacement time-histories and PI diagrams. An equivalent static force procedure was used to analyze the response of FRP retrofitted members. The theoretical displacement time-histories and pressure-impulse diagrams were then compared with experimental results to assess the ability to predict the response of walls, slabs and flexure dominant beams to dynamic blast loading.

6.2. Conclusions

Based on the literature review, experimental data, and theoretical analysis discussed in this thesis, the following conclusions can be reached:

- Existing literature on blast performance of externally bonded FRP retrofits is limited and generally qualitative in nature. This may be attributed to the high cost, safety concerns, technical challenges and sensitive nature of live explosive testing. Shock tube testing provides an excellent alternative for the simulation of blast-induced shock waves that can be used to generate much needed test data.

- Externally bonded FRP retrofits significantly increase the strength and stiffness of reinforced concrete flexure members. Without exception, a significant reduction in maximum displacement and time-to-maximum displacement for all specimens retrofitted with externally bonded CFRP was observed over corresponding as-built members.

- At failure, the maximum support rotation for as-built one-way wall panel strips was between *7°* and *10°*. The corresponding CFRP retrofitted wall strips were able to survive the same simulated explosions and sustain elastic support rotations of approximately *2°* – a reduction in displacement level of approximately *3.5* to *5* times the as-built response. Prior to failure, the CFRP retrofitted wall strips were able to sustain elastic support rotations of between *2°* and *4°*, depending on the failure mode.

- Although the capacity of the shock tube was not sufficient enough to generate large inelastic behaviour of the two-way slab plates, a similar reduction in support rotations

was observed when externally bonded CFRP retrofits were applied to two-way slab companion specimens.

- Due to the high strength/low stiffness mechanical properties of CFRP, retrofitted specimens generally remained elastic prior to failure. During the initial inbound displacement phase, kinetic energy of the specimen is stored as elastic strain energy in CFRP. However, as the traditional mechanisms of energy dissipation have been eliminated through retrofitting (i.e. crushing of concrete and yielding of steel), all the elastic strain energy is violently released as kinetic energy during the rebound phase. This results in large rebound displacements, possibly leading to member failure caused by moment reversals. Accordingly, blast resistant structures incorporating externally bonded FRP composites must be designed to account for the increased elasticity and corresponding rebound displacements. One acceptable solution would be to retrofit both faces with FRP to resist blast induced failure by moment reversal.

- Debonding of CFRP from concrete substrate was the exclusive failure mode for all retrofitted specimens. The thickness (and indirectly the stiffness) of the members is thought to play a role. Retrofitted specimens of companion set 1 and companion set 3 (*80 mm* and *75 mm* thick, respectively) failed by plate-end interfacial debonding, whereas the retrofitted specimens of companion set 2 (*120 mm* thick) failed by critical diagonal crack debonding. Retrofitting structures to increase their stiffness has shown to improve their blast resistance significantly, but also may alter the final failure mode from flexure to a flexure-shear debonding. Any potential blast retrofit should be designed for the possibility of all potential retrofit failure modes.

- The efficacy of FRP anchors at preventing or delaying premature debonding failure depends on the anticipated failure mode. It was observed that FRP anchors had no impact on retrofit performance when plate-end interfacial debonding, triggered by flexural action, was the primary failure mode. In this case, the retrofitted specimens with and without anchors failed at approximately the same strain level; *1.0%* for CS1-R2 versus *0.8%* for CS1-A. However, when the observed failure mode was dominated by diagonal crack debonding, FRP anchors improved the effectiveness of FRP sheets by delaying debonding (in specimen CS2-A), and resulting in an in-

creased retrofit strain of *0.9%* at failure, versus the specimen without the anchors (CS2-R) debonding at *0.6%* strain. Therefore, the direction of debonding propagation – either away from the plate-end (*e.g.* plate-end debonding) or towards the plate-end (*e.g.* critical diagonal crack debonding) – had an impact on FRP anchor performance. Regardless of the anticipated debonding mode, specimens with FRP anchors always developed a minimum strain of approximately *0.8%* at failure, whereas those without the anchors could develop a minimum FRP strain of approximately *0.6%* due to premature debonding.

- FRP anchor failure was caused by shearing of the anchor bends caused by stress concentrations at these locations.

- The analytical displacement time-histories obtained through single degree of freedom analysis correlate well with those obtained experimentally. The degree of compatibility between predicted and experimental results is in direct proportion to the level of refinement associated with the derivation of the force-deformation characteristics used in the dynamic analysis. This implies that the modelling techniques used in this analysis can accurately be applied to both as-built and retrofitted wall panels and slab plates.

- The displaced shapes obtained from inelastic analysis of the one-way wall panels correlate well with those obtained experimentally. This implies that the analytical load-mass transformation factors used in the dynamic analysis accurately describe member behaviour at all levels of response up to maximum displacement. Furthermore, this suggests that the elastic component of deformations – typically ignored at large inelastic displacement levels in other simplified analytical models – can have a significant impact on the dynamic response of the system.

- Analytical results obtained for retrofitted specimens using an equivalent static force procedure correlate well with those results obtained experimentally and those obtained by detailed SDOF analysis. This implies that using an equivalent static force procedure to analyze or design FRP retrofitted members subjected to blast loading would yield results which are conservative, yet still describe the experimental data

with a reasonable level of accuracy. It is important to note that the accuracy of an ESF procedure is directly dependent on how closely the true force-deformation and pressure time-history match the idealizations used in analysis.

6.3. Retrofit Recommendations

Based on the results and observations presented in this document, the following are recommended for the design of blast resistant FRP retrofits of flexure dominant reinforced concrete beams, wall and slabs:

- To ensure that composite action is maintained, FRP retrofitted members should be designed such that the bond between externally bonded FRP and the concrete substrate is not lost during response to design blast loads.

- It is recommended that no dynamic increase factor be applied to carbon fibre retrofit systems to due to that lack of apparent high strain-rate effect during dynamic response.

- In the absence of FRP anchors that mechanically fasten the FRP sheets to the concrete substrate, it is recommended that the maximum tensile strain in FRP, prescribed by CSA S806-02, be used as the maximum tensile design strain under blast loading conditions.

- When FRP anchors are used to mechanically fasten the FRP sheets to the concrete substrate, the design strain in surface bonded FRP can be taken as 0.8%, provided that the maximum FRP stress does not exceed $\phi_F f_{Fu}$ specified in CSA S806-02.

- Despite a reduction in retrofitted member stiffness due to yielding of steel, reinforced concrete members will likely exhibit quasi-elastic behaviour, provided integrity of the retrofit system is maintained. Therefore, it is recommended that elastic equivalent SDOF transformation factors be used in dynamic analysis.

- The SDOF method is an acceptable method of performing dynamic analysis of retrofitted structures. Analysis of retrofitted structures using an equivalent static force procedure can be expected to yield reasonable results.

- Blast resistant structures incorporating externally bonded FRP composites should be designed to survive moment reversal caused by rebound displacements during free vibration response. Accordingly, it is recommended that structures be retrofitted on both the inbound and rebound face to mitigate the potential of blast-induced failure by moment reversal. The design rebound displacement may be determined from dynamic analysis or may be conservatively assumed as equal to the maximum inbound displacement.

- Detailing and anchorage of FRP sheets used in blast retrofits should follow the requirements of CSA S806-02.

- The effectiveness of FRP anchors may be increased by inserting the anchors at a slight angle relative to concrete substrate, countersinking the anchor holes, and orienting the fan blades in the direction of largest expected tensile stresses.

6.4. Recommendations for Future Research

Based on the research described in this thesis, the following areas require further study:

- Investigate the temporal and positional distribution of high strain-rate effects in reinforced concrete members subject to blast loading.

- Investigate the effect of blast-induced high strain-rates on bond and development length of both reinforcing steel and externally bonded fibre reinforced polymer composites.

- Study the effect of blast induced moment reversal on reinforced concrete flexure members retrofitted with externally bonded fibre reinforced polymer composites.

- Further simulated blast testing of externally bonded fibre reinforced polymer composites incorporating FRP anchors to establish upper bound of anchor performance and optimize anchor configuration.

- Static testing of FRP anchors applied to unbonded FRP sheets to optimize anchor configuration to reduce stress concentrations.

- Static testing of reinforced concrete one- and two-way flexure members to investigate the effect of plastification on the single degree of freedom load-mass transformation factors used in dynamic analysis. Furthermore, such static testing could also be used to calibrate the plastic hinge formation algorithm used to define the analytical force-deformation characteristics.

References

American Concrete Institute (2008). Guide *for the design and construction of externally bonded FRP systems for strengthening concrete structures*, ACI Committee 440, Report 440.2R-08, Farmington Hills, MI.

American Society of Civil Engineers (1999). *Structural Design for Physical Security: State of the Practice,* ASCE Structural Engineering Institute, Reston, VI.

BASF Construction Chemicals, LLC. (2007) "MBRACE CF-130 Product Data," Manufacturer material data sheet.

Biggs, J. M. (1964). *Introduction to Structural Dynamics.* McGraw-Hill, New York, NY.

Bischoff, P. H., and Perry, S. H. (1991). "Compressive behaviour of concrete at high strain-rates," *Materials Research Society Symposia Proceedings,* 64, 151-165.

Bischoff, P. H., and Perry, S. H. (1995). "Impact behaviour of plain concrete loaded in uniaxial compression." *Journal of Engineering Mechanics,* 121(6), 685-693.

Buchan, P. A., and Chen, J. F. (2007). "Blast resistance of FRP composites and polymer strengthened concrete and masonry structures – A state-of-the-art review." *Composites: Part B,* 38(5-6), 509-522.

CEB-FIP (1993). *Model Code 90 for Concrete Structures*, Federation International de la preconstraint, CEB Bulletin No. 213/214, Paris.

CSA (2004). *Design of concrete structures*, CSA Standard A23.3-04. Canadian Standards Association, Mississauga, Ontario.

CSA (2007). *Design and construction of building components with fibre-reinforced polymers*, CSA Standard S806-02. Canadian Standards Association, Mississauga, Ontario.

Dunkman, D. A., Yousef, A. E. A., Karve, P. M., and Williamson, E. B. (2009). "Blast performance of prestressed concrete panels." *Proceedings of the 2009 Structures Congress – Don't Mess with Structural Engineers: Expanding Our Role,* 1297-1306.

Esparza, E. D. (1986). Blast measurements and equivalency for spherical charges at small scaled distances. International Journal of Impact Engineering, 4 (1), 23-40.

Fu, H. C., Erki, M. A., and Seckin, M. (1991). "Review of Effects of Loading Rate on Reinforced Concrete." *Journal of Structural Engineering*, 117(12), 3660-3679.

Fyfe CO. LLC. (2009). "Tyfo SCH-41S-1 Composite Product Data," Manufacturer material data sheet.

Harding, J., and Welsh, L. M. (1983). "A tensile testing technique for fibre-reinforced composites at impact rates of strain." *Journal of Materials Science,* 18(6), 1810-1826.

Hognestad, E. (1951). "Study of combined bending and axial load in reinforced concrete members." *University of Illinois – Engineering Experiment Station – Bulletin Series,* Bul. No 399, 128p.

Kinney, G. F., and Graham, K. J. (1985). *Explosive Shocks in Air,* 2nd ed., Springer-Verlag, New York, N.Y.

Lam, L., and Teng, J. G. (2001). "Strength of RC cantilever slabs bonded with GFRB strips." *Journal of Composites of Construction,* 5(4), 221-227.

Lawver, D., Daddazio, R., Oh, G. J., Lee, C. K. B., Pifko, A. B., and Stanley, M. (2003). "Simulating the response of composite reinforced floor slab subjected to blast loading." *American Society of Mechanical Engineers, Applied Mechanics Division (AMD),* 254, 15-21.

Lloyd, A. (2010). "Performance of reinforced concrete columns under shock tube induced shock wave loading," Master's thesis, University of Ottawa, Ottawa, Ontario.

Lloyd, A., Jacques, E., Saatcioglu, M., Palermo, D., Nistor, I., and Tikka, T. (2010) "Capabilities and Effectiveness of using a Shock Tube to Simulate Blast Loading on Structures and Structural Components," Submitted for review, ACI Special Publication on Blast, Pittsburgh, PA.

Malvar, L. J., and Crawford, J. E. (1998a). "Dynamic Increase Factors for Concrete." *Proceedings of the Twenty-Eighth DDESB Seminar,* DoD Explosives Safety Board, Orlando, FL.

Malvar, L. J., and Crawford, J. E. (1998b). "Dynamic Increase Factors for Steel Reinforcing Bars." *Proceedings of the Twenty-Eighth DDESB Seminar,* DoD Explosives Safety Board, Orlando, FL.

Magnusson, J. (2007). "Structural concrete elements subjected to blast loading." Licentiate thesis, KTH, Department of Civil and Architectural Engineering, Stockholm, Sweden.

Mays, G. C., and Smith, P. D. (1995). *Blast effects on buildings; Design of buildings to optimize resistance to blast loading*. Thomas Telford, London, UK.

Mosalam, K. M., and Mosallam, A. S. (2001). "Nonlinear transient analysis of reinforced concrete slabs subjected to blast loading and retrofitted with CFRP composites," *Composites Part B:* Engineering, 32(8), 623-636.

Orton, S. L., Jirsa, J. O., and Bayrak, O. (2008). "Design considerations for carbon fibre anchors." *Journal of Composites for Construction,* 12(6), 608-616.

Ozbakkaloglu, T., and Saatcioglu, M. (2005). "FRP Stay-in-Place Formwork for Seismic Resistant High-Strength Concrete Columns." *ACI Special Publication, SP-230: 7th International Symposium on Fiber-Reinforced (FRP) Polymer Reinforcement for Concrete Structures*, 1593-1612.

Ozbakkaloglu, T., and Saatcioglu, M. (2009). "Tensile Behaviour of FRP Anchors in Concrete," *Journal of Composites for Construction*, 13(2), 82–92.

Quattlebaum, J. B., Harries, K. A., and Petrou, M. F. (2005). "Comparison of three flexural retrofit systems under monotonic and fatigue loads." *Journal of Bridge Engineering*, 10(6), 731-740.

Razaqpur, G. A., Tolba, A., and Contestabile, E. (2007). "Blast loading response of reinforced concrete panels reinforced with externally bonded GFRP laminates." *Composites Part B: Engineering,* 38(5-6), 535-546.

Razvi, S. R., and Saatcioglu, M. (1999). "Analysis and design of concrete columns for confinement." *Earthquake Spectra,* 15(4), 791-811.

Robert, S. D., and Johnson, C. F. (2009). "Blast response of conventional and high performance reinforced concrete panels." *Proceedings of the 2009 Structures Congress – Don't Mess with Structural Engineers: Expanding Our Role,* 1142-1150.

Ross, C. A., Purcell, M. R., and Jerome, E. L. (1997). "Blast response of concrete beams and slabs externally reinforced with fiber reinforced plastics (FRP)." *Structures Congress – Proceedings: Building to Last,* 1, 673-677.

Saatcioglu, M., Serrato, F., and Foo, S. (2005). "Seismic Performance of Masonry Infill Walls Retrofitted with CFRP Sheets," *ACI Special Publication, SP-230: 7th International Symposium on Fiber-Reinforced (FRP) Polymer Reinforcement for Concrete Structures*, 341–354.

Sawyer, H. A. (1964). "Design of Concrete Frames for Two Failure Stages." *Proceedings International Symposium of the Flexural Mechanics of Reinforced Concrete, SP-12*, ACI, 405-431.

Silva, P. F., and Lu, B. (2007). "Improving the blast resistance capacity of RC slabs with innovative composite materials." *Composites: Part B,* 38(5-6), 523-534.

Smith, P. D., and Hetherington, J. G. (1994). *Blast and ballistic loading of structures,* Butterworth-Heinemann, Oxford, UK.

Teng, J. F., Smith, S. T., Yao, J., and Chen, J. F. (2003). "Intermediate crack-induced debonding in RC beams and slabs." *Construction and Building Materials,* 17(6-7), 447-462.

Teng, J. G., and Chen, J. F. (2009). "Mechanics of debonding in FRP-plated RC beams." *Proceedings of the Institution of Civil Engineers, Structures and Buildings,* 162(SB5), 335-345.

Toutlemonde, F., Rossi, P., Boulay, C., Gourraud, C., and Guedon, D. (1995). "Dynamic behaviour of concrete: tests of slabs with a shock tube." *Materials and Structures*, 28(179), 293-298.

Unified Facilities Code (UFC) 03-340-02 (2008). *Structures to Resist the Effects of Accidental Explosions*, United States of America Department of Defense, Washington, D.C.

Appendix A: Experimental Displacement Time-History Comparisons

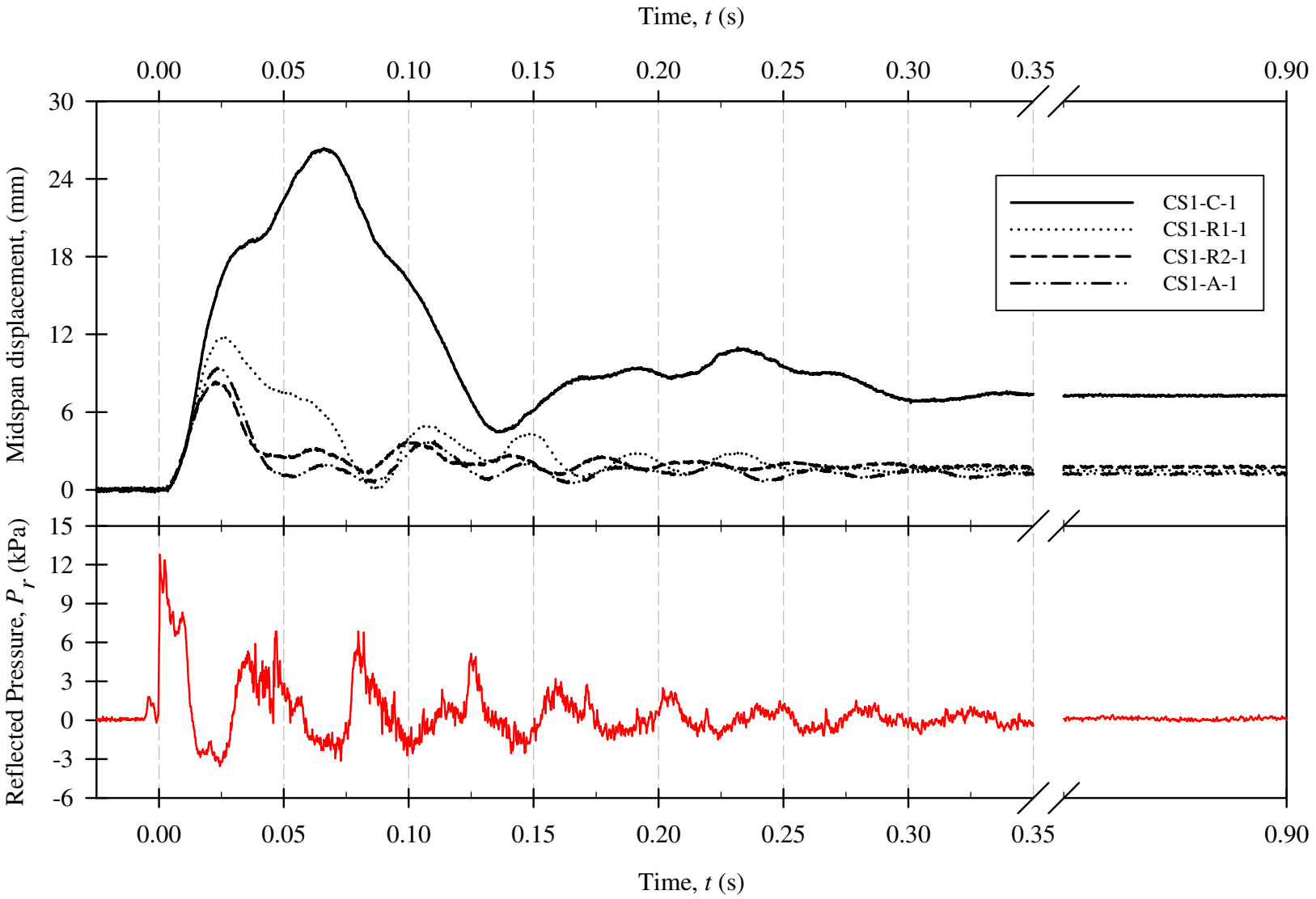

Figure A-1: Displacement Time-History Comparison for Companion Set CS1 with L_d=1830 mm and P_d~60 kPa.
(Typical pressure-time history record from shot CS1-C-1)

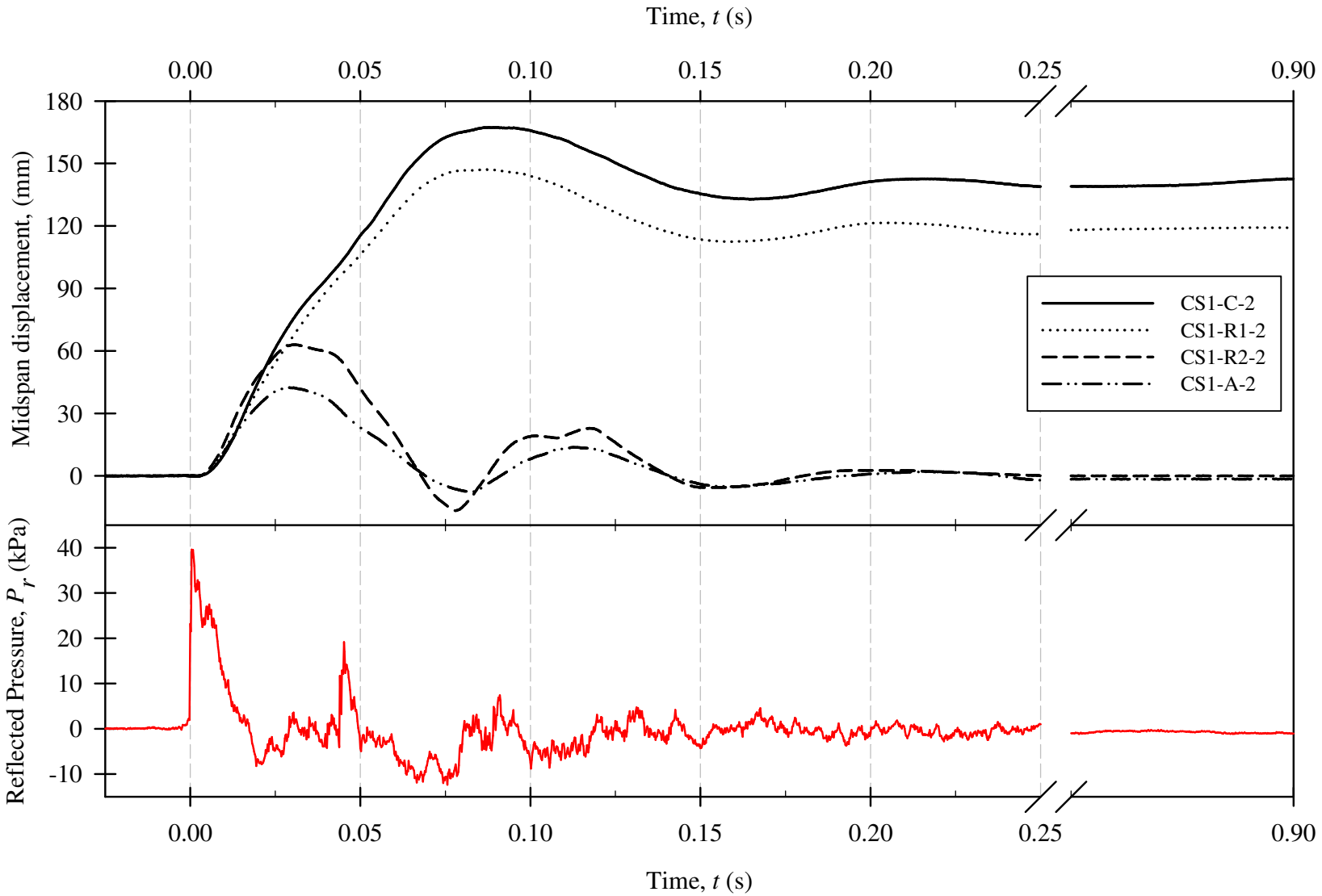

Figure A-2: Displacement Time-History Comparison for Companion Set CS1 with *L_d=1830 mm* and *P_d~240 kPa.*
(Typical pressure-time history record from shot CS1-C-2)

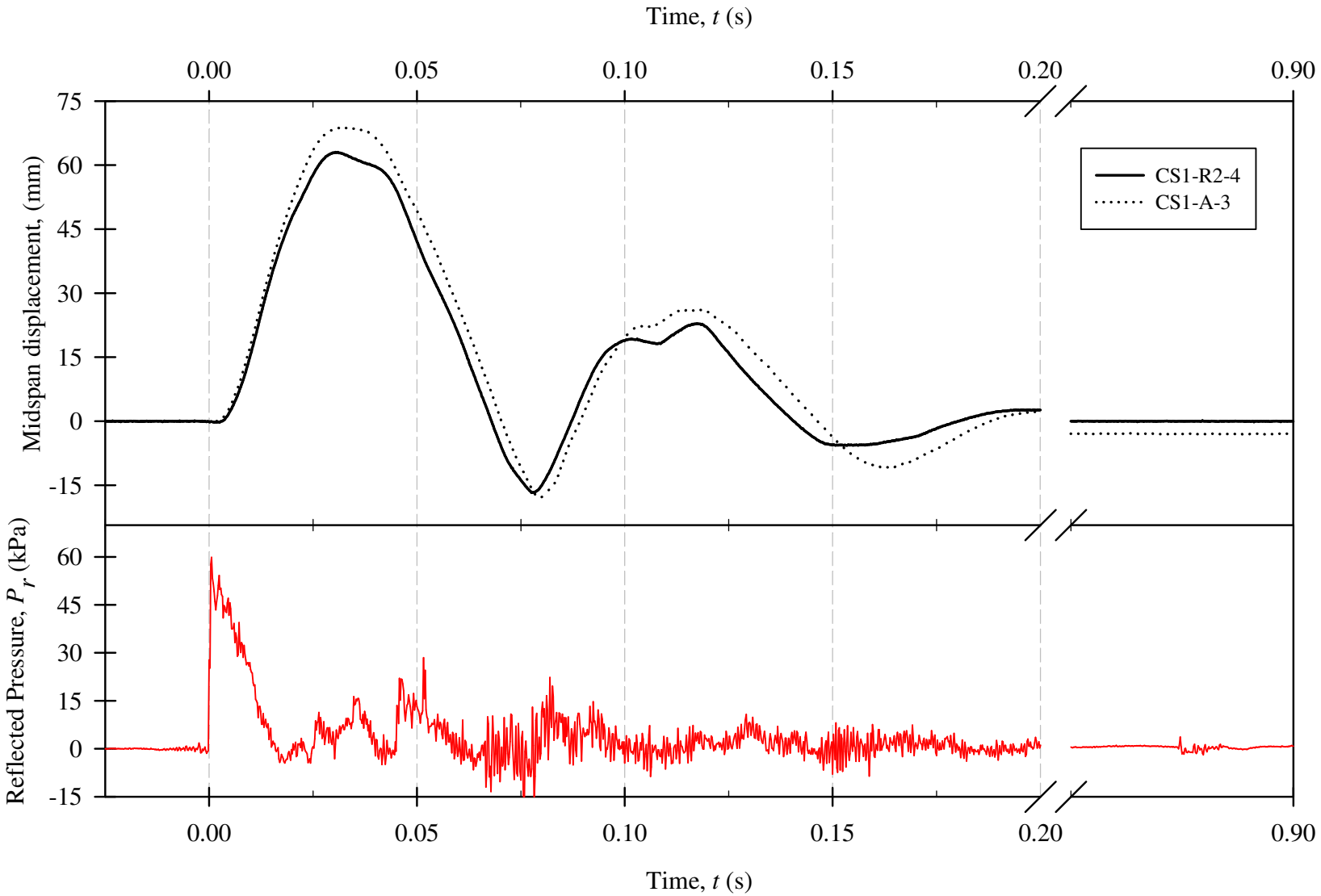

Figure A-3: Displacement Time-History Comparison for Companion Set CS1 with *L_d=1830 mm* and *P_d~352 kPa.*
(Typical pressure-time history record from shot CS1-R2-4)

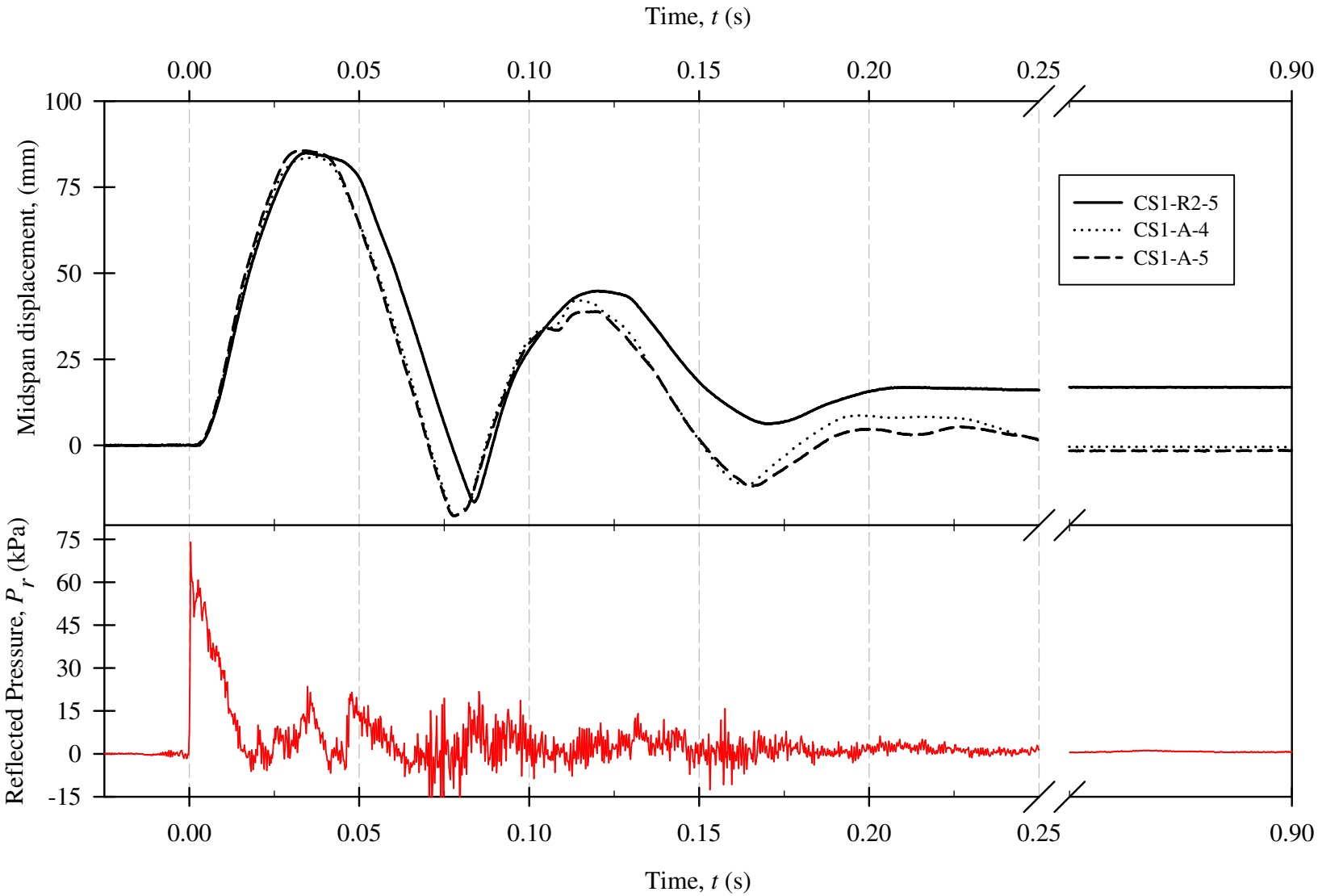

Figure A-4: Displacement Time-History Comparison for Companion Set CS1 with L_d=1830 mm and P_d~416 kPa.
(Typical pressure-time history record from shot CS1-R2-5)

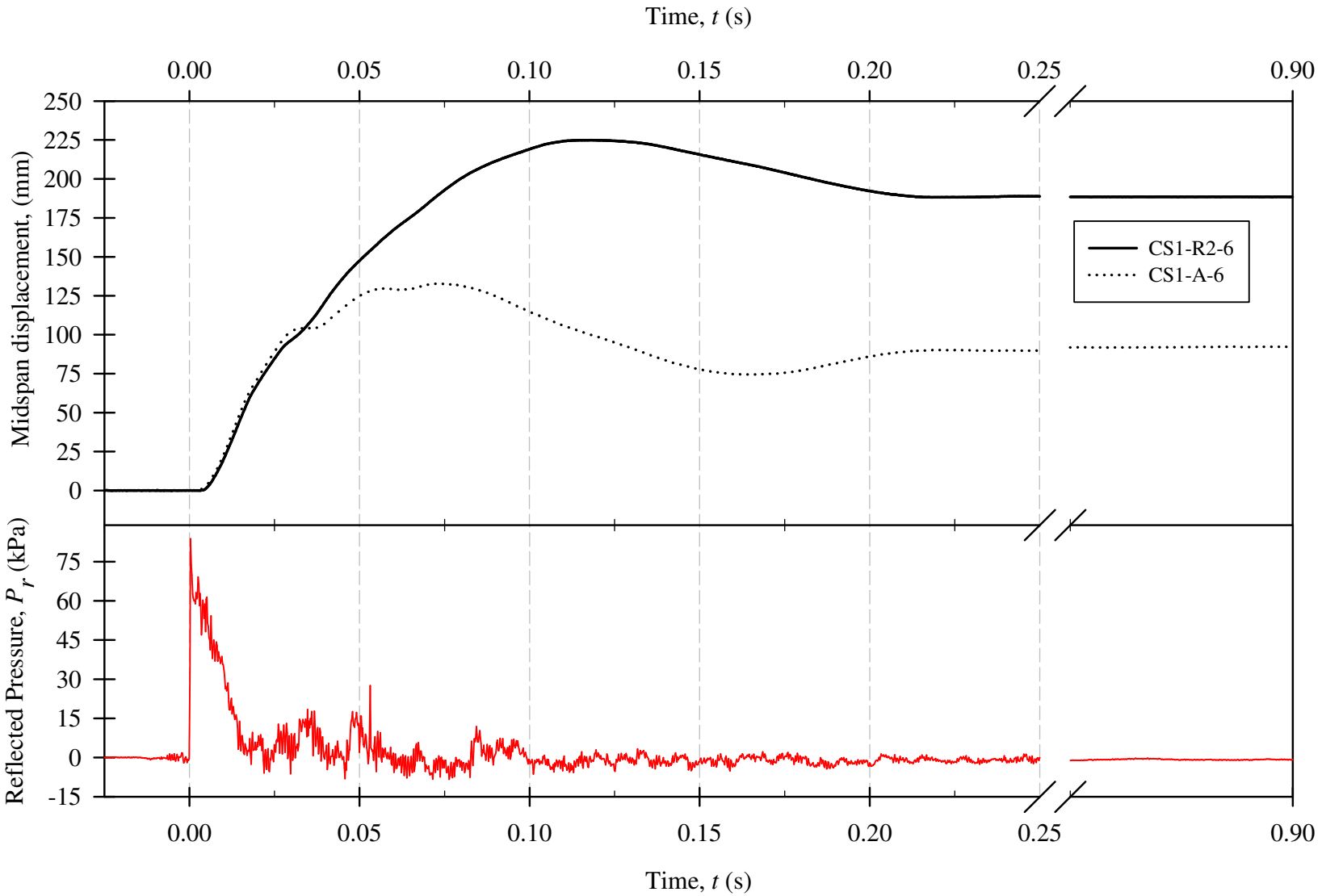

Figure A-5: Displacement Time-History Comparison for Companion Set CS1 with L_d=1830 mm and P_d~488 kPa.
(Typical pressure-time history record from shot CS1-R2-6)

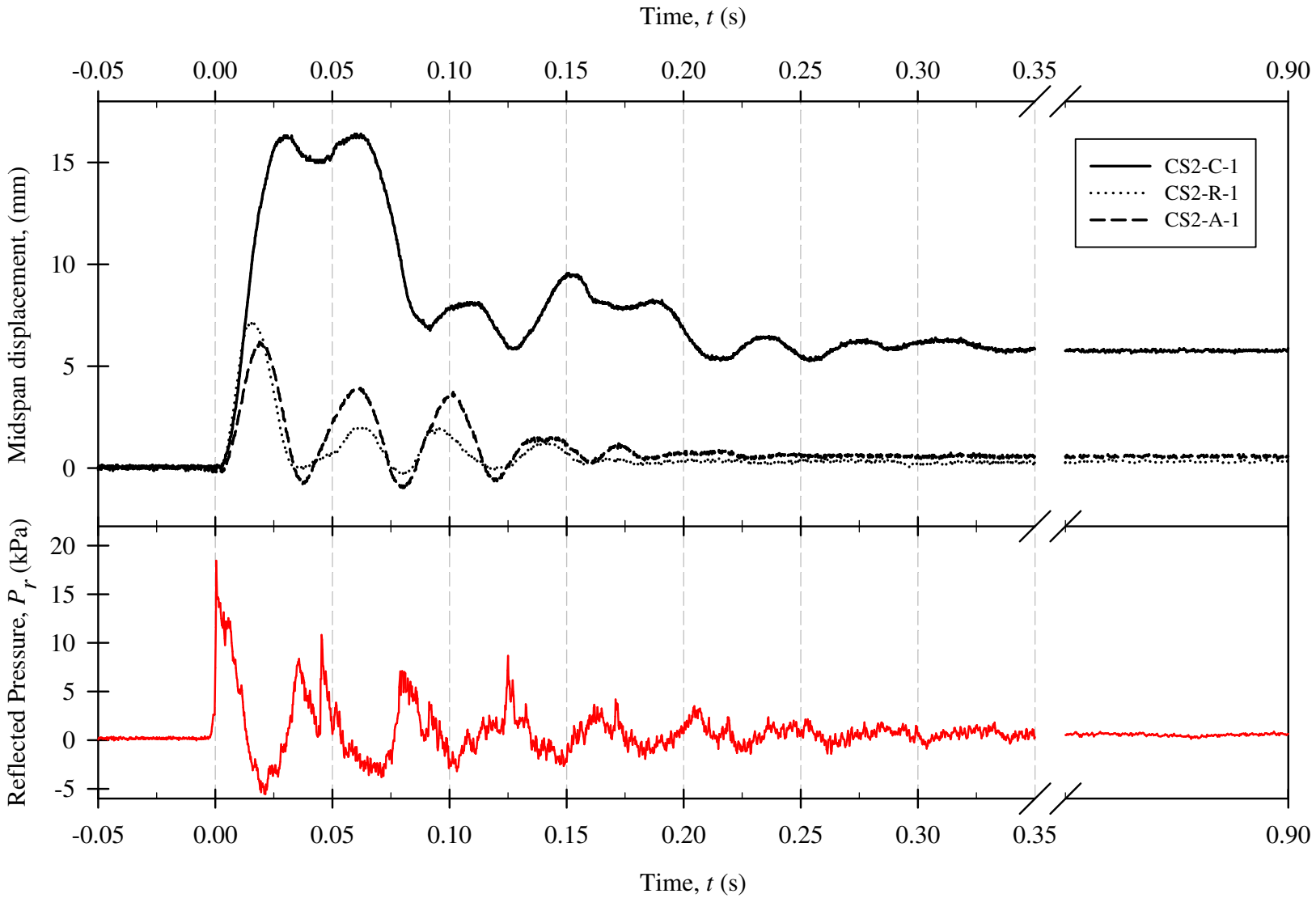

Figure A-6: Displacement Time-History Comparison for Companion Set CS2 with L_d=1830 mm and P_d~80 kPa.
(Typical pressure-time history record from shot CS2-C-1)

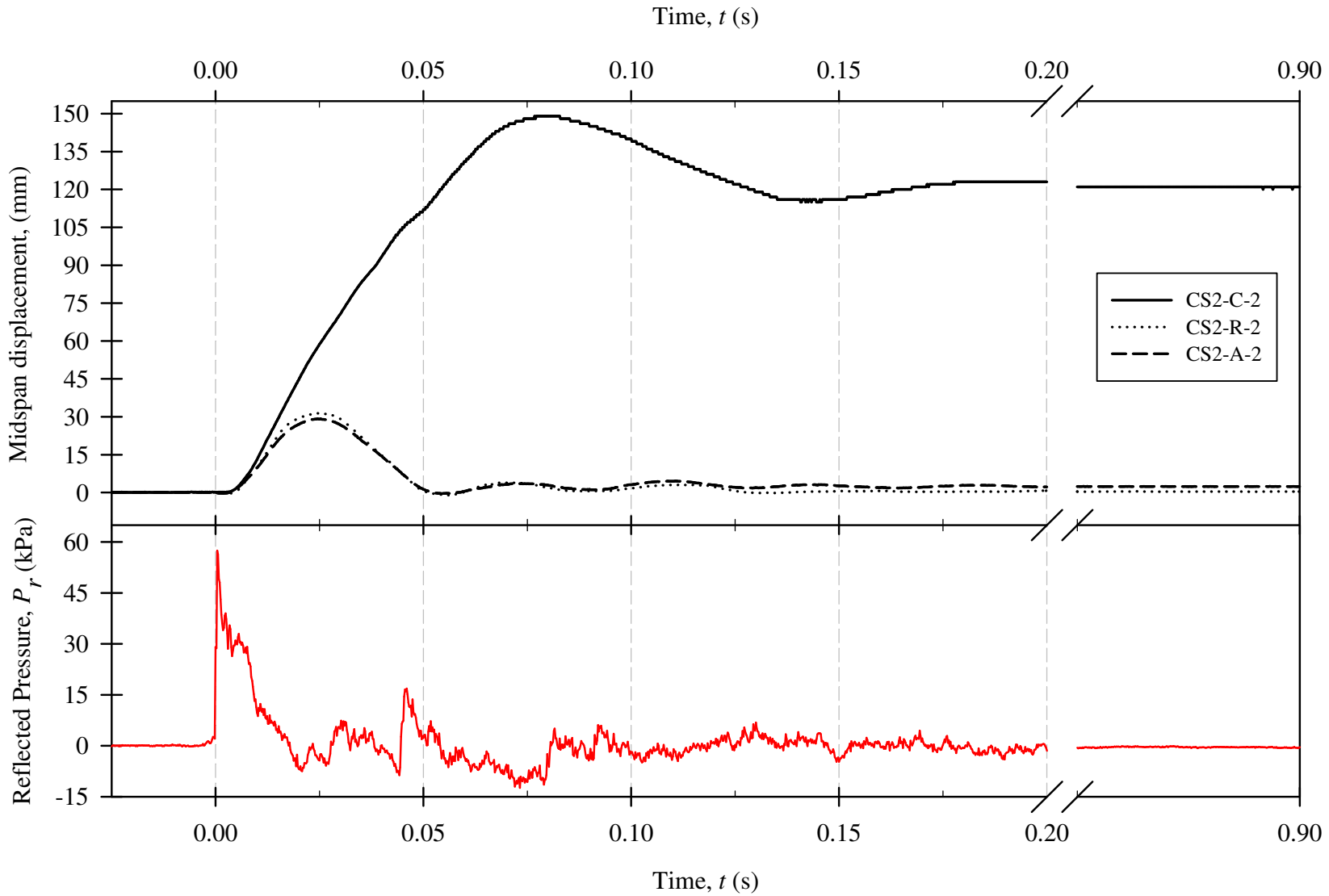

Figure A-7: Displacement Time-History Comparison for Companion Set CS2 with L_d=1830 mm and P_d~310 kPa.
(Typical pressure-time history record from shot CS2-C-2)

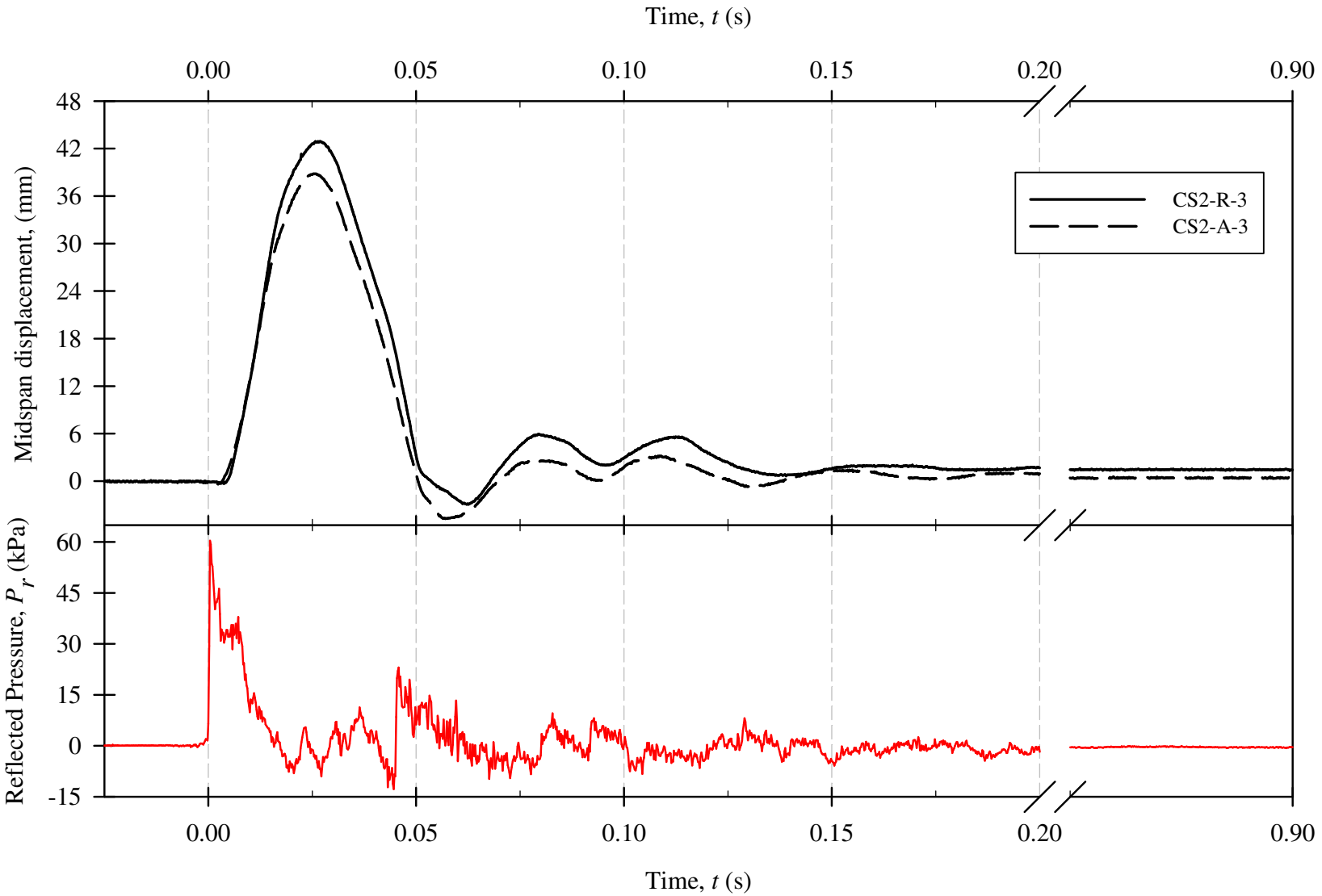

Figure A-8: Displacement Time-History Comparison for Companion Set CS2 with *L_d=1830 mm* and *P_d~360 kPa.*
(Typical pressure-time history record from shot CS2-R-3)

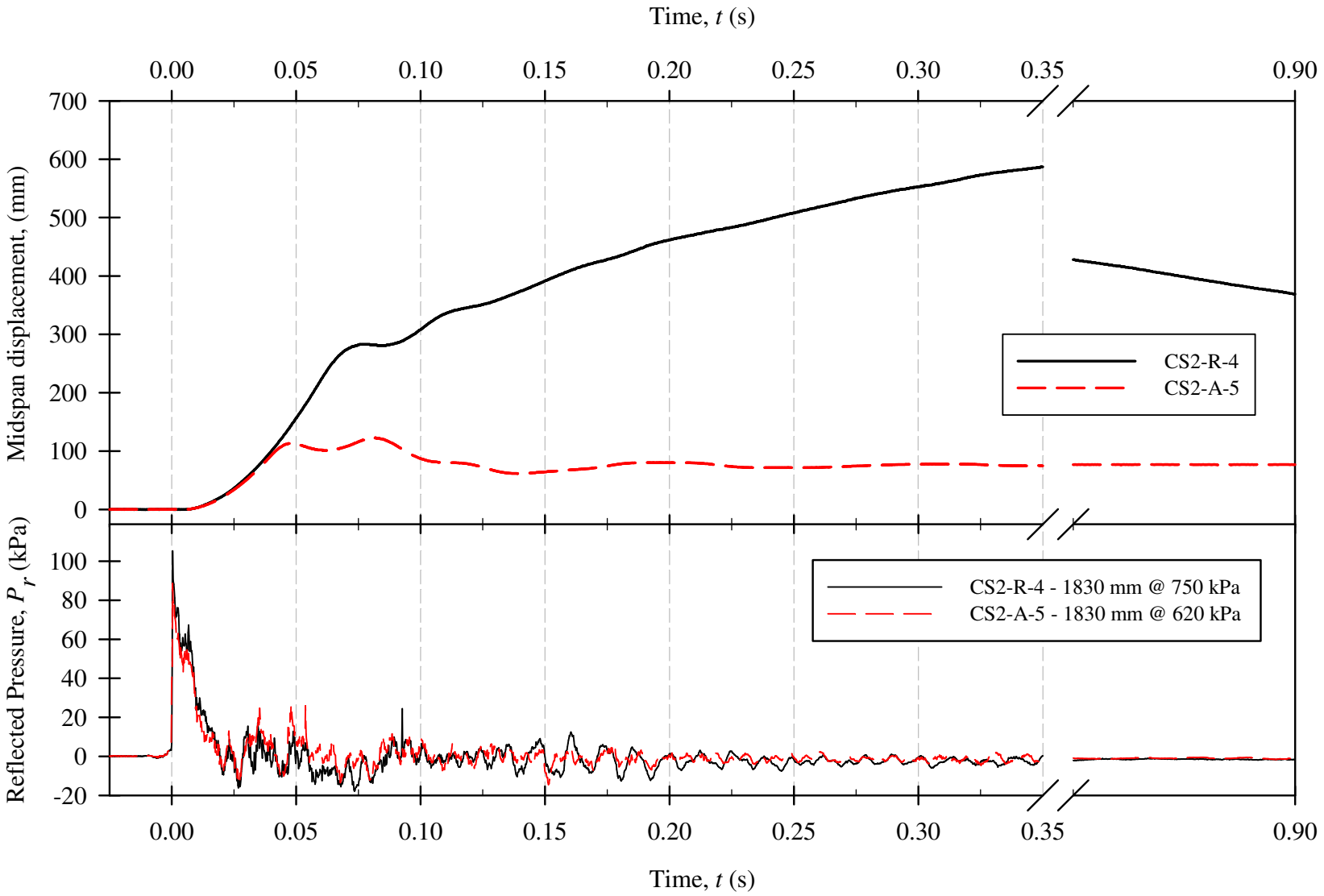

Figure A-9: Displacement Time-History Comparison for Companion Set CS2 with L_d=1830 mm and P_d=750 kPa for CS2-R and P_d=620 kPa for CS2-A.

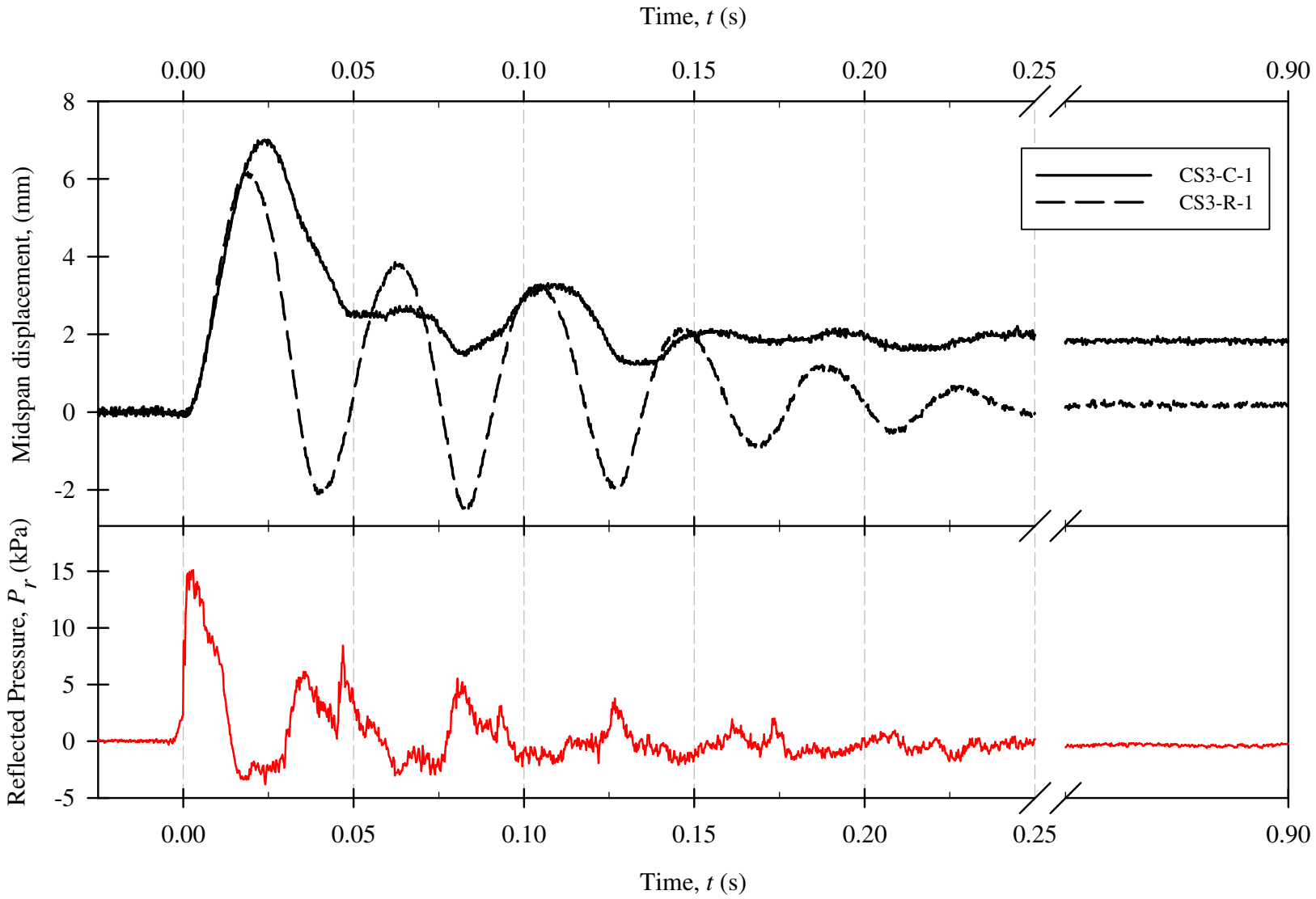

Figure A-10: Displacement Time-History Comparison for Companion Set CS3 with L_d=1830 mm and P_d~80 kPa.
(Typical pressure-time history record from shot CS3-C-1)

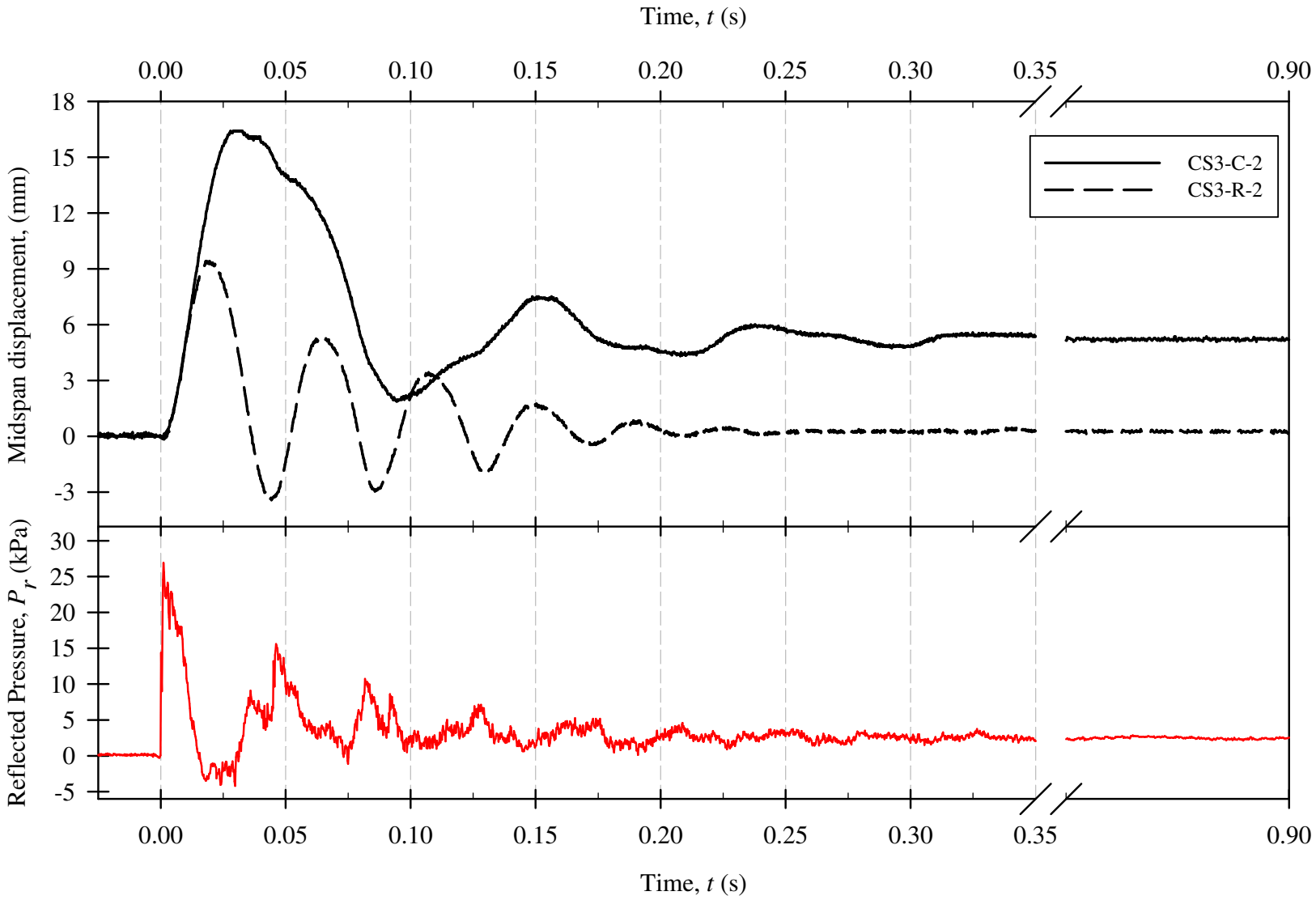

Figure A-11: Displacement Time-History Comparison for Companion Set CS3 with L_d=1830 mm and P_d~133 kPa.
(Typical pressure-time history record from shot CS3-C-2)

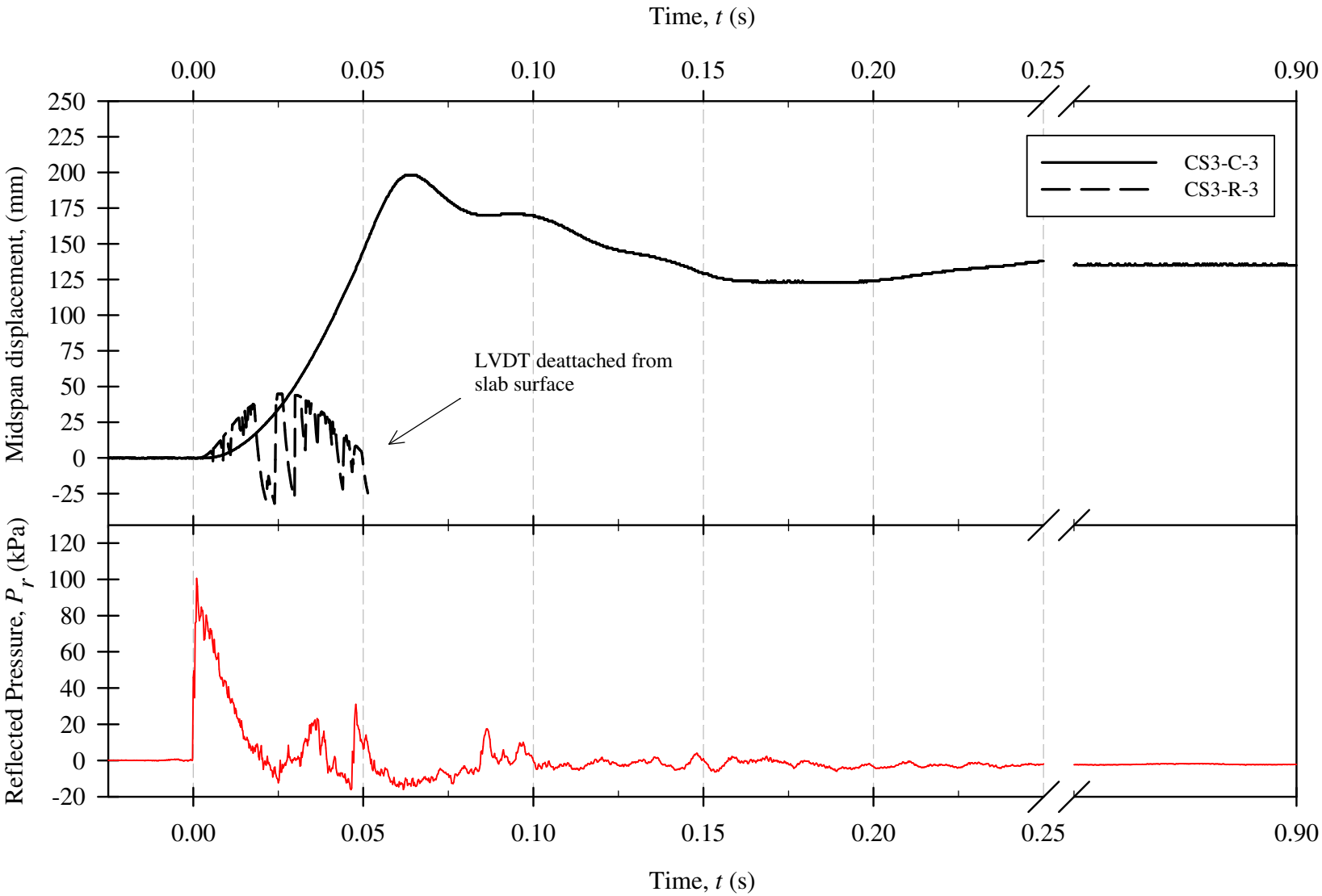

Figure A-12: Displacement Time-History Comparison for Companion Set CS3 with L_d=1830 mm and P_d~663 kPa.
(Typical pressure-time history record from shot CS3-C-3)

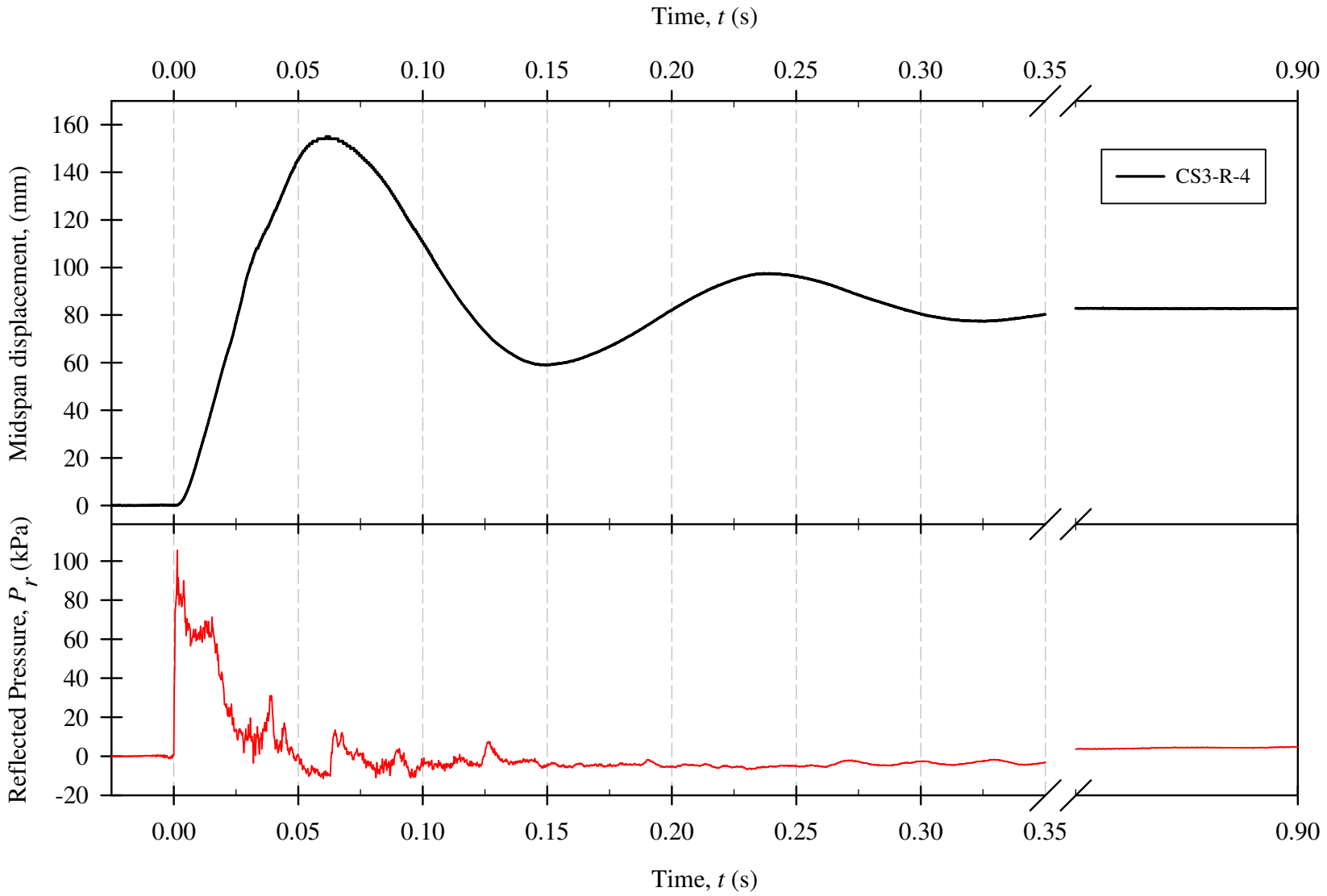

Figure A-13: Displacement Time-History Comparison for Companion Set CS3 with L_d=3660 mm and P_d=718 kPa.

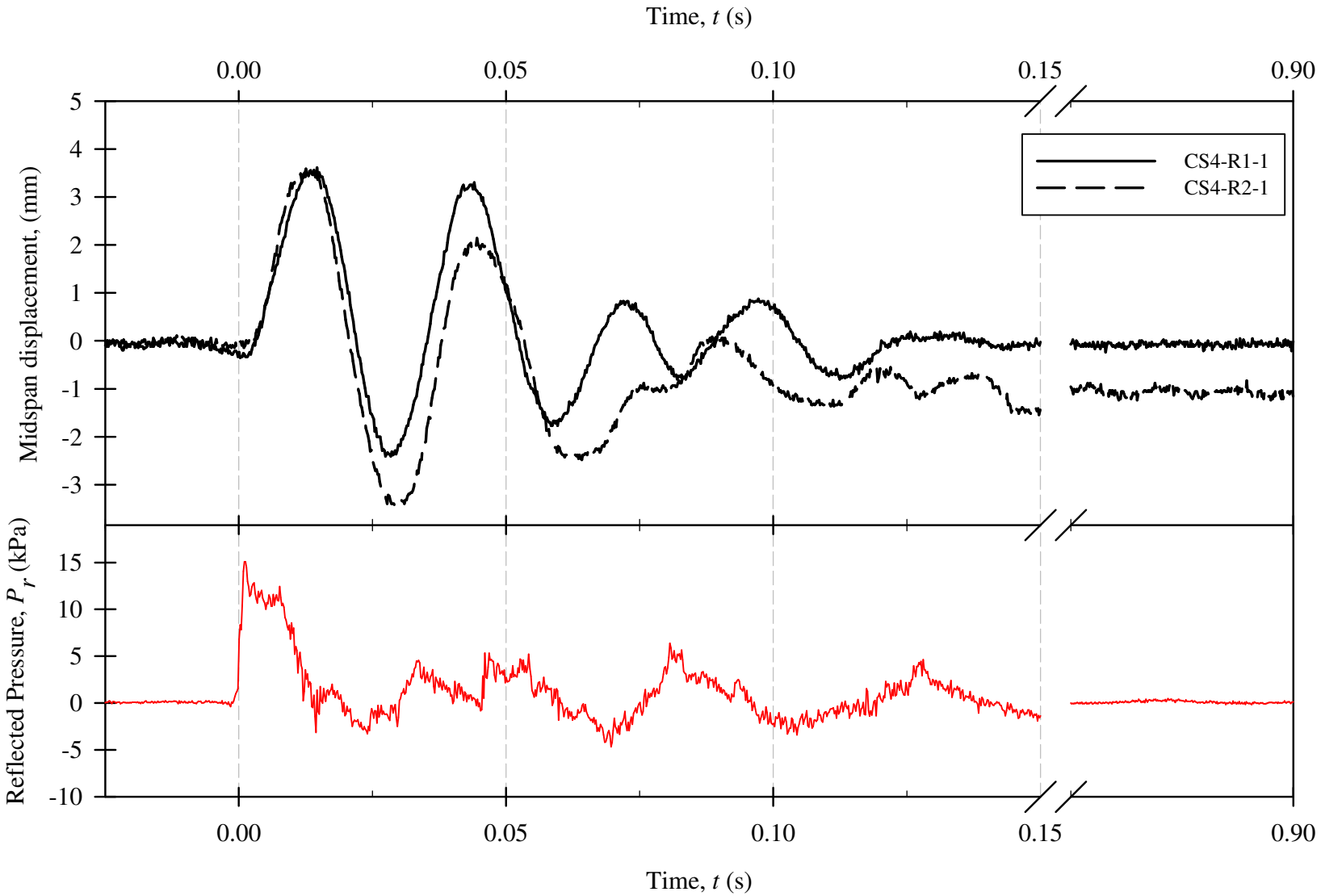

Figure A-14: Displacement Time-History Comparison for Companion Set CS4 with L_d=1830 mm and P_d~80 kPa.
(Typical pressure-time history record from shot CS4-R1-1)

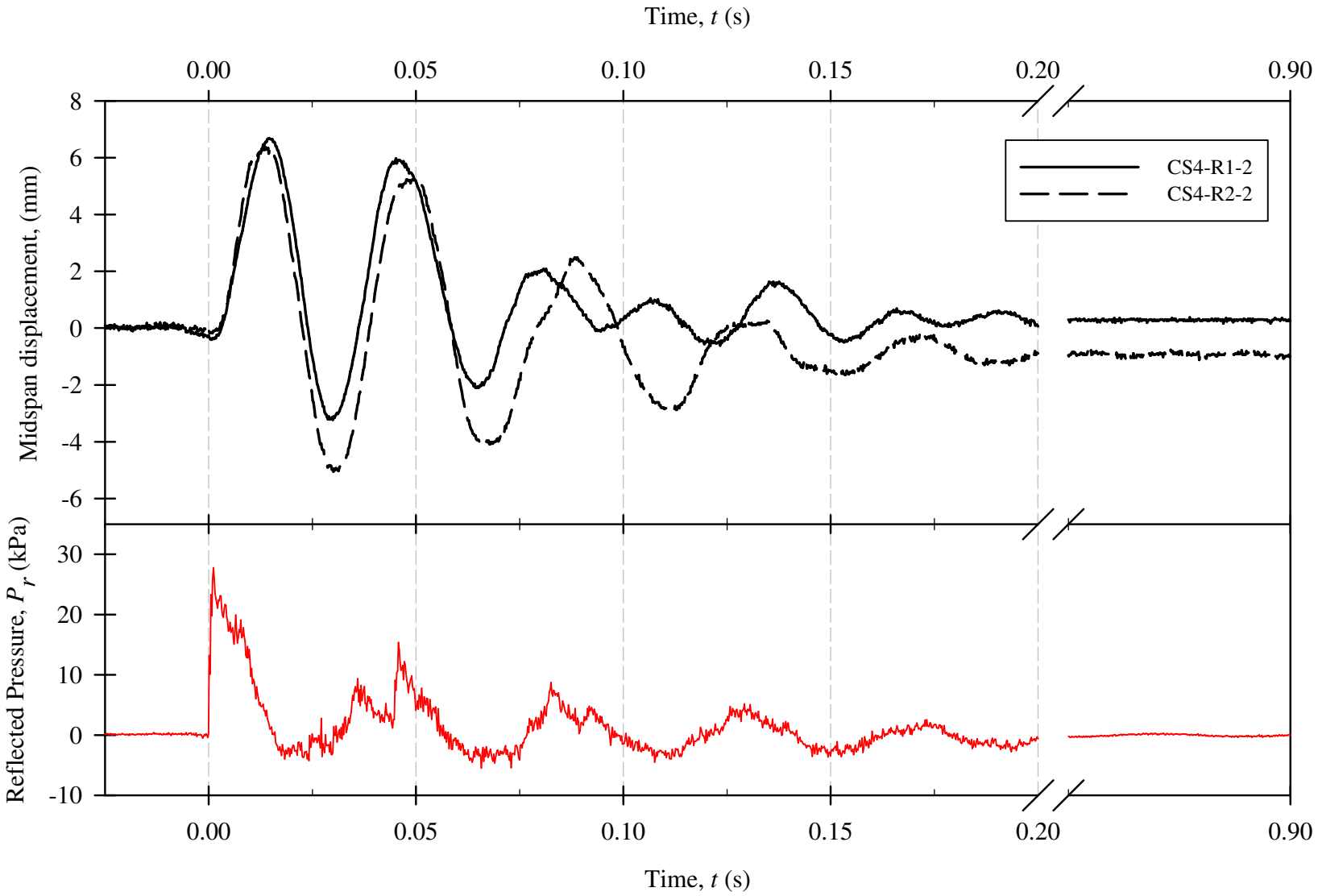

Figure A-15: Displacement Time-History Comparison for Companion Set CS4 with L_d=1830 mm and P_d~135 kPa.
(Typical pressure-time history record from shot CS4-R1-2)

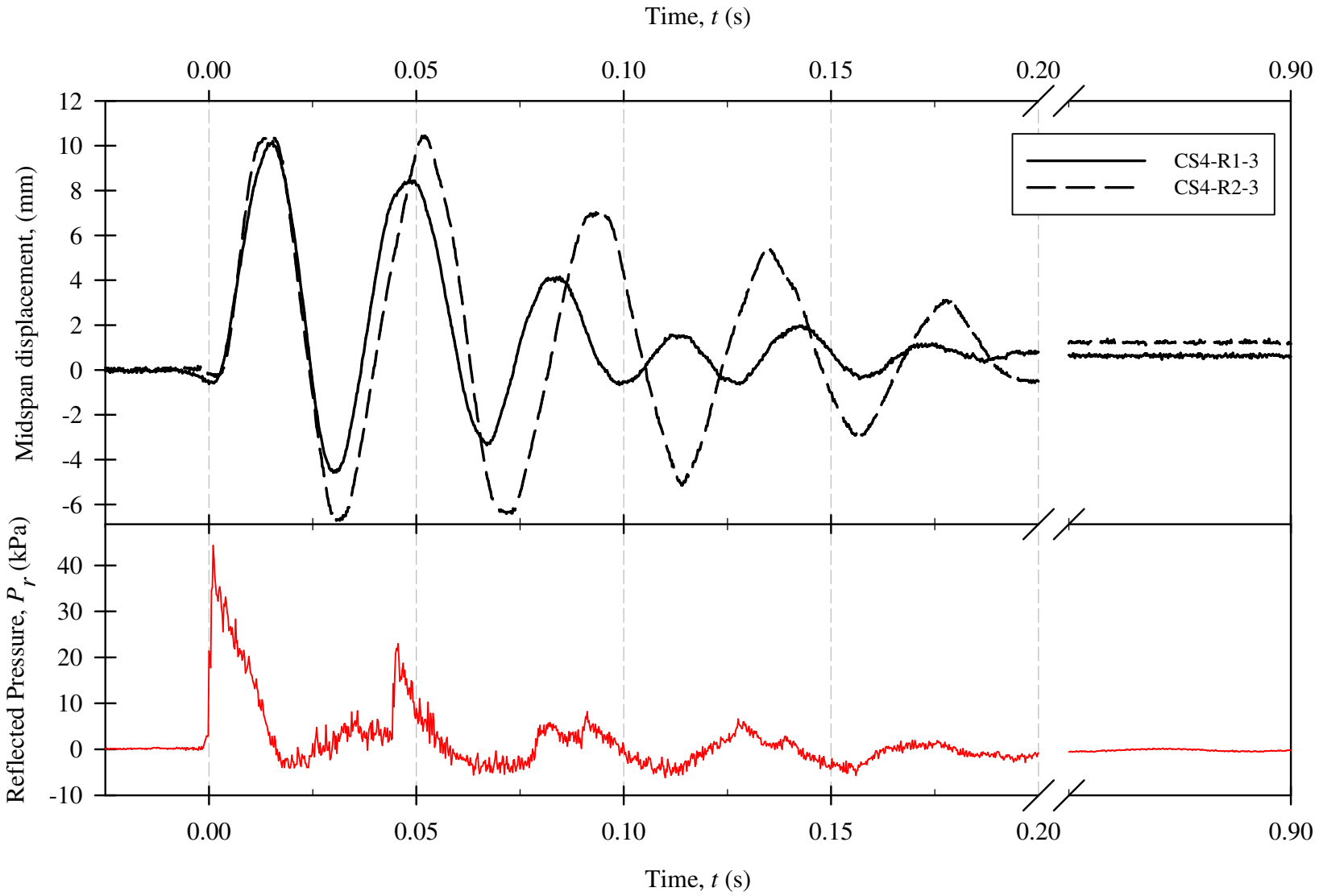

Figure A-16: Displacement Time-History Comparison for Companion Set CS4 with L_d=1830 mm and P_d~215 kPa.
(Typical pressure-time history record from shot CS4-R1-3)

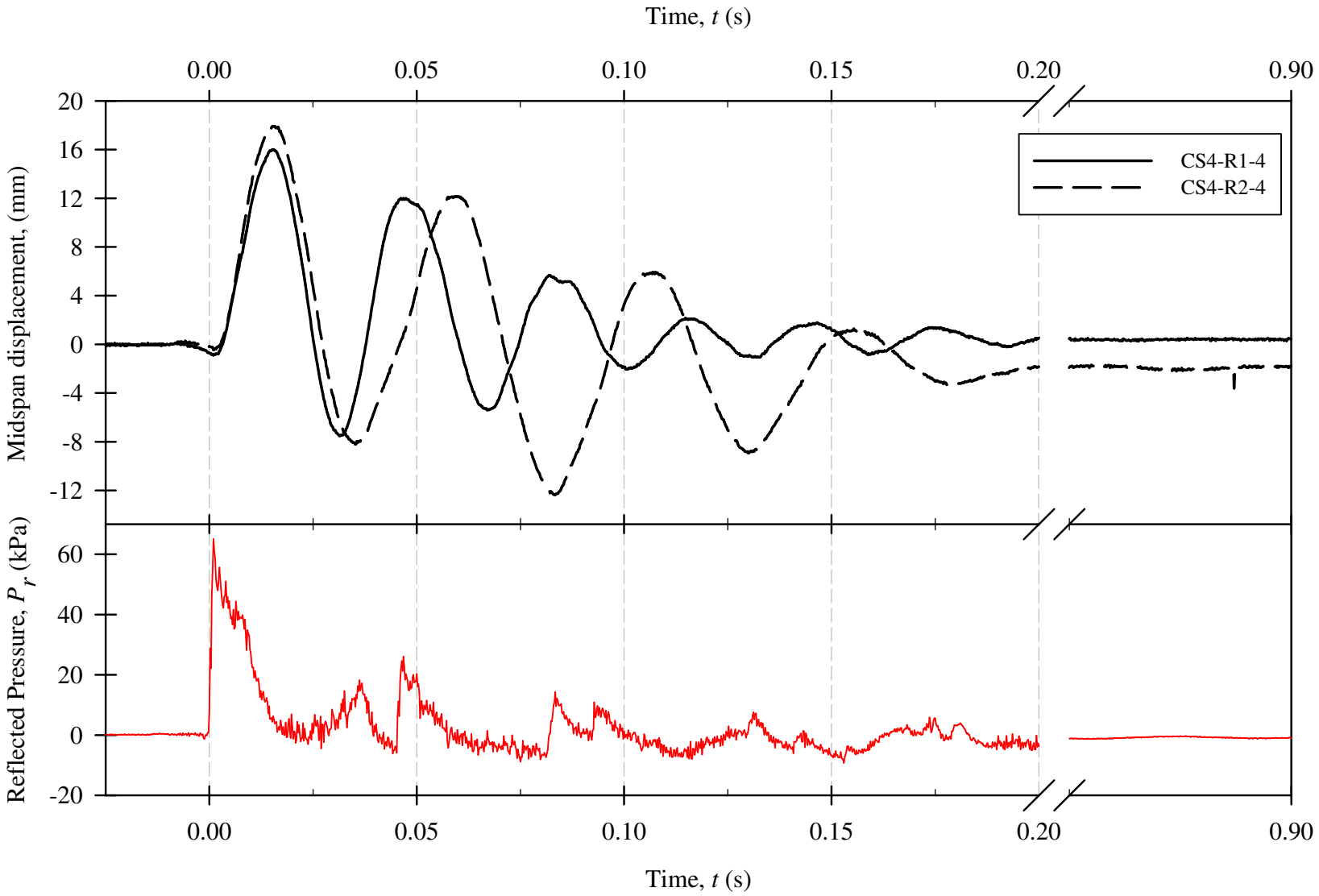

Figure A-17: Displacement Time-History Comparison for Companion Set CS4 with L_d=1830 mm and P_d~378 kPa.
(Typical pressure-time history record from shot CS4-R1-4)

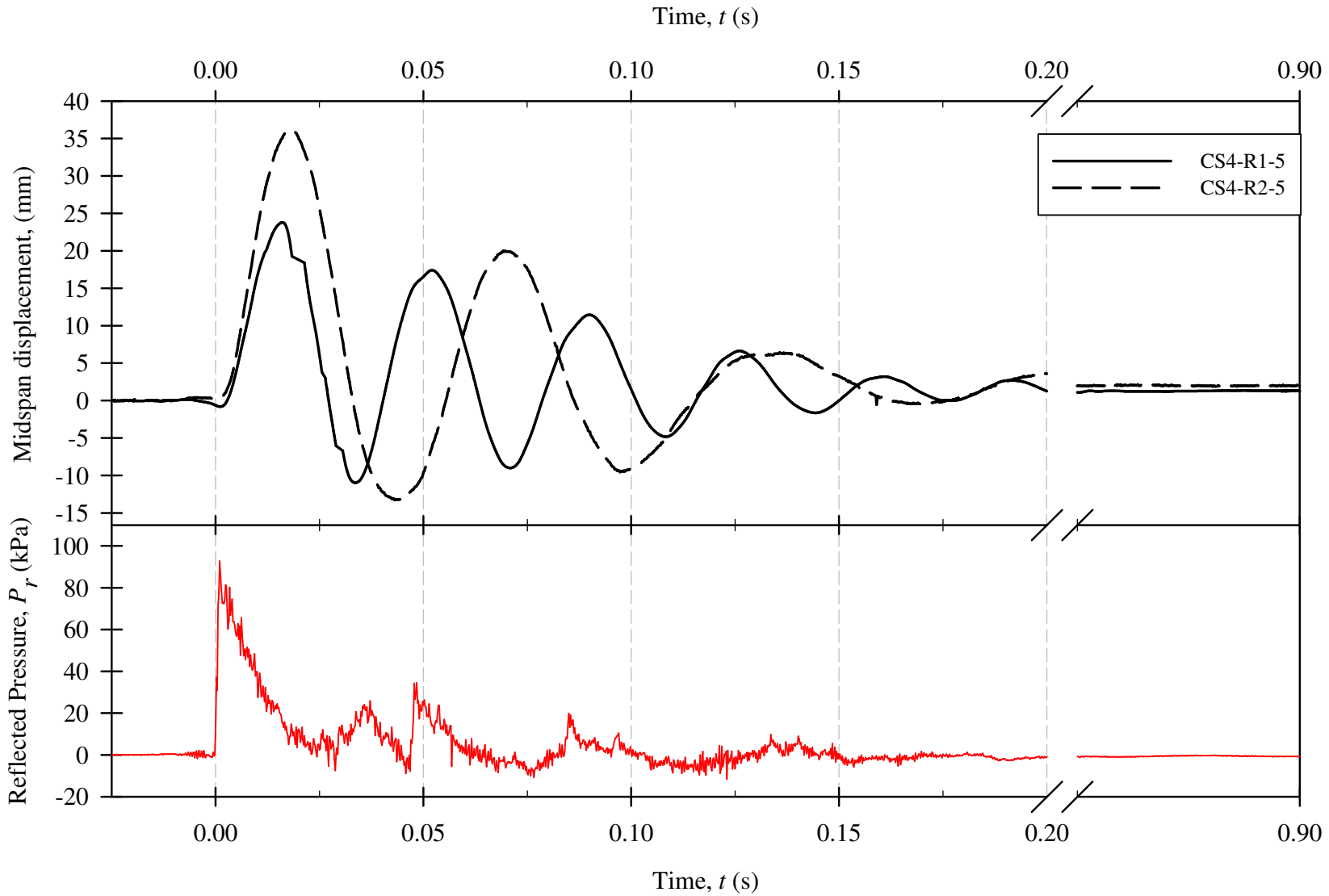

Figure A-18: Displacement Time-History Comparison for Companion Set CS4 with L_d=1830 mm and P_d~615 kPa.
(Typical pressure-time history record from shot CS4-R1-5)

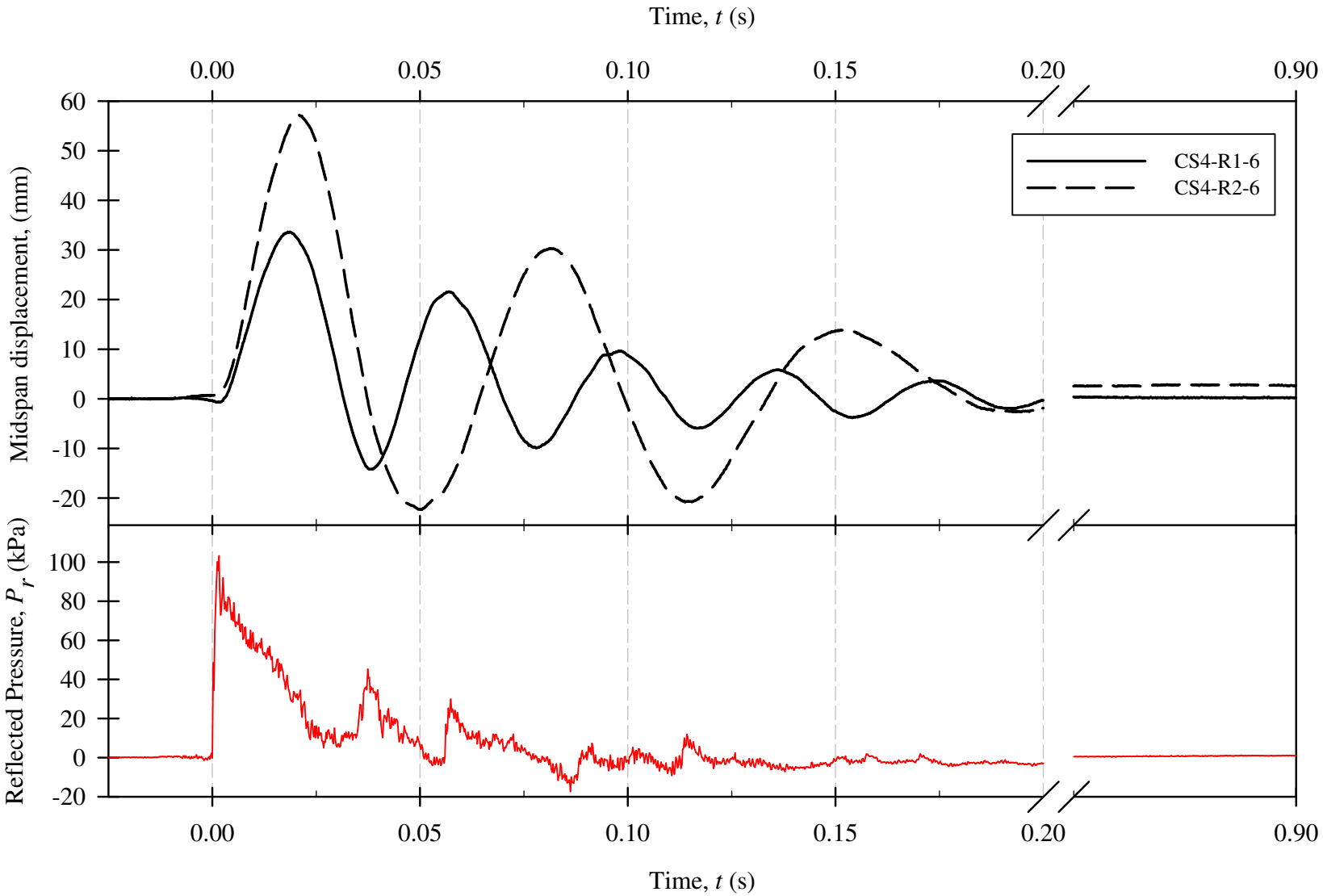

Figure A-19: Displacement Time-History Comparison for Companion Set CS4 with L_d=2745 mm and P_d~680 kPa.
(Typical pressure-time history record from shot CS4-R1-6)

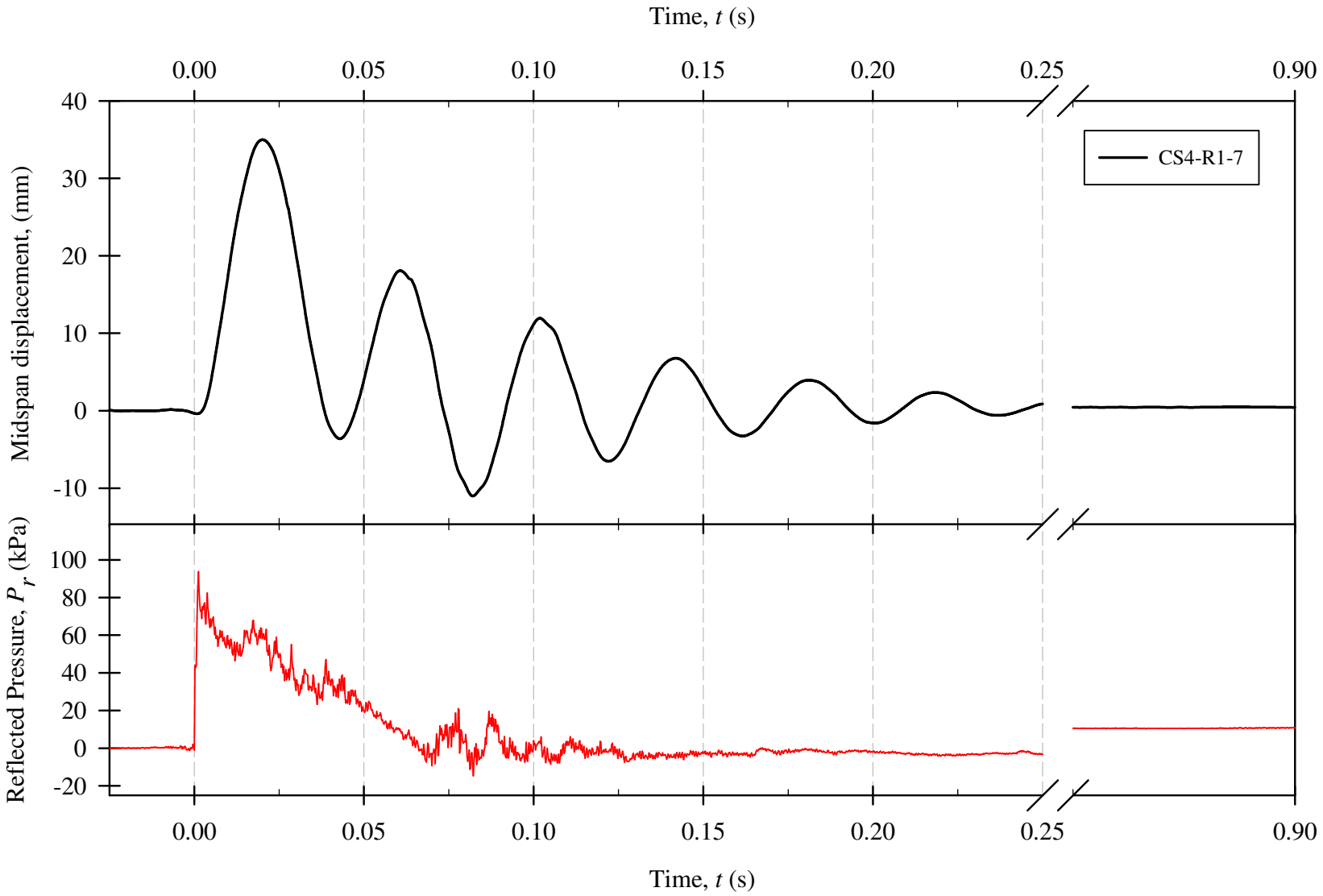

Figure A-20: Displacement Time-History Comparison for Companion Set CS4 with L_d=4880 mm and P_d~613 kPa.
(Typical pressure-time history record from shot CS4-R1-7)

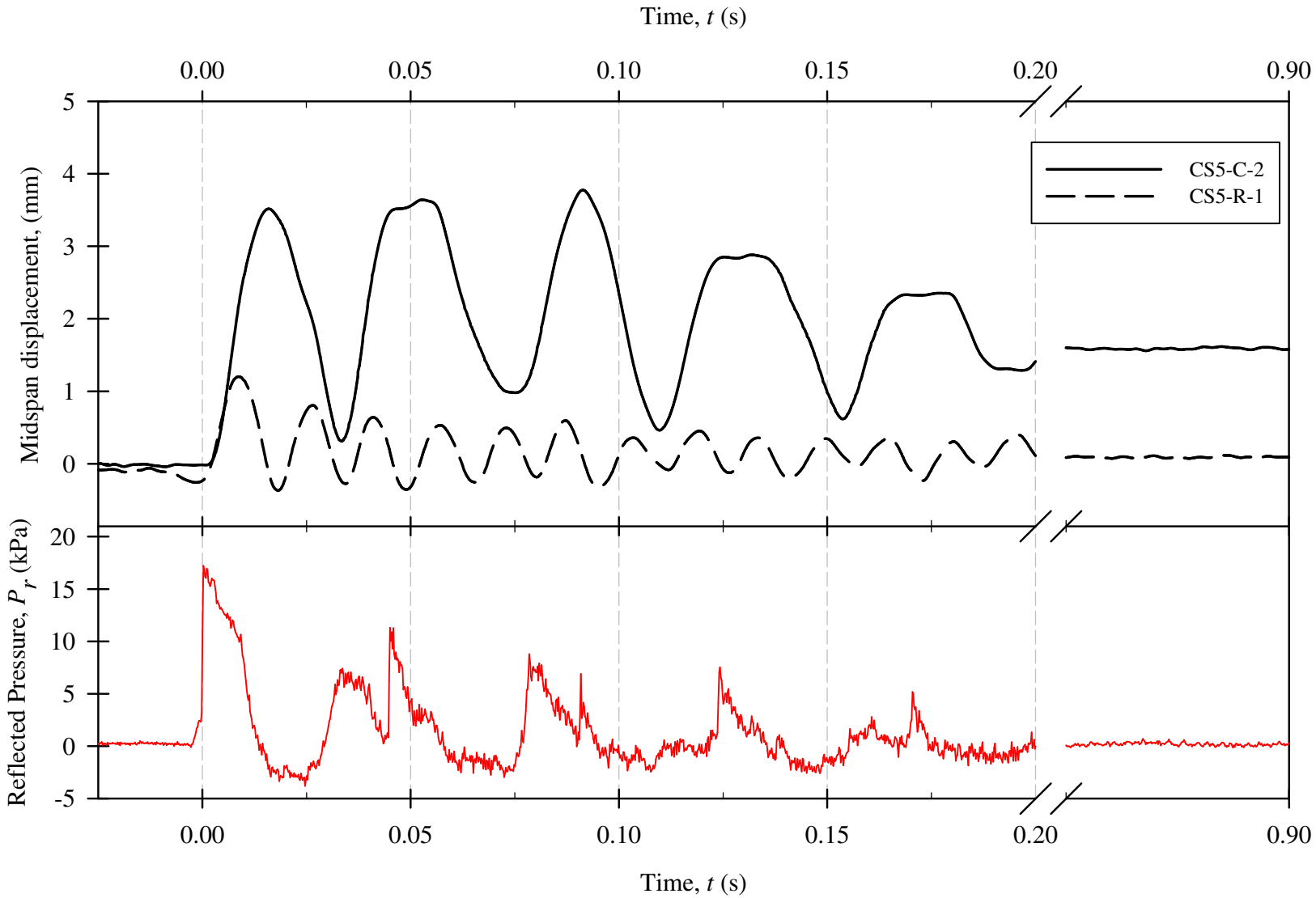

Figure A-21: Displacement Time-History Comparison for Companion Set CS5 with L_d=1830 mm and P_d~77 kPa.
(Typical pressure-time history record from shot CS5-C-2)

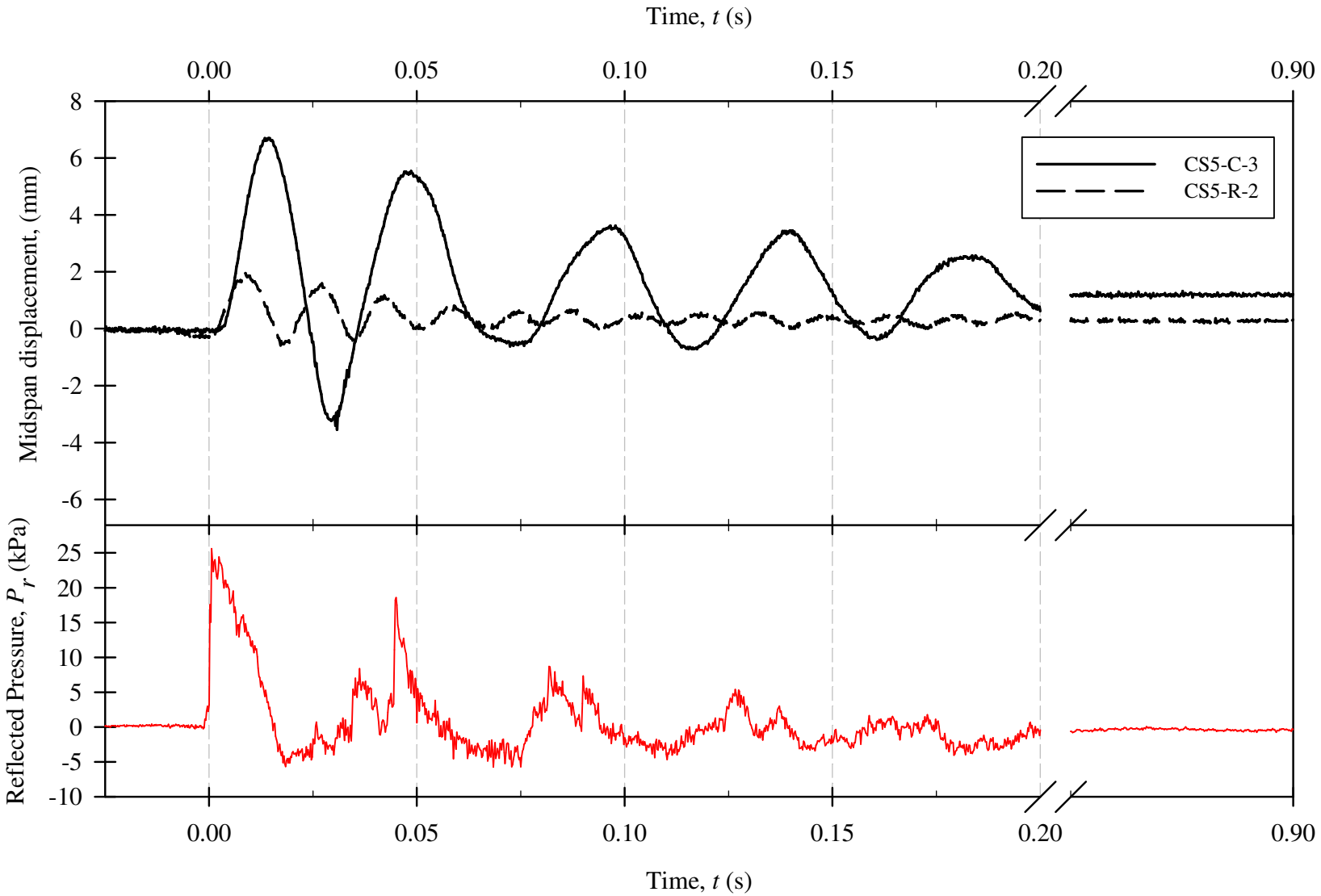

Figure A-22: Displacement Time-History Comparison for Companion Set CS5 with L_d=1830 mm and P_d~125 kPa.
(Typical pressure-time history record from shot CS5-C-3)

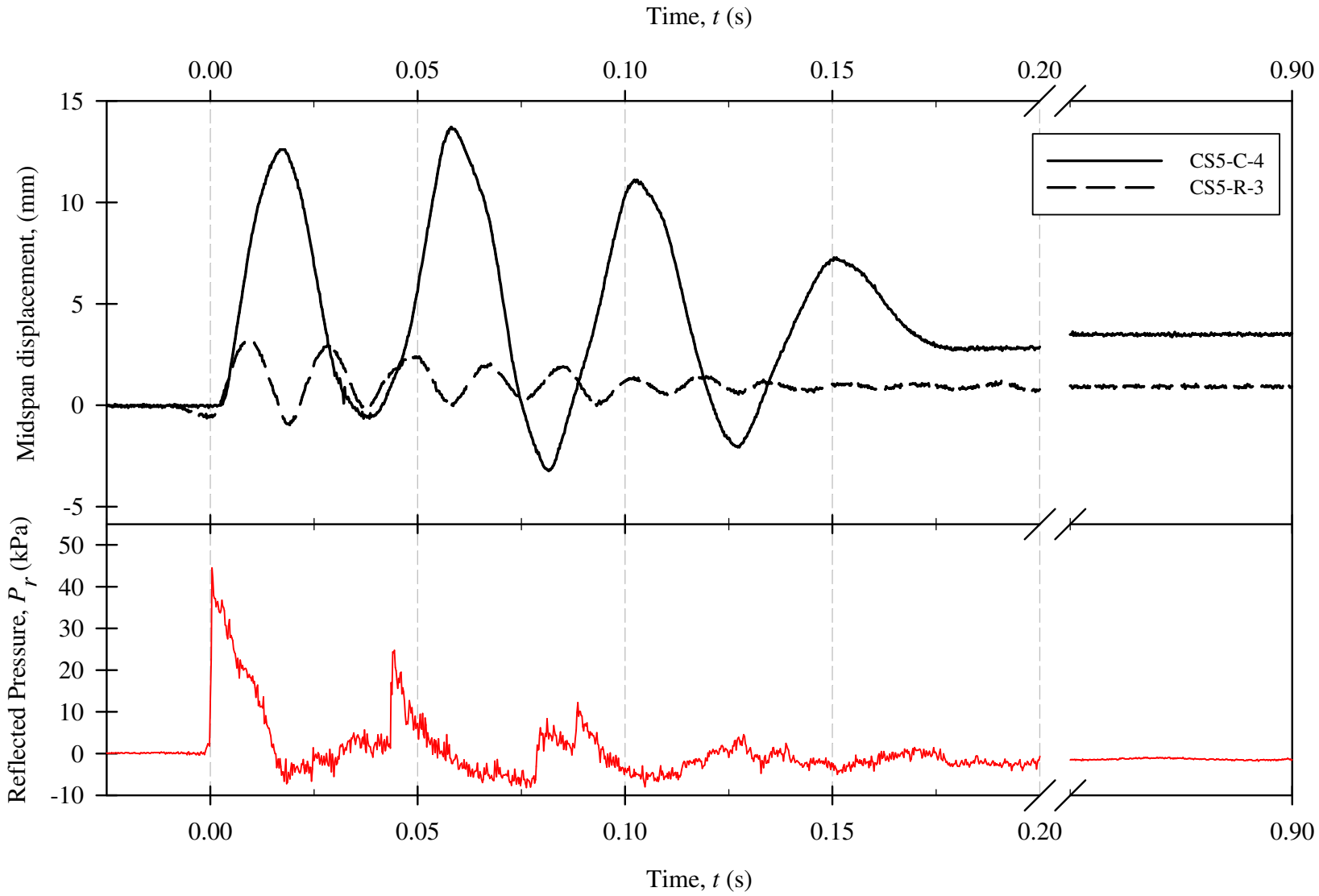

Figure A-23: Displacement Time-History Comparison for Companion Set CS5 with L_d=1830 mm and P_d~216 kPa.
(Typical pressure-time history record from shot CS5-C-4)

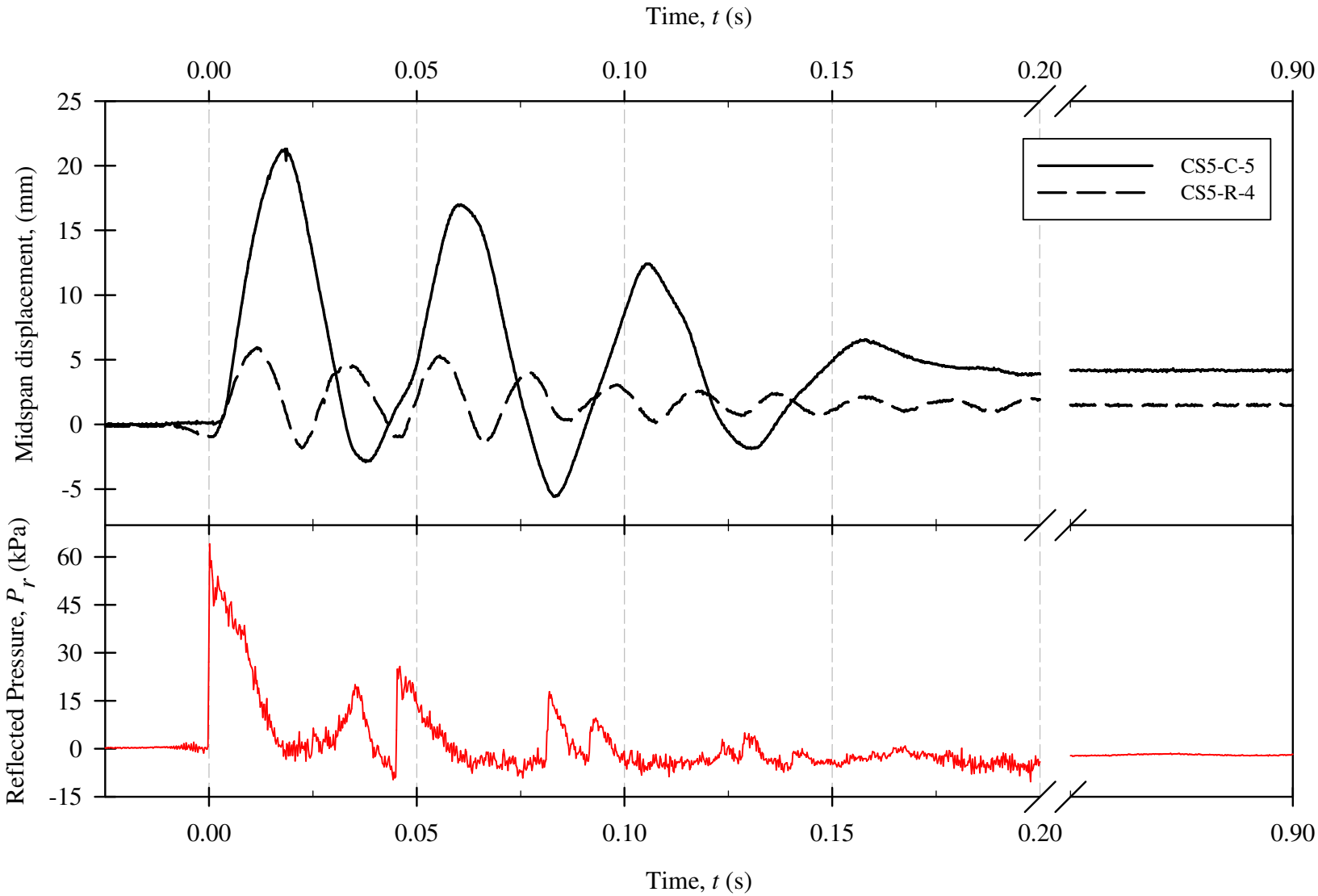

Figure A-24: Displacement Time-History Comparison for Companion Set CS5 with L_d=1830 mm and P_d~355 kPa.
(Typical pressure-time history record from shot CS5-C-5)

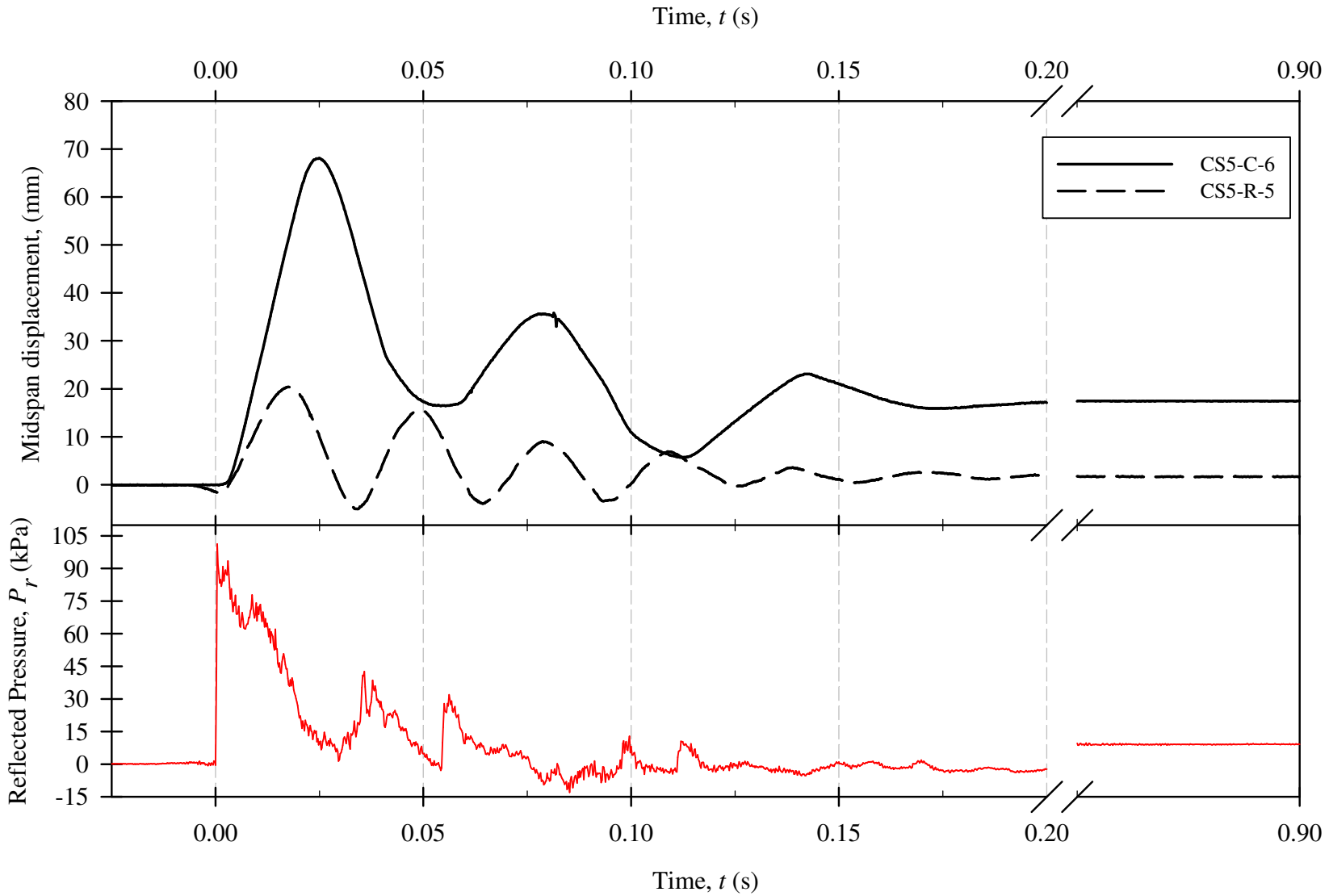

Figure A-25: Displacement Time-History Comparison for Companion Set CS5 with L_d=2745 mm and P_d~700 kPa.
(Typical pressure-time history record from shot CS5-C-6)

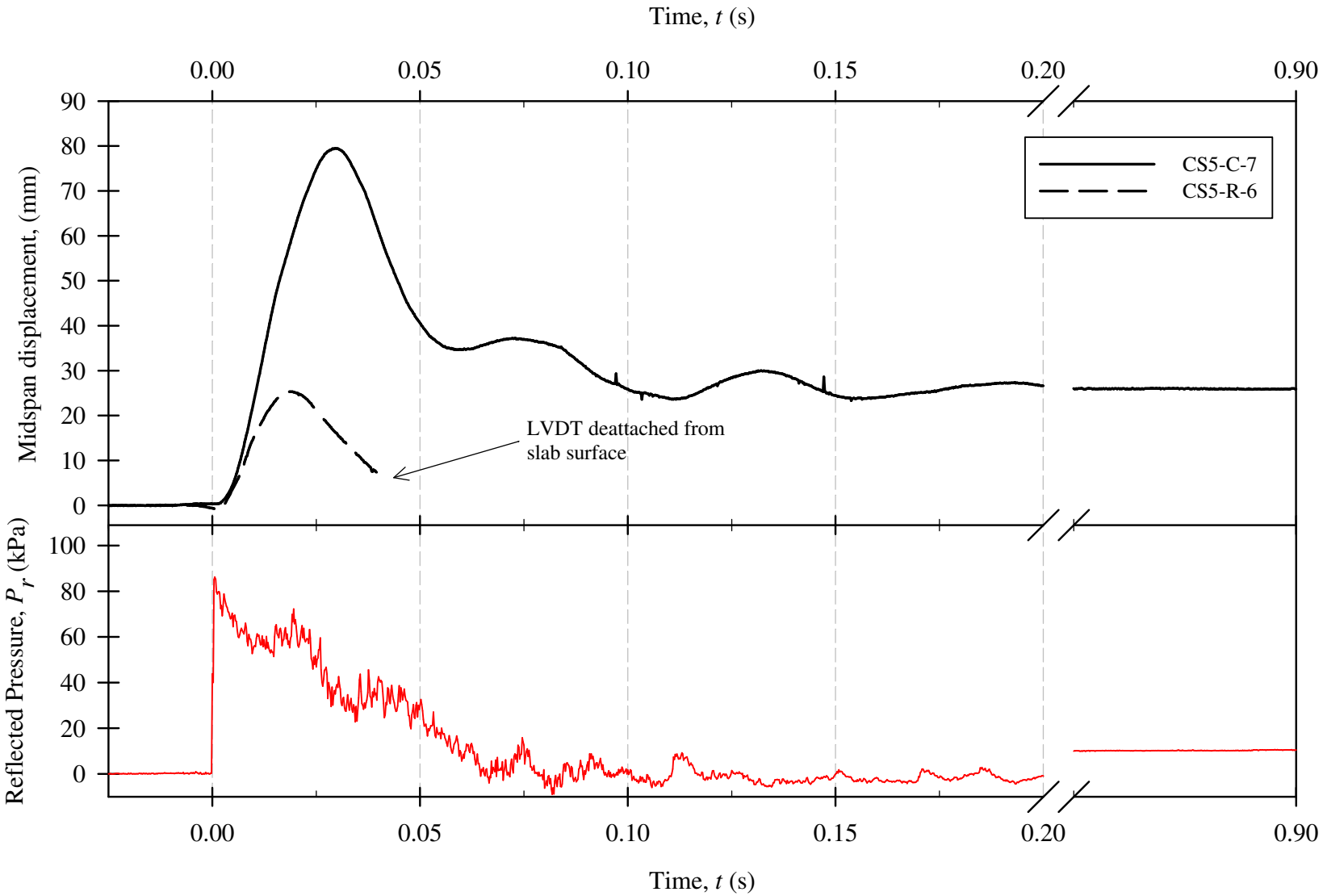

Figure A-26: Displacement Time-History Comparison for Companion Set CS5 with L_d=4880 mm and P_d~650 kPa.
(Typical pressure-time history record from shot CS5-C-7)

Appendix B: SDOF Displacement Time-Histories

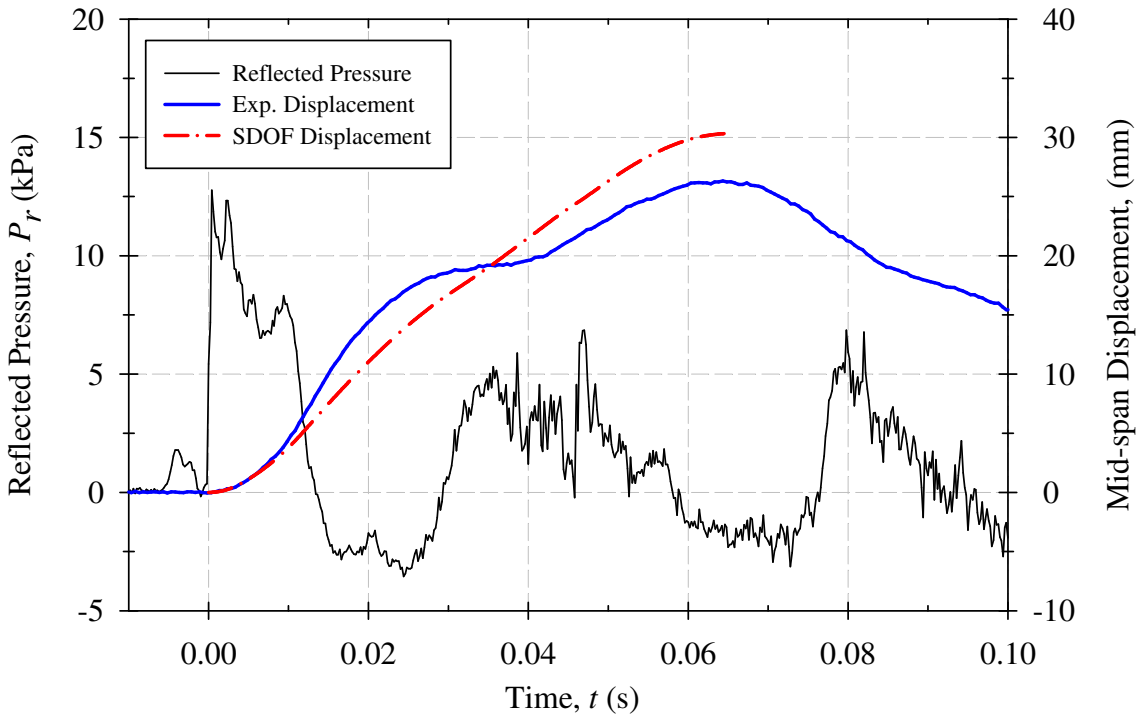

Figure B-1: Experimental mid-span slab displacements plotted against those predicted by SDOF analysis for CS1-C - Shot 1.

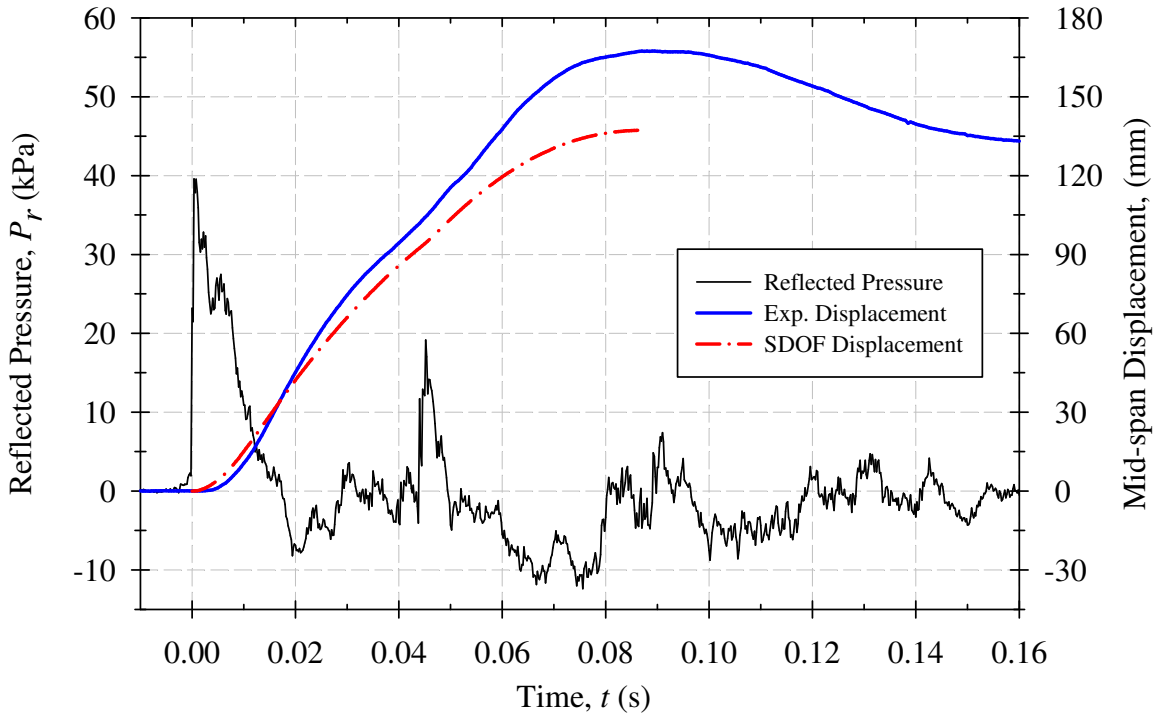

Figure B-2: Experimental mid-span slab displacements plotted against those predicted by SDOF analysis for CS1-C - Shot 2.

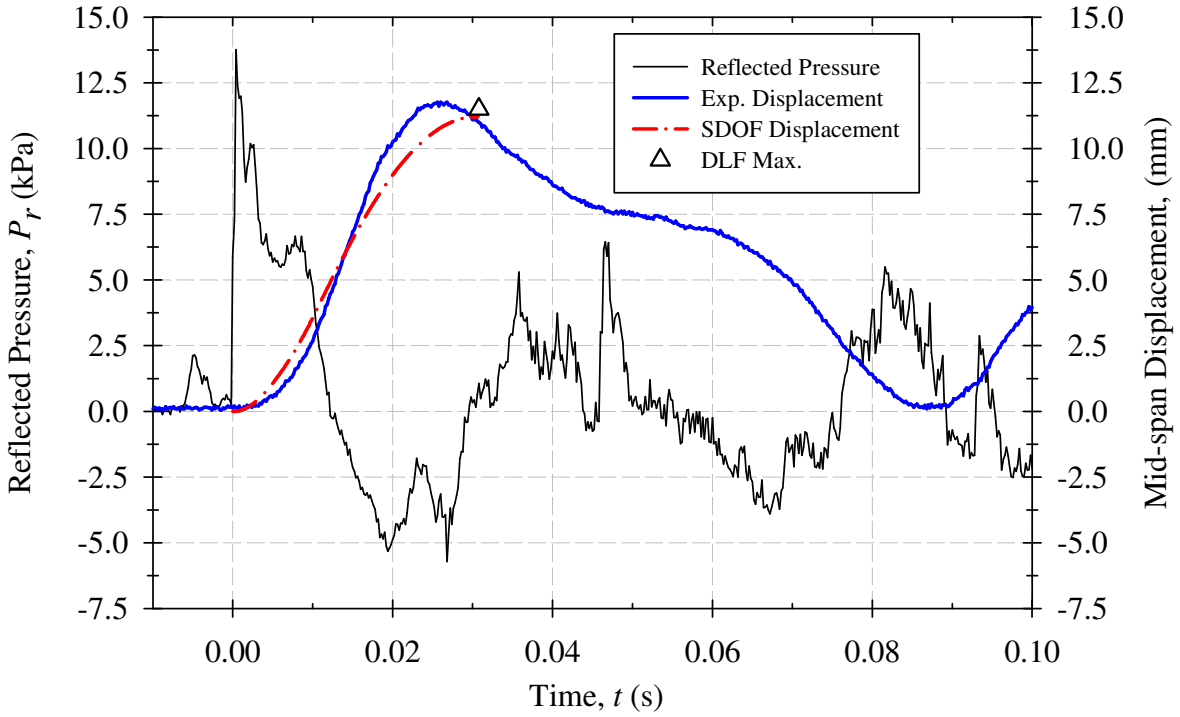

Figure B-3: Experimental mid-span slab displacements plotted against those predicted by SDOF analysis for CS1-R1 - Shot 1.

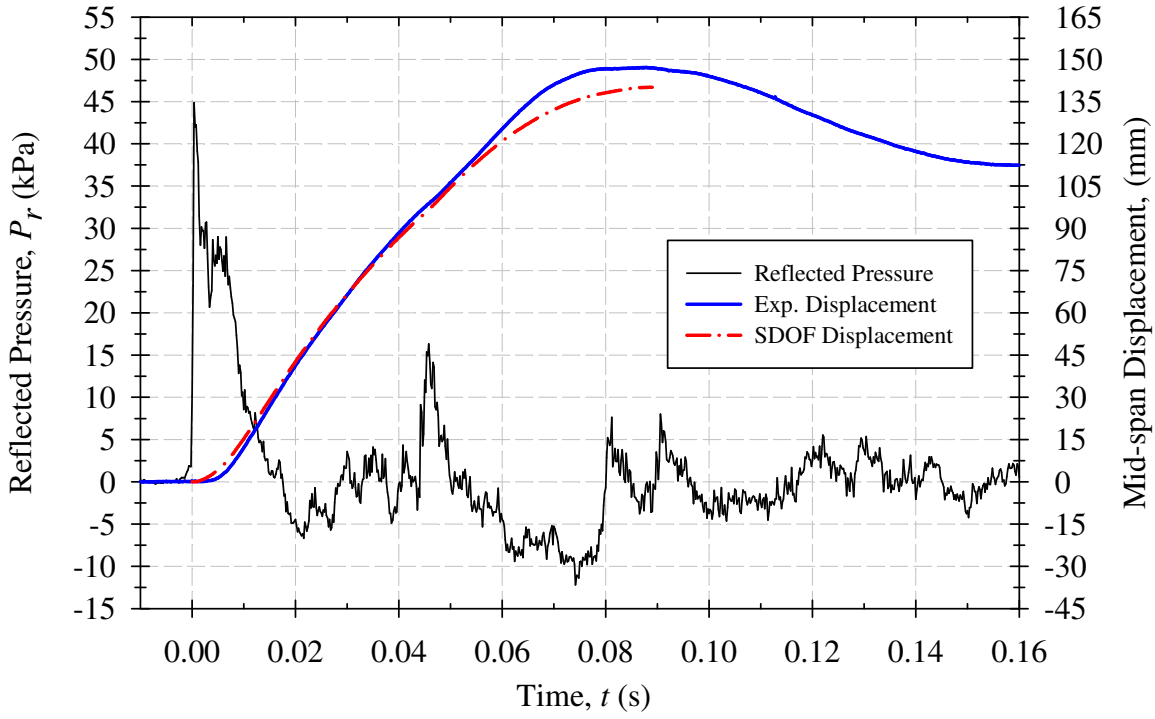

Figure B-4: Experimental mid-span slab displacements plotted against those predicted by SDOF analysis for CS1-R1 - Shot 2.

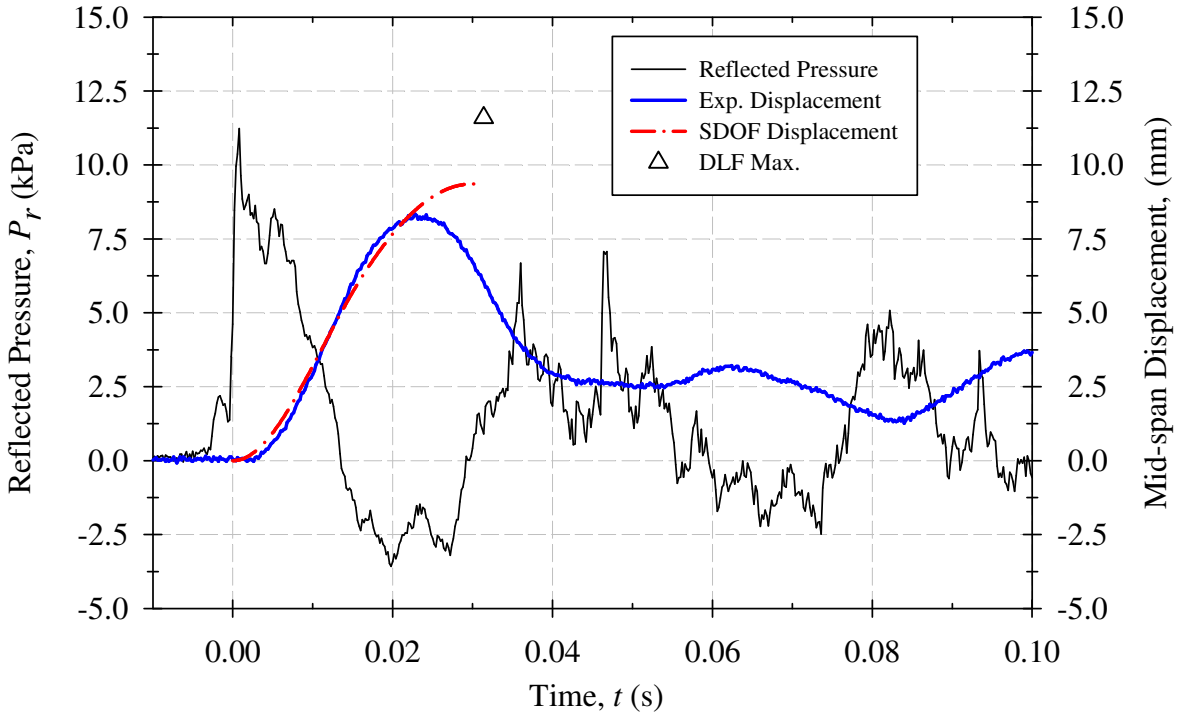

Figure B-5: Experimental mid-span slab displacements plotted against those predicted by SDOF analysis for CS1-R2 - Shot 1.

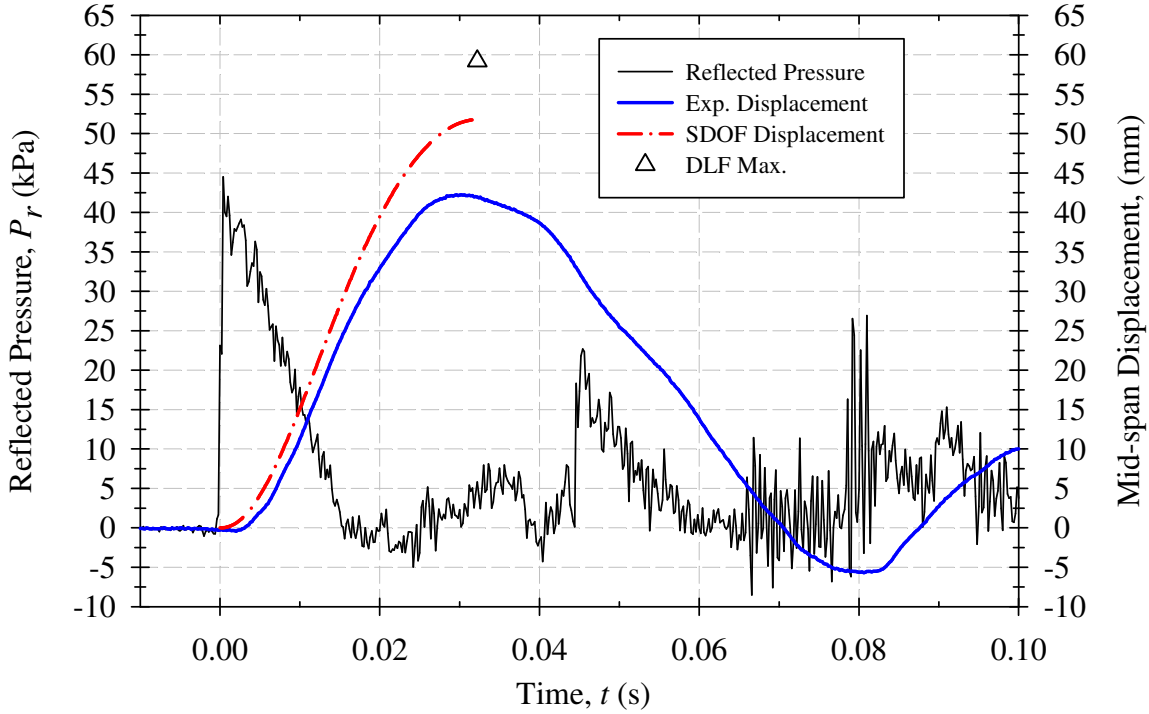

Figure B-6: Experimental mid-span slab displacements plotted against those predicted by SDOF analysis for CS1-R2 - Shot 2.

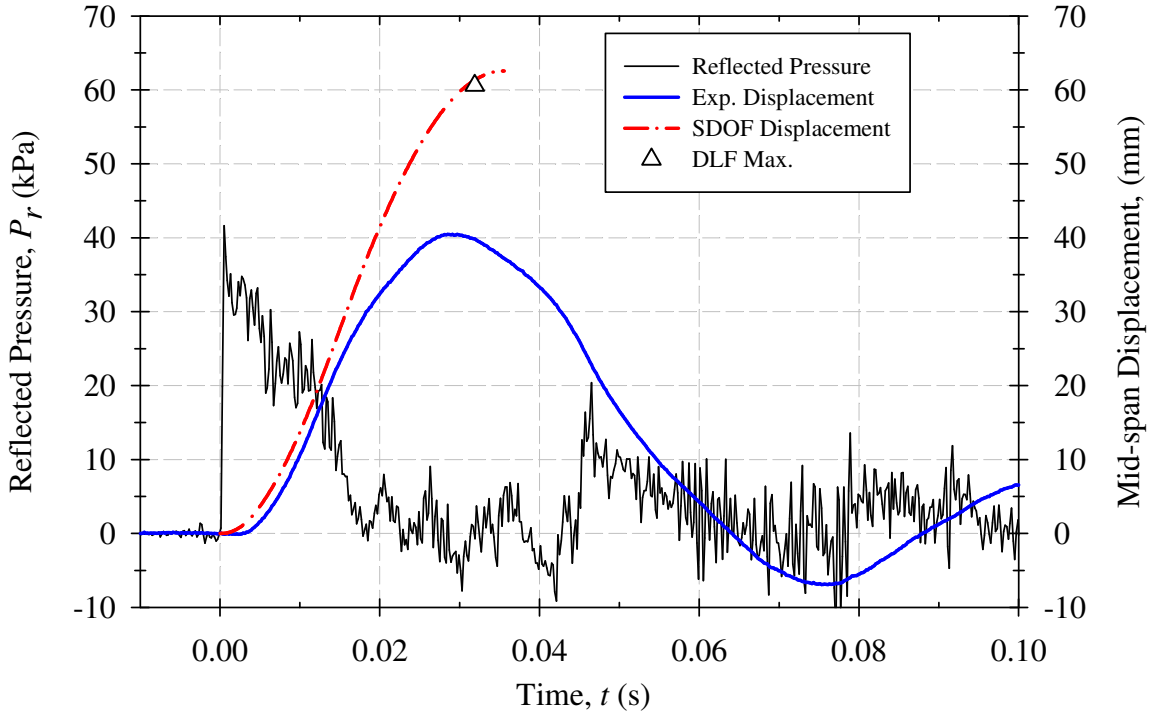

Figure B-7: Experimental mid-span slab displacements plotted against those predicted by SDOF analysis for CS1-R2 - Shot 3.

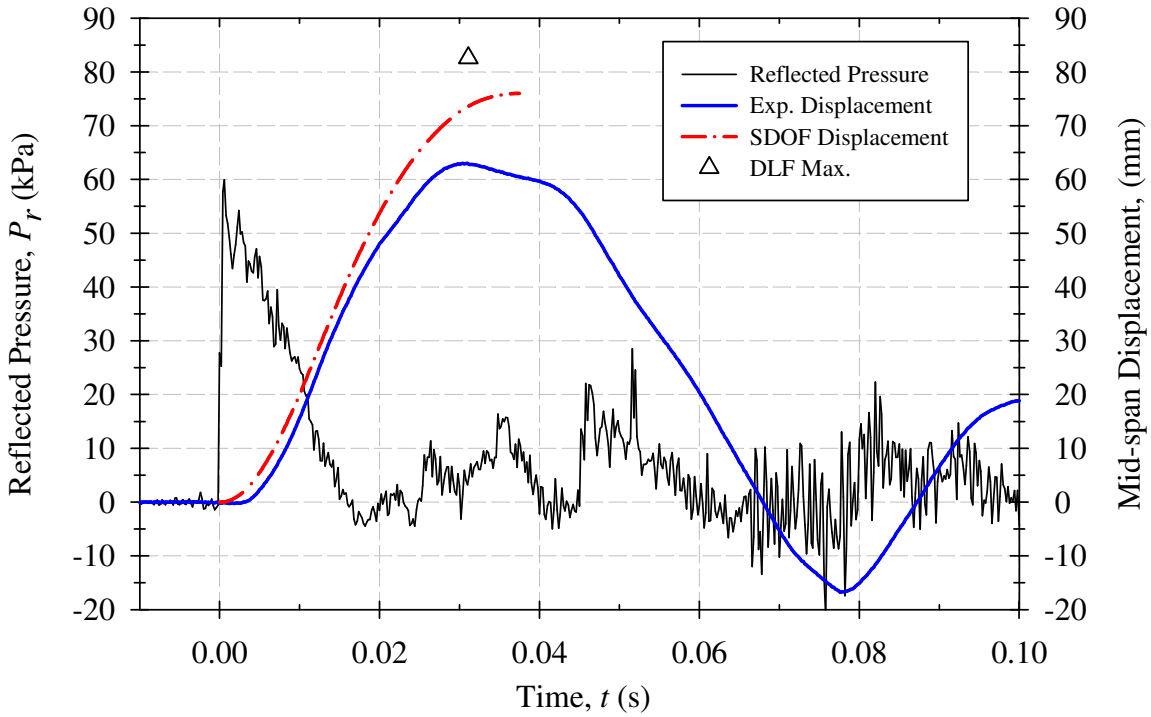

Figure B-8: Experimental mid-span slab displacements plotted against those predicted by SDOF analysis for CS1-R2 - Shot 4.

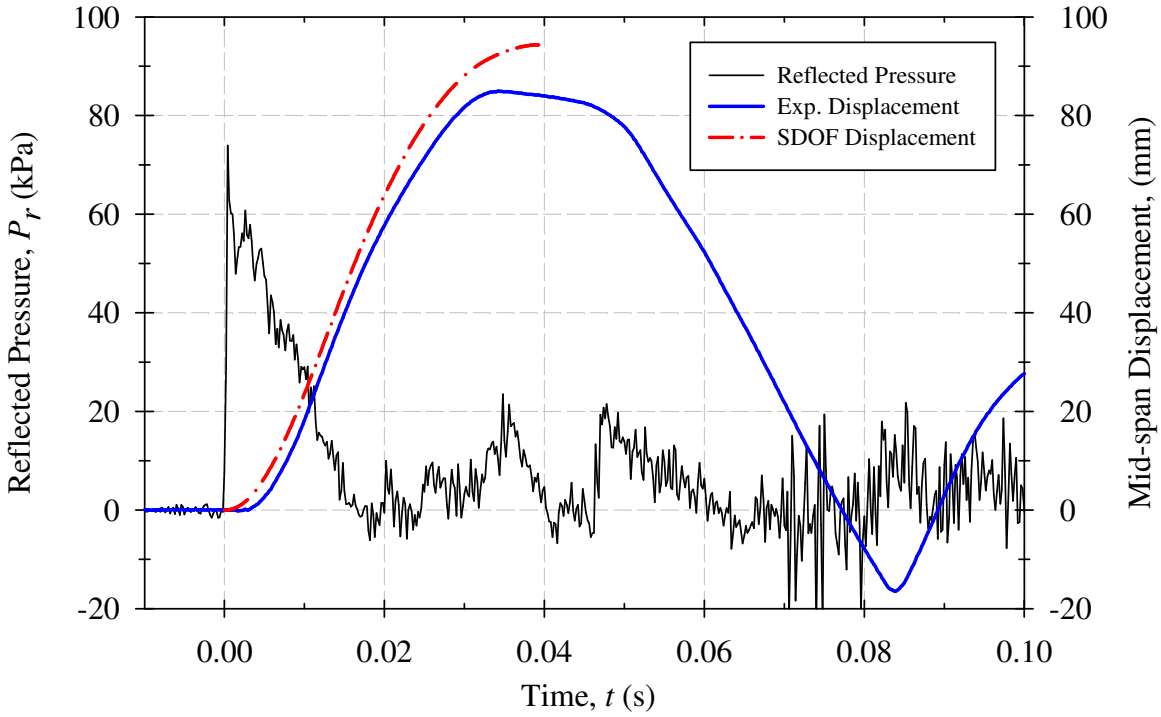

Figure B-9: Experimental mid-span slab displacements plotted against those predicted by SDOF analysis for CS1-R2 - Shot 5.

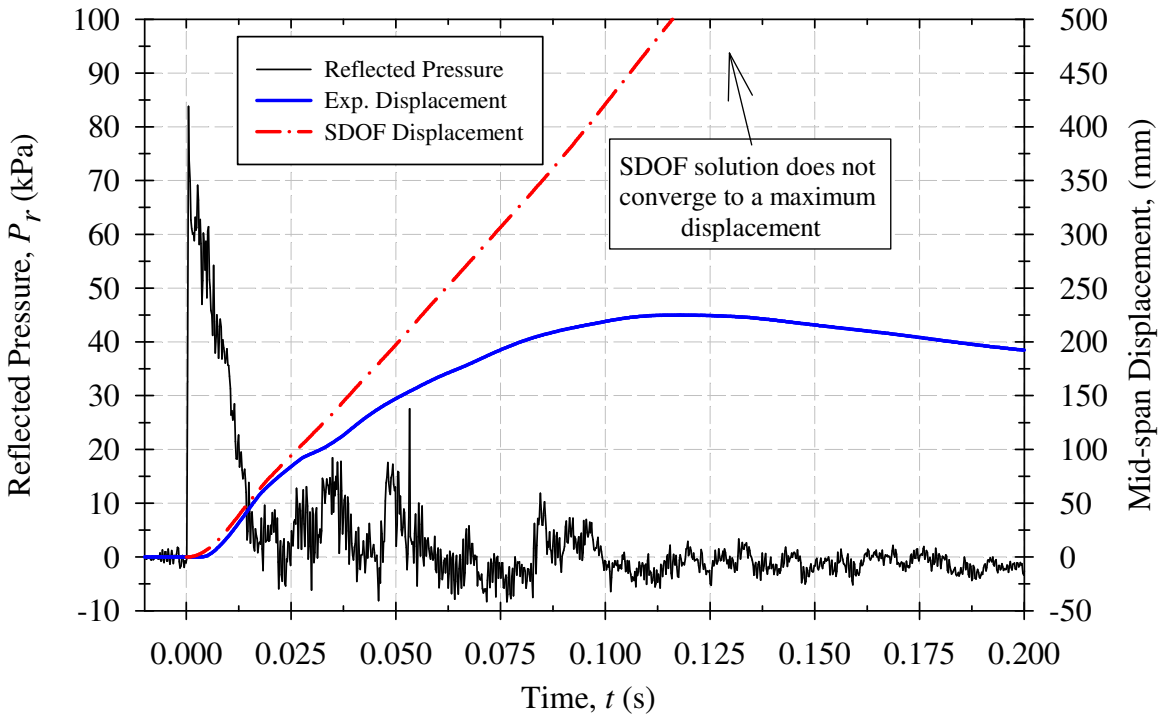

Figure B-10: Experimental mid-span slab displacements plotted against those predicted by SDOF analysis for CS1-R2 - Shot 6.

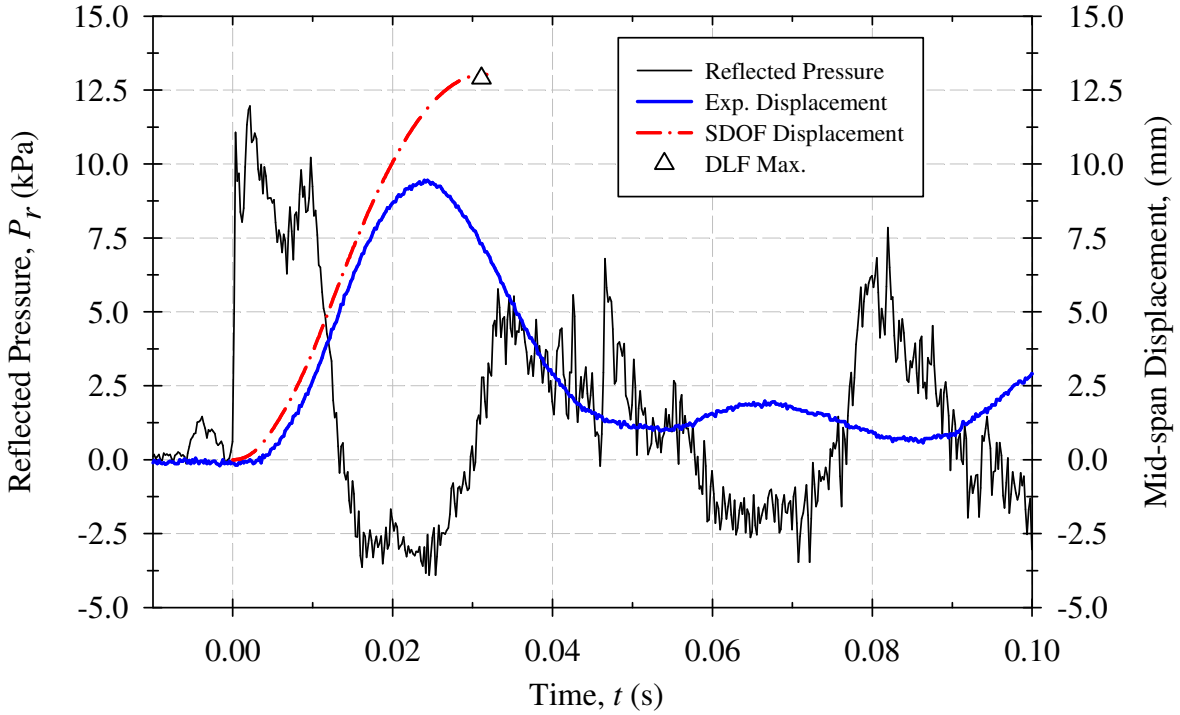

Figure B-11: Experimental mid-span slab displacements plotted against those predicted by SDOF analysis for CS1-A - Shot 1.

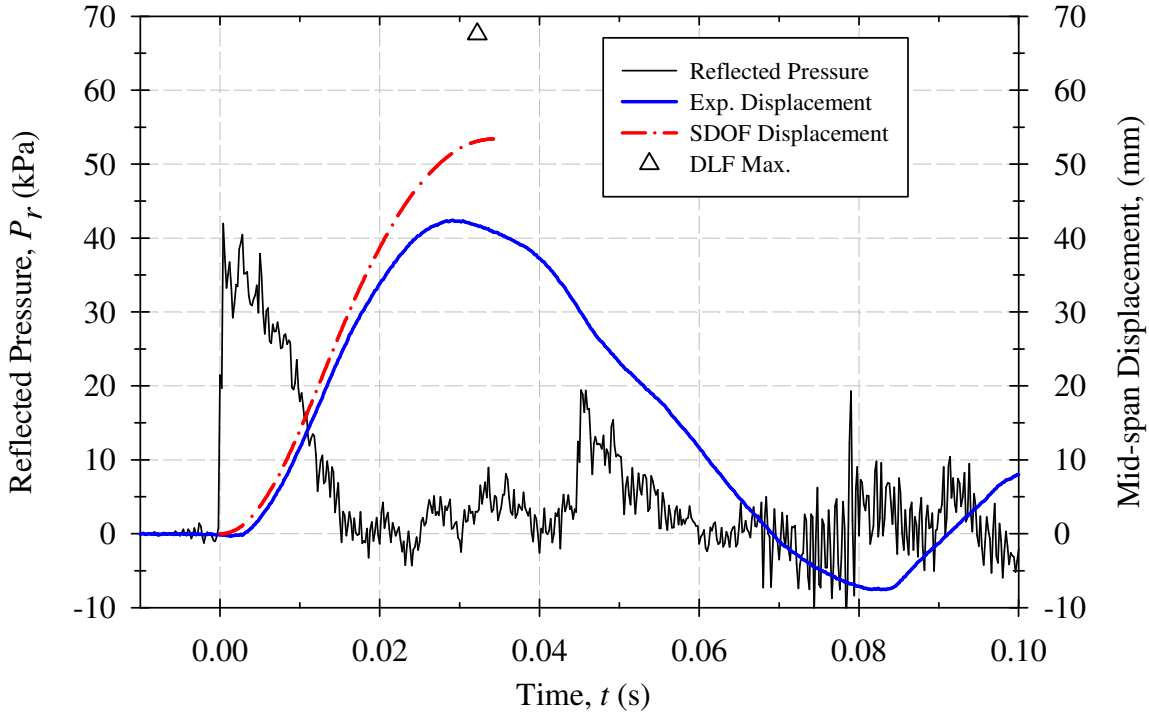

Figure B-12: Experimental mid-span slab displacements plotted against those predicted by SDOF analysis for CS1-A - Shot 2.

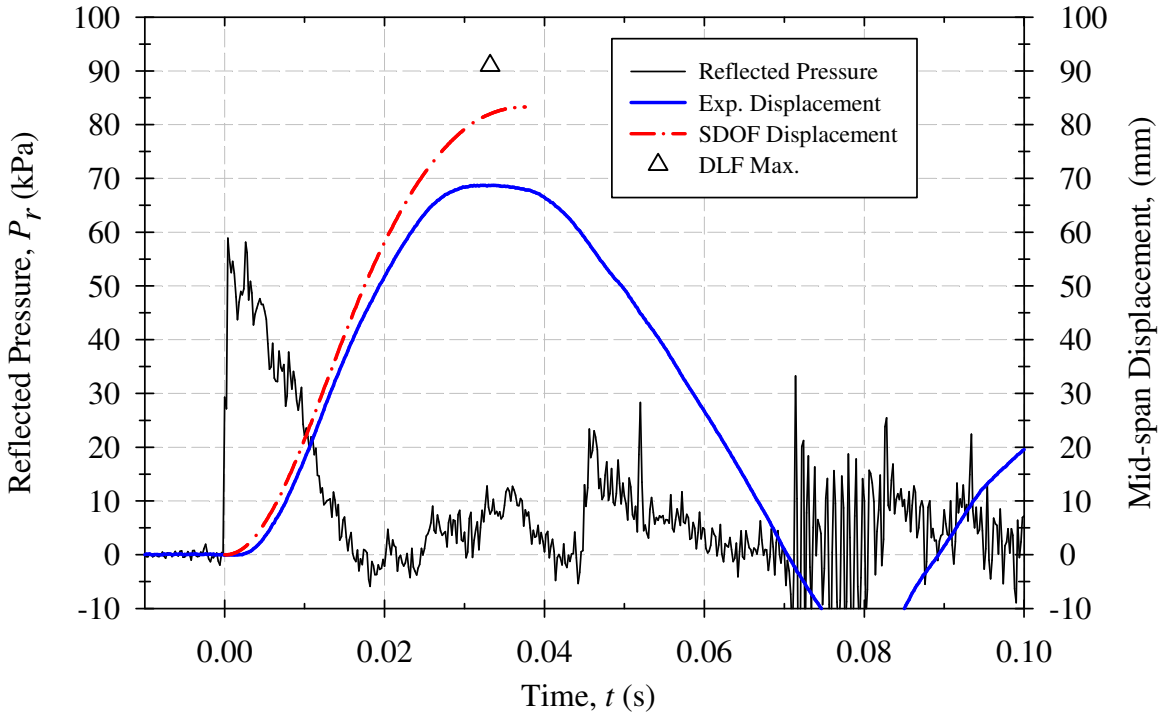

Figure B-13: Experimental mid-span slab displacements plotted against those predicted by SDOF analysis for CS1-A - Shot 3.

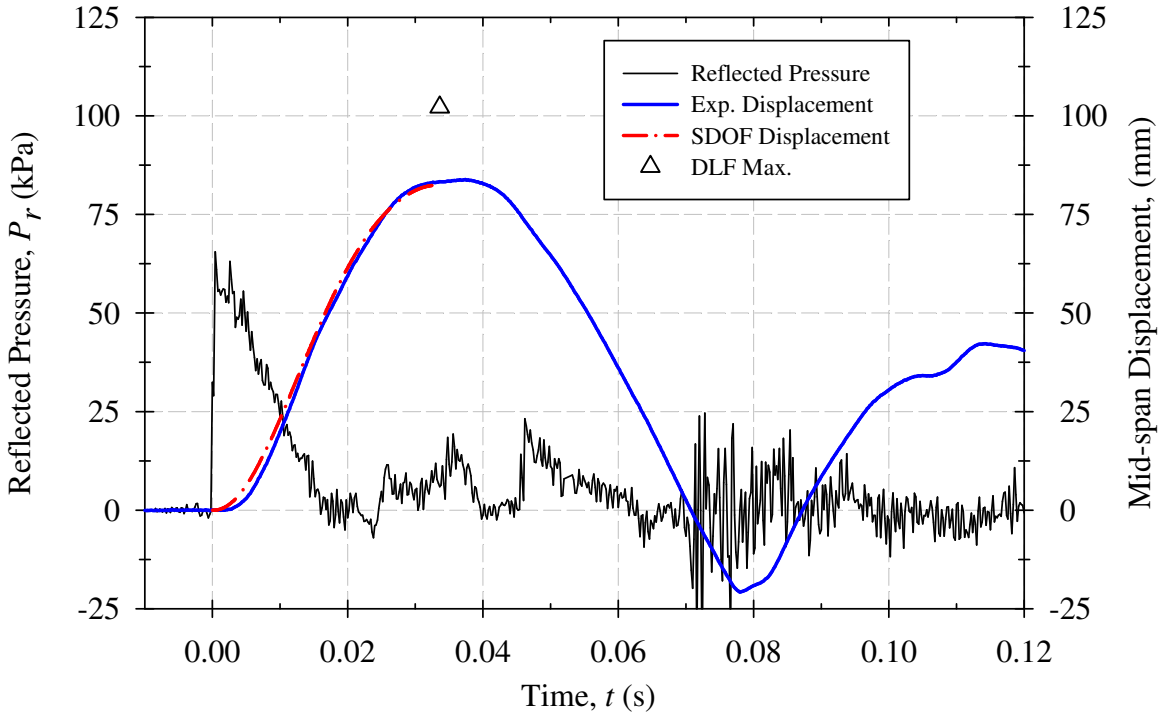

Figure B-14: Experimental mid-span slab displacements plotted against those predicted by SDOF analysis for CS1-A - Shot 4.

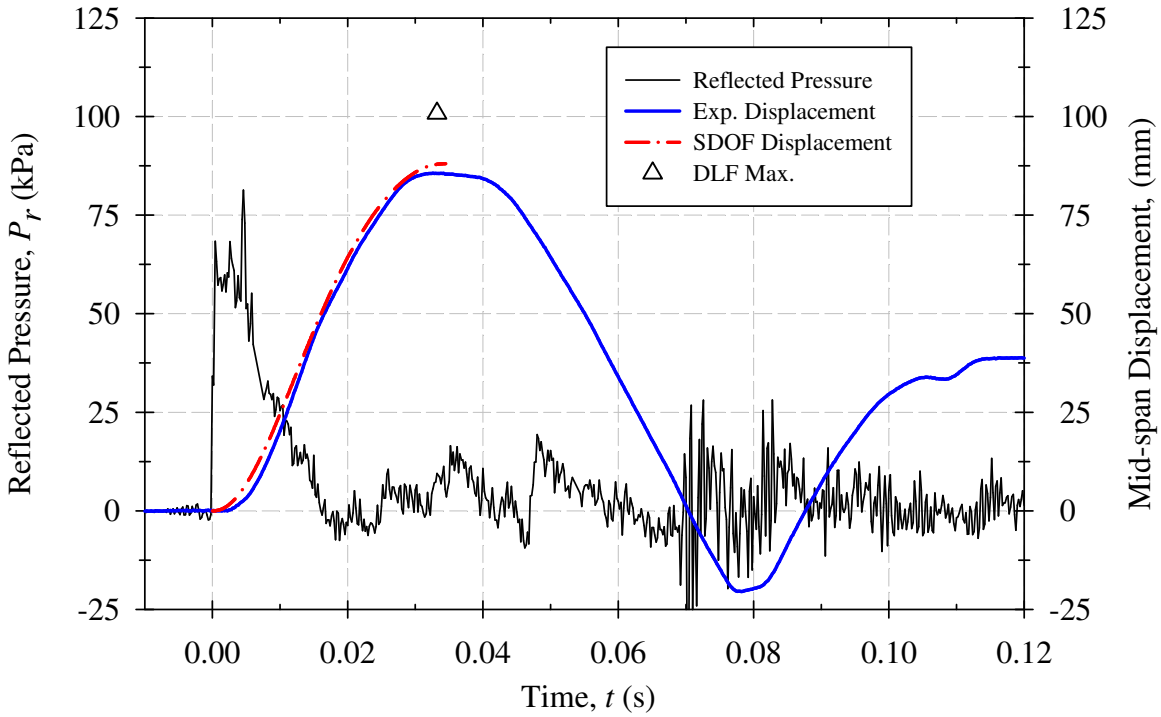

Figure B-15: Experimental mid-span slab displacements plotted against those predicted by SDOF analysis for CS1-A - Shot 5.

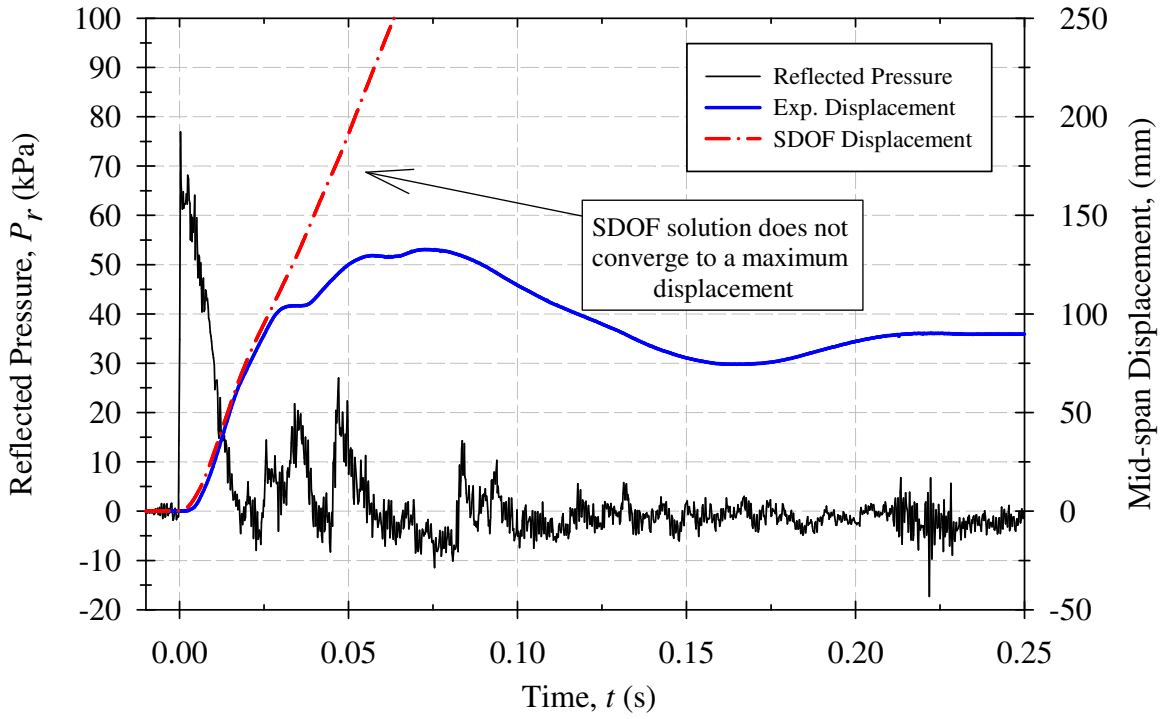

Figure B-16: Experimental mid-span slab displacements plotted against those predicted by SDOF analysis for CS1-A - Shot 6.

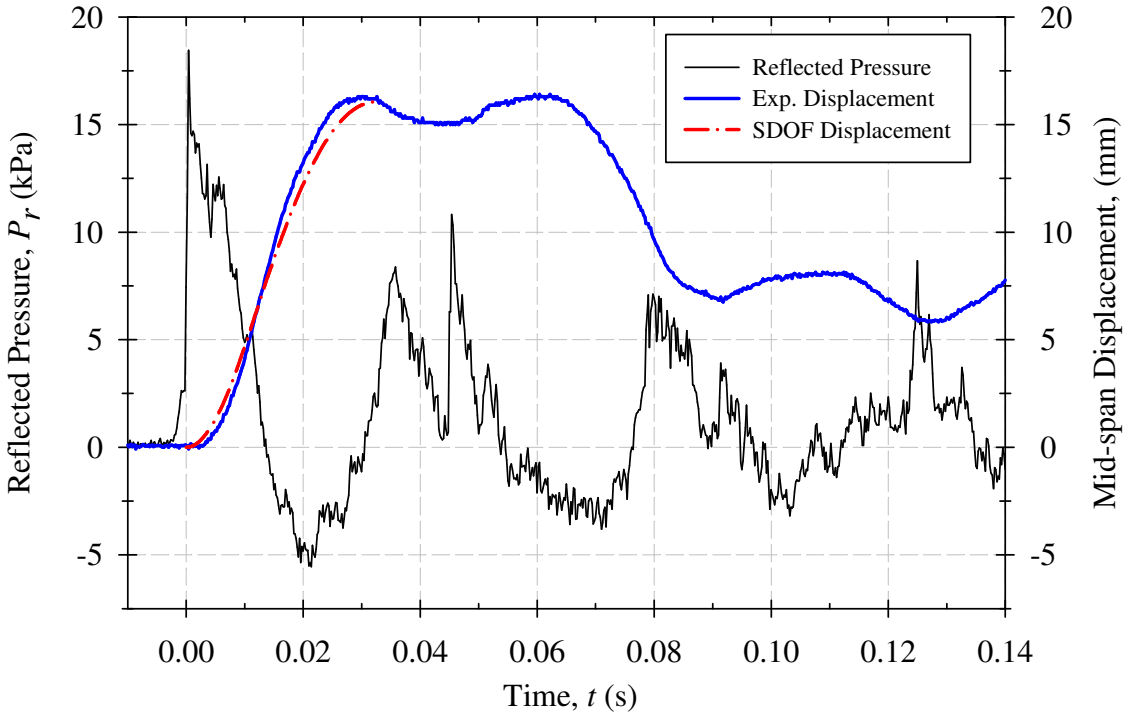

Figure B-17: Experimental mid-span slab displacements plotted against those predicted by SDOF analysis for CS2-C - Shot 1.

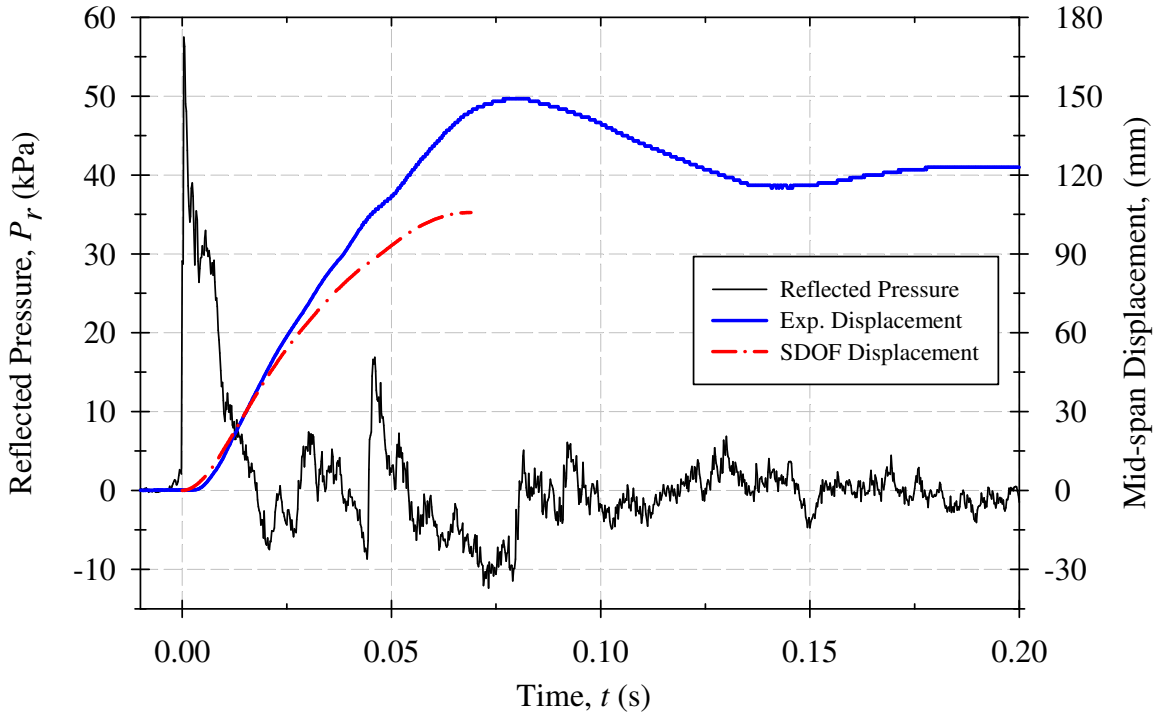

Figure B-18: Experimental mid-span slab displacements plotted against those predicted by SDOF analysis for CS2-C - Shot 2.

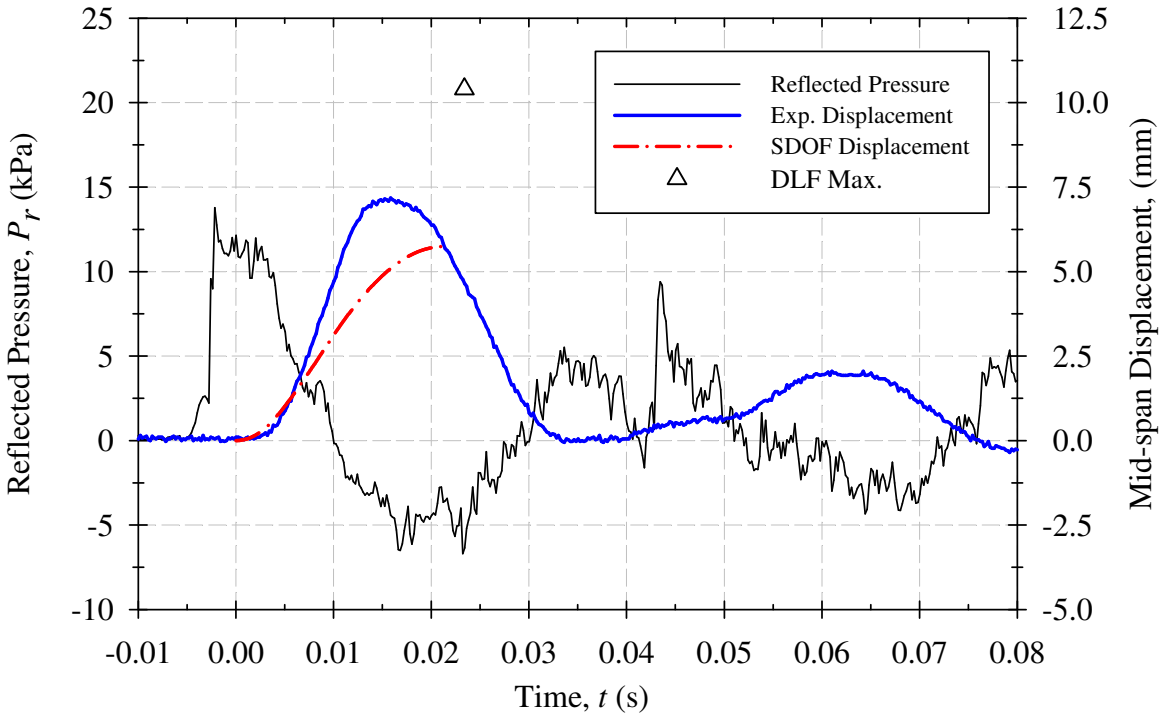

Figure B-19: Experimental mid-span slab displacements plotted against those predicted by SDOF analysis for CS2-R - Shot 1.

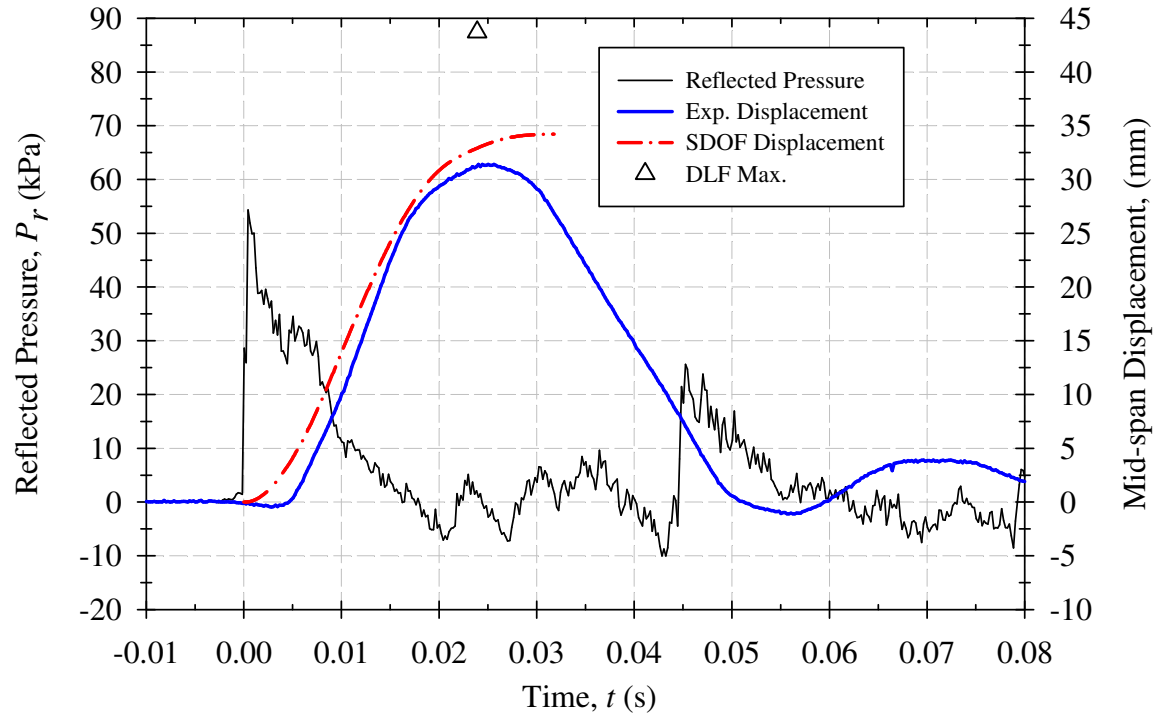

Figure B-20: Experimental mid-span slab displacements plotted against those predicted by SDOF analysis for CS2-R - Shot 2.

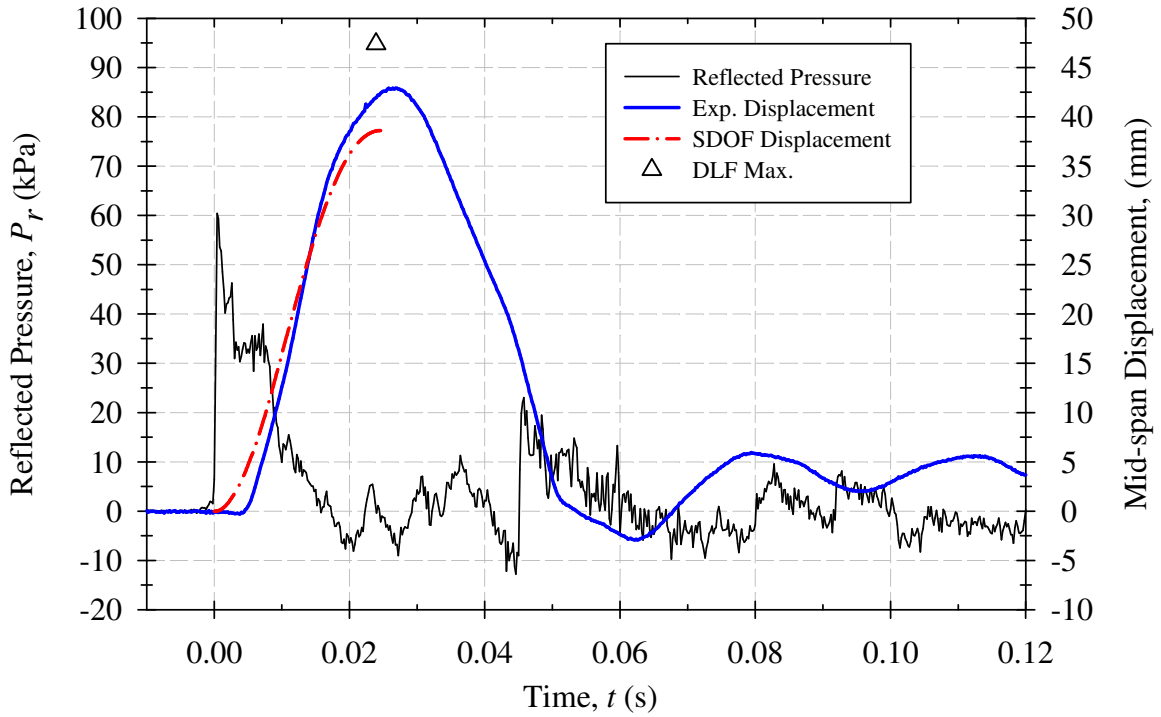

Figure B-21: Experimental mid-span slab displacements plotted against those predicted by SDOF analysis for CS2-R - Shot 3.

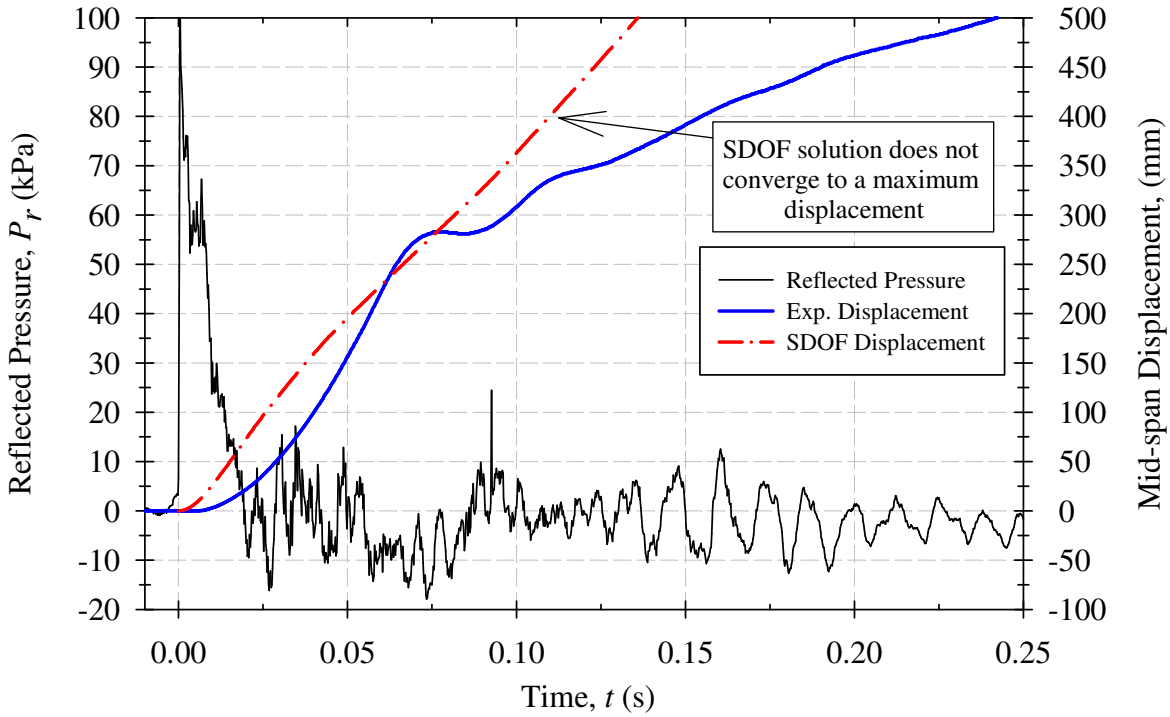

Figure B-22: Experimental mid-span slab displacements plotted against those predicted by SDOF analysis for CS2-R - Shot 4.

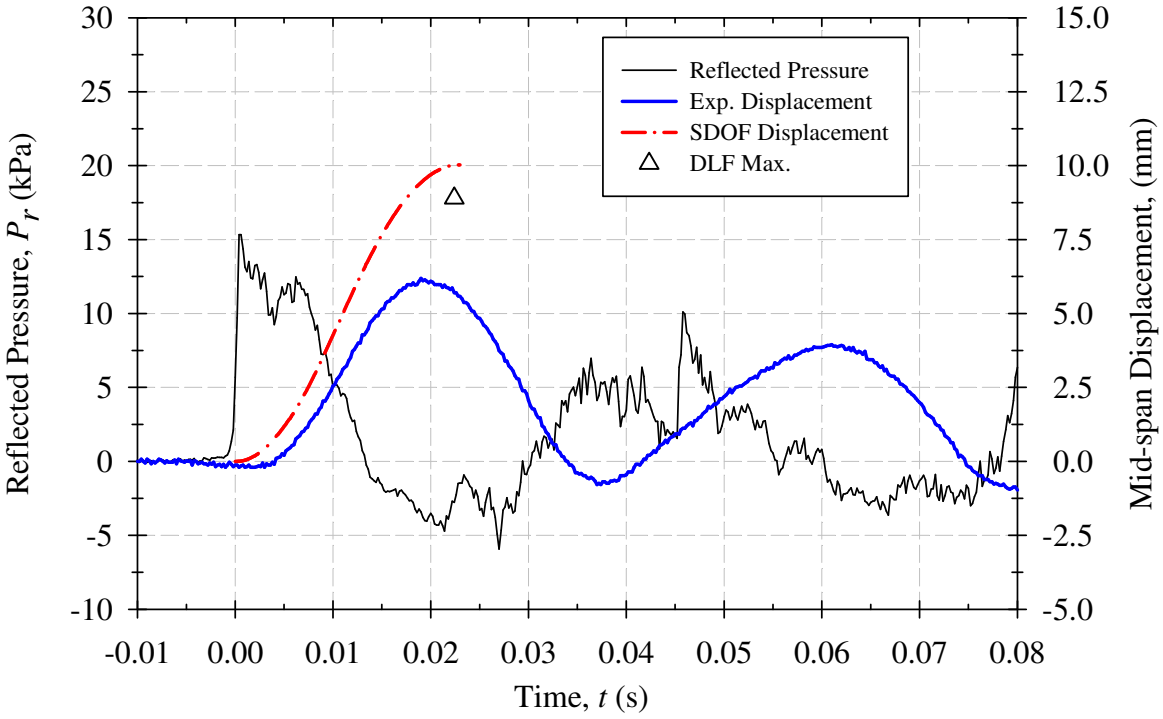

Figure B-23: Experimental mid-span slab displacements plotted against those predicted by SDOF analysis for CS2-A - Shot 1.

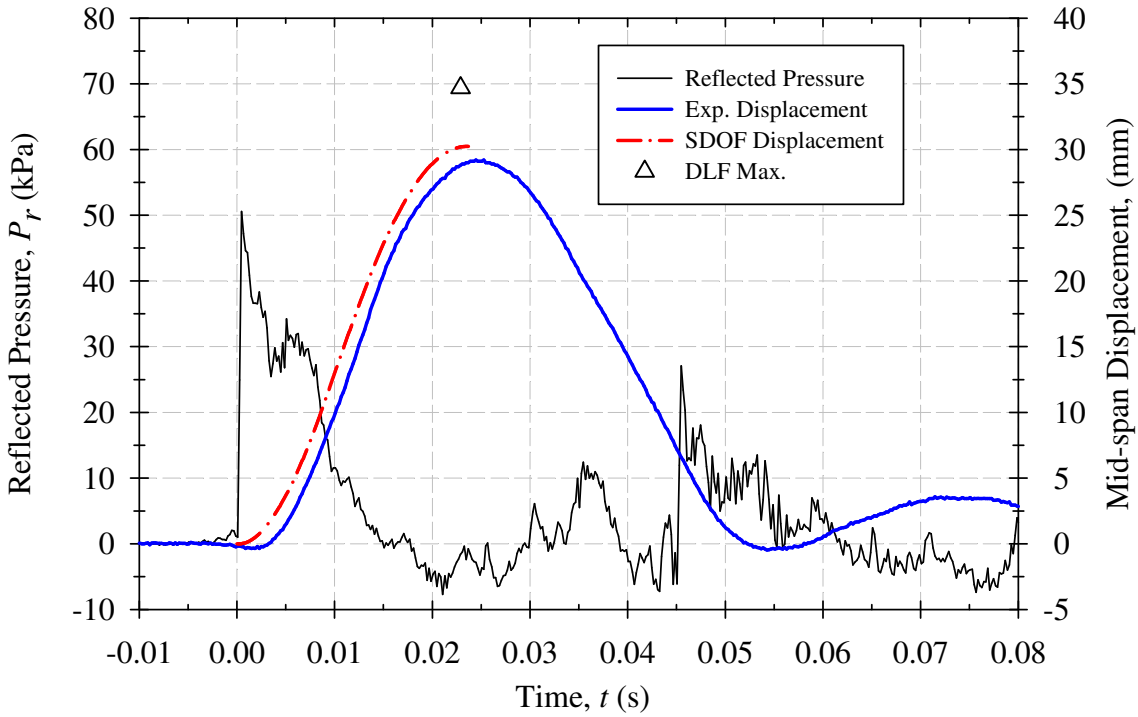

Figure B-24: Experimental mid-span slab displacements plotted against those predicted by SDOF analysis for CS2-A - Shot 2.

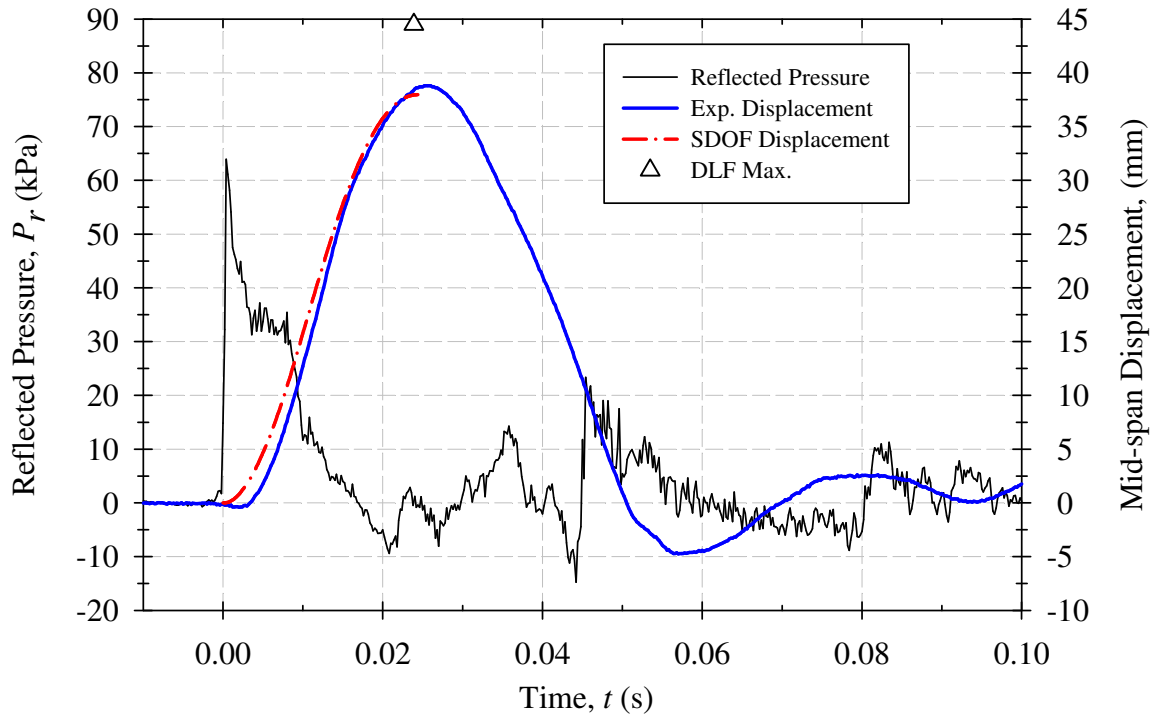

Figure B-25: Experimental mid-span slab displacements plotted against those predicted by SDOF analysis for CS2-A - Shot 3.

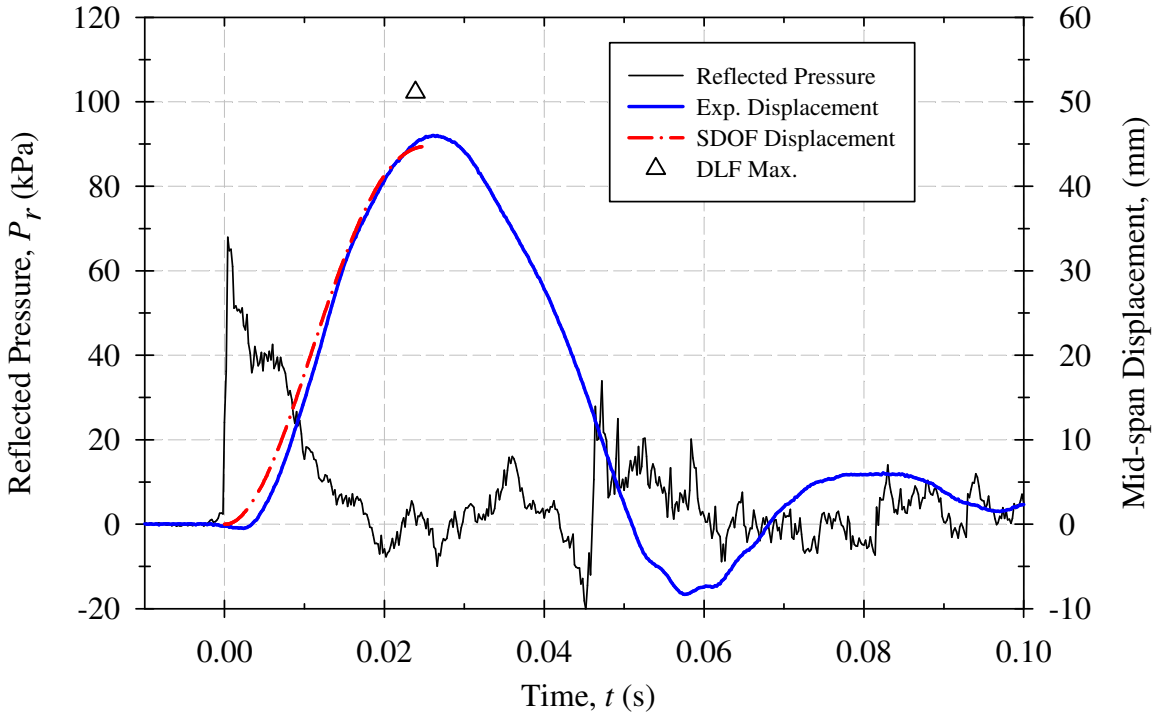

Figure B-26: Experimental mid-span slab displacements plotted against those predicted by SDOF analysis for CS2-A - Shot 4.

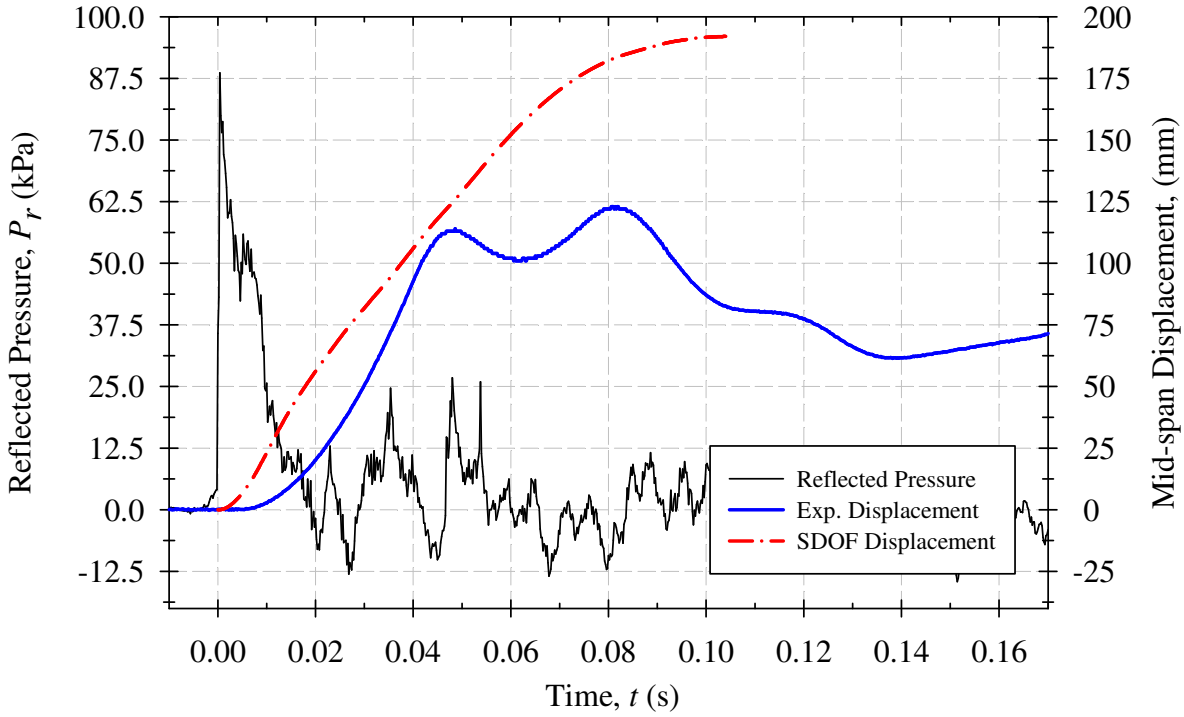

Figure B-27: Experimental mid-span slab displacements plotted against those predicted by SDOF analysis for CS2-A - Shot 5.

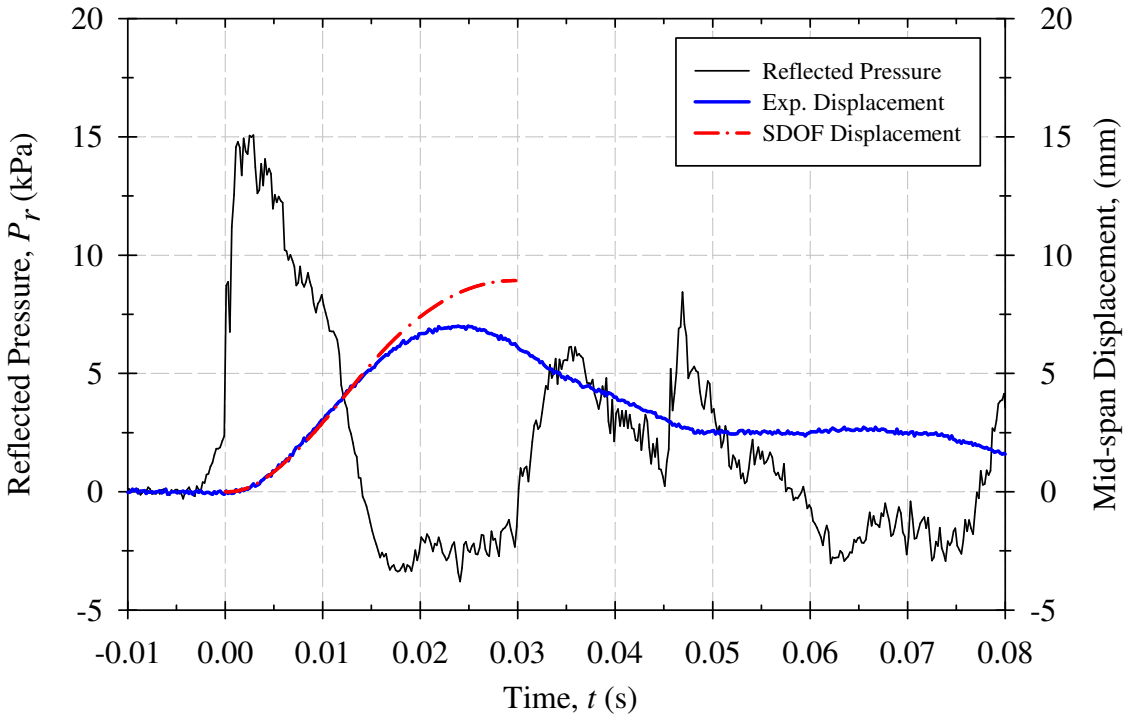

Figure B-28: Experimental mid-span slab displacements plotted against those predicted by SDOF analysis for CS3-C - Shot 1.

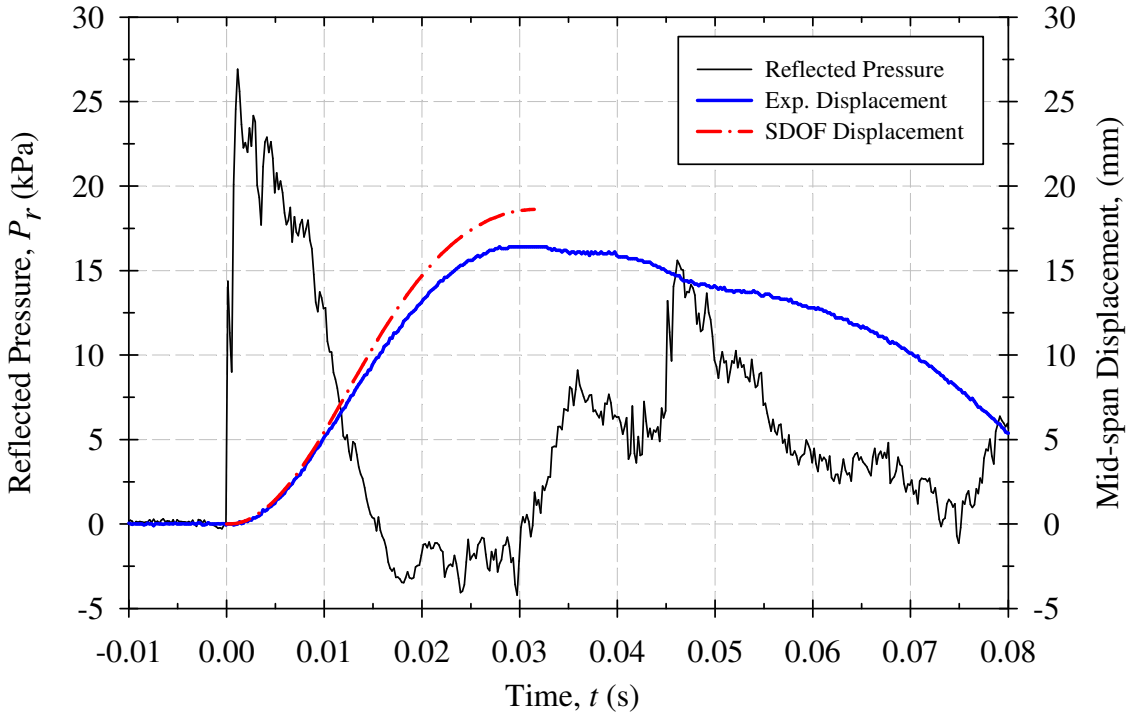

Figure B-29: Experimental mid-span slab displacements plotted against those predicted by SDOF analysis for CS3-C - Shot 2.

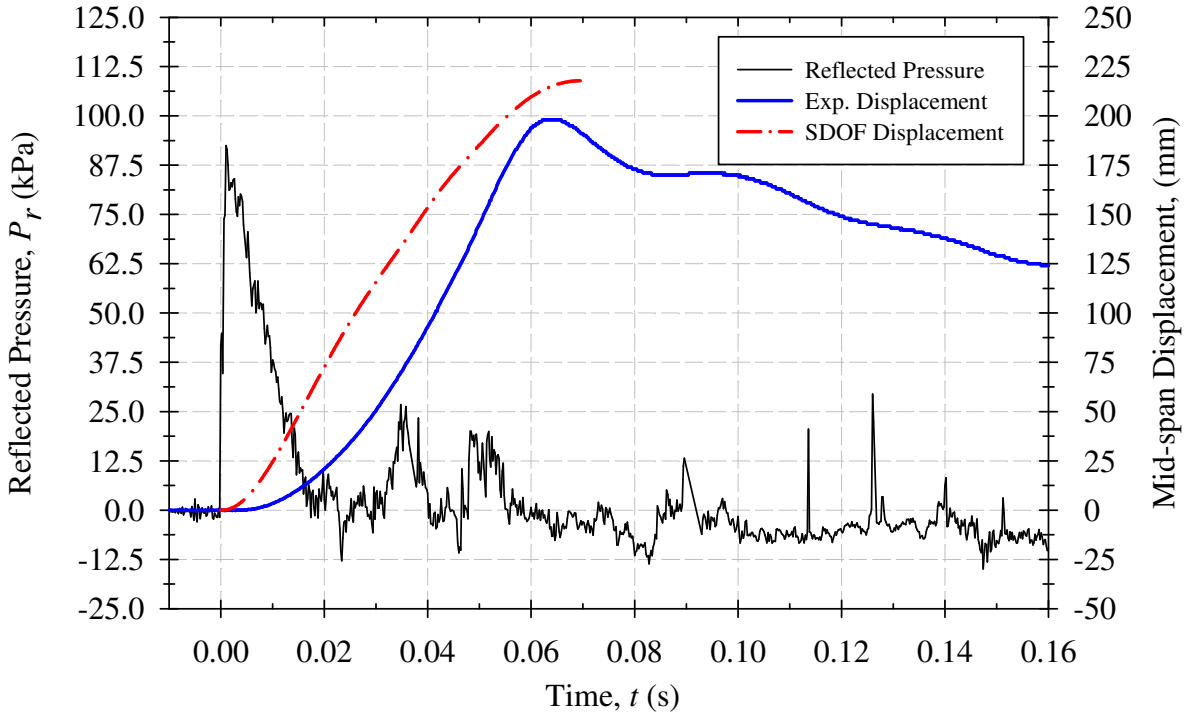

Figure B-30: Experimental mid-span slab displacements plotted against those predicted by SDOF analysis for CS3-C - Shot 3.

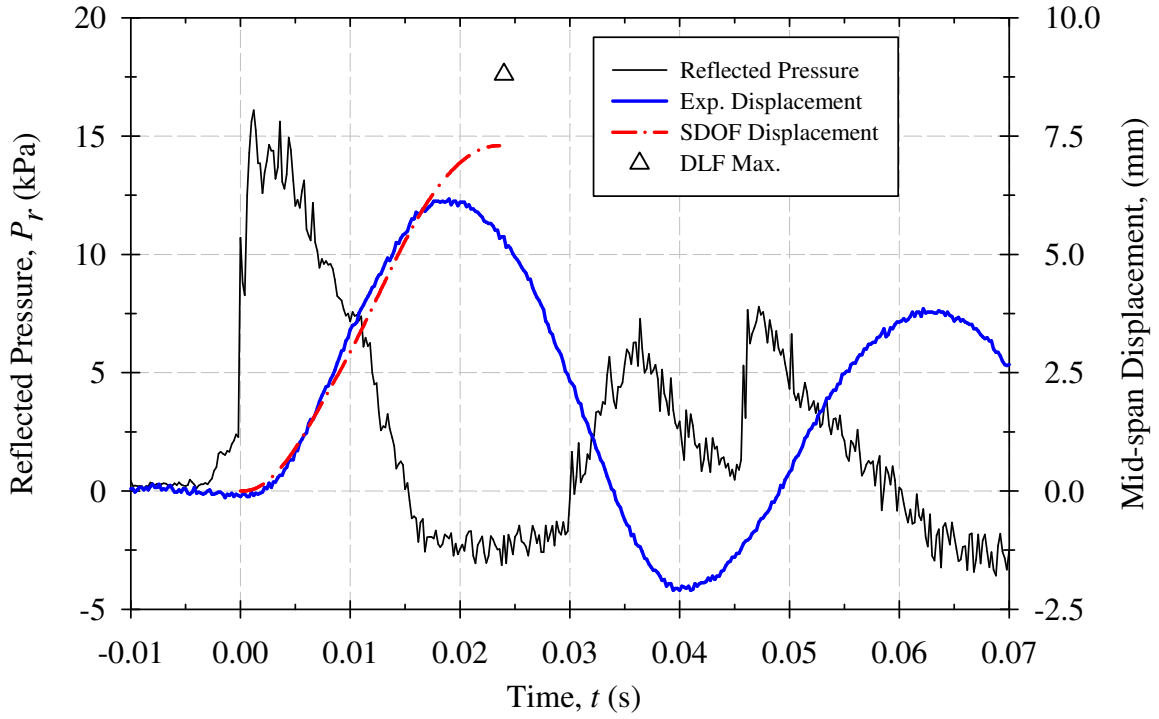

Figure B-31: Experimental mid-span slab displacements plotted against those predicted by SDOF analysis for CS3-R - Shot 1.

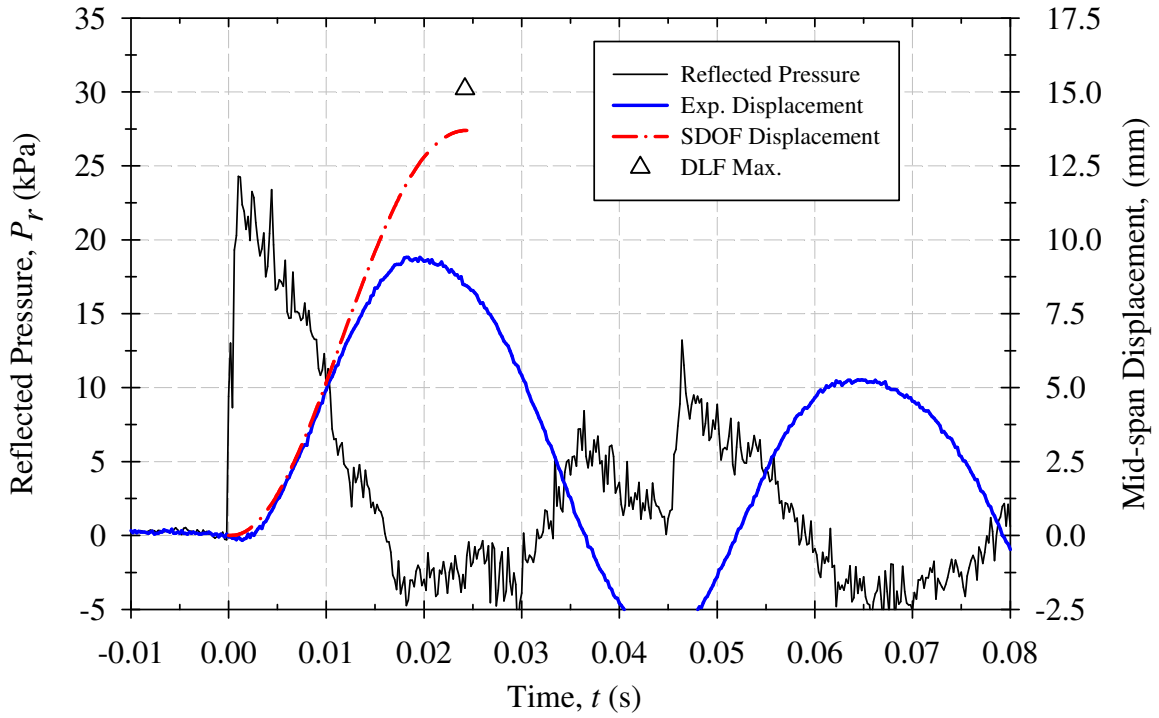

Figure B-32: Experimental mid-span slab displacements plotted against those predicted by SDOF analysis for CS3-R - Shot 2.

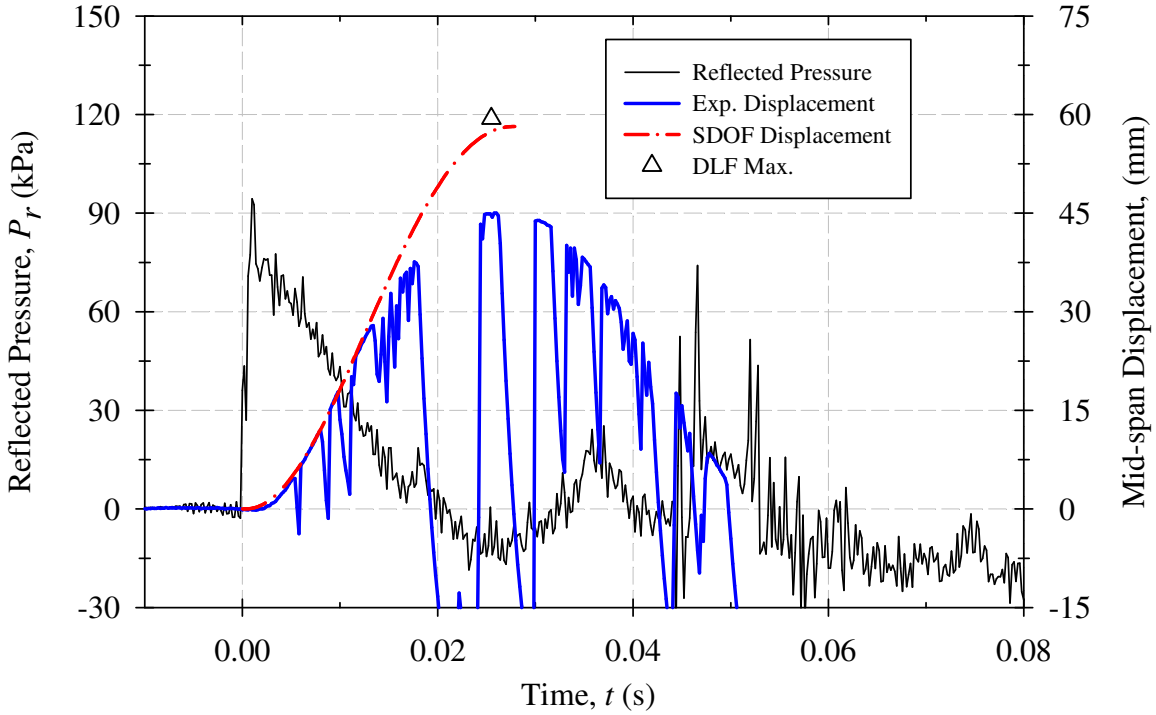

Figure B-33: Experimental mid-span slab displacements plotted against those predicted by SDOF analysis for CS3-R - Shot 3.

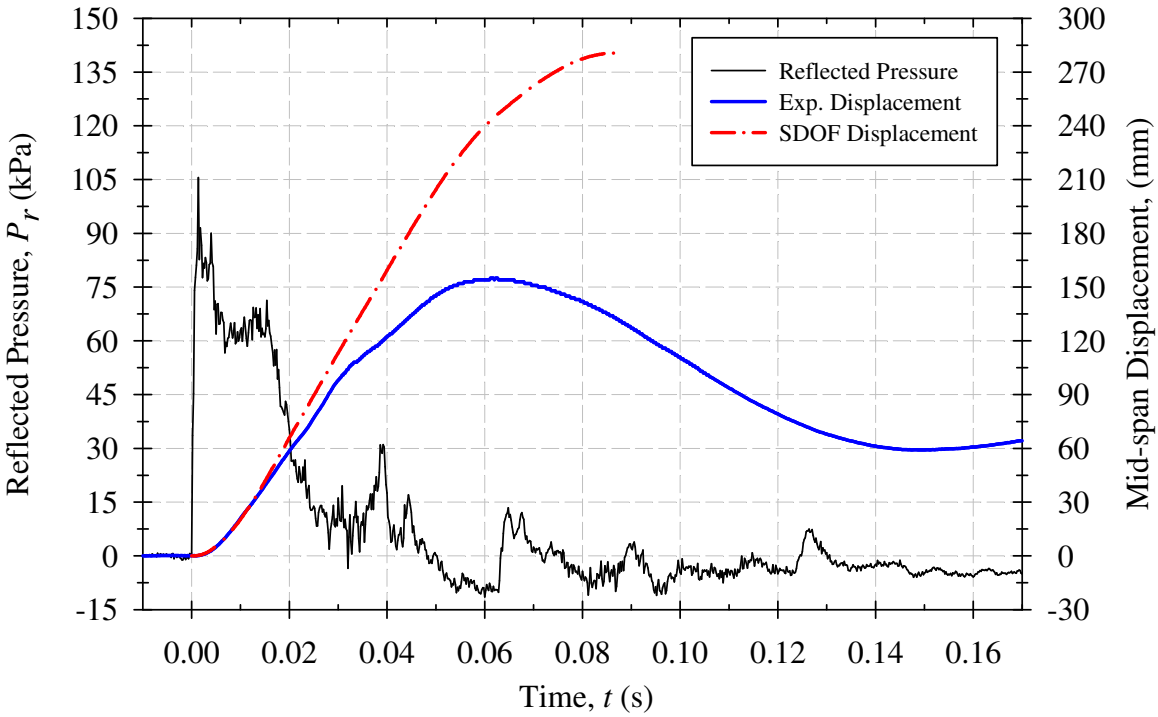

Figure B-34: Experimental mid-span slab displacements plotted against those predicted by SDOF analysis for CS3-R - Shot 4.

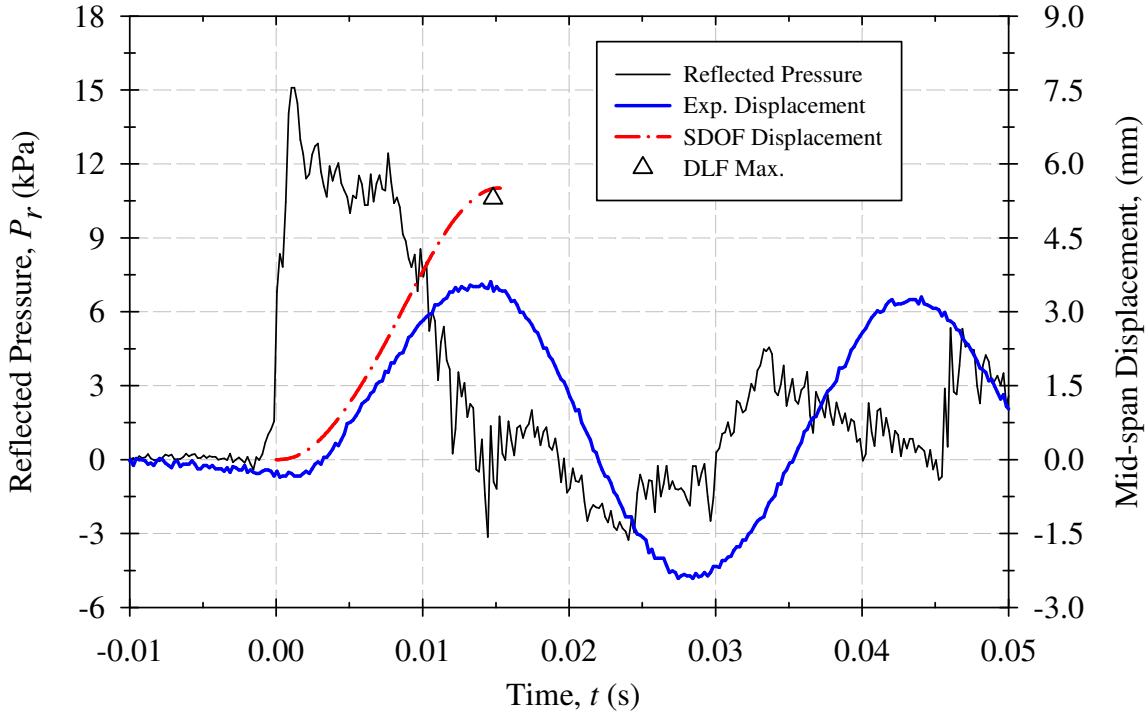

Figure B-35: Experimental mid-span slab displacements plotted against those predicted by SDOF analysis for CS4-R1 - Shot 1.

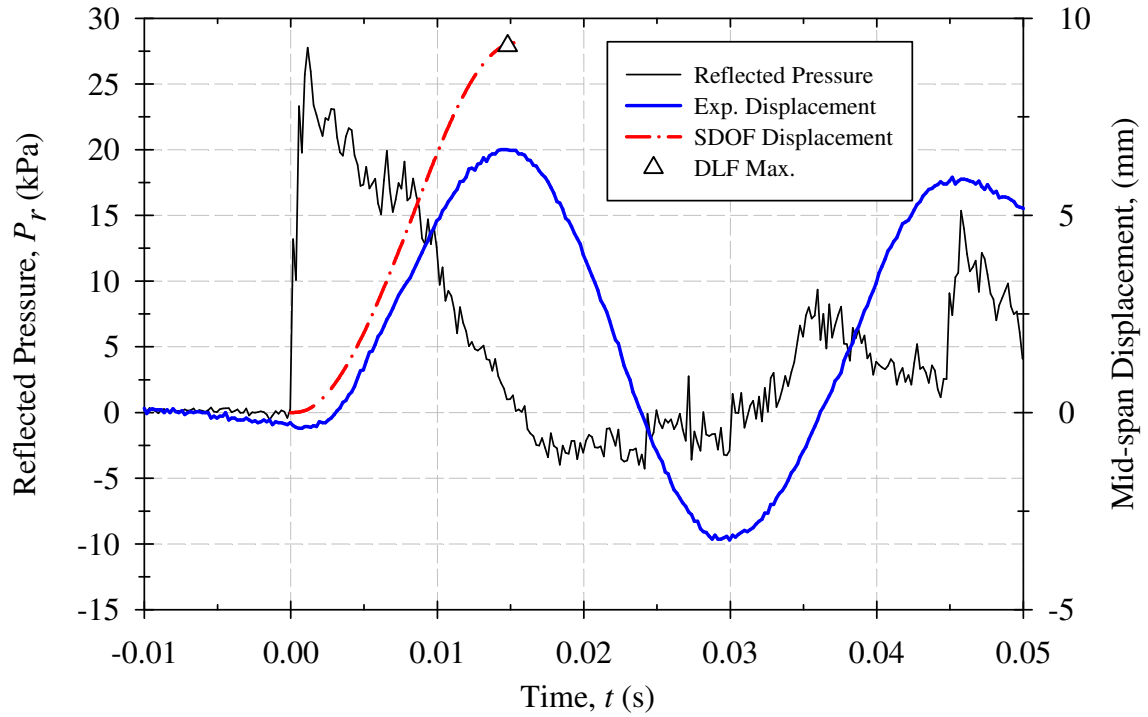

Figure B-36: Experimental mid-span slab displacements plotted against those predicted by SDOF analysis for CS4-R1 - Shot 2.

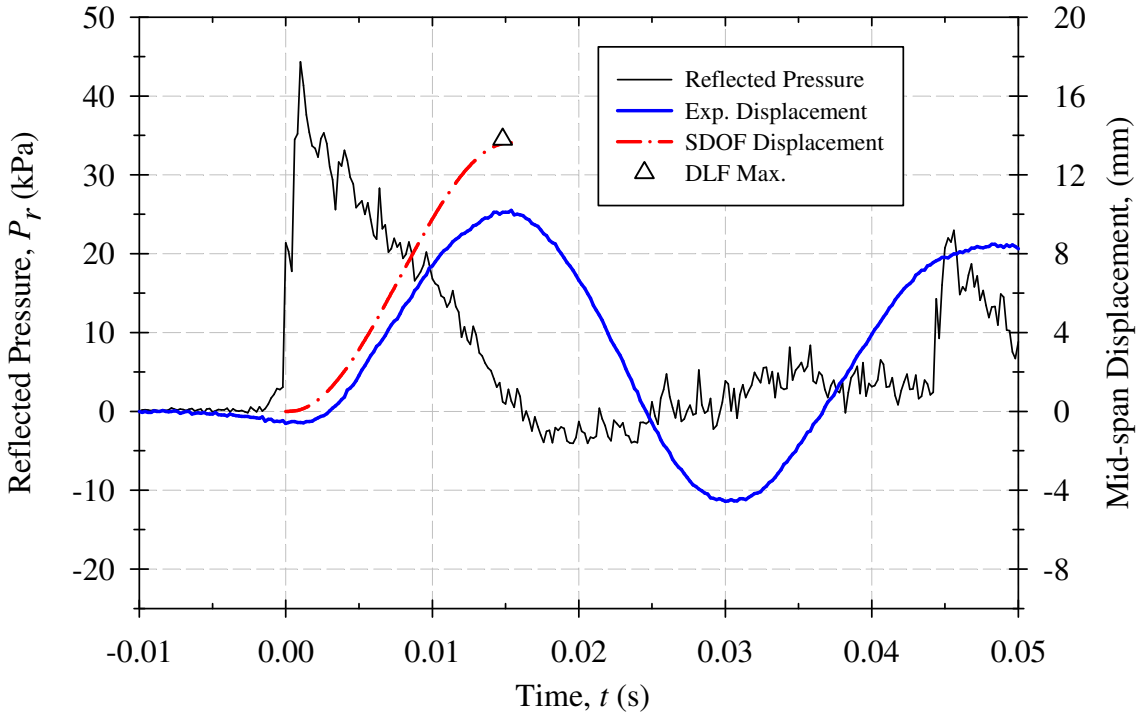

Figure B-37: Experimental mid-span slab displacements plotted against those predicted by SDOF analysis for CS4-R1 - Shot 3.

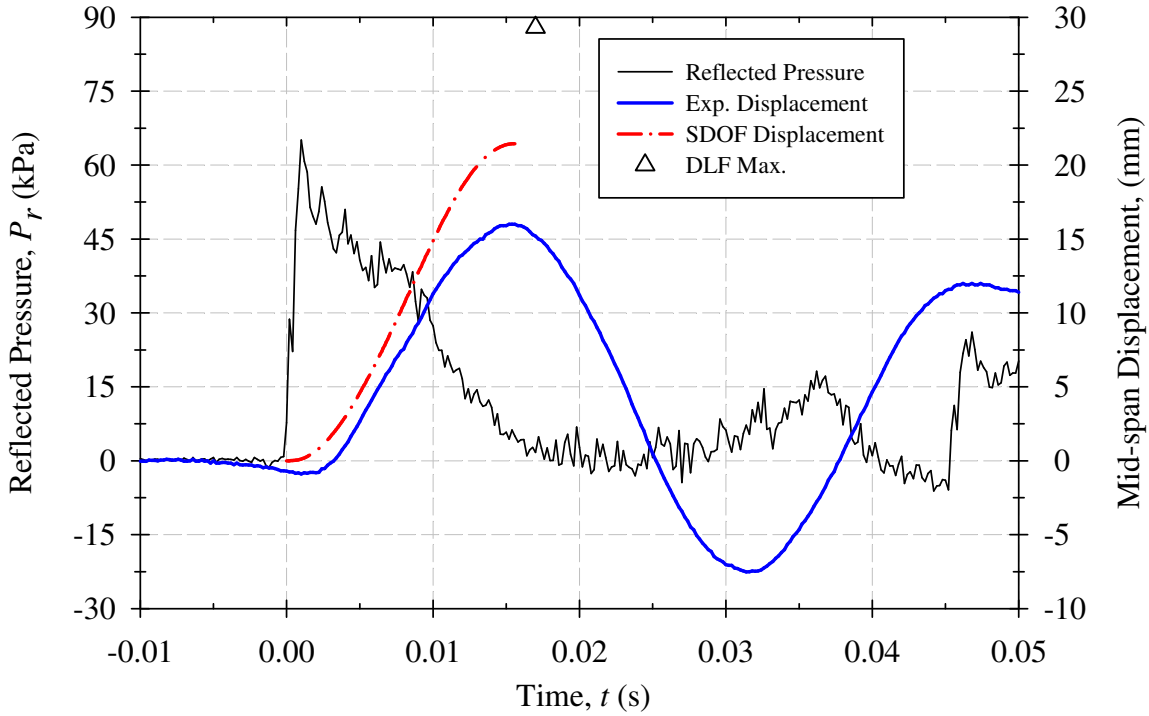

Figure B-38: Experimental mid-span slab displacements plotted against those predicted by SDOF analysis for CS4-R1 - Shot 4.

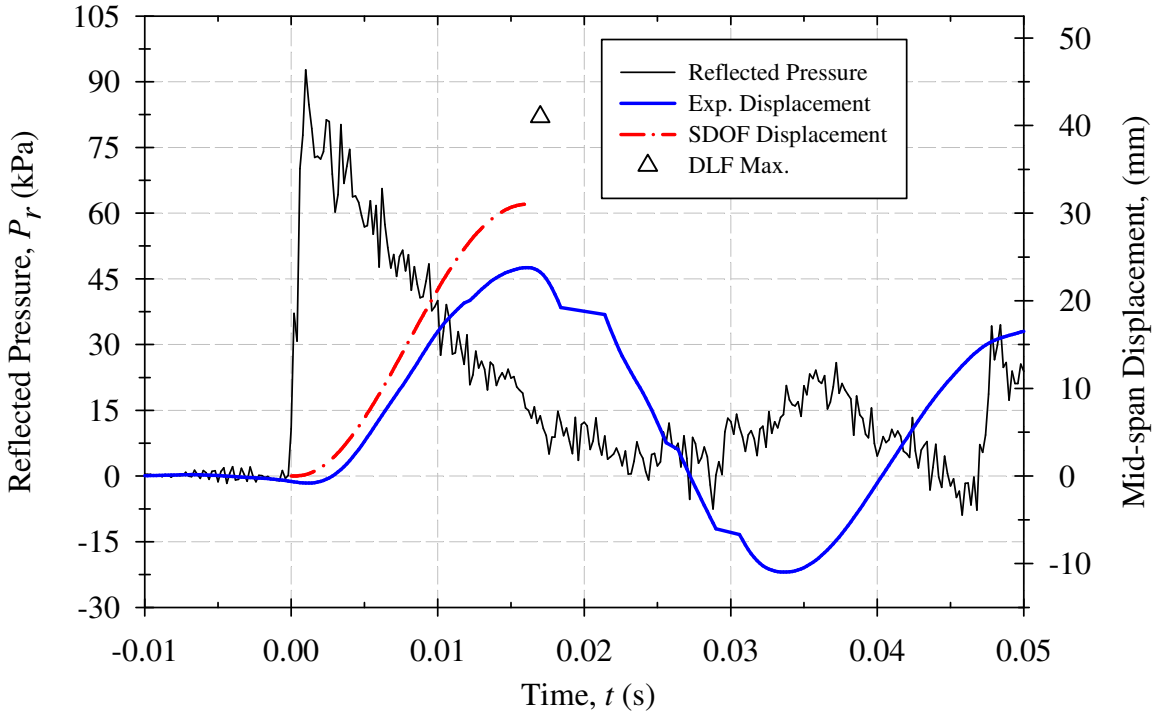

Figure B-39: Experimental mid-span slab displacements plotted against those predicted by SDOF analysis for CS4-R1 - Shot 5.

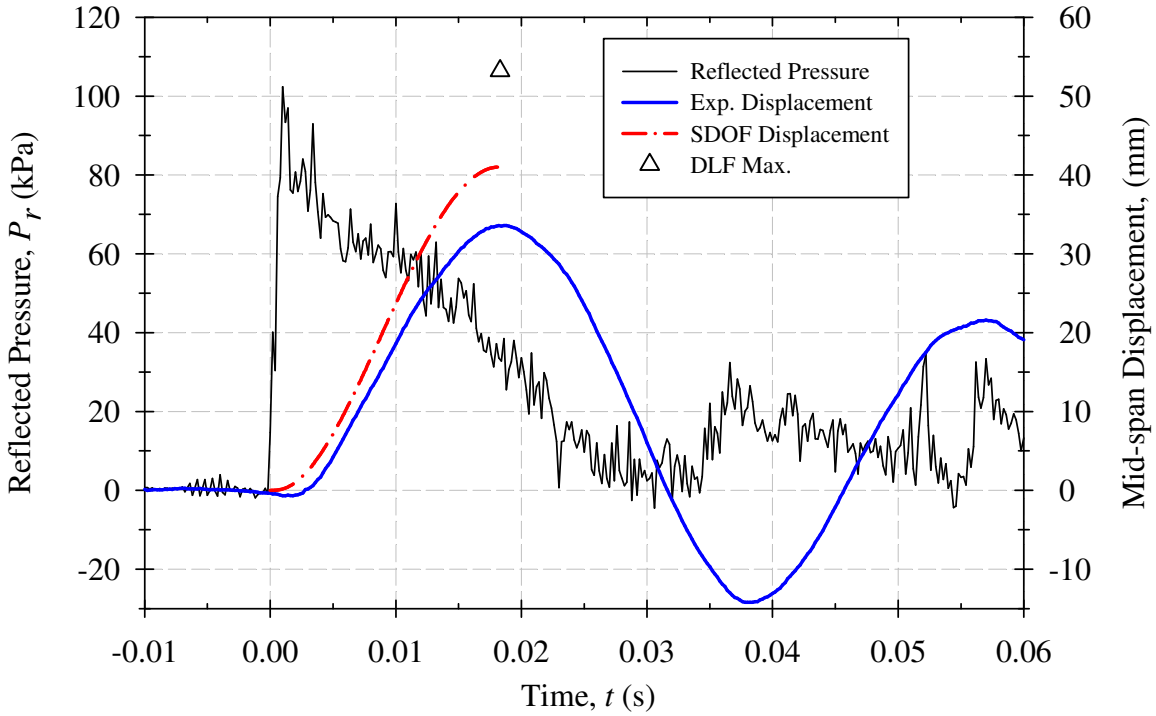

Figure B-40: Experimental mid-span slab displacements plotted against those predicted by SDOF analysis for CS4-R1 - Shot 6.

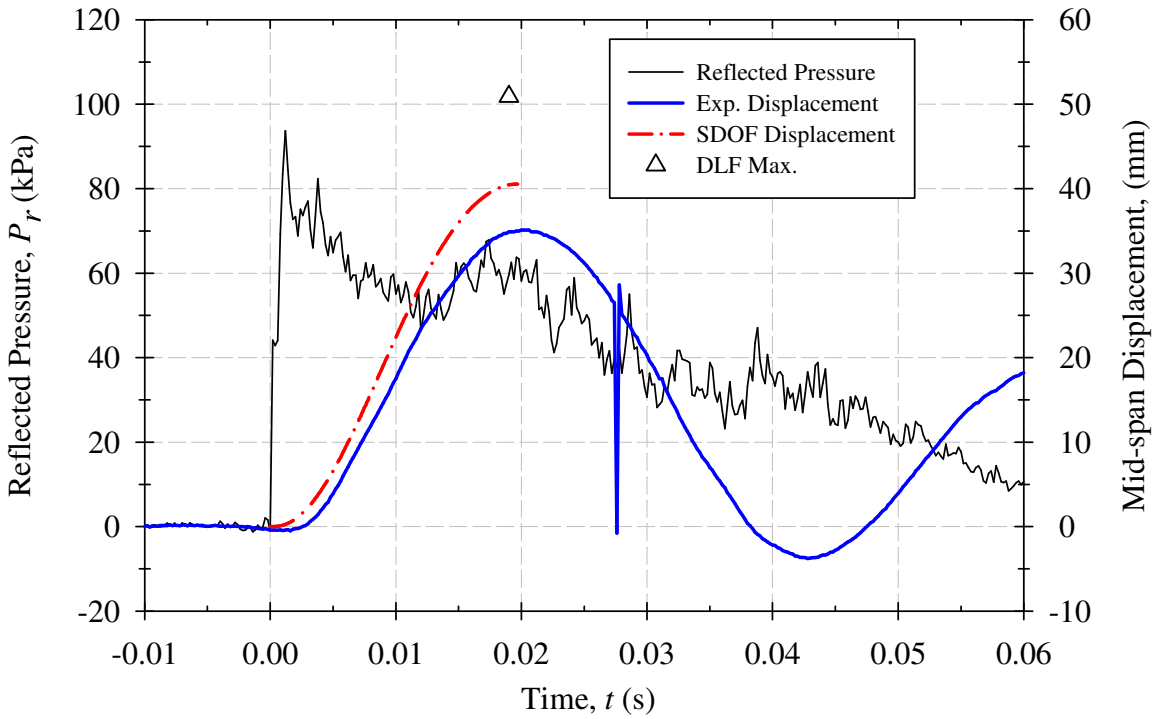

Figure B-41: Experimental mid-span slab displacements plotted against those predicted by SDOF analysis for CS4-R1 - Shot 7.

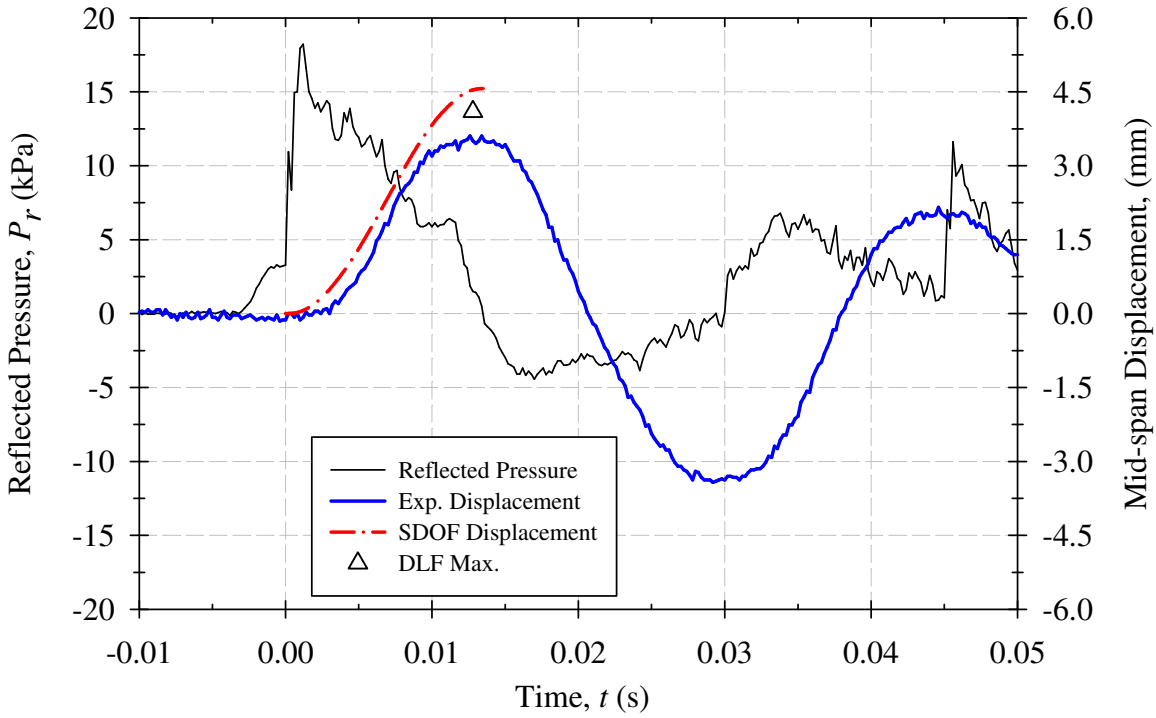

Figure B-42: Experimental mid-span slab displacements plotted against those predicted by SDOF analysis for CS4-R2 - Shot 1.

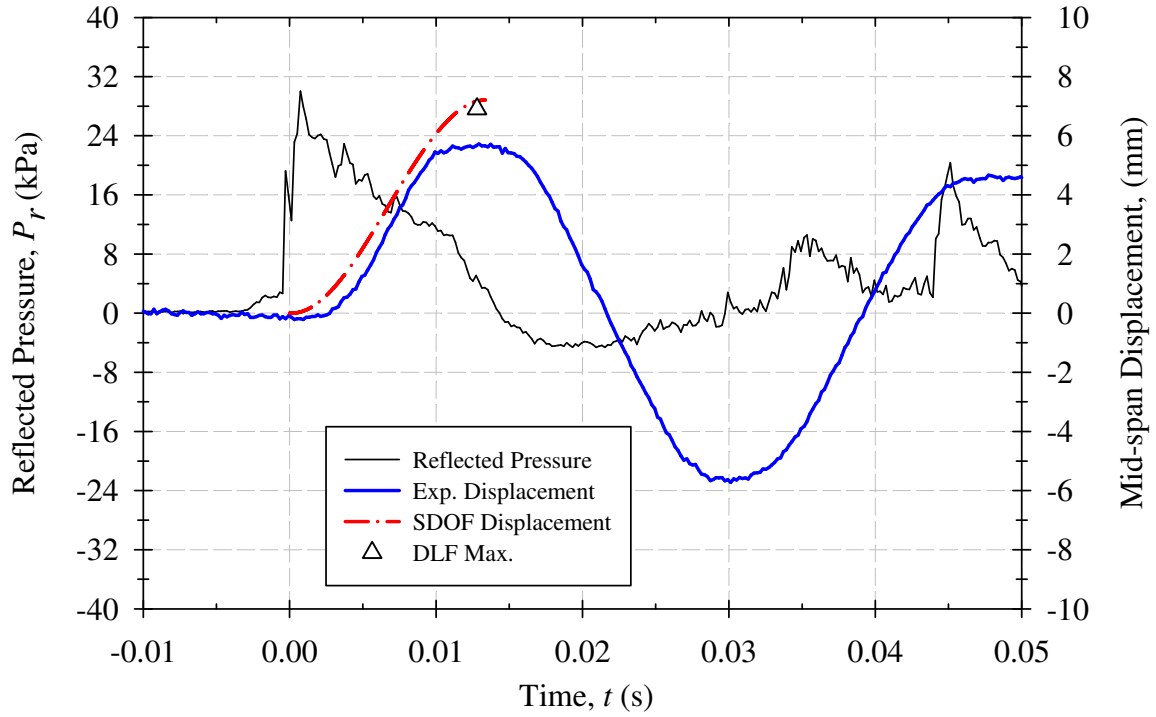

Figure B-43: Experimental mid-span slab displacements plotted against those predicted by SDOF analysis for CS4-R2 - Shot 2.

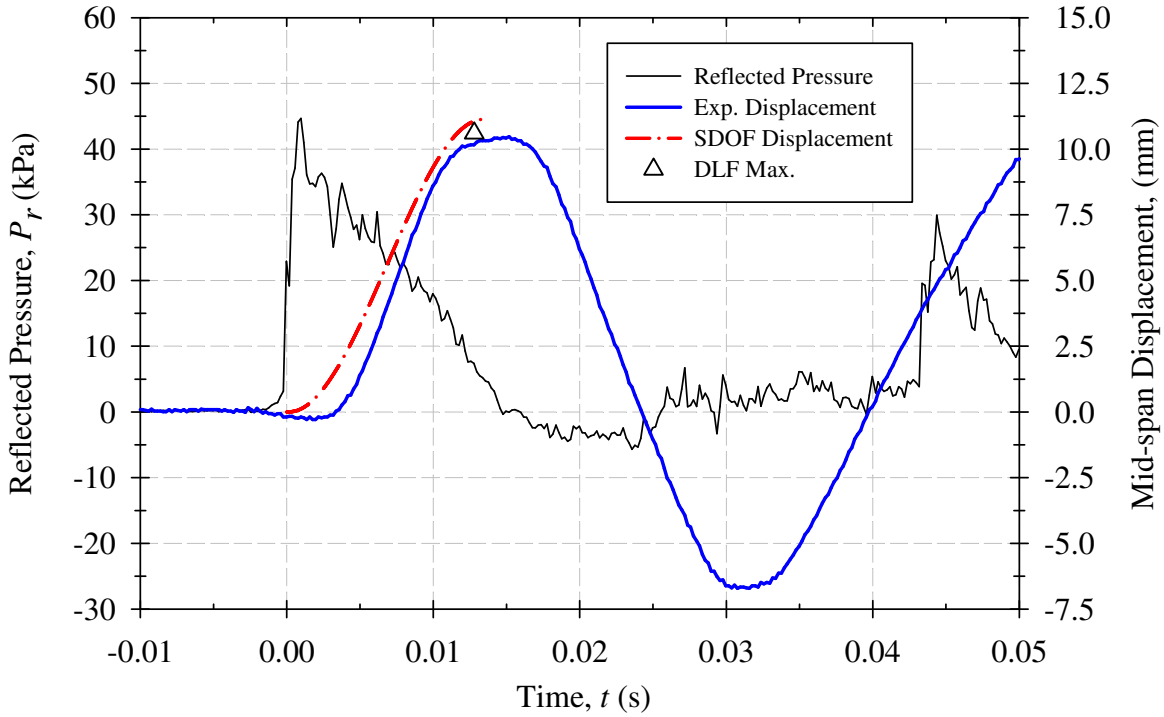

Figure B-44: Experimental mid-span slab displacements plotted against those predicted by SDOF analysis for CS4-R2 - Shot 3.

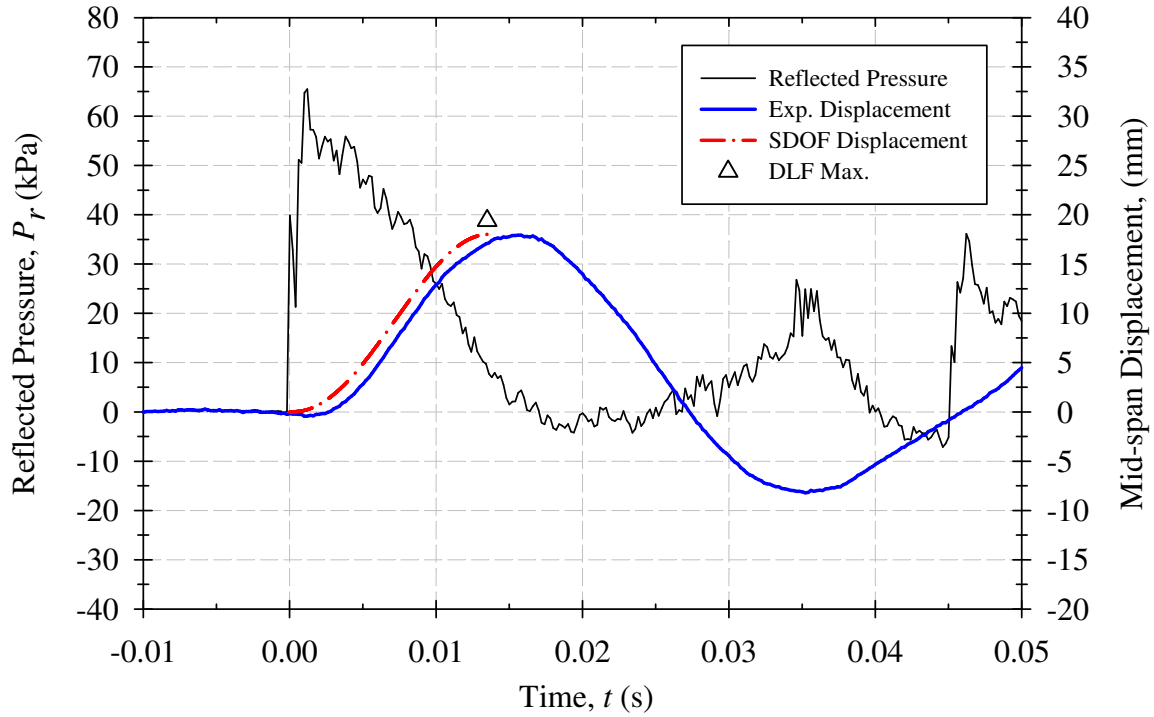

Figure B-45: Experimental mid-span slab displacements plotted against those predicted by SDOF analysis for CS4-R2 - Shot 4.

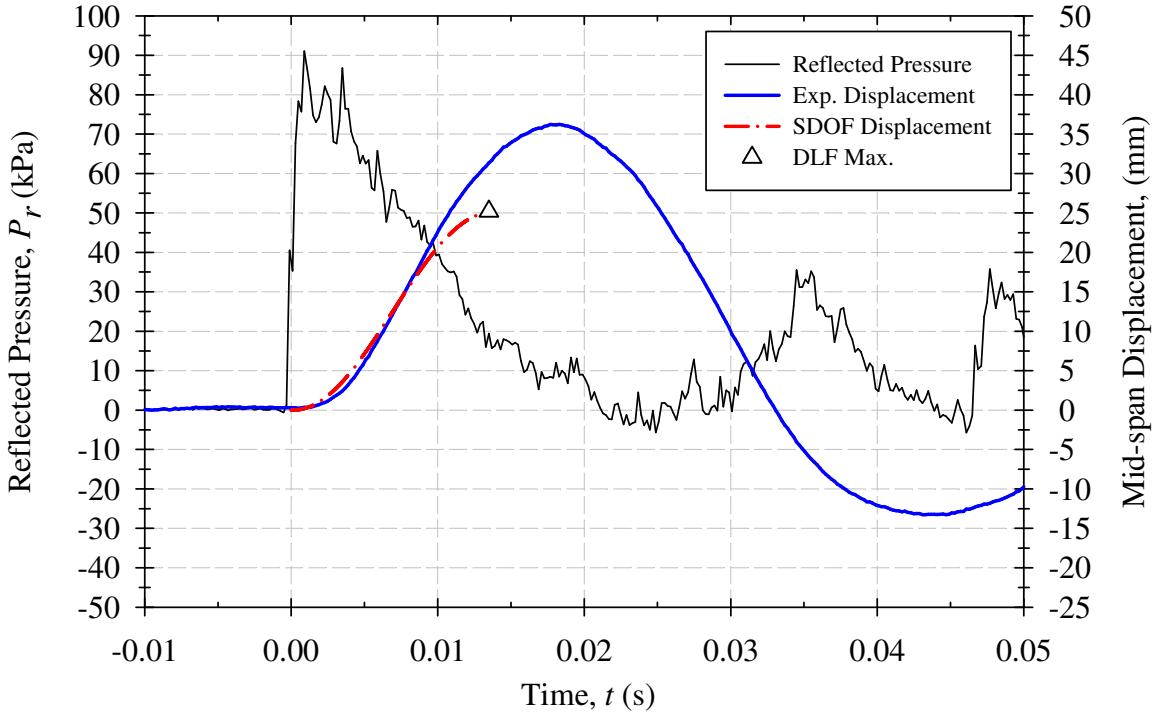

Figure B-46: Experimental mid-span slab displacements plotted against those predicted by SDOF analysis for CS4-R2 - Shot 5.

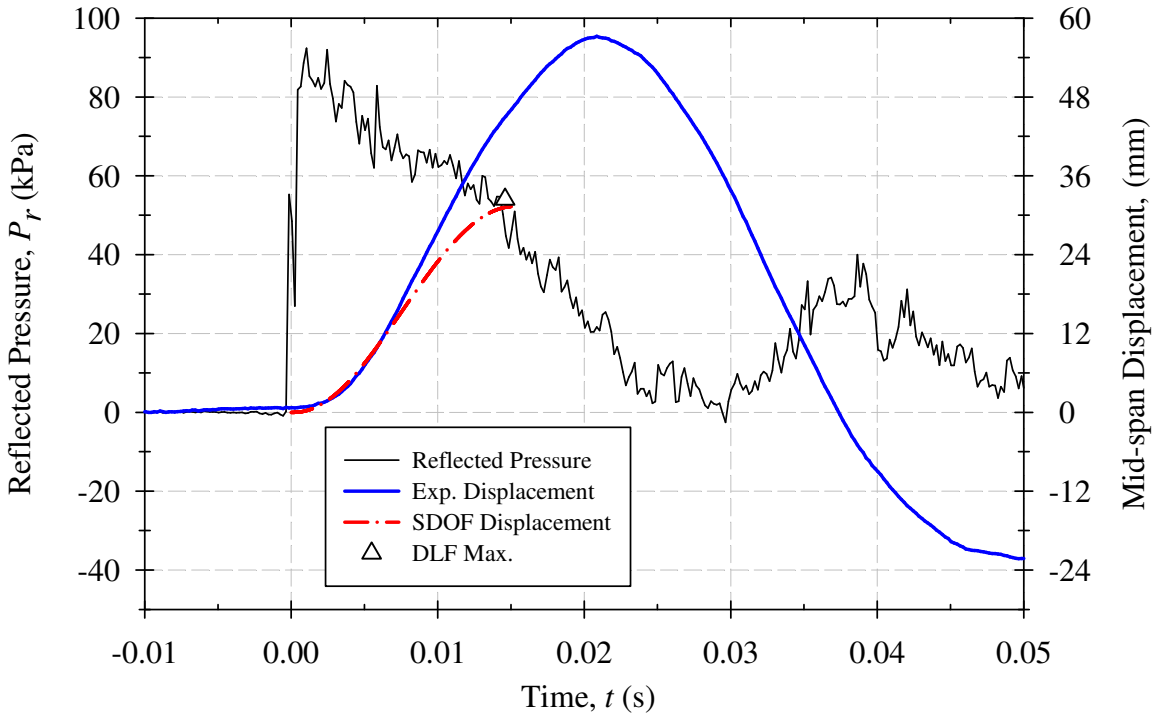

Figure B-47: Experimental mid-span slab displacements plotted against those predicted by SDOF analysis for CS4-R2 - Shot 6.

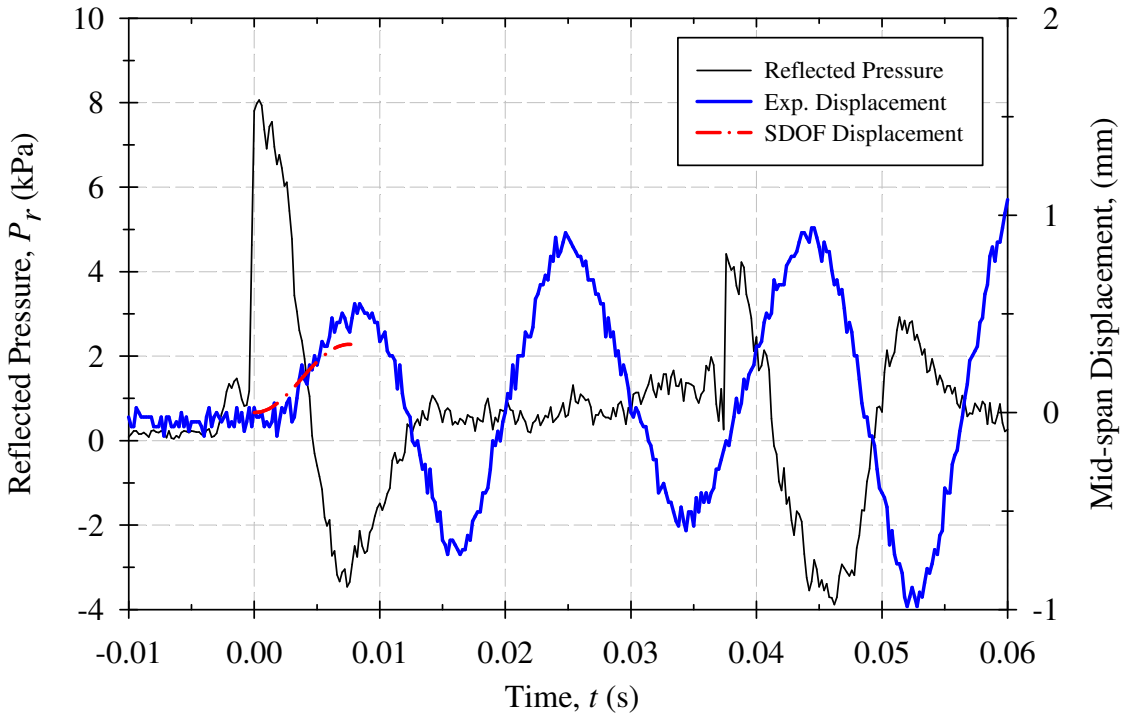

Figure B-48: Experimental mid-span slab displacements plotted against those predicted by SDOF analysis for CS5-C - Shot 1.

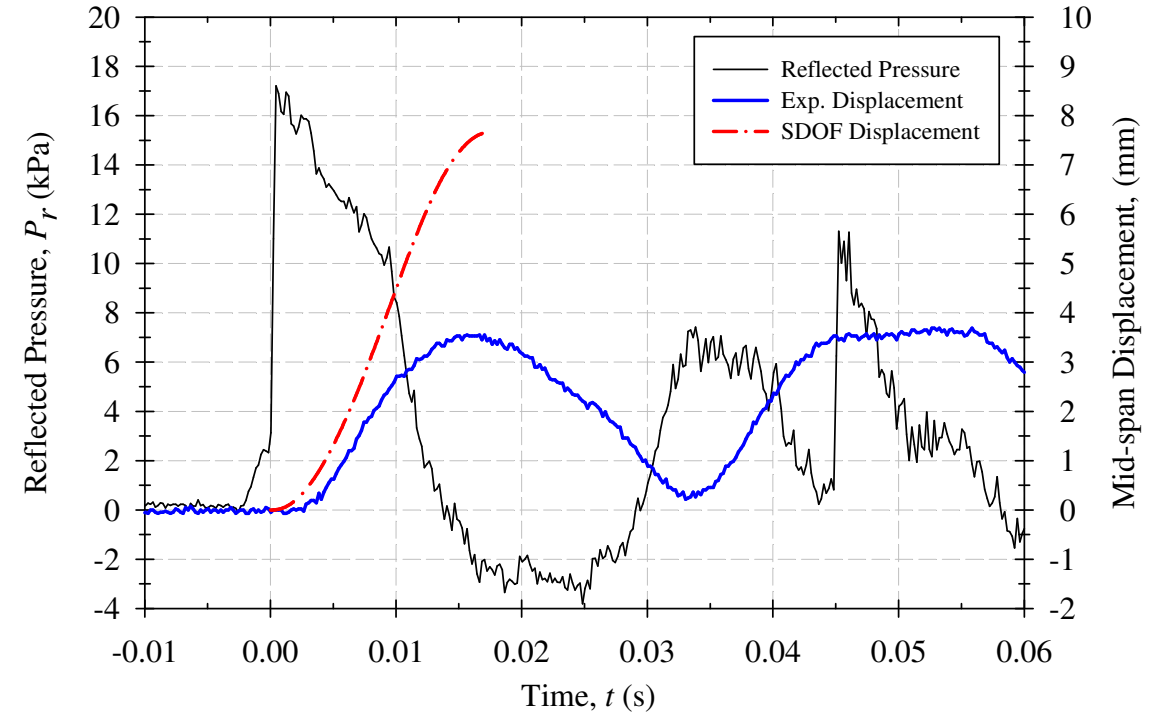

Figure B-49: Experimental mid-span slab displacements plotted against those predicted by SDOF analysis for CS5-C - Shot 2.

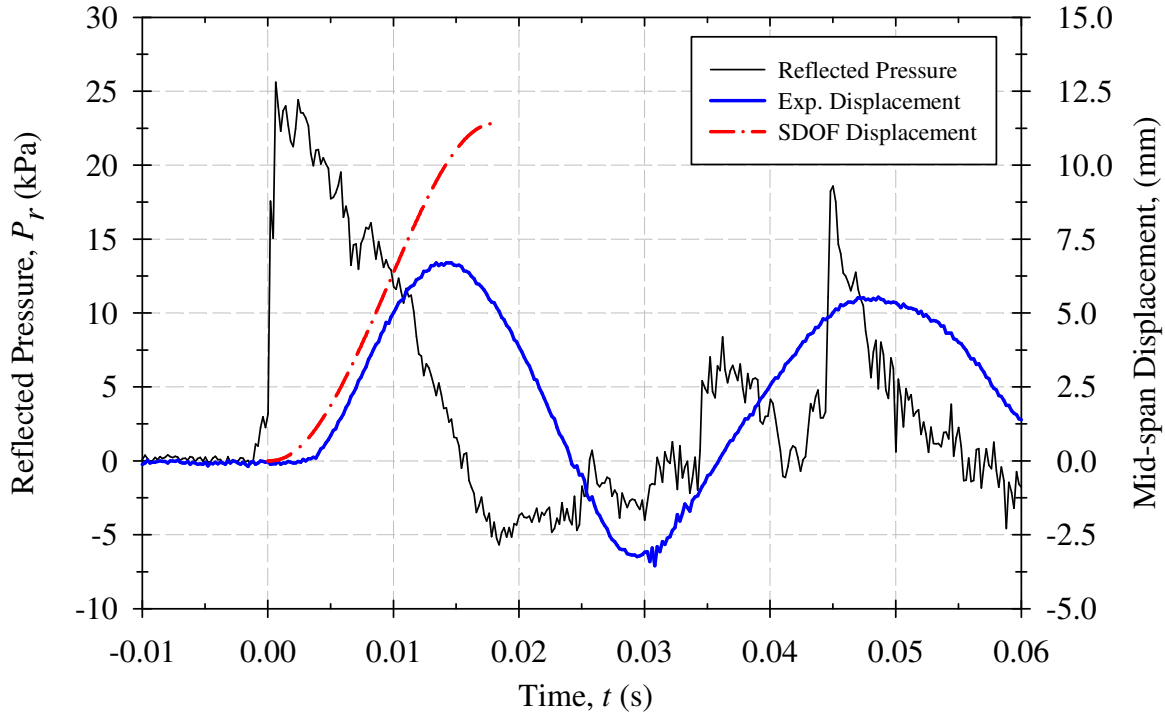

Figure B-50: Experimental mid-span slab displacements plotted against those predicted by SDOF analysis for CS5-C - Shot 3.

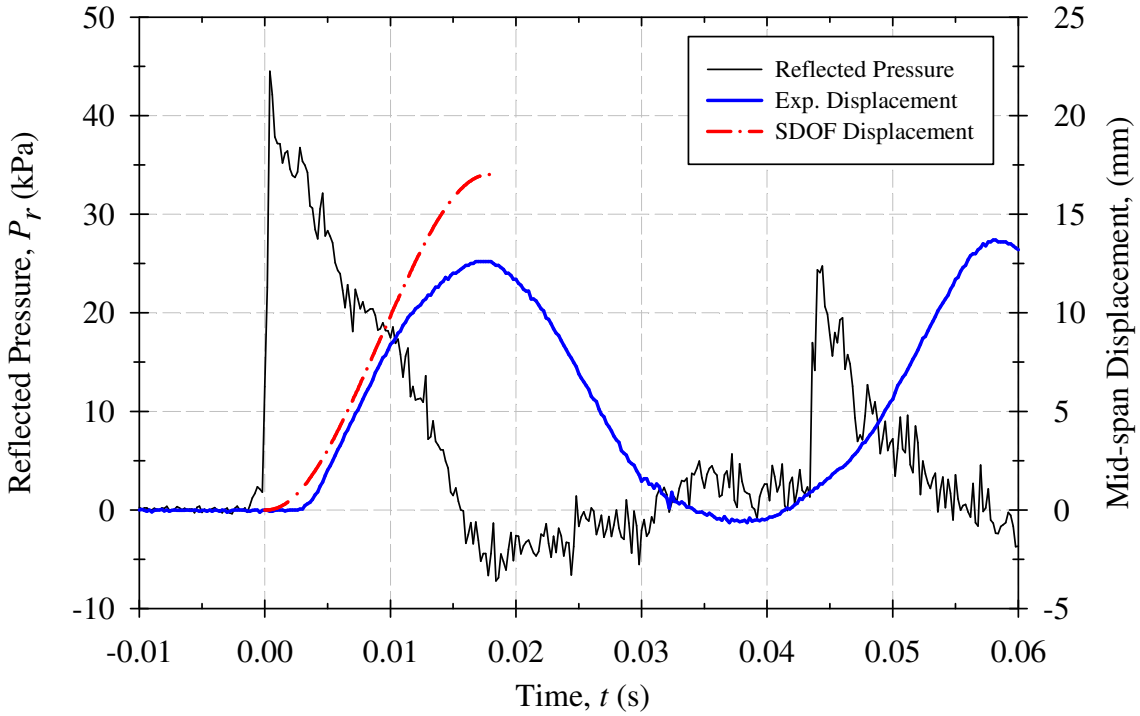

Figure B-51: Experimental mid-span slab displacements plotted against those predicted by SDOF analysis for CS5-C - Shot 4.

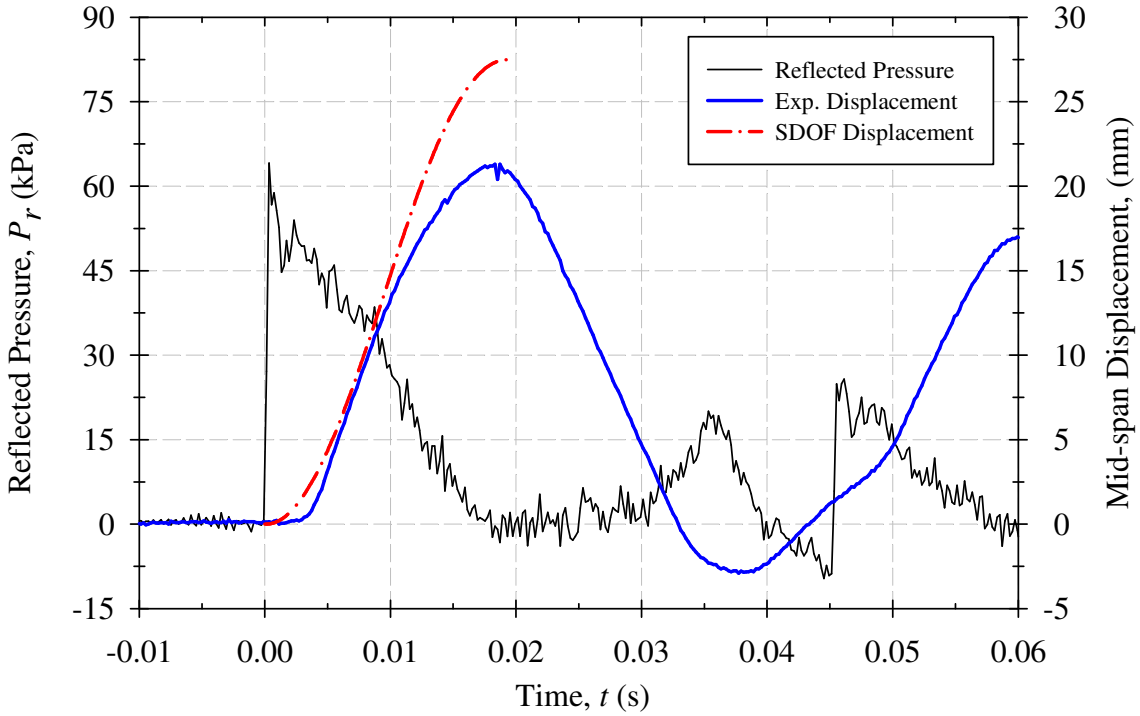

Figure B-52: Experimental mid-span slab displacements plotted against those predicted by SDOF analysis for CS5-C - Shot 5.

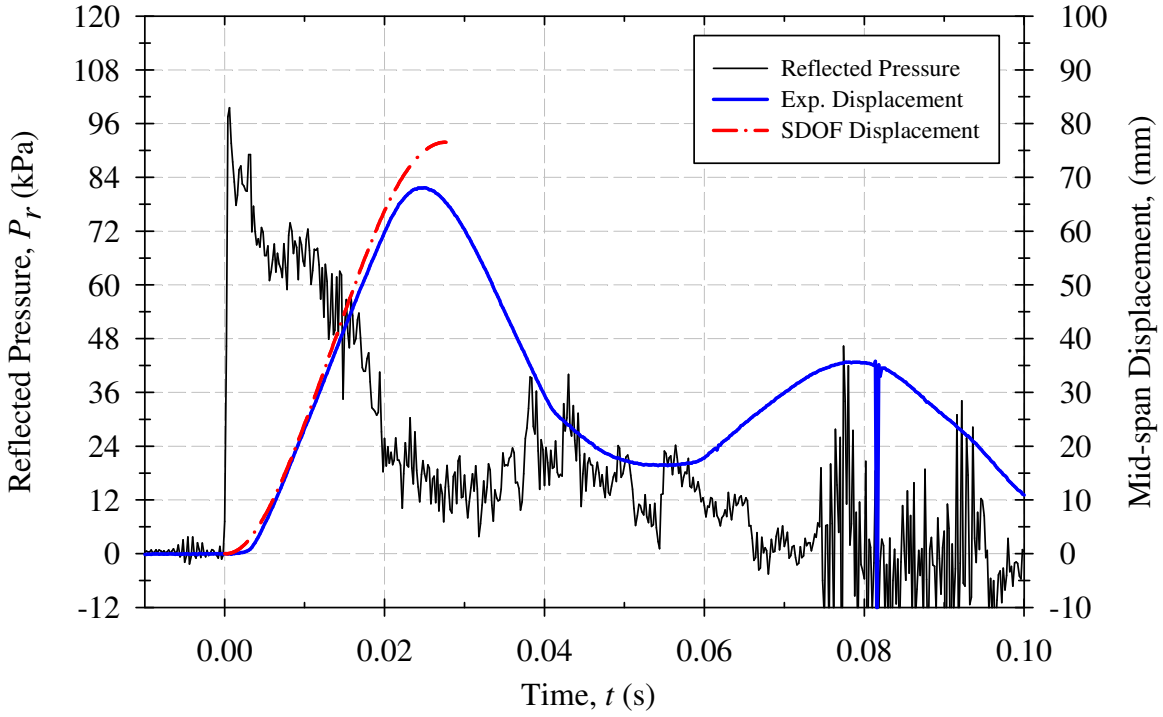

Figure B-53: Experimental mid-span slab displacements plotted against those predicted by SDOF analysis for CS5-C - Shot 6.

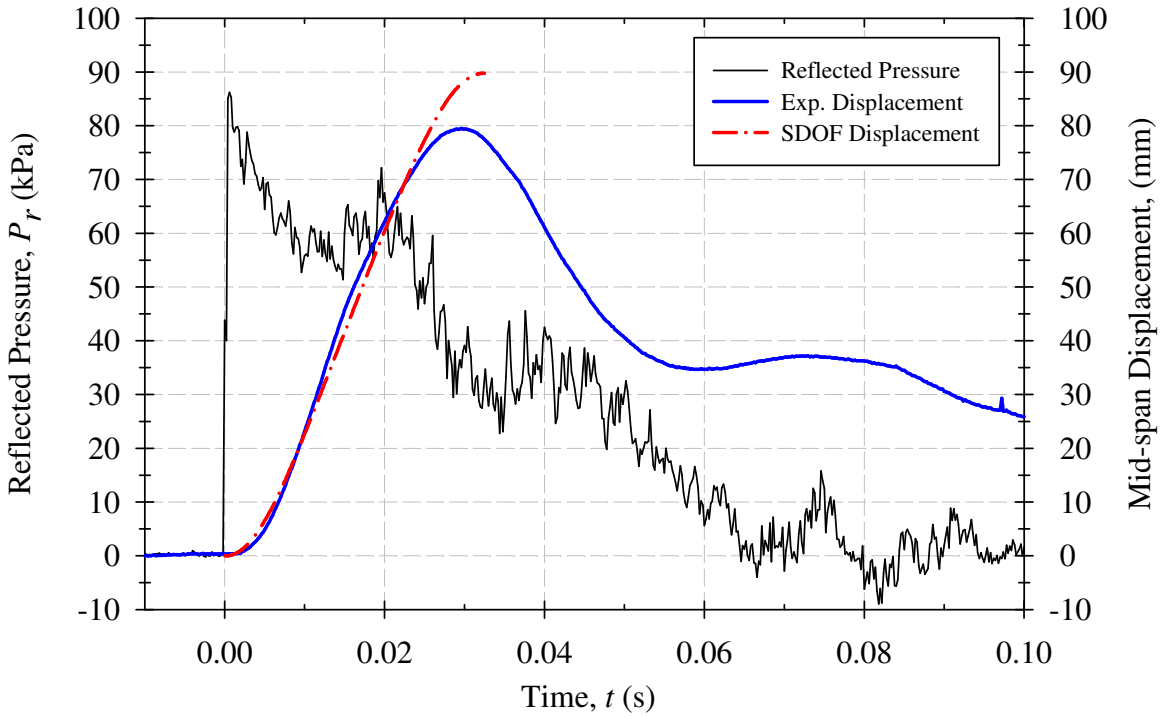

Figure B-54: Experimental mid-span slab displacements plotted against those predicted by SDOF analysis for CS5-C - Shot 7.

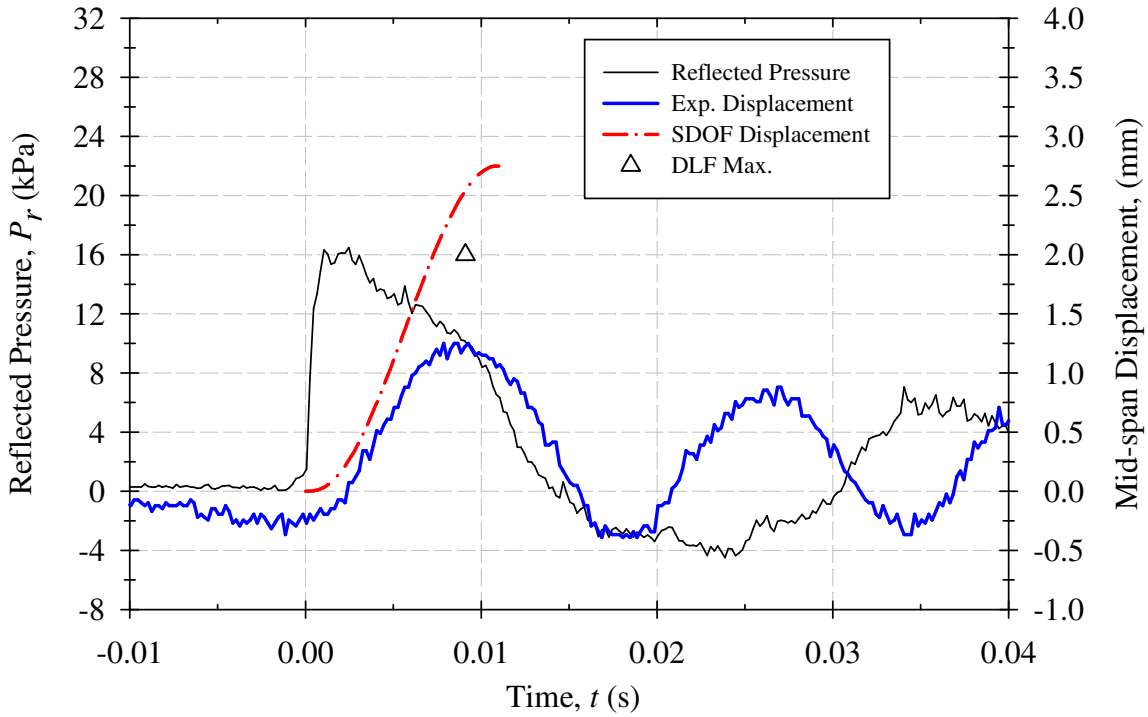

Figure B-55: Experimental mid-span slab displacements plotted against those predicted by SDOF analysis for CS5-R - Shot 1.

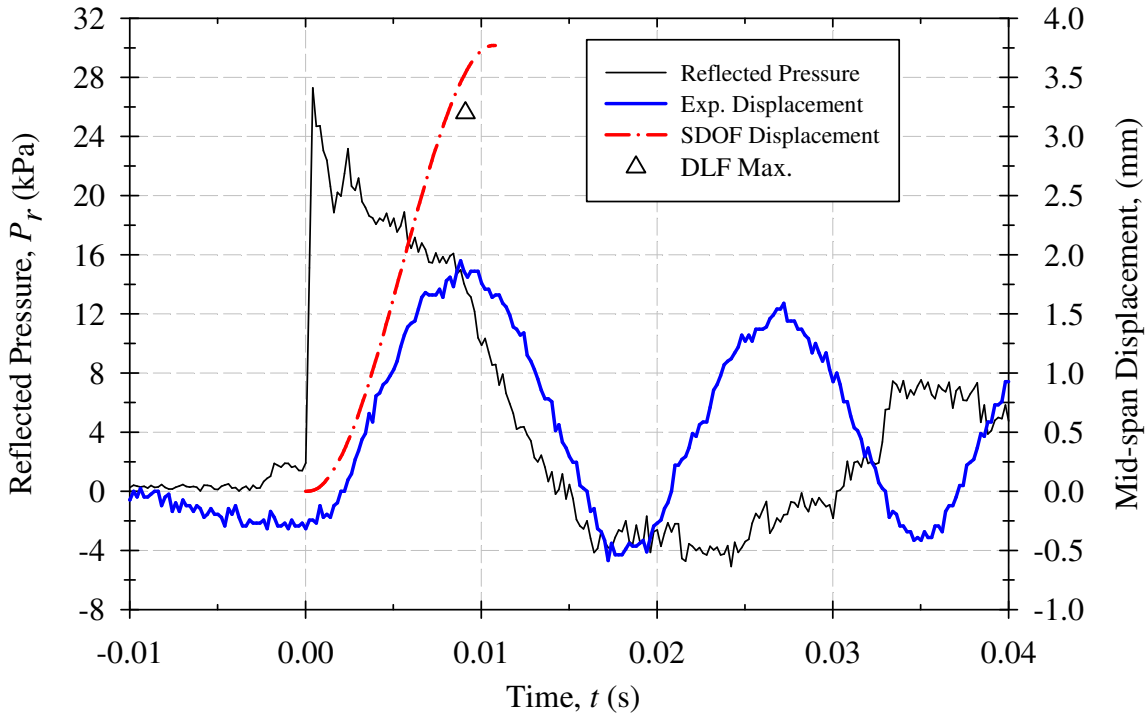

Figure B-56: Experimental mid-span slab displacements plotted against those predicted by SDOF analysis for CS5-R - Shot 2.

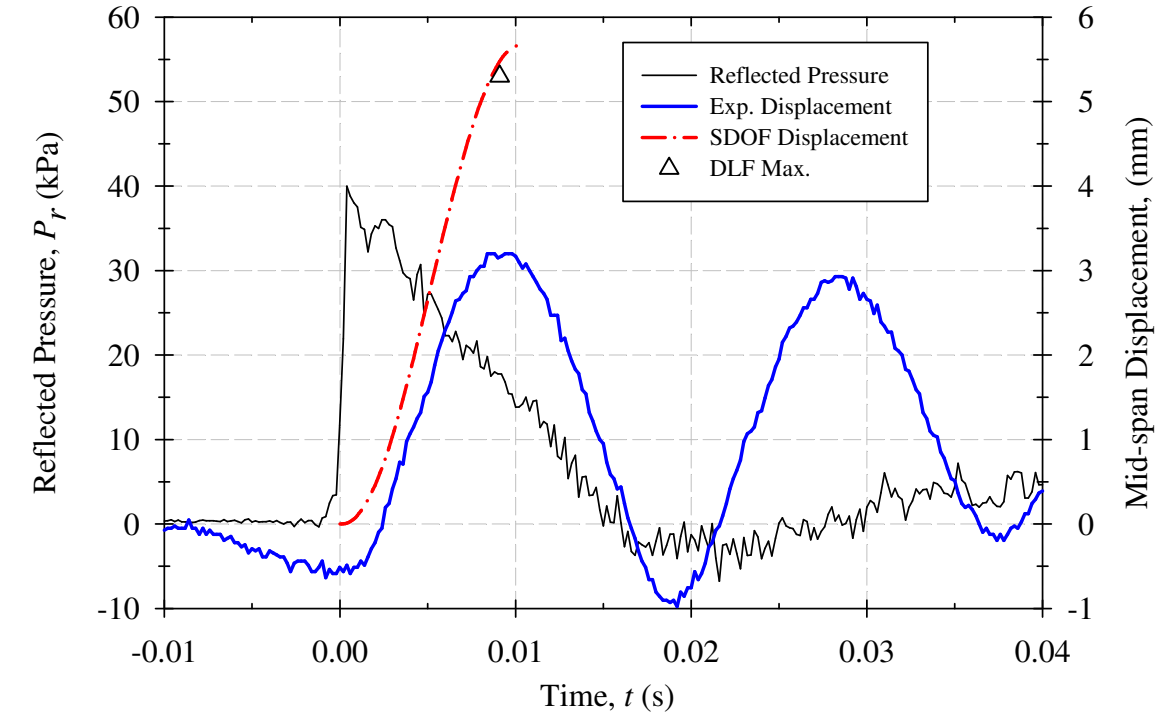

Figure B-57: Experimental mid-span slab displacements plotted against those predicted by SDOF analysis for CS5-R - Shot 3.

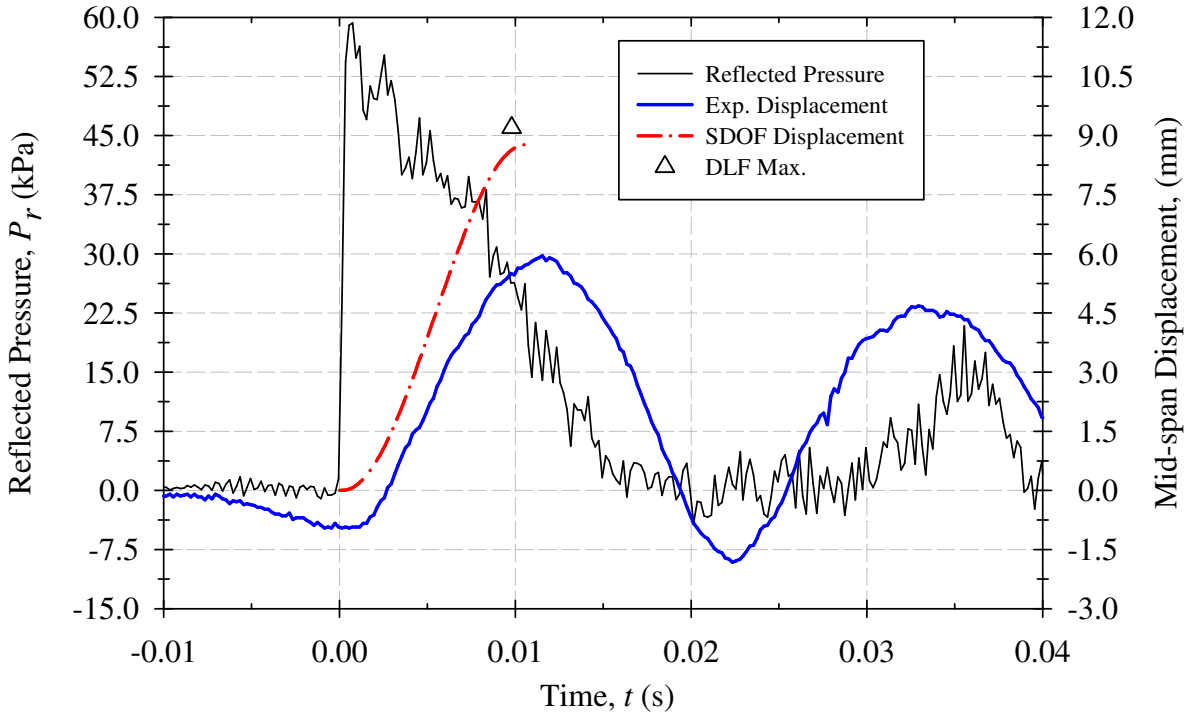

Figure B-58: Experimental mid-span slab displacements plotted against those predicted by SDOF analysis for CS5-R - Shot 4.

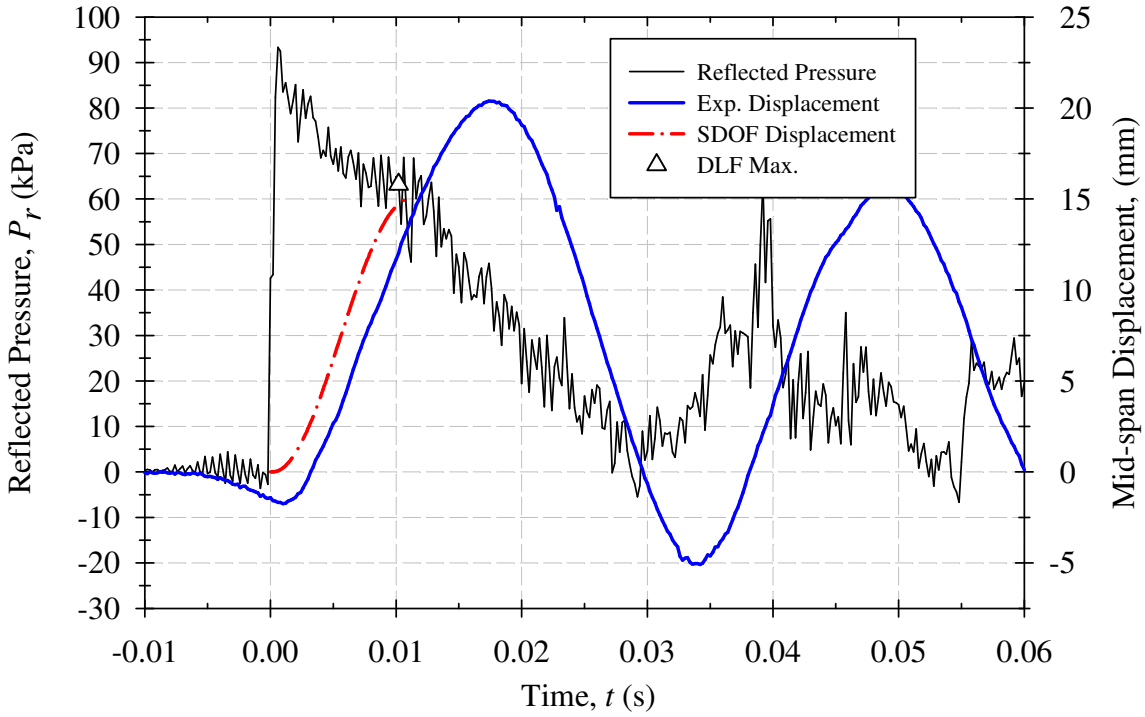

Figure B-59: Experimental mid-span slab displacements plotted against those predicted by SDOF analysis for CS5-R - Shot 5.

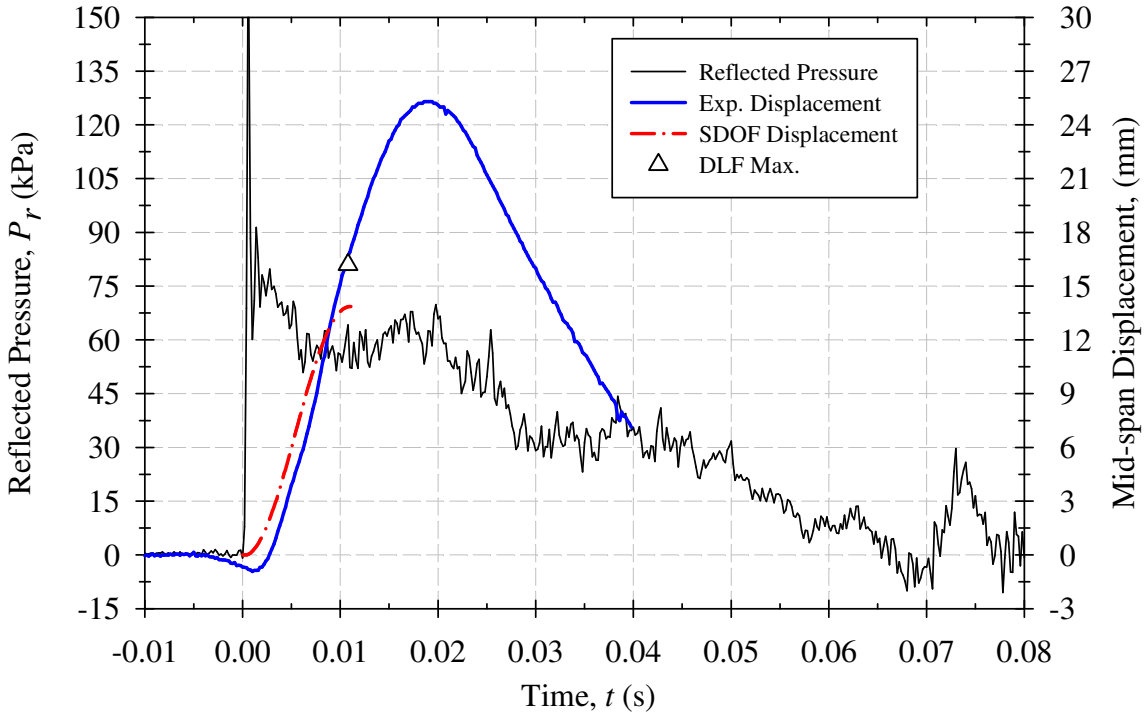

Figure B-60: Experimental mid-span slab displacements plotted against those predicted by SDOF analysis for CS5-R - Shot 6.

Appendix C: PI Diagrams

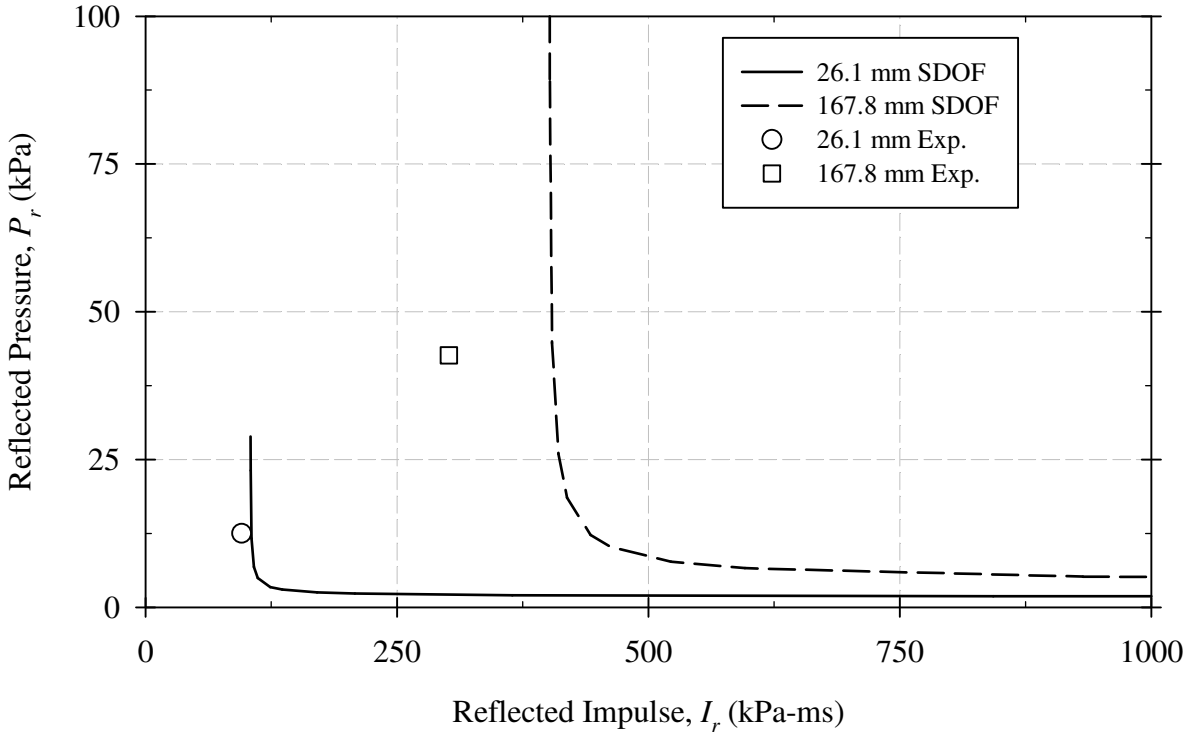

Figure C-1: Predicted PI Diagram with Experimental Pressure-Impulse Combination Overlay for Specimen CS1-C.

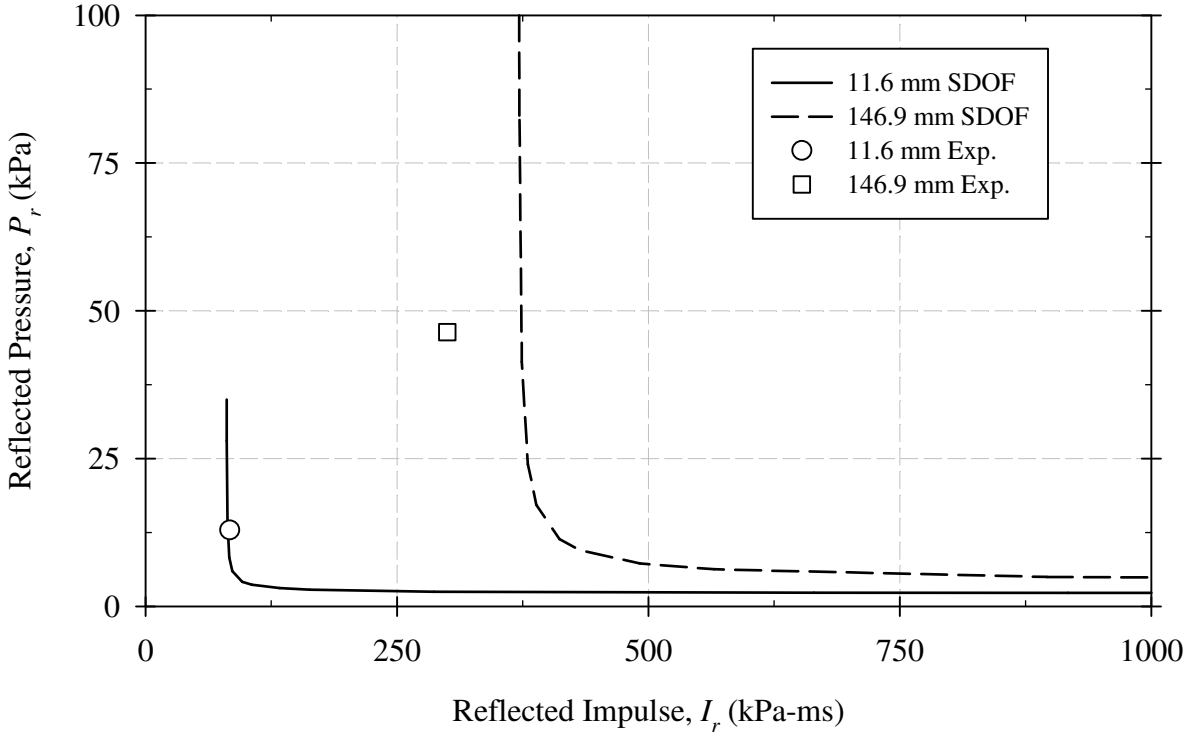

Figure C-2: Predicted PI Diagram with Experimental Pressure-Impulse Combination Overlay for Specimen CS1-R1.

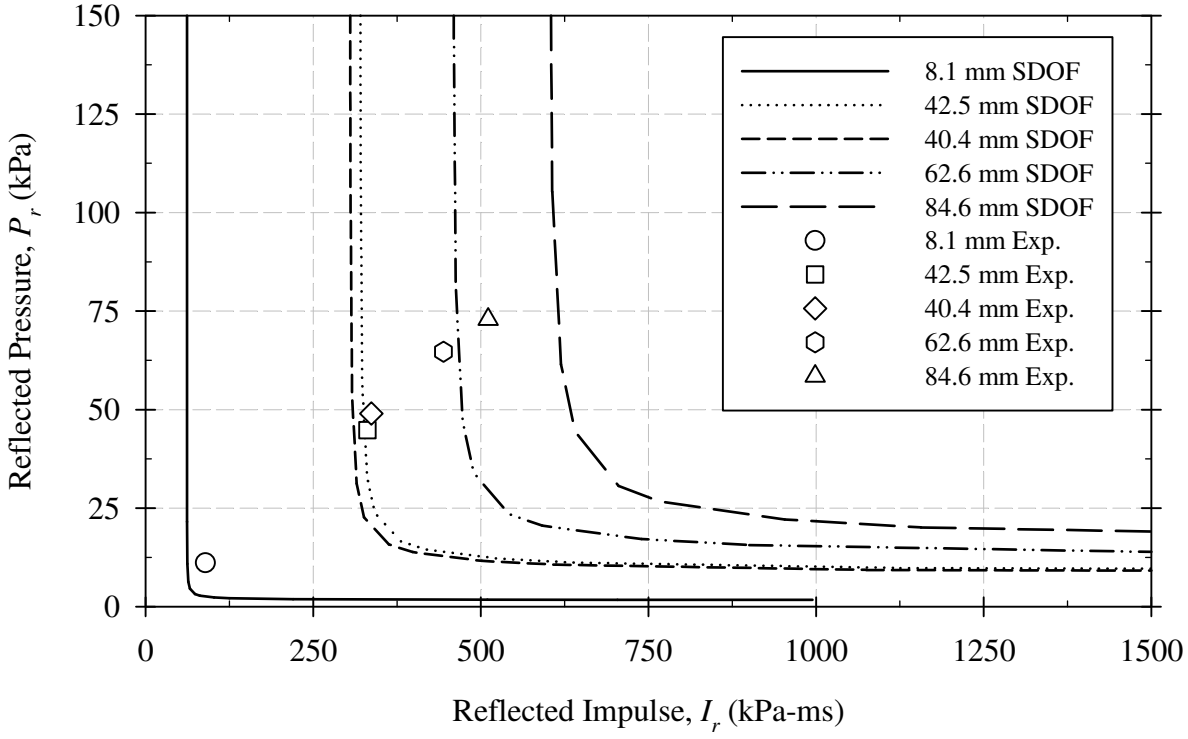

Figure C-3: Predicted PI Diagram with Experimental Pressure-Impulse Combination Overlay for Specimen CS1-R2.

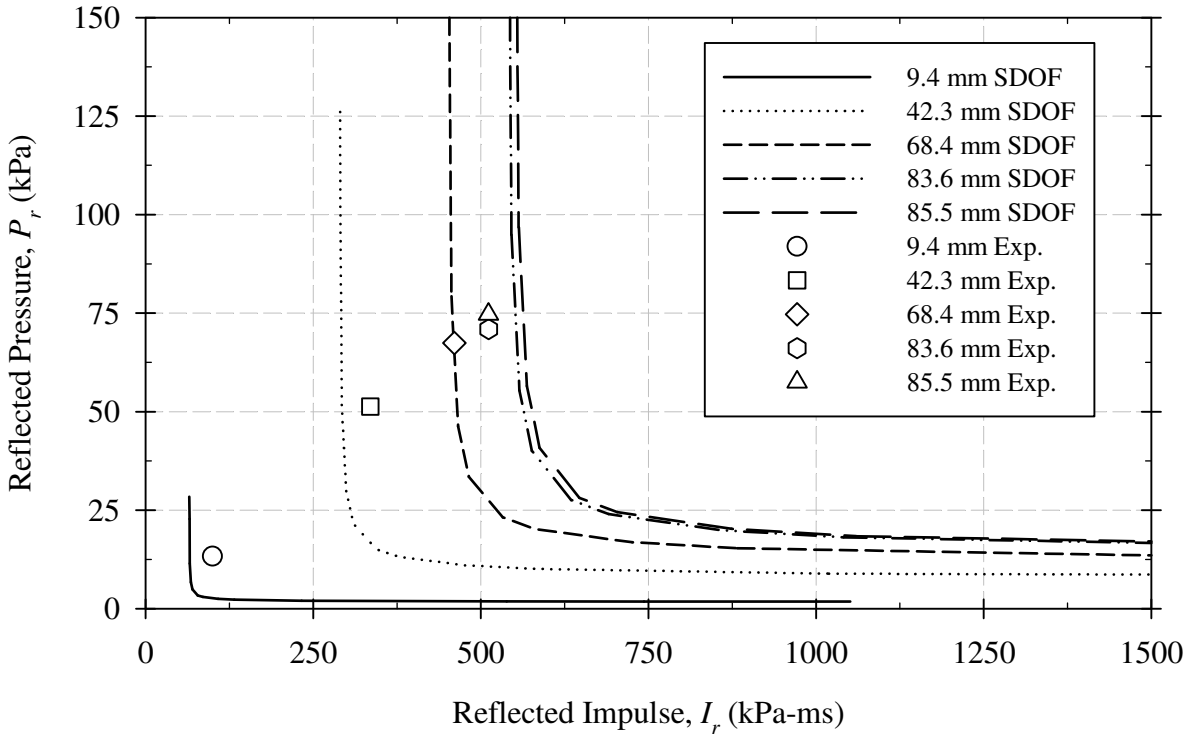

Figure C-4: Predicted PI Diagram with Experimental Pressure-Impulse Combination Overlay for Specimen CS1-A.

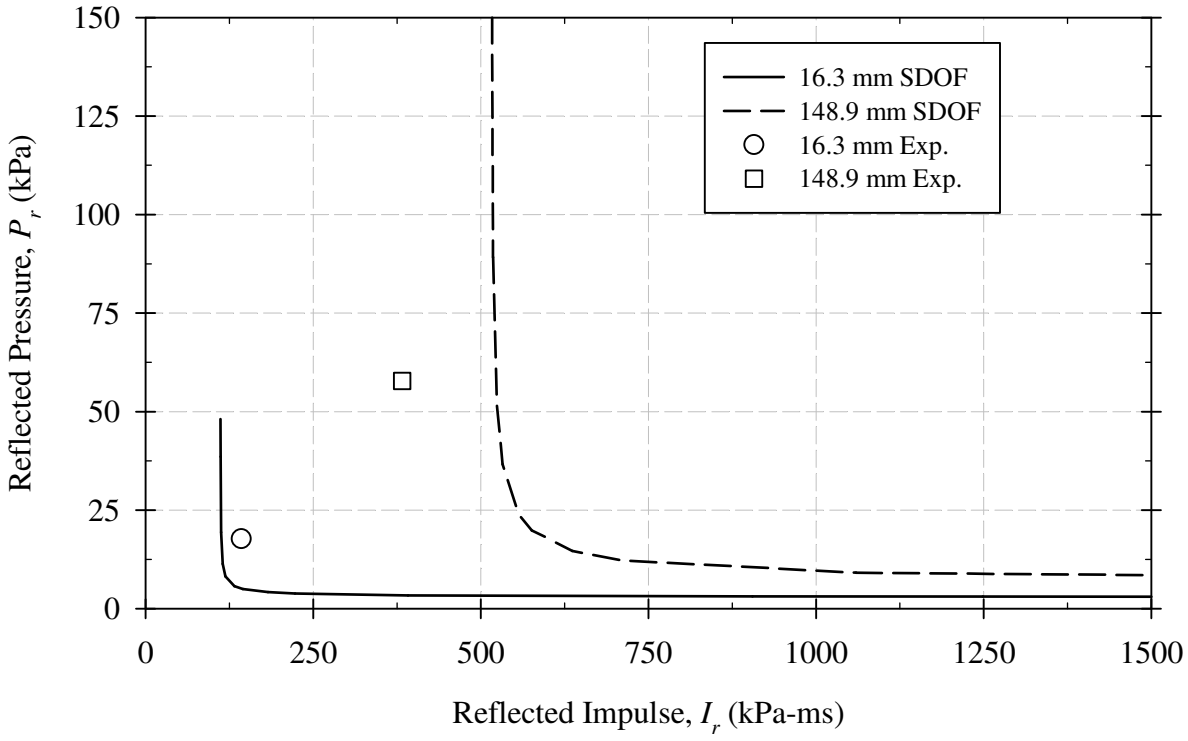

Figure C-5: Predicted PI Diagram with Experimental Pressure-Impulse Combination Overlay for Specimen CS2-C.

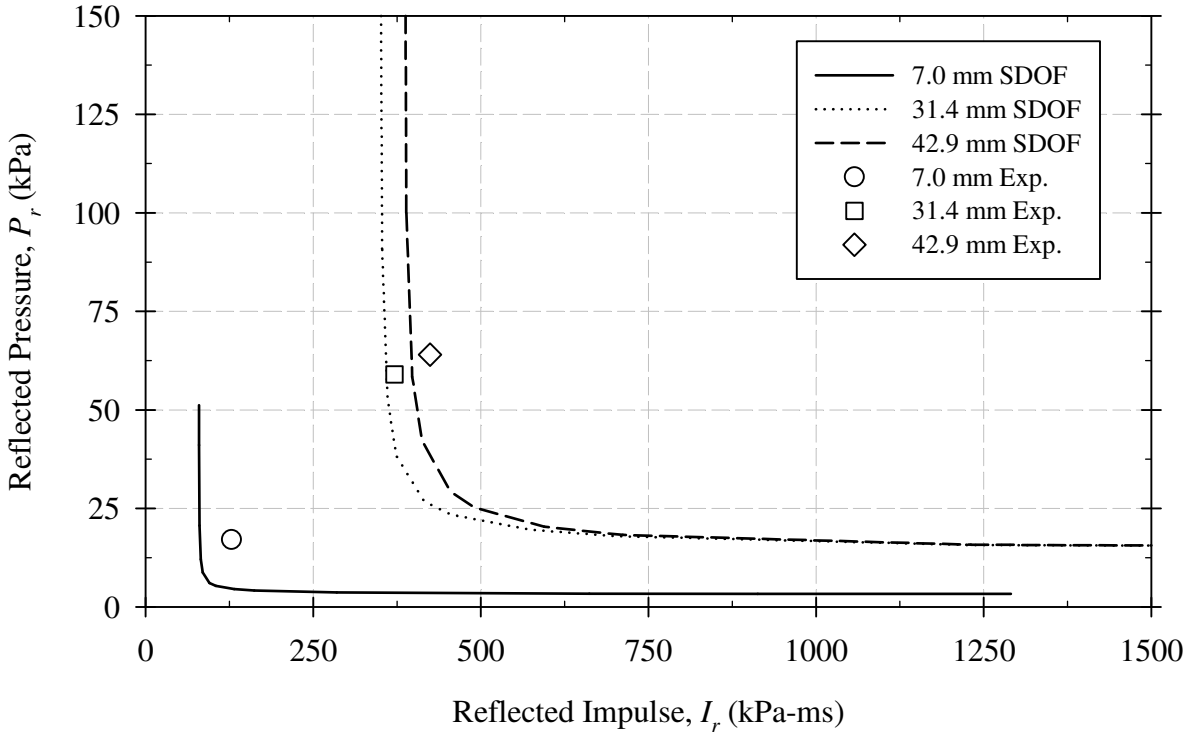

Figure C-6: Predicted PI Diagram with Experimental Pressure-Impulse Combination Overlay for Specimen CS2-R.

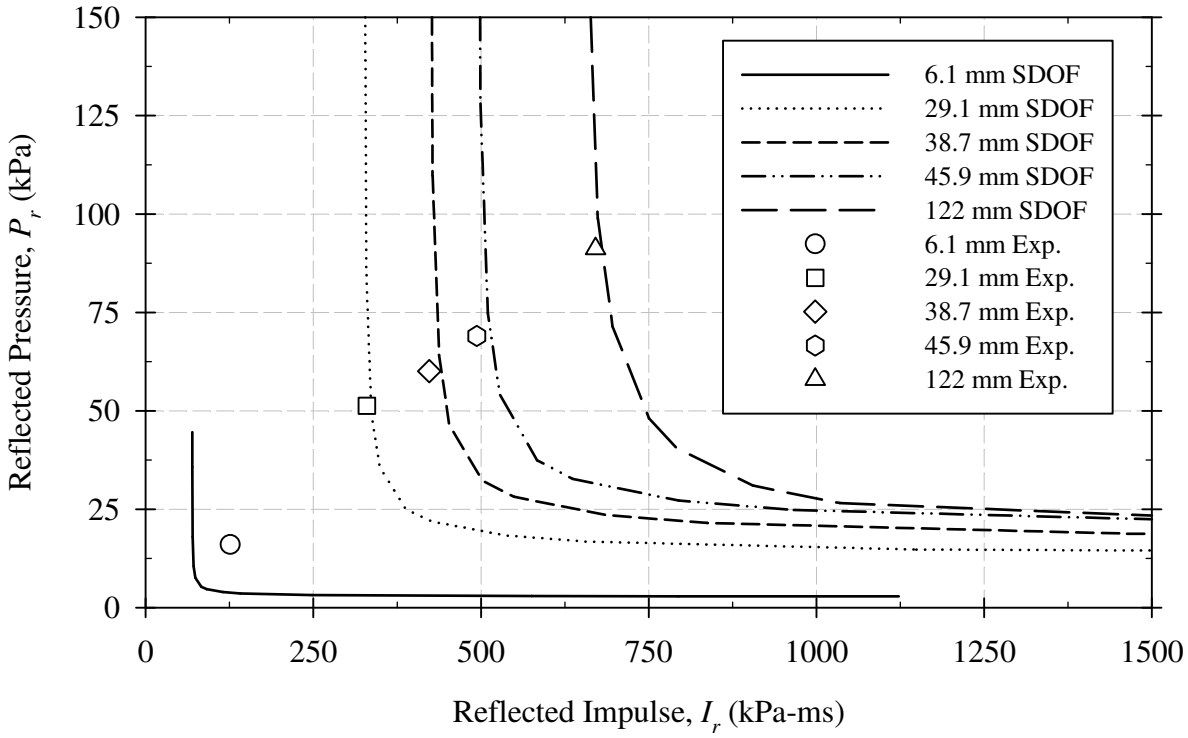

Figure C-7: Predicted PI Diagram with Experimental Pressure-Impulse Combination Overlay for Specimen CS2-A.

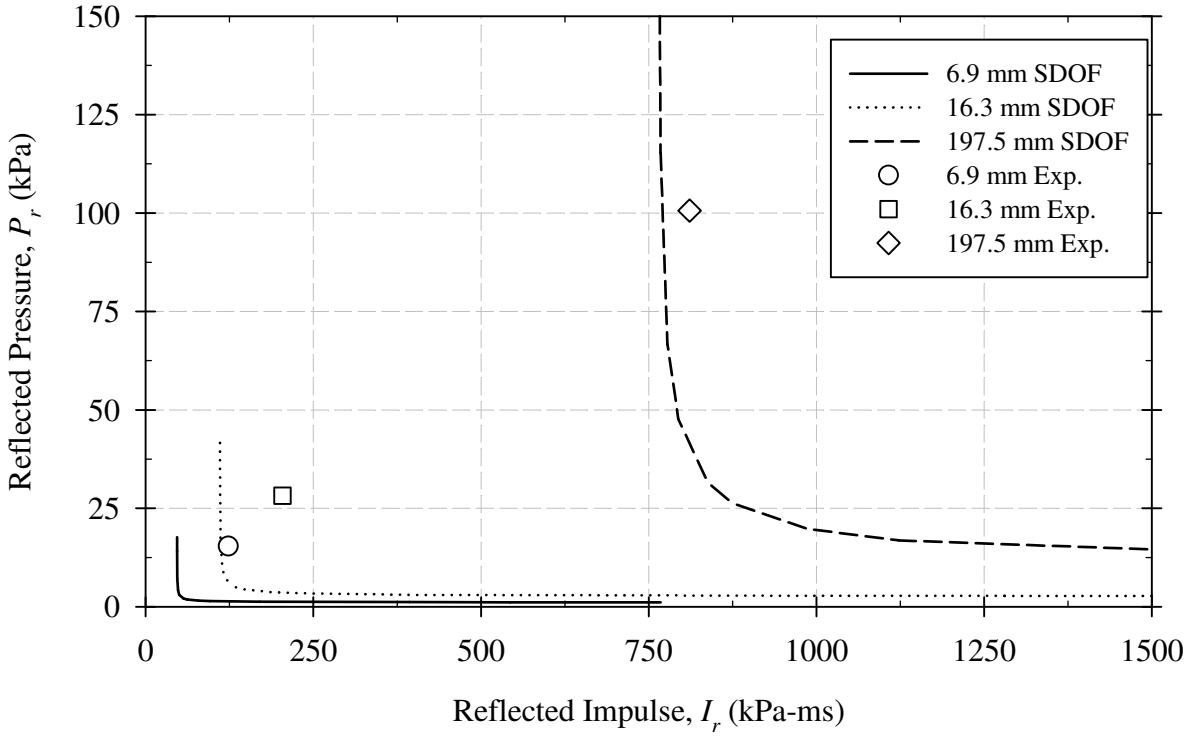

Figure C-8: Predicted PI Diagram with Experimental Pressure-Impulse Combination Overlay for Specimen CS3-C.

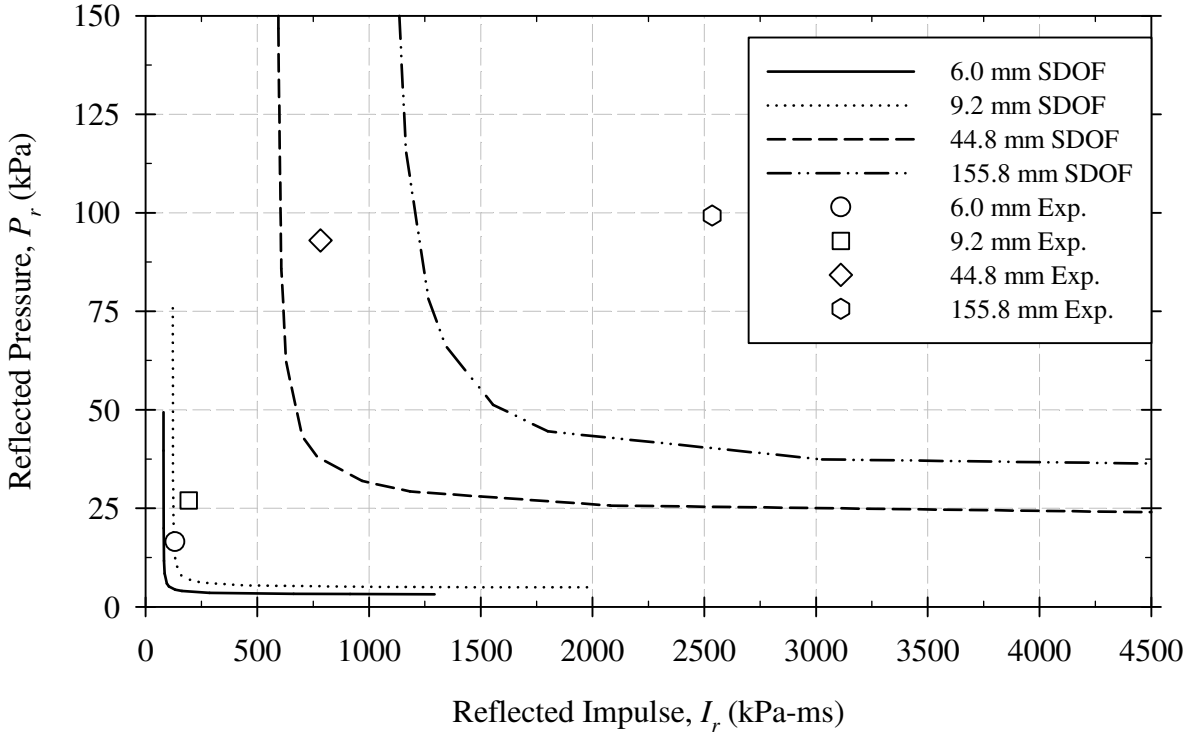

Figure C-9: Predicted PI Diagram with Experimental Pressure-Impulse Combination Overlay for Specimen CS3-R.

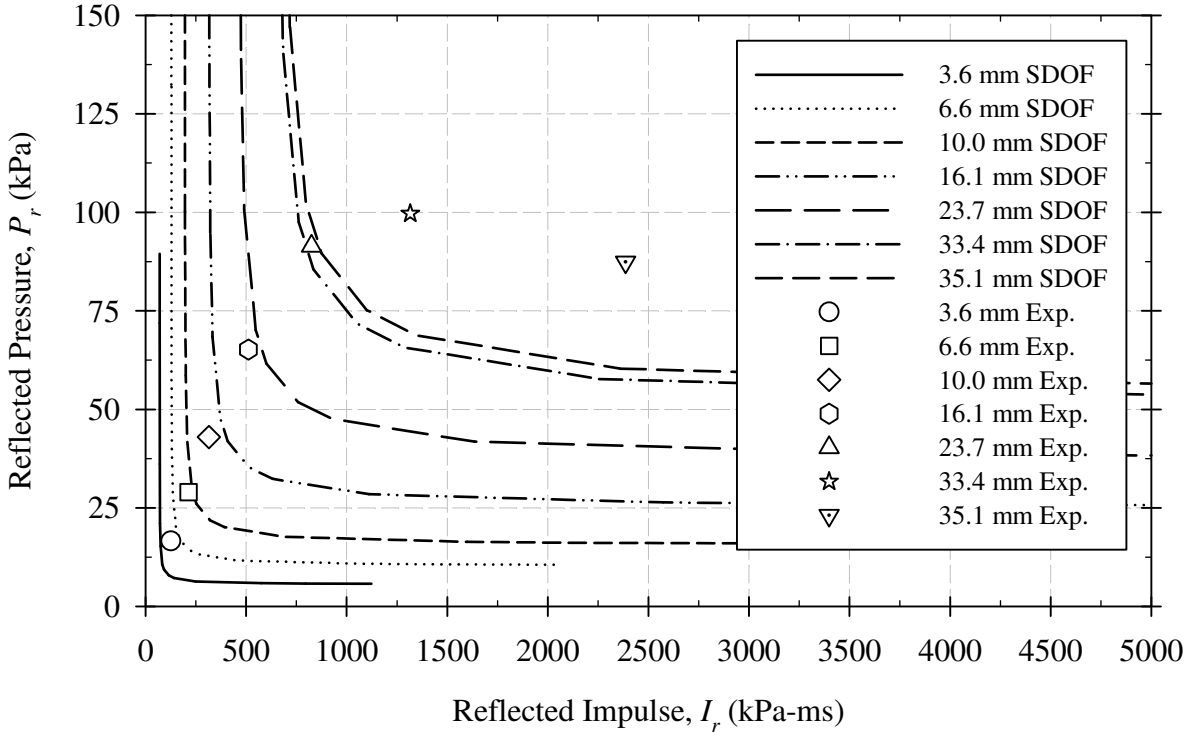

Figure C-10: Predicted PI Diagram with Experimental Pressure-Impulse Combination Overlay for Specimen CS4-R1.

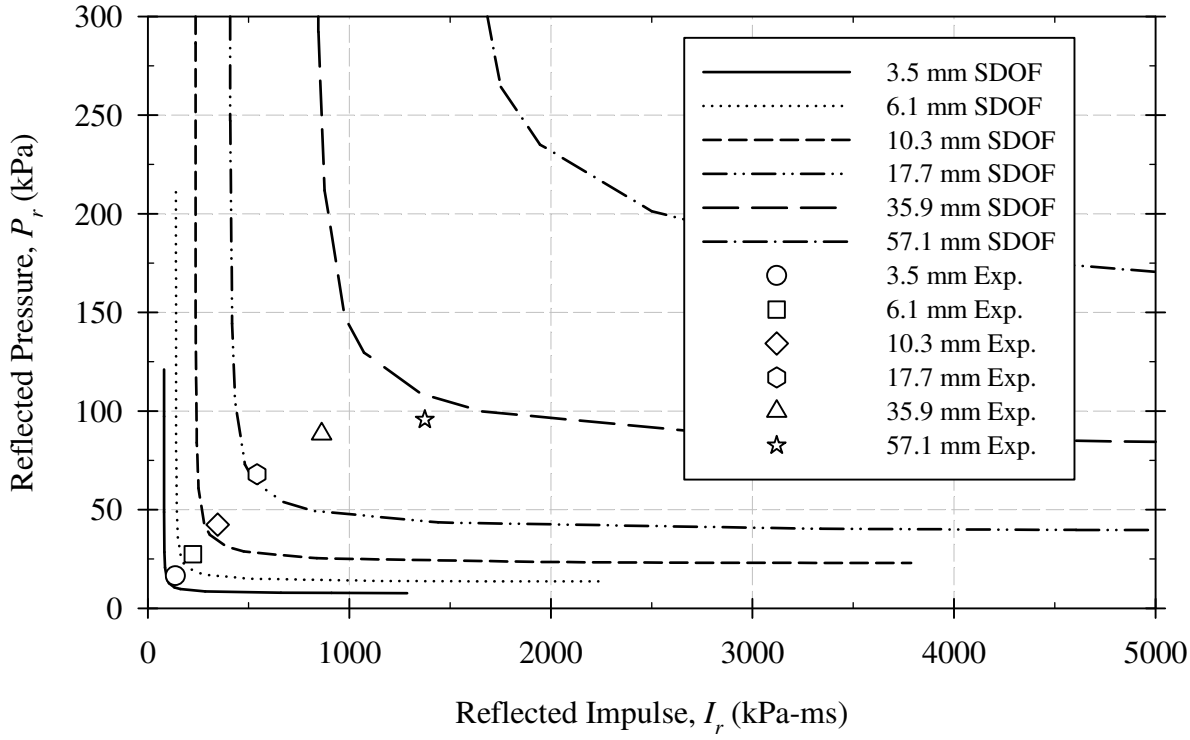

Figure C-11: Predicted PI Diagram with Experimental Pressure-Impulse Combination Overlay for Specimen CS4-R2.

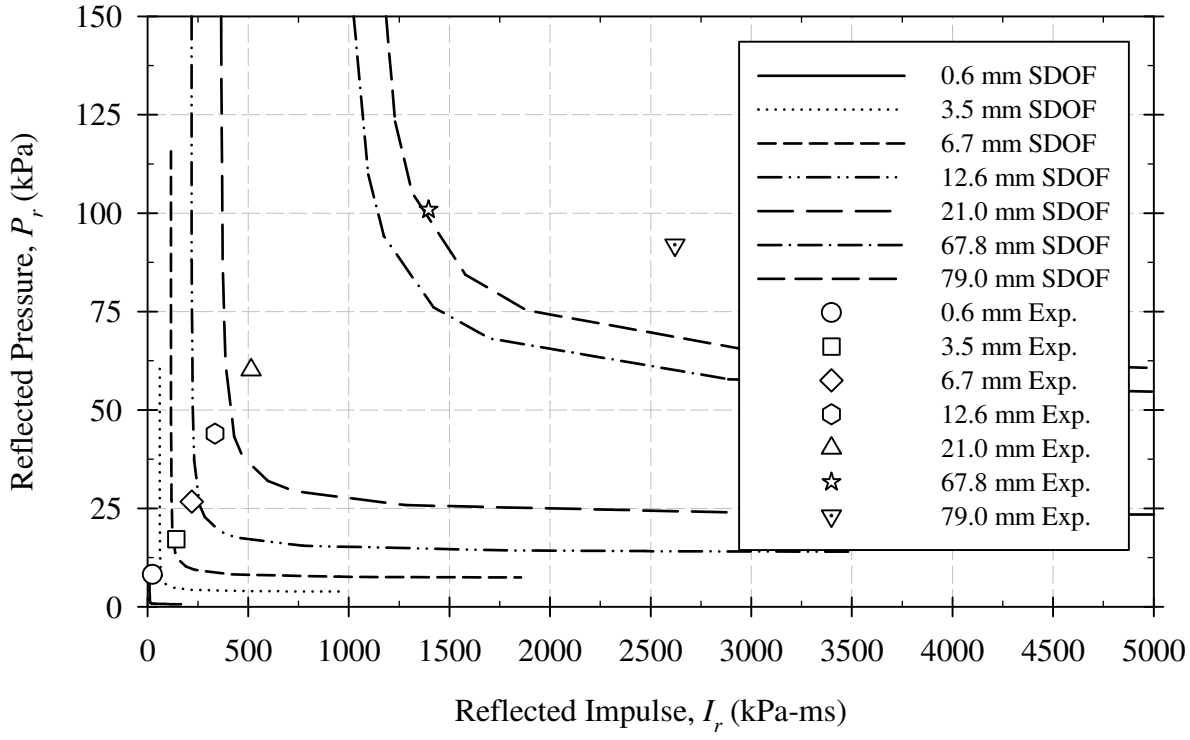

Figure C-12: Predicted PI Diagram with Experimental Pressure-Impulse Combination Overlay for Specimen CS5-C.

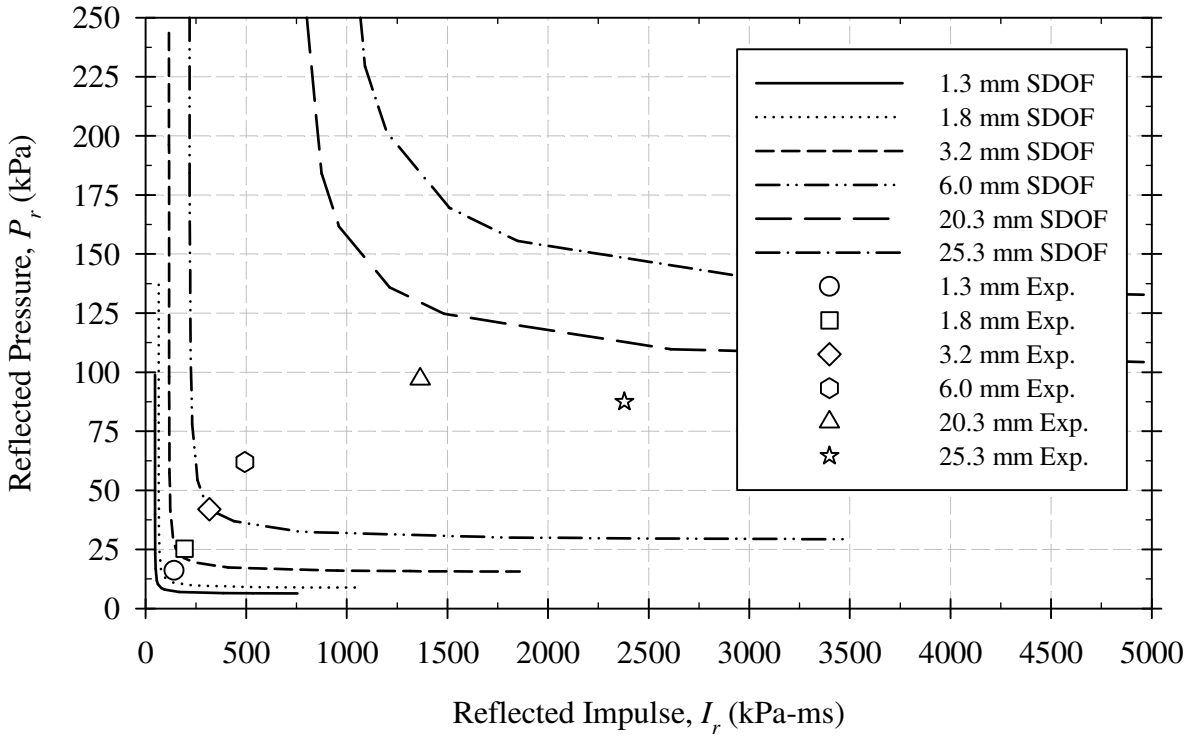

Figure C-13: Predicted PI Diagram with Experimental Pressure-Impulse Combination Overlay for Specimen CS5-R.